



HAL
open science

High quality van der Waals heterostructures for optoelectronics and spintronics

Emmanuel Courtade

► **To cite this version:**

Emmanuel Courtade. High quality van der Waals heterostructures for optoelectronics and spintronics. Physics [physics]. INSA de Toulouse, 2019. English. NNT : 2019ISAT0038 . tel-03457020

HAL Id: tel-03457020

<https://theses.hal.science/tel-03457020>

Submitted on 30 Nov 2021

HAL is a multi-disciplinary open access archive for the deposit and dissemination of scientific research documents, whether they are published or not. The documents may come from teaching and research institutions in France or abroad, or from public or private research centers.

L'archive ouverte pluridisciplinaire **HAL**, est destinée au dépôt et à la diffusion de documents scientifiques de niveau recherche, publiés ou non, émanant des établissements d'enseignement et de recherche français ou étrangers, des laboratoires publics ou privés.



THÈSE

En vue de l'obtention du

DOCTORAT DE L'UNIVERSITÉ DE TOULOUSE

Délivré par *l'Institut National des Sciences Appliquées de Toulouse (INSA)*
Discipline ou spécialité : *Nano-physique, nano-composants, nano-mesures*

Présentée et soutenue par *Emmanuel COURTADE*
Le 27/09/2019

Titre : *High quality van der Waals heterostructures for optoelectronics and spintronics*

JURY

Valia VOLIOTIS
Christophe VOISIN
Jacek KASPRZAK
Michel GOIRAN
Bernhard URBASZEK
Pierre RENUCCI

Professeure des Universités
Professeur des Universités
Chercheur au CNRS
Professeur des Universités
Directeur de recherche au CNRS
Professeur des Universités

Rapporteur
Rapporteur
Examineur
Examineur
Directeur de thèse
Co-directeur de thèse

Ecole doctorale : *Ecole Doctorale des Sciences De la Matière (EDSDM)*
Unité de recherche : *Laboratoire de Physique et Chimie des Nano-Objets (LPCNO)*
- UMR 5215

Directeur(s) de Thèse : *Bernhard URBASZEK et Pierre RENUCCI*
Rapporteurs : *Valia VOLIOTIS et Christophe VOISIN*

Summary

Summary

Atomically thin materials such as monolayers of graphite, called graphene, can be isolated with simple experimental methods. Since 2010 the research in atomically thin transition metal dichalcogenides (TMDs) such as MoS_2 and WSe_2 is one of the most active areas of condensed matter and materials physics research. This has several reasons : bulk TMD crystals have been studied since decades and are in the 2H phase semiconductors with an indirect bandgap. The gap remains indirect also for thinner crystals up to the bilayer limit, but when going from bilayer to monolayer the bandgap becomes direct and makes TMD monolayers interesting for applications in optoelectronics and for fundamental research in light-matter interaction. In addition to being direct, optical transitions at the K-points of the brillouin zone are governed by chiral optical selection rules. By using polarized light of right or left handedness optical transitions in the K^+ or K^- valley, respectively, can be addressed. The K^+ and K^- valleys are related by time reversal symmetry. This allows manipulating optically the valley index and allows interesting studies in the field of valleytronics. Here the target is to measure and understand valley polarization initialization and memory for potential applications. The valence and conduction bands at the K-points are spin split by the spin-orbit interaction, so in optical spectroscopy the valley and spin states are manipulated. Optical transitions are governed by electron-hole pairs, excitons, bound by Coulomb attraction leading to binding energies in the hundreds of meV range.

At the beginning of this thesis many of these interesting properties were inaccessible. Details of optical transitions and their polarization properties were masked by the low sample quality. In this thesis we report on the considerable improvement in sample quality. We detail the sample fabrication procedures developed at the LPCNO based on exfoliation and dry stamping. Our samples show spectrally narrow transitions approaching the homogeneous limit. This allows detailed studies of excitonic properties in applied magnetic fields and in charge-tunable structures using photoluminescence and differential reflection spectroscopy. We access important information such as the exciton binding energies and the fine-structure splitting of charged excitons and we outline open questions and future challenges in this research field.

Résumé

Des matériaux atomiquement minces tels que des monocouches de graphite, appelé graphène, peuvent être isolés avec des méthodes expérimentales simples. Depuis 2010, l'étude des monocouches de dichalcogénures de métaux de transition (TMD) tels que le

MoS_2 et le WSe_2 est l'un des champs les plus actifs en matière de recherche dans le domaine de la matière condensée et de la physique des matériaux. Ces nouveaux systèmes sont attractifs pour différentes raisons. Les cristaux de TMD sous forme de matériaux massifs ont été étudiés depuis des décennies et constituent, dans la phase 2H, des semi-conducteurs à bande interdite indirecte. Le gap reste également indirect pour les cristaux plus minces jusqu'à la limite de la bicouche, mais lorsque l'on passe de la bicouche à la monocouche, la bande interdite devient directe et rend les monocouches de TMD intéressantes en vue d'applications en optoélectronique, ainsi que, du point de vue de la recherche fondamentale, dans le domaine de l'interaction lumière-matière. En plus d'être directes, les transitions optiques aux points K de la zone de Brillouin sont régies par des règles de sélection optique chirales. En utilisant une lumière polarisée circulairement droite ou gauche, des transitions optiques dans la vallée K^+ ou K^- , respectivement, peuvent être adressées. Les vallées K^+ et K^- sont liées par la symétrie par inversion du temps. Ici, l'objectif est de mesurer et de comprendre l'initialisation de la polarisation des vallées et la durée de vie de cette polarisation en vue de potentielles applications. Les bandes de valence et de conduction aux points K sont scindées en spin par l'interaction spin-orbite. Ainsi, en spectroscopie optique, les états de vallée et de spin peuvent être manipulés, ouvrant des perspectives concernant une électronique alternative basée sur ces états (« valleytronics »). Les transitions optiques sont gouvernées par des paires électron-trou appelées excitons, liées par l'attraction de Coulomb conduisant à des énergies de liaison de l'ordre de plusieurs centaines de meV.

Au début de cette thèse, beaucoup de ces propriétés intéressantes étaient inaccessibles. Les détails des transitions optiques et de leurs propriétés de polarisation ont été masqués par la faible qualité optique des échantillons. Un point clé de cette thèse réside dans l'amélioration considérable de la qualité des échantillons. Nous détaillons les procédures de fabrication des échantillons développées au LPCNO qui dérivent de l'exfoliation et de méthodes sèches de stamping ne requérant pas l'utilisation de solvants. Nos échantillons montrent des transitions spectralement étroites approchant la limite homogène. Cela permet des études détaillées des propriétés excitoniques sous champs magnétiques appliqués et dans les structures à charge ajustable, en utilisant la spectroscopie de photoluminescence et de réflexion différentielle. Nous avons ainsi accès à des informations importantes telles que les énergies de liaison des excitons et la structure fine des excitons chargés, et nous soulignons les questions en suspens et les défis futurs dans ce domaine de recherche.

Acknowledgements

I was born not knowing, and have only had a little time to change that here and there.

Richard Feynman

To begin, I would like to thank Valia Voliotis, Christophe Voisin, Jacek Kasprzak and Michel Goiran for accepting to be part of the jury members of my thesis. Thank you for the time you dedicated to study my work and the interest that you demonstrated through your reports and questions.

After these three years as a PhD student at the LPCNO (Laboratoire de Physique et Chimie des Nano-Objets), I want to express my sincere acknowledgements to the people I had the chance to meet during my work. This thesis was indeed a great adventure for me, both for its scientific and human dimensions.

First, I am very thankful to my supervisor Bernhard Urbaszek who trusted me by accepting my application to this PhD. Bernhard was a real team manager, taking care of several PhD students and postdocs at the same time. He kept sure that everyone had a role to play during the research process, sharing the tasks between the different team members to make the research more effective by establishing a team spirit. This is essential to remain in the running in this very competitive research field of 2D transition metal dichalcogenides. I am also thankful for the trust that my supervisor put in me by giving me the opportunity to participate to very interesting projects such as our collaboration with the Hui Deng's team at the University of Michigan or the Rank Prize Meeting which gathered many renowned experts of our research area. Thank you for accompanying me during these three years.

When I joined the Quantum Optoelectronics group in october 2016, apart from some basic knowledge, I had to discover almost everything about transition metal dichalcogenide monolayers. I had to learn how to study them experimentally. Cédric Robert was here, from the beginning, to train me. He has shown me how to fabricate van der Waals heterostructures and how to perform spectroscopy on our samples. He has dedicated a lot of time for this, demonstrating teaching qualities. In addition, he followed regularly my work and is one of the person I worked the most with. Despite some failures and broken

samples he continued to trust me, always giving me some work to do.

Among the people without whom this experimental work would not have been possible, there is also Delphine Lagarde. She is always keeping an eye on the experimental setups making sure that they are operational so that we can use them. She improves these setups regularly and our experimental progress in spectroscopy and fabrication is strongly based on her work.

Xavier Marie is also undoubtedly a strong pillar of the Quantum Optoelectronics group. It was a great opportunity to work with you on TMD monolayers. Thank you for your communicative enthusiasm and the dynamism you put in managing teams. I am also grateful to you for giving me the chance to go to some interesting conferences such as the "GDR Graphene & Co" in Aussois and the "Journées de la Matière Condensée (JMC)" in Grenoble.

I will not forget Thierry Amand who was also very available to talk about Physics. I will remember your passion for Physics and its mathematical tools (such as Group Theory!). I also appreciated our discussions about non scientific subjects. Thank you for your time Thierry. For sure you will leave an indelible mark in the history of the group.

I am grateful to Pierre Renucci for his constant encouragements and his human qualities. I will remember your strong interest and dedication for education.

Among the permanent members of the team, Andrea Balocchi and Helene Carrere will always remain for me the nice and dynamic teachers I knew when I was a student at INSA. Even if we did not work on the same subjects, it was a pleasure to rub shoulders with you.

Then, of course, there are all the non permanent members. The PhD students: Sawsen Azaizia, Marco Manca, Maxime Mauguet, Bo Han, Shivangi Shree. The postdoctoral researchers: Fabian Cadiz, Gang Wang, Maher Nafouti and Honghua Fang.

Marco, you began your PhD 4 months before me. We started almost at the same time so we overcame a lot of similar obstacles! Now that this is finished, I wish you good luck for your future life and work!

Thank you Fabian for working with me on spectroscopy experiments during the first months of my PhD. When I arrived, as a new PhD student, it was reassuring to work with you as you are a nice and calm person with excellent scientific skills. I wish you a bright future at the Ecole Polytechnique.

Shivangi, I liked working with you in a friendly atmosphere. And I think everyone will remember your legendary communicative smile. May the serendipity be with you during your future long hours of exfoliation! Thanks for your constant help. In particular I will

never forget how helpful and encouraging you were with me the day of my defense! Thanks a lot Shivangi!

Dear Bo, we spent long time working together (on AFM measurements, fabrication, spectroscopy etc...). It was always a pleasure because you are a good scientist and also because I like your sense of humor. You will always remain Golden Fingers... The one who is able to find the best optical spectrum on a sample by changing position with a simple flick!

Honghua, I wish you good luck to you and your family for your future life in Beijing.

Even if we did not work on the same subject, I often interacted with you Maxime. It was a pleasure to discuss with you about everything. Thank you for having been so welcoming!

Sawsen, we discussed together repeatedly and had several interesting conversations. I hope your future will fulfill your expectations. Have a peaceful life and be a good teacher!

Maher, even if you did not stay for long in our group, I appreciated speaking with you. Also, I think we will both remember how difficult it was to put back this aluminum wire in the needle when we made bondings on your sample!

Outside our Quantum Optoelectronics team, other people helped me to pursue my work. The LPCNO is composed of several teams which have developed expertises in different subjects. This is a strong advantage as it is possible to ask for help when we do not master a particular subject. Among the people who helped me I want especially to thank Benjamin Lassagne and Alexandre Pierrot without whom I could not have performed all my AFM measurements on our van der Waals heterostructures. During this work I also had the opportunity to work with Mélodie Humbert who was a motivated master student in our team at this time; now that you are working on your PhD I wish you the best for the future! Also I want to thank Etienne Palleau who helped us to try fabrication techniques with polymer stamps such as the pick-up method with PC. I also have to express my acknowledgments for Iann Gerber who is working regularly with us by bringing his theoretical expertise (for example performing DFT calculations). More generally I want to express my acknowledgements for all the people working at the LPCNO who helped me occasionally or regularly.

I also liked to rub shoulders with friends and colleagues at LPCNO. I enjoyed discussing with Nicolas Mille, Pierre Moritz, Stéphane Faure, Romain Platel, François Guérin, Marc Respaud, Sébastien Pinot... You all contributed to make the laboratory a nice working environment.

I am also grateful to many people outside of LPCNO. First, next to LPCNO in the INSA campus, I want to thank the team from AIME with whom LPCNO interacts, espe-

cially for sample fabrication. In Toulouse, Mathieu Pierre from LNCMI helped me several times (for example to do bondings on my samples or for the contact patterning with E-beam lithography). Thank you Mathieu for having been so available. Also I want to thank Bénédicte Warot-Fonrose and Robin Cours, from CEMES, who helped us by performing TEM measurements of the cross-section of some of our van der Waals heterostructures. This was quite helpful to assess our sample quality and this experiment has been an important additional proof of the high quality of our samples. Also from CEMES, I want to thank Vincent Paillard and Aurélien Cuche who started recently with Bernhard an interesting collaboration to couple TMD monolayers with nano-resonators. I am sure the future of this team work will be fruitful.

Outside Toulouse, we also worked with many other people from France and other countries: Scott Crooker from Los Alamos, Mikhail Glazov and Marina Semina from Ioffe Institute, Takashi Taniguchi and Kenji Watanabe from NIMS in Japan, Siamak Nakhaie, Lutz Geelhaar and João Marcelo Lopes from Paul-Drude Institute in Berlin, Sefaattin Tongay from Arizona State University... And the list could be undoubtedly longer!

I want also to highlight here a great experience I was able to live thanks to my PhD supervisor Bernhard and Hui Deng from the University of Michigan. I had the great opportunity to go to the US to work during one month in the Randall Laboratory in Ann Arbor with the local team. I especially met Long Zhang and Jason Horng. This was an excellent experience to discover another working environment. Thank you for this experience which will remain in my mind forever!

These three years of work would not have been the same without the presence of my friends (Thomas, Aurélien, David, Florian, Julien, Valentin...), for me our cohesive group will always remain united.

To finish this section I want to particularly thank my family which is always on my side in the good and the bad moments. I thank my brother Alexandre and my father. Finally, I thank my dear mum who found some of her last strengths to stay among us until the end of my PhD.

Contents

Introduction	1
1 Introduction to Transition Metal Dichalcogenide monolayers	3
1.1 Why this interest for 2D materials?	3
1.2 2D Transition Metal Dichalcogenides	5
1.2.1 TMD crystal structure	5
1.2.2 Band structure	7
1.2.3 Excitons in TMD monolayers	10
1.2.4 Circular dichroism in TMD monolayers	17
1.3 Towards devices with TMD monolayers	21
1.4 Conclusions	24
2 Sample fabrication and experimental setups	25
2.1 An overview of fabrication techniques	25
2.1.1 The PDMS deterministic transfer method	26
2.1.2 Other techniques to assemble structures on the substrate	29
2.1.3 Assembling the structure on the polymer stamp: the pick-up technique	31
2.1.4 Growth and synthesis techniques	34
2.2 Sample fabrication	36
2.2.1 TMD monolayer identification	36
2.2.2 Selecting hBN layers	37
2.2.3 The problem of polymer residues	41
2.2.4 Interlayer contaminants	44
2.3 Introduction to optical spectroscopy techniques	50
2.3.1 Optical spectroscopy setup	50
2.3.2 Reflectivity experiments	54
2.3.3 Photoluminescence (PL)	56
2.3.4 Polarization-resolved experiments	59
2.4 Conclusions	61
3 Optical spectroscopy of TMD monolayers encapsulated in hexagonal boron nitride	62
3.1 Motivations for hBN encapsulation	62
3.1.1 Inhomogeneous broadening of TMD monolayers on SiO_2	62

3.1.2	Unstable emission characteristics of TMD monolayers on SiO_2 . . .	64
3.1.3	Hexagonal Boron Nitride as a new substrate	65
3.1.4	HBN capping: protecting TMD monolayers from environment	67
3.2	hBN-encapsulated samples: an optical study	68
3.2.1	Sample fabrication	68
3.2.2	Approaching homogeneous linewidth	68
3.2.3	Temperature-dependent measurements	70
3.2.4	Valley polarization measurements	75
3.3	Excitonic states in hBN-encapsulated MoS_2 monolayers	80
3.3.1	Optical spectroscopy of excited exciton states	80
3.3.2	Interferences in the van der Waals heterostructure	82
3.3.3	Influence of dielectric environment on excitons	85
3.4	Hybrid heterostructure with bottom hBN grown by MBE	86
3.5	Conclusions	90
4	Charge Tunable structures (MoS_2, $MoSe_2$, WSe_2)	92
4.1	Trions: three-particle bound states	92
4.2	Fabrication of charge tunable structures	93
4.3	MoS_2 charge tunable structure	95
4.4	$MoSe_2$ charge tunable structure	97
4.5	WSe_2 charge tunable structure	100
4.5.1	Calculation of trion binding energies	100
4.5.2	Spectroscopy and charge tuning	102
4.5.3	Trion fine structure	103
4.5.4	Neutral and charged biexcitons	107
4.6	Conclusions	111
	Conclusion	112
	List of publications	120
	Conferences	122
5	Résumé en Français	123

Introduction

I joined the LPCNO ("Laboratoire de Physique et Chimie des Nano-Objets") in october 2016 to work in the quantum optoelectronics group, specialized in the optical study of semiconductors. This group which has developed an expertise in research on quantum wells and quantum dots now dedicates a large part of its work to a new kind of system: Transition Metal Dichalcogenide (TMD) monolayers, which are the materials studied in this thesis work. This relatively young and competitive research area started to grow rapidly in 2010 when it was discovered that two-dimensional (2D) TMDs have a direct bandgap [1, 2] in contrast to their bulk counterpart. These materials then revealed new interesting properties such as strong light-matter interactions governed by robust excitons with high binding energies and also unusual valley properties giving rise to circular dichroism. In addition to generating interest by themselves, 2D TMDs are layered materials which can be combined with other layered materials into so-called van der Waals heterostructures. When I joined the team, efforts were made to fabricate and analyse van der Waals heterostructures consisting in 2D TMDs encapsulated between hexagonal boron nitride (hBN) layers. This new development line brought unprecedented access to high sample quality which leads to high optical quality with spectra dominated by transitions with narrow linewidth. Joining the team at this precise moment was particularly interesting as the improved sample quality enabled distinguishing and studying optical transitions which were so far hidden due to broad linewidths. This research axis opened new doors and perspectives both in sample fabrication and optical spectroscopy.

I dedicated a large amount of time to fabricate and/or design new van der Waals heterostructures, trying to develop or improve fabrication techniques. I also had the opportunity to conduct optical spectroscopy experiments which are reported in this thesis work. This thesis thus enabled me following the whole research process, from sample fabrication to their optical study and analysis of exciton physics. The aim of this thesis is to present some of our most prominent experimental results obtained during the last three years, especially with hBN/TMD monolayer/hBN van der Waals heterostructures.

In the first chapter, a general presentation of transition metal dichalcogenide monolayers is presented with focus being made on some of their most interesting properties: band structure, valley properties, excitons with high binding energies.

The second chapter is dedicated to sample fabrication and presentation of our optical spectroscopy setup. Emphasis is put on fabrication techniques of van der Waals heterostructures derived from the mechanical exfoliation method, as these methods were used in the LPCNO. A large part of the chapter underlines some of my contributions to

identify pros and cons of fabrication techniques used by our research team in order to improve our sample quality. The optical spectroscopy setups used to conduct reflectivity and photoluminescence (PL) experiments are described at the end of the chapter.

The third chapter presents experimental results obtained with hBN/TMD monolayer/hBN van der Waals heterostructures for the main members of the TMD family: MoS_2 , $MoSe_2$, WS_2 and WSe_2 . The first sections of the chapter describe and identify the main problems arising for 2D TMDs which are not encapsulated between hexagonal boron nitride (hBN). Then, emphasis is put on the improved optical quality of the encapsulated 2D TMDs, underlining the effects of the new dielectric environment. I further describe how the optical properties measured depend on the TMD monolayer but also on thin film interference effects in encapsulated samples with atomically sharp interfaces.

The fourth chapter reports results obtained with TMD monolayer charge tunable samples, that is samples for which the doping level can be controlled by applying a voltage. These measurements reveal the existence of a three-particle complex called trion. Also named charged exciton, it is either comprised of two electrons and one hole or of two holes and one electron. Spectroscopic analysis for MoS_2 and $MoSe_2$ monolayers is shown to measure the trion binding energy. Then, a detailed study of the case of WSe_2 monolayer is presented, highlighting the existence of two different type of trions: intervalley and intravalley trions, as the electron states are described by spin and also valley quantum numbers.

The final chapter gives a quick overview of additional results obtained in this thesis work and underlines some perspectives for the future works which could be undertaken to carry on research on TMD monolayers.

Chapter 1

Introduction to Transition Metal Dichalcogenide monolayers

1.1 Why this interest for 2D materials?

The advent of nanotechnology made it possible to study materials reaching extreme dimensional limits: 2D (quantum wells), 1D (nanowires), 0D (quantum dots). Beyond quantum wells which are already used in the semiconductor industry, we focus in this thesis on 2D materials down to the atomic monolayer limit.

To understand this growing interest for 2D materials in general, it is relevant to first cite one famous member of this large family: graphene. Konstantin Novoselov and Andre Geim received the Nobel prize in Physics in 2010 [3] for their "groundbreaking experiments regarding the two-dimensional material graphene.". Graphene is basically a monolayer of carbon atoms arranged in a hexagonal structure as illustrated in Fig 1.1. It can be obtained from graphite, which is a layered material, that is a material composed of graphene layers which are weakly bound between themselves by van der Waals forces. With a simple technique called micromechanical cleavage (also called exfoliation), it is possible to obtain graphene. It is stable and exhibits fascinating physical properties such as intrinsic mobilities as high as $2 \times 10^5 \text{ cm}^2 \text{V}^{-1} \text{s}^{-1}$ at room temperature [4], large thermal conductivities [5], unbeatable mechanical properties which make graphene the "strongest material ever measured" [6]. These properties make graphene a very promising candidate for the future of electronics where the constant miniaturization will lead to new problems linked to statistical and quantum effects. However, graphene lacks a bandgap necessary for many applications. Graphene is not a semiconductor but a semimetal. Due to this absence of a bandgap, graphene-based transistors do not exhibit high on/off ratios necessary for effective switching and digital logic, for example.

Fortunately, graphite is not the only representative of the layered materials family. As shown in Fig 5.1, this family is vast, and many different types of materials exist: semiconductors, metals, insulators, superconductors... Like for the case of graphene, these materials present the advantage to be easily fabricated using exfoliation [7]. This technique, by far easier to develop and cheaper than growth methods such as molecular beam epitaxy (MBE), also explains why 2D materials became an important research field acces-

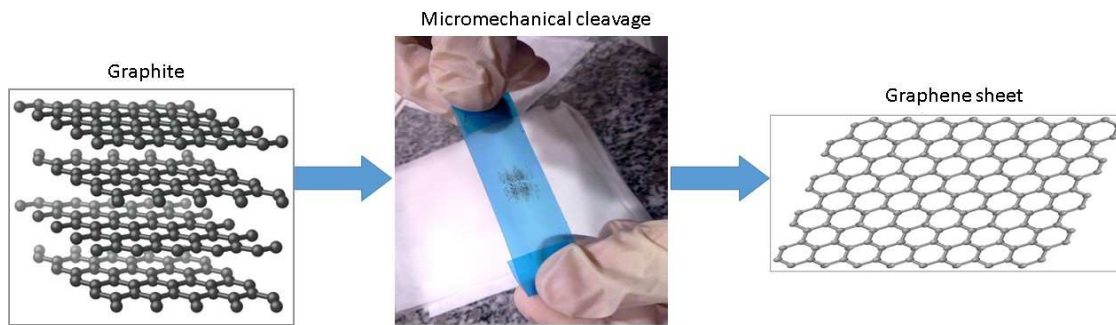


Figure 1.1: Graphene can be obtained from graphite by micromechanical cleavage.

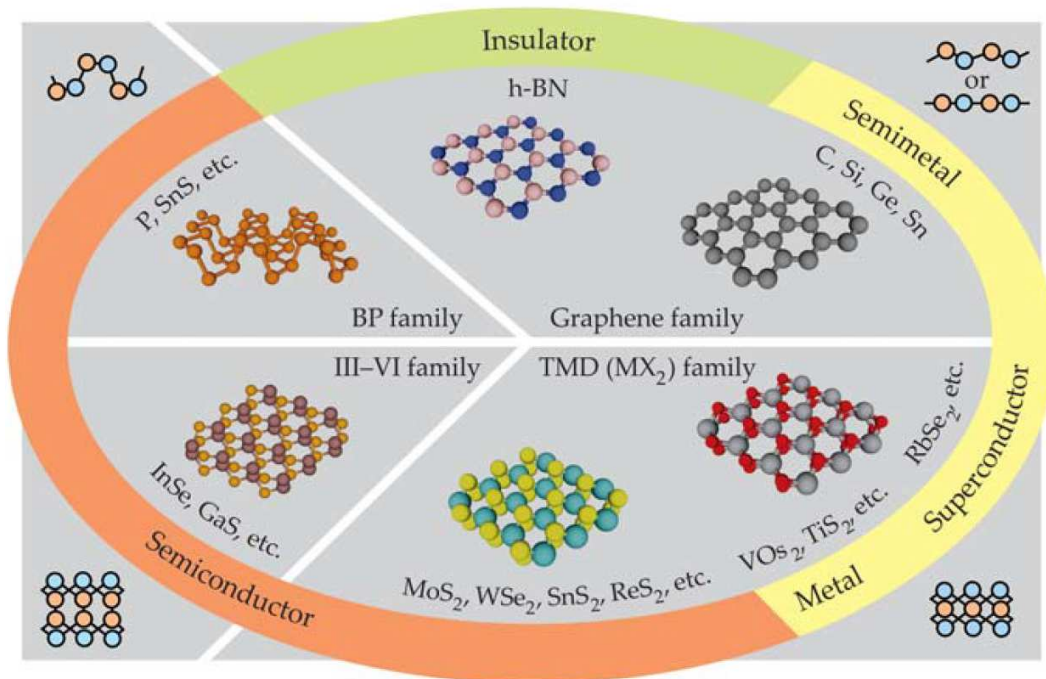


Figure 1.2: The vast family of 2D materials. Figure extracted from [8].

sible to many groups.

Moreover, using similar fabrication methods, it is possible to stack layers from different materials in order to obtain van der Waals heterostructures with new physical properties [9], as it is illustrated in Fig 5.2. The layers are simply deposited one on top of each other and the cohesion of the structure is ensured by van der Waals forces. In this case, another advantage compared to techniques like MBE is that lattice matching with the substrate material is not required. Nonetheless, given the current state, exfoliation is not adapted for industrial large scale fabrication because of its low yield and randomness. However, we will see in chapter 2 that this technique is applicable at a research level and it enables many groups working on physical properties of new artificial heterostructures. As the most successful van der Waals structures fabricated by exfoliation are better identified and understood, MBE and CVD efforts can subsequently be focused on the most promising materials.

An important point to emphasize is the diversity of materials available. As illustrated

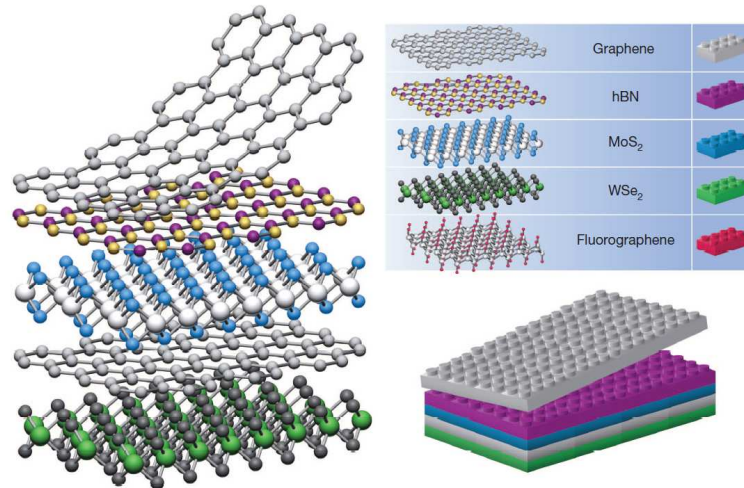


Figure 1.3: Illustration of the assembly of a van der Waals heterostructure, also represented in a very simple view as the assembly of Lego[®] building blocks. Figure extracted from [9].

in Fig 1.4, for 2D semiconductors, the range of bandgap energies covered goes from 0 eV (graphene) to 6 eV (boron nitride). This makes it in principle possible to use these materials for a wide range of applications:

- thermal imaging for wavelengths greater than 1200 nm.
- fiber communications where wavelengths of 1300 and 1550 nm are used.
- photovoltaics with semiconductors absorbing light in the 700-1000 nm range.
- displays and light emitting diodes (LEDs) in the visible range.

Among all these materials, the group VIB Transition Metal Dichalcogenides (TMDs) are semiconductors with sizeable bandgaps between 1.0 and 2.0 eV for the main representatives of the family (MoS_2 , WS_2 , $MoSe_2$, WSe_2 , $MoTe_2$). They are particularly studied for their optoelectronics properties since 2010, when it was discovered that going from bulk to monolayer samples, TMDs undergo a transition from an indirect to a direct bandgap which makes them promising materials for optoelectronics applications [1, 2], for example to fabricate transparent and flexible devices.

1.2 2D Transition Metal Dichalcogenides

In this section, we are reviewing the structure of Transition Metal Dichalcogenides (TMDs) and their main optoelectronics properties.

1.2.1 TMD crystal structure

Transition Metal Dichalcogenides are materials with the chemical formula MX_2 where M is a transition metal from group IV (Ti, Zr, Hf...), group V (V, Nb, Ta...) or group VI

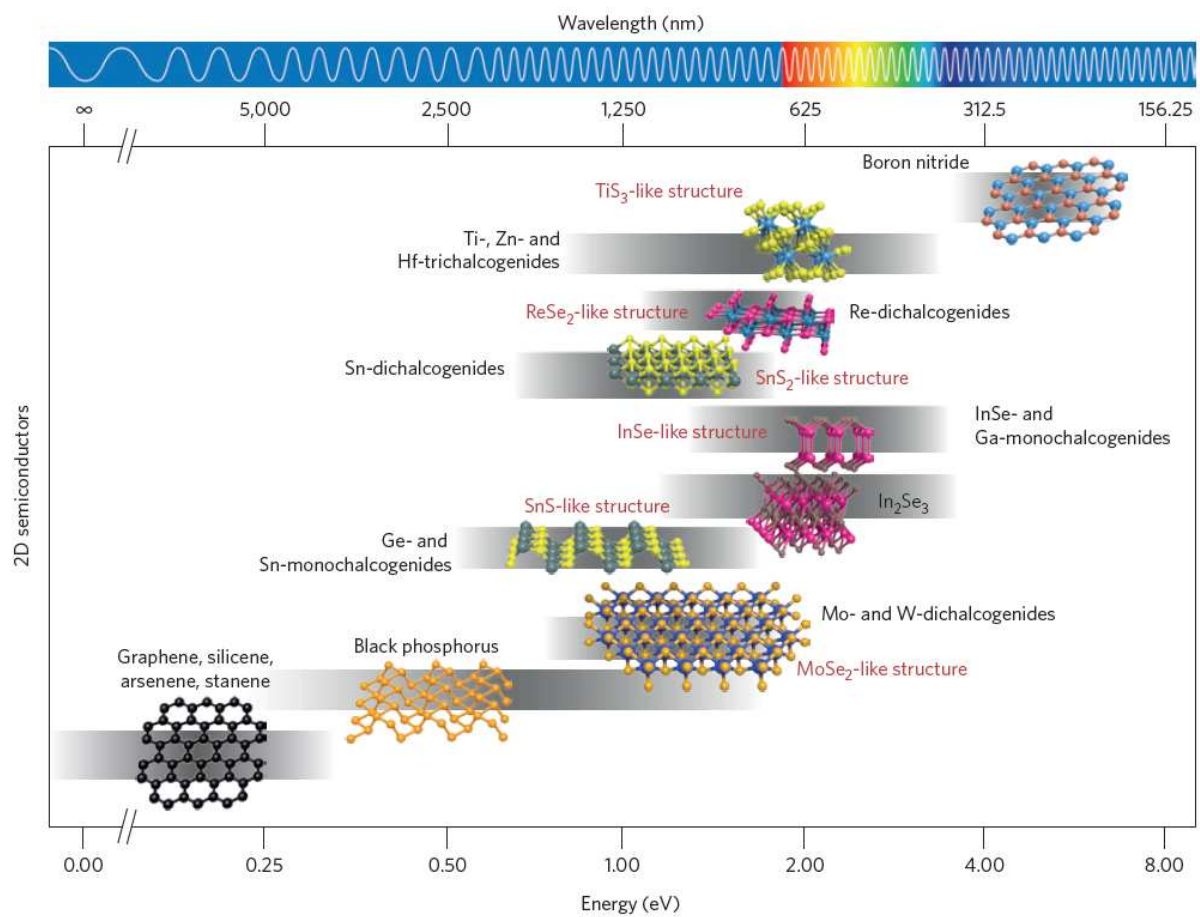


Figure 1.4: Bandgap range covered by different 2D semiconductors. Figure extracted from [10].

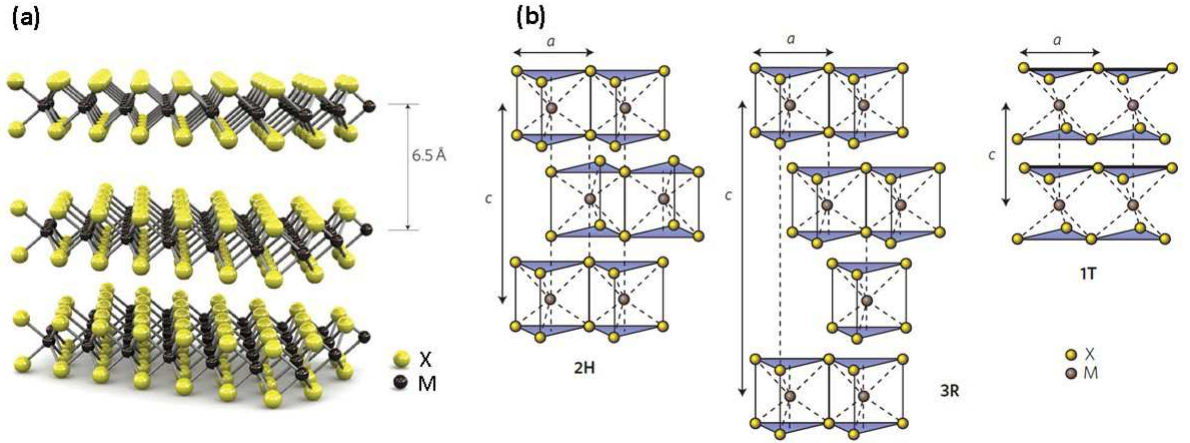


Figure 1.5: (a) 3D representation of a transition metal dichalcogenides trilayer in the 2H phase with monolayers spaced by an interlayer spacing of ~ 6.5 Å. Figure extracted from [11]. (b) Different structural polytypes: a is the lattice parameter in the range 3.1 to 3.7 Å for different materials and c is the stacking index which is related to the number of layers in each stacking order. The 2H phase is the one we are studying in this thesis work occurring for instance in naturally mined MoS_2 . Figure extracted from [12].

(Mo, W...) and X a chalcogen atom (S, Se or Te). In this thesis we focus on the group VIB TMDs (MoS_2 , $MoSe_2$, $MoTe_2$, WS_2 , WSe_2).

They are layered materials, with strong covalent bonds in the layer plane and weak van der Waals forces between the layers. They can form different phases which are illustrated in Fig 5.3 (b), in this work we will focus on the 2H phase with trigonal prismatic coordination which is the phase the most likely to be found in nature and also in grown bulk material. The layers, of thickness ~ 6.5 Å, have the form X-M-X with a transition metal plane between two chalcogen planes. All these planes form hexagonal lattices.

For a long time these materials have been used as lubricants due to the weak van der Waals forces between the layers. Now, like for graphene, this property makes it possible to exfoliate TMD monolayers and to study their properties.

1.2.2 Band structure

One of the most interesting properties of TMD monolayers is their direct bandgap. When going from 3D to 2D, theoretical and experimental work show a transition from an indirect to a direct bandgap as shown in Fig 5.4. The bandstructure changes due to two main effects: quantum confinement and the change in orbitals hybridization.

As shown in Fig 1.7, the conduction band states at K-point are mainly due to d -orbitals from the transition metal atoms M which are sandwiched between the two layers of chalcogen atoms. These orbitals are less influenced by the interlayer coupling, that is why the conduction band at K-point is not affected by the change in layer number, as illustrated in Fig 5.4 (a). However, at local minima between K and Γ points, the conduction band moves with the layer number increasing the value of the indirect bandgap until the material becomes direct in the monolayer limit. Again, this can be related to the conduction band states at this point which are due to a combination of p -orbitals from

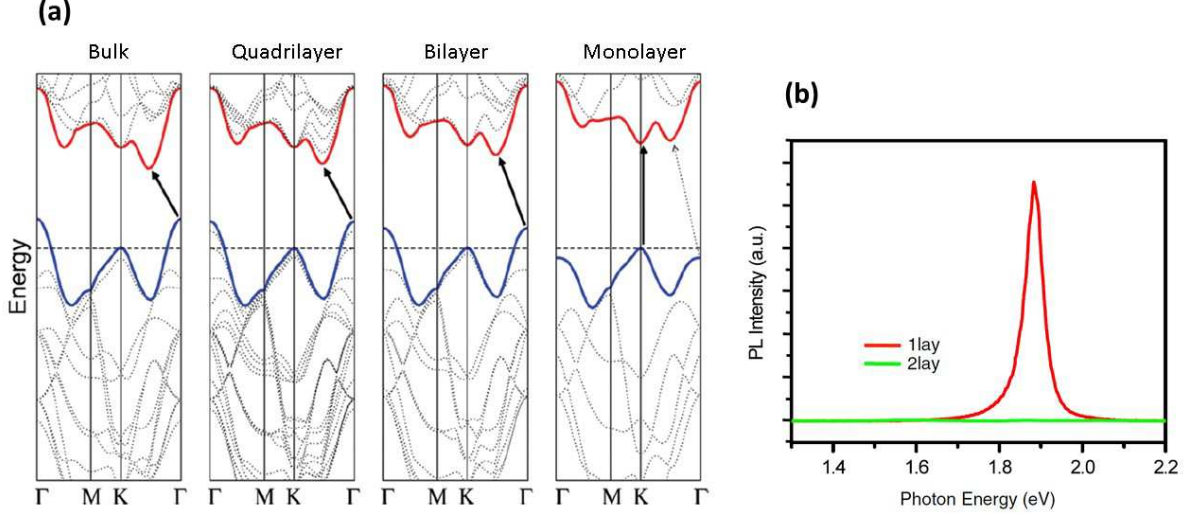


Figure 1.6: **(a)** Density Functional Theory calculation for bulk, quadrilayer, bilayer and monolayer MoS_2 . In the monolayer limit, the bandgap is direct. Figure extracted from [2]. **(b)** Photoluminescence spectra for a MoS_2 bilayer (green) and monolayer (red). Inset shows the evolution of the quantum yield with the layers number. Figure extracted from [1].

	MoS_2	$MoSe_2$	WS_2	WSe_2	$MoTe_2$	WTe_2
Δ_{SO}^{VB} (HSE,LDA) in meV	148	186	429	466	219	484
Δ_{SO}^{VB} (PBE,PBE) in meV	148	184	425	462	213	480
Averaged experimental value	≈ 145	≈ 191	≈ 394	≈ 440	-	-

Table 1.1: Spin-orbit splitting values Δ_{SO}^{VB} calculated using DFT with different techniques: Heyd-Scuseria-Ernzerhof (HSE) exact-exchange density functional, Perdew-Burke-Ernzerhof (PBE) generalized gradient approximation to the exchange-correlation potential, Local Density Approximation (LDA). For comparison, averaged experimental values are given. All values are extracted from [13].

the chalcogen atoms and d -orbitals of the metal atoms. In this case, the p -orbitals from the chalcogen atoms are strongly influenced by the interlayer coupling effect, explaining why the conduction band energy at this point changes with layer number.

For a more realistic analysis of TMD band structure, spin orbit effects have to be taken into account. This effect is particularly important in TMDs and gives rise to large splittings, especially in valence bands [14]. The DFT-calculated bandstructures of TMD monolayers with and without spin-orbit effect are presented in Fig 1.8 for four different materials.

The values of the splitting Δ_{SO}^{VB} in the valence band are quite large as shown in Table 5.1. It is noticeable that Δ_{SO}^{VB} is larger for W-compounds than for Mo-compounds because W atoms are heavier.

In the conduction band, there is also a spin-orbit splitting, though smaller than in valence band. Calculated values are given in Table 5.2, experimental values still need to be reliably obtained, as explained in the following chapters.

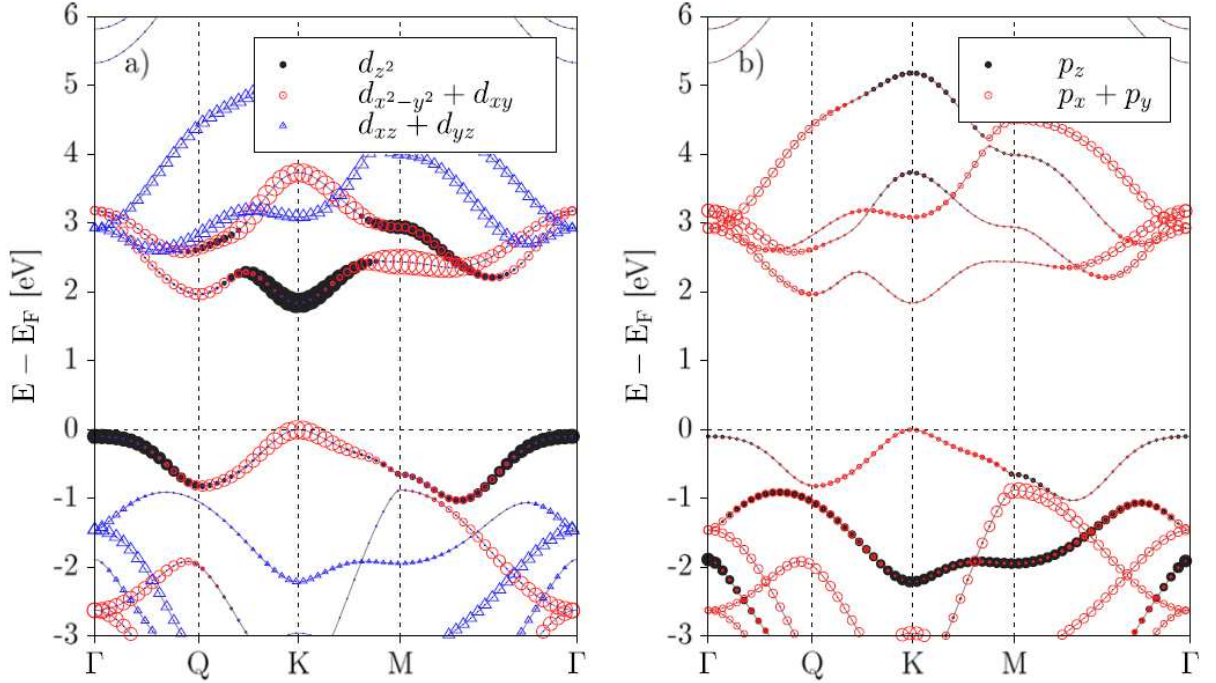


Figure 1.7: Bandstructure of MX_2 monolayer with atomic orbital weights proportional to the size of the symbols. (a) d -orbital weights of the transition metal atom. (b) p -orbital weights of the chalcogen atoms. Figures extracted from [13].

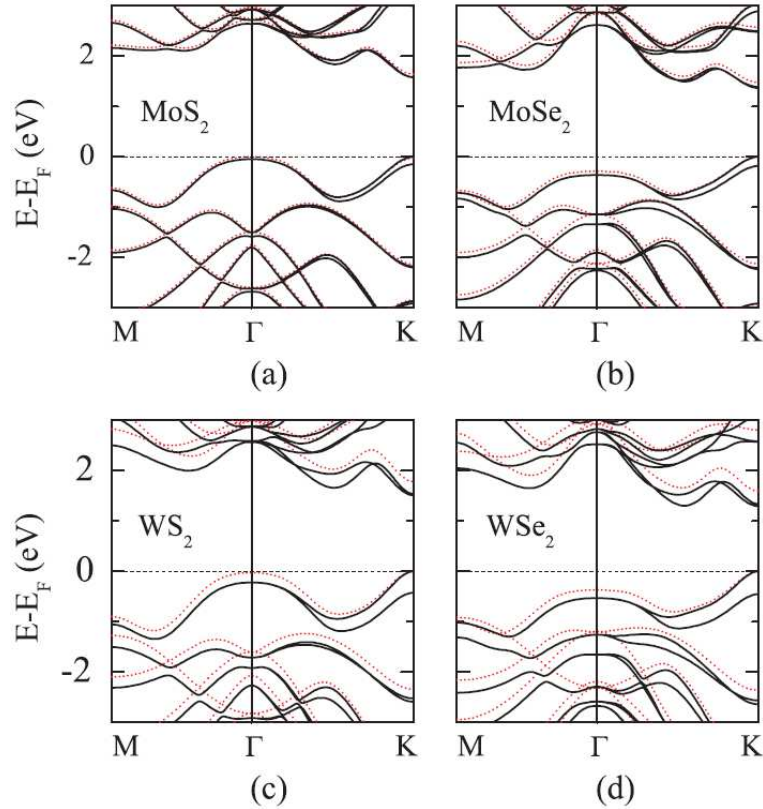


Figure 1.8: DFT calculations by taking into account spin-orbit coupling (black solid lines) and without it (red dashed lines). Figure extracted from [14].

	MoS_2	$MoSe_2$	WS_2	WSe_2	$MoTe_2$	WTe_2
Δ_{SO}^{CB} (HSE,LDA) in meV	3	22	-32	-37	36	-52
Δ_{SO}^{CB} (PBE,PBE) in meV	3	20	-31	-37	32	-54

Table 1.2: Spin-orbit splitting values Δ_{SO}^{CB} calculated using DFT. Values extracted from [13].

1.2.3 Excitons in TMD monolayers

Optical properties of TMDs are dominated by Coulomb bound electron-hole pairs called excitons. These quanta of excitations in solids were described for the first time by Frenkel in 1931 [15, 16]. Bringing enough energy to a semiconductor, an electron from the valence band can be excited to the conduction band leaving behind an empty state in the valence band termed hole (see Fig 5.5 (a)). For example a photon with momentum \vec{q} can generate an exciton. Due to momentum conservation, the following relation holds for the exciton momentum: $\vec{K}_{exc} = \vec{k}_e + \vec{k}_h = \vec{q}$ with \vec{k}_e the momentum of the electron and \vec{k}_h the momentum of the hole forming the exciton. In general, the photon wavevector can be neglected compared to crystal momentum; taking for example an excitation wavelength of 632.8 nm (HeNe laser), the corresponding wavevector is $\|\vec{q}\| = \frac{2\pi}{\lambda} \approx 9.9 \times 10^5 \text{ cm}^{-1}$ whereas a typical length across the Brillouin zone is 10^8 cm^{-1} .

It is possible to distinguish two main types of excitons: Frenkel and Wannier-Mott excitons. Frenkel excitons are also called tightly-bound excitons because their radius is of the order of the crystal lattice parameter. They are mainly present in insulators and molecular crystals. By contrast, Wannier-Mott excitons are also named free excitons due to their delocalized character and have a radius which extends over many atoms. They are mainly present in inorganic crystals such as semiconductors.

The electron and the hole which form this bound state have relative motions which are strongly correlated as illustrated in Fig 1.10 (b) for an exciton in a 2D TMD crystal. The position of the electron is clearly linked to the position of the hole. Then it is important to distinguish these relative positions and the motion of whole pair-states exciton which corresponds to the motion of the exciton center of mass having a wavevector \vec{K}_{exc} .

Our target is to estimate orders of magnitude for exciton binding energies, excited exciton states, their spatial extension and oscillator strength - all quantities which we analyse in detail in the experiments performed during this thesis. First, we develop our arguments for the three dimensional case in an effective mass approximation [17, 18], we can consider the exciton as an hydrogen-like or positronium-like system with a Coulomb interaction given by:

$$V(|\vec{r}_e - \vec{r}_h|) = \frac{-e^2}{4\pi\epsilon_0\epsilon_r|\vec{r}_e - \vec{r}_h|} \quad (1.1)$$

with e the charge of the electron, ϵ_0 the vacuum permittivity, ϵ_r the relative permittivity of the medium, r_e the electron position and r_h the hole position.

Like for an hydrogen atom, the exciton has different excited states which are represented in Fig 5.5 (b) with different principal quantum numbers n_B . This is the exciton

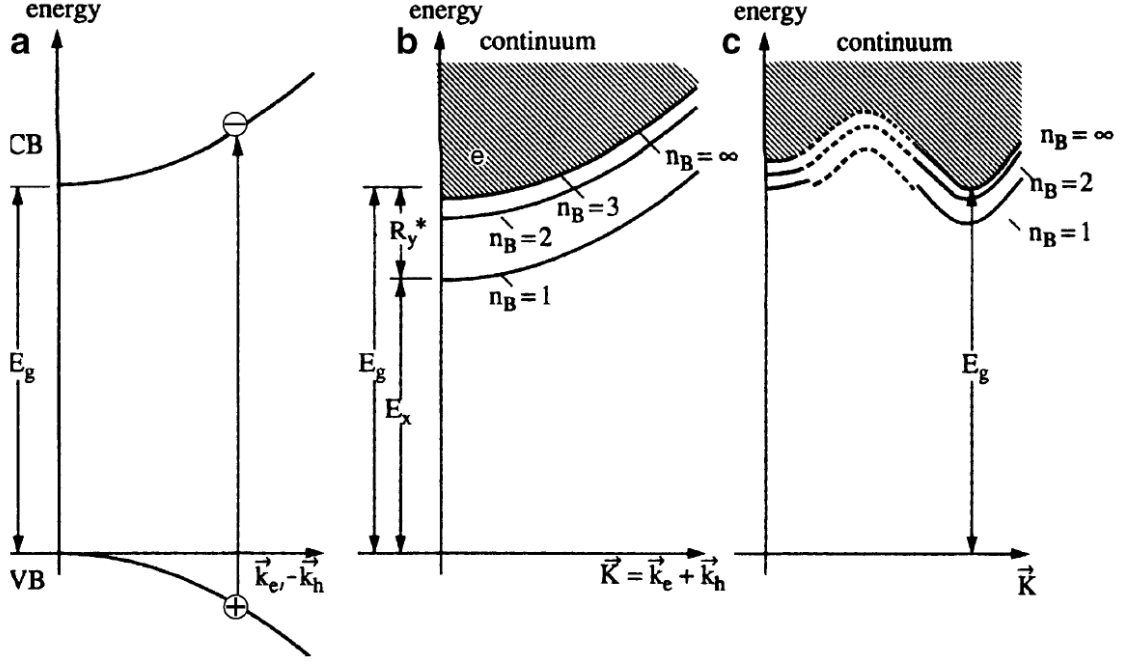


Figure 1.9: Different representations of an exciton: (a) in the scheme of valence and conduction bands, in the exciton picture for a direct exciton (b) and an indirect one (c). Figure extracted from [19].

Rydberg series.

The wavefunction of an exciton can be written as [19]:

$$\Psi(\vec{K}_{exc}, n_B, l, m) = \Omega^{-1/2} e^{i\vec{K}_{exc}\vec{R}} \Phi_e(\vec{r}_e) \Phi_h(\vec{r}_h) \Phi_{n_B, l, m}^{env}(\vec{r}_e - \vec{r}_h) \quad (1.2)$$

where $\Omega^{-1/2}$ is the normalization factor, $\Phi_{e,h}(\vec{r}_{e,h})$ are the wave packets for electrons and holes, $\Phi_{n_B, l, m}^{env}(\vec{r}_e - \vec{r}_h)$ is the envelope function of the relative electron-hole motion and \vec{R} is the position of the center of mass given by:

$$\vec{R} = \frac{(m_e \vec{r}_e + m_h \vec{r}_h)}{m_e + m_h} \quad (1.3)$$

We note that the relative electron-hole motion and the centre of mass motion are separated such as the exciton wavefunction can be simply noted $\Psi(\vec{R}, \vec{r}_e - \vec{r}_h) = G(\vec{R})F(\vec{r}_e - \vec{r}_h)$ [22]. In order to determine the total energy of exciton states, the Schrödinger equation must be solved for these two components of the exciton wavefunction. That is to say, $HG(\vec{R}) = EG(\vec{R})$ and $HF(\vec{r}_e - \vec{r}_h) = EF(\vec{r}_e - \vec{r}_h)$ must be solved.

Solving the Schrödinger equation for the envelope function of the relative electron-hole motion and for simple spherical bands, enables determining bound states energies of the exciton (1s, 2s, 3s ...), where 1, 2, 3 are the principal quantum numbers n_B . The problem is analogous to the one of an hydrogen atom [23]:

$$E_{n_B} = -R_y^* \frac{1}{n_B^2} \quad (1.4)$$

where n_B is the principal quantum number and R_y^* is the exciton Rydberg energy given

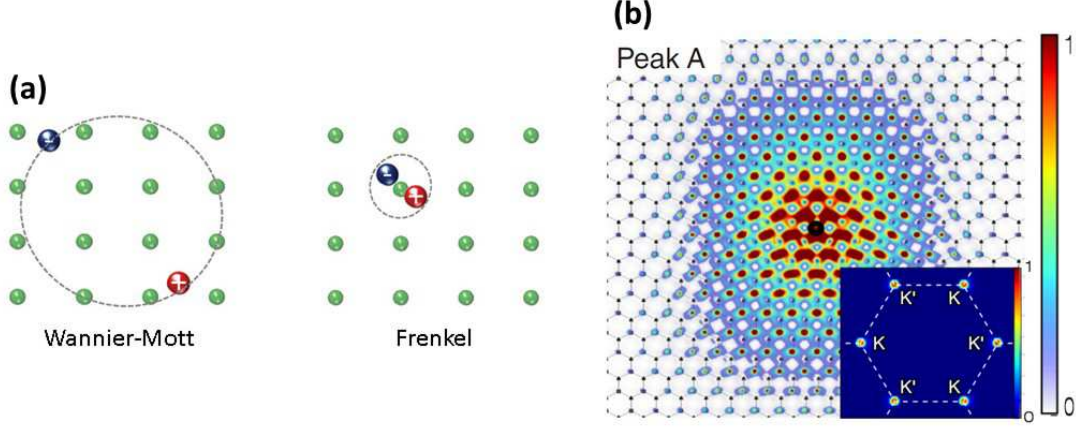


Figure 1.10: **(a)** The two main types of excitons: Wannier-Mott or free exciton, and Frenkel, or tightly bound exciton. Figure extracted from [20]. **(b)** In a 2D TMD crystal, for a hole fixed at the origin, the modulus squared of the electron wavefunction is represented in color scale. The inset shows the wavefunction in reciprocal space including K^+ and K^- exciton states. Figure extracted from [21].

by:

$$R_y^* = 13.6 \frac{\mu}{m_0} \frac{1}{\epsilon^2} \quad (1.5)$$

with m_0 the electron rest mass and μ the reduced exciton mass:

$$\mu = \frac{m_e m_h}{m_e + m_h} \quad (1.6)$$

Solving the Schrödinger equation for the center of mass motion gives the dispersion relation of the exciton:

$$E(\vec{K}_{exc}) = \frac{\hbar^2 |\vec{K}_{exc}|^2}{2M_{exc}} \quad (1.7)$$

with $M_{exc} = m_e + m_h$ the exciton mass.

Finally, the total energy of exciton states is given by [19]:

$$E_{exc}(n_B, \vec{K}_{exc}) = E_g - R_y * \frac{1}{n_B^2} + \frac{\hbar^2 |\vec{K}_{exc}|^2}{2M_{exc}} \quad (1.8)$$

with E_g the free carrier bandgap. In the exciton picture of Fig 5.5 (b), energy levels for different n_B are shown. When $n_B \rightarrow \infty$, energies tend to the continuum which corresponds to the free carrier bandgap, that is unbound electron-hole pairs.

We can also define the exciton bohr radius which corresponds to the radius of the electron-hole orbit for $n_B = 1$:

$$a_B^{exc} = a_B^H \epsilon \frac{m_0}{\mu} \quad (1.9)$$

with a_B^H the hydrogen Bohr radius. Actually, the exciton Bohr radius changes with the principal quantum number n_B . In a first approximation the following relation can be considered [19]:

$$a_B(n_B) \propto a_B^{exc} n_B \quad (1.10)$$

The different energy levels visible in Fig 5.5 (b) can give different transitions in spectroscopy experiments. The signal amplitude of these transitions is assessed through a quantity without dimensions called oscillator strength f_{n_B} . With increasing n_B , oscillator strength is decreasing like [19]:

$$f_{n_B} \propto n_B^{-3} \quad (1.11)$$

This rough effective mass approach already gives us interesting information about excitonic states. First, the binding energy of the exciton, which is defined as the energy difference between the free carrier bandgap and E_{exc} of Eq 1.8 $E_B = E_g - E_{exc}$, decreases when n_B increases. In contrast, as shown in Eq 1.10, the exciton radius increases with n_B as electron and hole are less strongly bound.

Now we underline again that these relations are valid in three dimensions. In 2D, which is the case we are interested in, the situation is different. The motion of the electron and hole is restricted to a 2D plane so $\overrightarrow{K}_{exc} = \overrightarrow{K}_x + \overrightarrow{K}_y$. As a consequence the total exciton energies are given by [19]:

$$E_{exc}^{2D}(n_B, \overrightarrow{K}_{exc}) = E_g + E_Q - R_y^* \frac{1}{(n_B - \frac{1}{2})^2} + \frac{\hbar^2 |\overrightarrow{K}_{exc}|^2}{2M_{exc}} \quad (1.12)$$

with E_Q the quantization energy of electron and hole which are confined in 2D. The sum $E_g + E_Q = E_g + E_e(n_z = 1) + E_h(n_z = 1)$ is called effective bandgap E_g^{eff} . It corresponds to the energetic distance between the first quantized electron and hole subbands. The binding energies of 2D excitons are:

$$E_B = R_y^* \frac{1}{(n_B - \frac{1}{2})^2} \quad (1.13)$$

Similarly, the bohr radius and the oscillator strength of an excitonic state are different in 2D [19]:

$$a_B \propto a_B^H \left(n_B - \frac{1}{2} \right) \quad (1.14)$$

$$f_{n_B} \propto \left(n_B - \frac{1}{2} \right)^{-3} \quad (1.15)$$

Basically, when going from 3D to 2D, n_B has to be replaced by $(n_B - \frac{1}{2})$. This considerably changes the binding energies. If we take for instance $n_B = 1$, in 3D we obtain a binding energy of R_y^* whereas in 2D it is $4R_y^*$. So the binding energies are larger in 2D compared to 3D. Also the oscillator strengths are higher in 2D. We will see that these general trends will play an important role in the case of our TMD monolayers.

Reducing dimensions from 3D to 2D influences the density of states as illustrated in Fig 1.11 (a). Taking into account the excitonic effects, we expect excitonic transitions to appear below the free particle bandgap as in Fig 1.11 (b). Indeed most emission and absorption spectra presented for high quality samples in the following chapters are dominated by the $n=1$ excitonic transition.

After this general introduction about excitons, the following part is dedicated to intro-

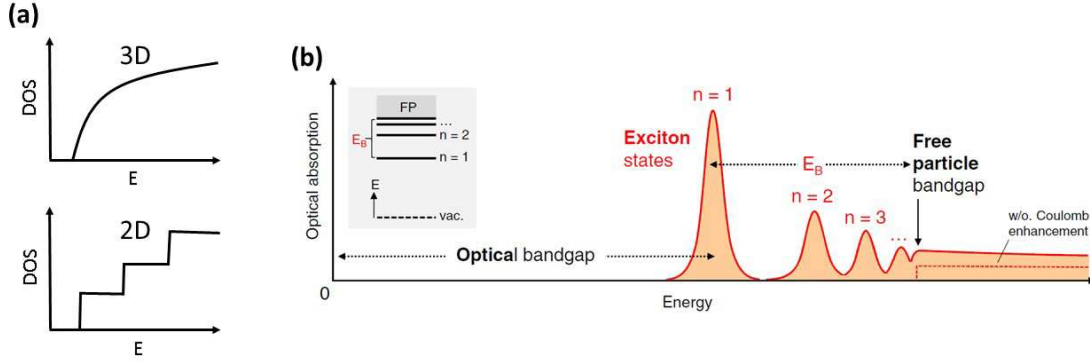


Figure 1.11: (a) Comparison of the density of states in 3D and 2D. (b) Absorption for a 2D semiconductor taking into account the excitonic effects. Difference between optical bandgap and the free particle bandgap is highlighted. Figure extracted from[24].

ducing the study of excitons in TMD monolayers. With the simple hydrogenic model, we have addressed several concepts which can be applied to excitons in 2D TMDs. Excitons in 2D TMDs have a radius of the order of a few nm, which makes them of an intermediate type, between Frenkel and Wannier-Mott excitons. However, it appears that the Wannier-Mott approach describes their main properties in practice.

One of the most striking properties of excitons in TMD monolayers is their binding energy. Indeed, their binding energy is of the order of several hundreds of meV, which is considerable if we compare with other semiconductors such as GaAs (~ 10 meV) or ZnO (~ 60 meV). Several reasons can explain these large binding energies.

First, as explained before, reduction of dimensionalities from 3D to 2D increases the binding energies (see Eq 1.8 and 5.3). We can indeed imagine that electron and hole are confined to a 2D plane and so are closer in space, therefore Coulomb interaction should be larger between these particles.

Second, electric field lines between the electron and the hole extend around the TMD monolayer, so the exciton "feels" the surrounding dielectric environment. In most experiments conducted until now, this environment (vaccum, SiO_2 , hBN etc...) has a smaller dielectric constant compared to the TMD, so overall this leads to a reduced dielectric screening for a 2D exciton compared to a 3D exciton in a bulk TMD. This reduced dielectric screening generates higher binding energies. This can be understood easily if we take the simple hydrogen model with Eq 5.3 and 5.2.

2D excitons in TMDs have a high reduced mass $\mu \approx 0.25 m_0$, and again by considering the simple hydrogenic model (Eq 5.3 and 5.2), it is clear that an increase of μ induces an increase of the binding energy. We realize that this value is particularly large if we draw a parallel with GaAs for which $\mu \approx 0.06 m_0$. This is linked to the effective electron and hole masses m_e and m_h in K-valleys which are also large $\sim 0.5 m_0$ [13]. Indeed, $\mu = \frac{m_e m_h}{m_e + m_h}$.

Experimentally, it is possible to determine the binding energy E_B . We recall that $E_B = E_g - E_{opt}$ where E_g is the free particle bandgap and E_{opt} is the optical bandgap as shown in Fig 1.11 (b) and Fig 1.12 (a). One possibility is to measure E_g using techniques such as Scanning Tunnelling Spectroscopy (STS) like in Fig 1.12 (b). The optical bandgap is determined by using optical spectroscopy experiments such as PL or reflectivity. If we

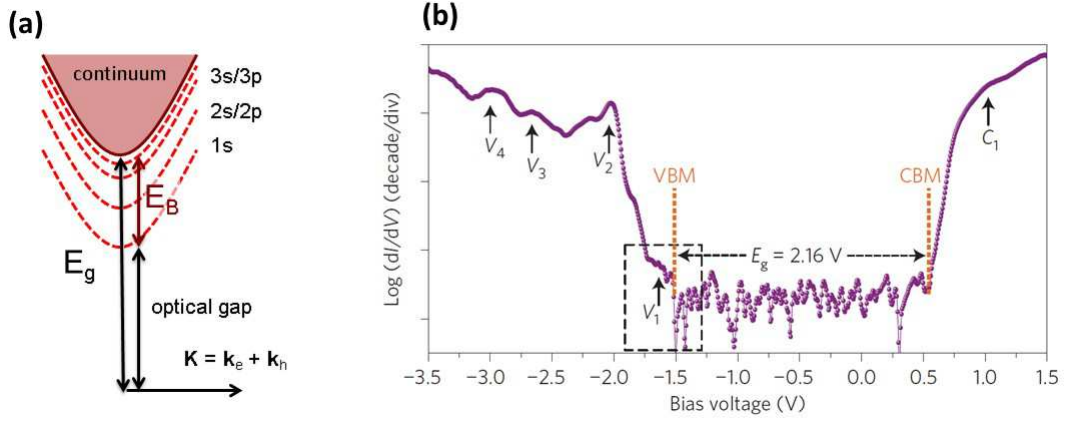


Figure 1.12: (a) Exciton picture highlighting the difference between the free particle bandgap E_g and the optical bandgap. (b) Example of a STS measurement showing the valence band maximum (VBM) and the conduction band minimum (CBM). The value for E_g can be measured. Figure extracted from [25].

refer to the density of states in 2D of Fig 1.11 (a), in principle it should be possible to detect the onset of absorption related to the free particle bandgap. In practice, optical identification of E_g is very difficult due to the merging of this threshold with excitonic states as it is illustrated in Fig 1.11 (b). In addition there are several exciton series A and B, linked to valence states split by the spin-orbit interaction.

However, using only optical spectroscopy, it is still possible to determine E_B . The idea is to use the Rydberg series of the excitonic states [26, 27, 28, 29, 30, 31]. When $n_B \rightarrow \infty$, the energy tends to the free particle bandgap, so measuring the energies for different excitonic states (1s, 2s, 2p, 3s ...) and by extrapolation the value of E_g can be deduced. Using such a technique, it is interesting to note that the Rydberg series actually deviate from what is expected using the simple hydrogenic model [27]. Using a more appropriate potential called Rytova-Keldysh potential gives results in better agreement with the data [32, 33]:

$$V(r) = \frac{-e^2}{8\epsilon_0 r_0} \left(H_0 \left(\frac{\kappa r}{r_0} \right) - Y_0 \left(\frac{\kappa r}{r_0} \right) \right) \quad (1.16)$$

where e is the electron charge, ϵ_0 is the vacuum permittivity, r_0 is the screening length, κ is an average dielectric constant and H_0 and Y_0 are the Struve and Neumann functions. The screening length is given by $r_0 = 2\pi\chi_{2D}$ with χ_{2D} the 2D polarizability of the monolayer. The average dielectric constant is given by $\kappa = \frac{1}{2}(\epsilon_{top} + \epsilon_{bottom})$ with ϵ_{top} and ϵ_{bottom} the dielectric constants of the top and bottom dielectric layers surrounding the monolayer.

Through the study of hBN-encapsulated TMD monolayers, we will address this problem of the influence of the dielectric environment on exciton binding energies in chapter 3 section 3.3.3. It is important to underline that many different values of exciton binding energies can be found in the literature probably owing to different samples (CVD, exfoliated...), dielectric environment and experimental techniques (STS, PL, reflectivity, PLE, 2P-PLE, SHG...), although all these results agree on the order of magnitude of the exciton binding energy of several hundreds meV.

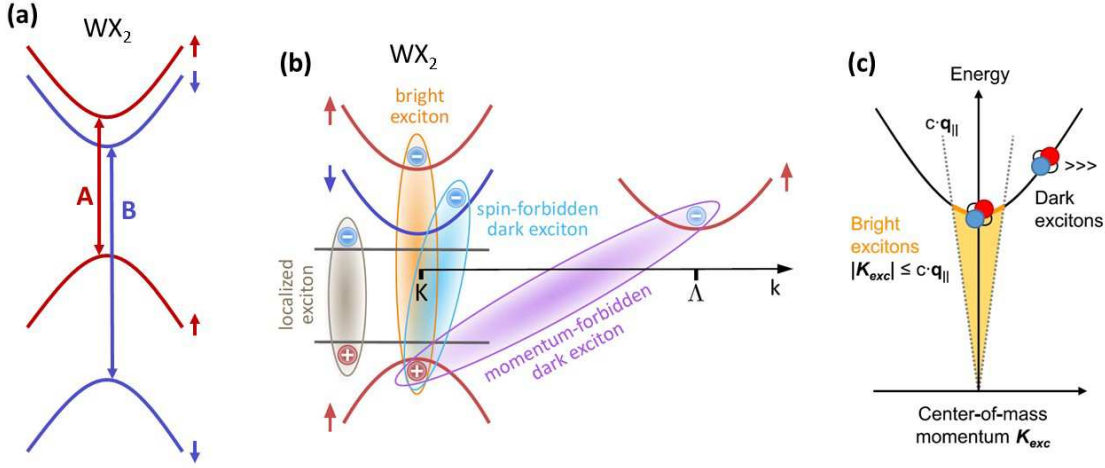


Figure 1.13: **(a)** Schematic of A and B exciton transitions at the K-valley in a W-based compound such as WS_2, WSe_2 . **(b)** Still in W-based compound. Illustration of different types of excitons: bright, dark, localized, indirect. Figure extracted from [40]. **(c)** Schematic representation of the exciton dispersion and the photon dispersion $cq_{||}$, also called light cone. Excitons inside the light cone are optically active and are called "bright excitons", whereas excitons outside are optically inactive and are called "dark excitons". Figure extracted from [24].

For the moment, we have considered the main exciton optically active in our TMD monolayers called the A-exciton (see Fig 1.13 (a)). However it is important to underline that different types of excitons exist in these systems such as B-exciton, localized excitons, dark excitons, interlayer excitons... A first way to distinguish them is to consider the ones which are optically active and the ones which are optically inactive. There are different conditions for an exciton to be optically active. First, looking at Fig 1.13 (b), we can see that only the spin-allowed transitions are bright. Then it has also to be momentum-allowed, as illustrated in Fig 1.13 (b) and (c) where the bright excitons are in the light cone. As the photon wavevector is small, we can say that the exciton wavevector $\vec{K}_{exc} = \vec{k}_e + \vec{k}_h$ is almost zero. It means that, even if the exciton is composed of an electron at the K+ point and a hole at K- point, when a bright exciton recombines, it recombines at the center of the Brillouin zone Γ .

Scattering events with excitons, electrons, phonons and impurities can change spin and momentum of an exciton changing its bright/dark character.

In recent experiments, it has been possible to observe the spin-forbidden dark excitons [34, 35, 36, 37, 38]. Selection rules show that these states are dipole-allowed for excitations with an out-of-plane electric field E_z in contrast to bright excitons which are dipole-allowed for in-plane electric fields E_x or E_y [39]. The symmetry and the physical arguments are similar for the well studied TE and TM modes of heavy hole and light hole transitions in III-V quantum wells.

In addition, other exciton complexes such as charged excitons (trions) or biexcitons can be observed. All these different excitonic transitions make the optical spectra rich, and sometimes difficult to interpret like in the case of tungsten-compounds with still many open questions at the time of writing. The study of exciton species and their identification

is important both fundamentally and for future applications. The free excitons give a good insight of the intrinsic band structure of semiconductors. Localized excitons which bind to impurities or defects give important information about the materials purity and about the nature of the impurities. It has been shown in the past that these impurity analysis are of a great importance to reach an effective and controlled doping of the material [41].

The main axis of this thesis work is the study of excitonic properties of TMD monolayers encapsulated into hBN van der Waals heterostructures (hBN/TMD monolayer/hBN). We will study in chapter 3 optical response of these systems using spectroscopic experiments. In chapter 4, we will focus on charged excitons in charge-tunable structures.

It has been underlined that excitons in 2D TMDs are strongly bound. We want to note here that taking into account these high binding energies of several hundreds of meV, recent theoretical results have predicted that in this case the distinction between direct and indirect optical transitions is more difficult [42], as optical transition energies will be very different from calculated single-particle band structure using DFT, for example.

As a consequence of having a large binding energy and strong oscillator strength the intrinsic radiative lifetime is very short, about 1 ps. This can be gleaned from time resolved photoluminescence data [43] and also four-wave mixing experiments [44].

1.2.4 Circular dichroism in TMD monolayers

When going from bulk to a TMD monolayer, the inversion symmetry of the crystal is broken. The space group for a bulk TMD is D_{6h} whereas the point group for a TMD monolayer is D_{3h} . Due to this inversion asymmetry in monolayers, inequivalent K^+ and K^- valleys emerge at the corners of the hexagonal Brillouin zone, as shown in Fig 5.6.

This energetically degenerate but inequivalent valleys give rise to a growing field in physics called "valleytronics". Valley pseudospins $\tau=+1$ and $\tau=-1$ are associated respectively to K^+ and K^- valleys. "Valleytronics" is the manipulation of this valley degree of freedom of electrons, analogously to spintronics which refers to the manipulation of the spin degree of freedom [45].

Actually, selective optical excitation of valleys in momentum space is possible. This is what is called circular dichroism or valley selective optical selection rules which result from the inversion symmetry breaking mentioned above [46]. σ^+ and σ^- circularly polarized light can excite K^+ and K^- valleys respectively. This selective excitation of valleys has been proved experimentally, especially through photoluminescence (PL) experiments which revealed a conservation of the polarization. For instance if K^+ valleys are excited with a σ^+ polarized laser, a σ^+ -polarized PL is measured [47, 48, 49, 50].

These selection rules may seem similar to spin-dependent optical activity in GaAs, however it is important to insist on the fact that the physical origin is different, here the different valleys give rise to this circular dichroism, for example spin down and spin up states in the K^+ valley are both addressed with σ^+ light (see Fig 5.8).

This circular dichroism can be measured experimentally in PL and it is assessed by

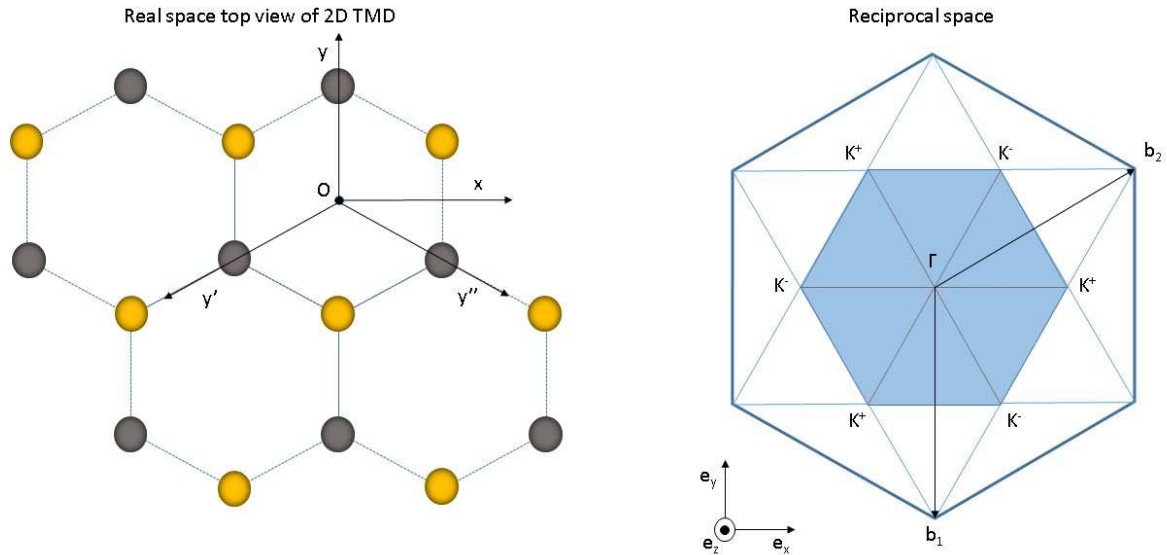


Figure 1.14: Real and reciprocal space of a 2D TMD. The shaded area corresponds to the first Brillouin zone. In real space the point group of the crystal is D_{3h} with a rotation axis of order 3 (Oz), 3 axis of order 2 (Oy , Oy' , Oy''), one mirror operation σ_h defined from (xOy) and 3 mirror operations ($\sigma_v, \sigma'_v, \sigma''_v$ defined from the planes (yOz), ($y'Oz$), ($y''Oz$)). In reciprocal space, at the corners of the Brillouin zone (K^+ and K^-), the point group is C_{3h} ; due to inequivalent K valleys the symmetry is lowered (order 2 axis and the corresponding mirror symmetries σ_v, σ'_v and σ''_v are suppressed).

the degree of circular polarization given by:

$$P_c = \frac{I_{\sigma^+} - I_{\sigma^-}}{I_{\sigma^+} + I_{\sigma^-}} \quad (1.17)$$

where I_{σ^+} and I_{σ^-} are respectively the σ^+ -polarized and σ^- -polarized PL intensities. An example of a measurement of circular polarization is shown in Fig 5.7 (a).

In fact, P_c is different from the initial circular polarization P_0 which is created by the circularly polarized laser. In this case, the circular polarization degree measured in time integrated measurements can be expressed as [51]:

$$P_c = \frac{P_0}{1 + \frac{\tau}{\tau_s}} \quad (1.18)$$

where P_0 is the initially created polarization, τ is the exciton (electron-hole pair) lifetime and τ_s is the polarization decay time. Basically if τ is short compared to τ_s , the exciton recombines before the polarization is lost.

Taking into account the spin-orbit splitting and the breaking of inversion symmetry, in a single-particle picture, K-valleys can be represented like in Fig 5.8. The spin-orbit splitting in conduction bands is different for Mo-based and W-based compounds. As a consequence the optically active states correspond to the lower band for MoX_2 and to the higher conduction band for WX_2 . These spin-allowed transitions are called bright, whereas the spin-forbidden ones are logically qualified as dark.

With Fig 5.8 we understand that, in the case of an intervalley scattering event, the

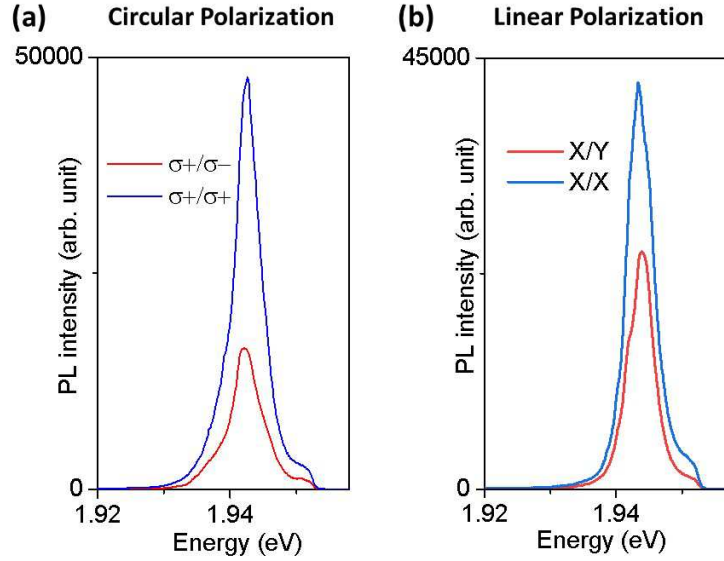


Figure 1.15: PL polarization measurements on a MoS_2 monolayer sample at cryogenic temperature. **(a)** Example of circular polarization measurements. In blue, co-circular ($\sigma + / \sigma +$) and in red, cross-circular ($\sigma + / \sigma -$). **(b)** Example of linear polarization measurements. In blue, co-linear (X/X) and in red, cross-linear (X/Y).

electron or hole has to change spin to go from one valley to the other or it can keep its spin but has to overcome the spin-orbit splitting, which is quite large for the valence bands. Thus we would expect polarization to be protected in this single particle picture by the large spin-orbit splittings. However, this approach is not sufficient as experiments reveal evidence of valley depolarization. Pump-probe [52, 53] and Kerr rotation [54] experiments have shown that valley polarization presents fast decay times τ_s of the order of some ps. In brief, to understand the microscopic origin of this loss in polarization, we cannot use the simple single-particle vision of Fig 5.8, but we need to consider excitons, bound electron-hole pairs, initialized in either $|+1\rangle$ or $|-1\rangle$ states. For exciton polarization decay times τ_s of the order of ps have been measured. This time is competitive with the exciton lifetime τ , explaining why polarization is partially lost. The physical mechanism behind this intervalley scattering is based on Coulomb long range exchange interaction [39, 55], as sketched in Fig 1.17. Excitons can be submitted to fast intervalley exciton transition due to this long range exchange interaction. This long range exchange interaction can be seen as an effective magnetic field causing spin precession and decoherence of excitons [54].

In addition to circular polarization, it is also interesting to study TMDs' optical response to linearly polarized excitation (see Fig 5.7 (b)). In this case, the linearly-polarized light excites both K^+ and K^- valleys, generating a coherent superposition of states called "valley coherence" [56]. In other words, we generate optical alignment of excitons. Then analysing the emission of the neutral exciton, for instance in PL, shows that it is linearly polarized. It means that there is a conservation of the coherent superposition of states initially created.

Examples of these different polarization properties will be presented in section 3.2.4 for an hBN/ MoS_2 monolayer/hBN sample. Magneto-optical experiments will also demon-

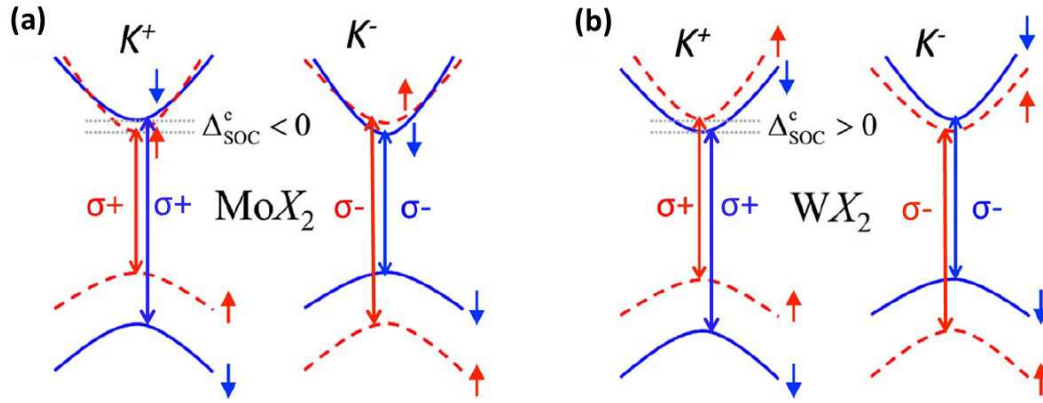


Figure 1.16: Representation of K^+ and K^- valleys for Mo- and W-compounds. The valleys can be selectively excited with σ^+ and σ^- polarized light. Electron spins notations for both conduction and valence bands. Figure extracted from [24]

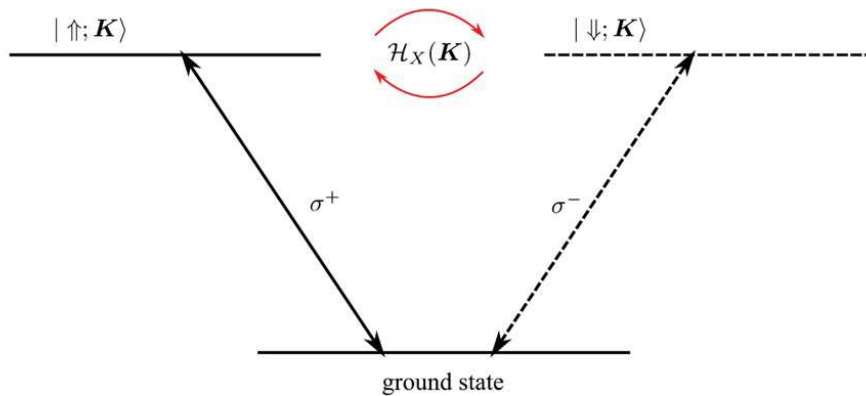


Figure 1.17: Sketch representing the bright excitonic states in the K valleys with optical selection rules denoted by σ^+ and σ^- . \uparrow and \downarrow represent the exciton pseudospins associated to the valleys. These two bright excitons are coupled by long-range Coulomb exchange interaction noted $\mathcal{H}_X(\mathbf{K})$. Figure extracted from [39].

strate that valley state superpositions can be manipulated in applied magnetic field. In general in TMD monolayers, the exciton polarization is studied on ps time scales because of the intrinsic radiative lifetime of the order of 1 ps. Much longer polarization memory up to microseconds can be measured for resident carriers, not excitons [57].

1.3 Towards devices with TMD monolayers

TMD monolayers appear as good candidates for potential applications in optoelectronics. First, they are direct gap semiconductors. They have interesting optical-selection rules giving rise to a new field called valleytronics. Their optical properties are governed by excitons with high binding energies which are therefore still stable at room temperature. Atomically thin films are especially attractive for flexible optoelectronics. Compared to bulk semiconductors, they could represent a great gain of space and could be produced at low cost on large areas. Optoelectronic devices based on TMD monolayers could fulfill different functions: electroluminescence, photodetection, photovoltaics, valleytronics... Here we outline a few research axis, the open challenges in terms of material quality and large scale sample fabrication will be discussed in detail throughout this thesis. For the first device prototypes, the main architectures which have been adopted are represented in Fig 1.18. Basically, there are separated into three principal categories: 2D Homostructures based on one 2D material, 2D Heterostructures based on the association of different 2D materials, and Mixed-dimensional structures based on a 2D material combined with a 0D, 1D or 3D material. Among these structures, we can also distinguish between the vertical and the lateral structures. The vertical structures can be produced by approaches such as deterministic transfer methods [58], which are presented in chapter 2. However lateral structures cannot be fabricated with these techniques and rely on bottom-up approaches such as Chemical Vapor Deposition (CVD) growth. These different approaches have a common objective: obtaining a PN junction which is required to fabricate optoelectronic devices such as LEDs or solar cells.

Electroluminescence comes from the radiative recombination of electron-hole pairs which have been generated by an electrical current. It is possible to generate electroluminescence using a unipolar current. In this case, one type of carrier is injected in the monolayer. Subsequently, excitons can form through Joule heating [60] or impact excitation [61]. However, to reach better efficiencies, it is necessary to form a PN junction. This can be done using a split-gate geometry to generate electrostatic doping. For example it was done with WSe_2 as the active material [62, 63]. The monolayer doping can be controlled independently above the two electrodes giving the four following functioning regimes: NN, PP, NP, PN. Using a bipolar current both electrons and holes are injected in the structure. They form excitons which recombine radiatively. Electroluminescence efficiencies, which correspond to the ratio of output optical power over the input electrical power, reached between 0.1 and 1% for this kind of lateral PN junctions. Vertical device geometries have also been studied. One of these structure is shown in Fig 1.19 (a), it consists of a TMD monolayer encapsulated between hBN and graphene electrodes: graphene/hBN/TMD monolayer/hBN/graphene. Electrons are injected in the monolayer

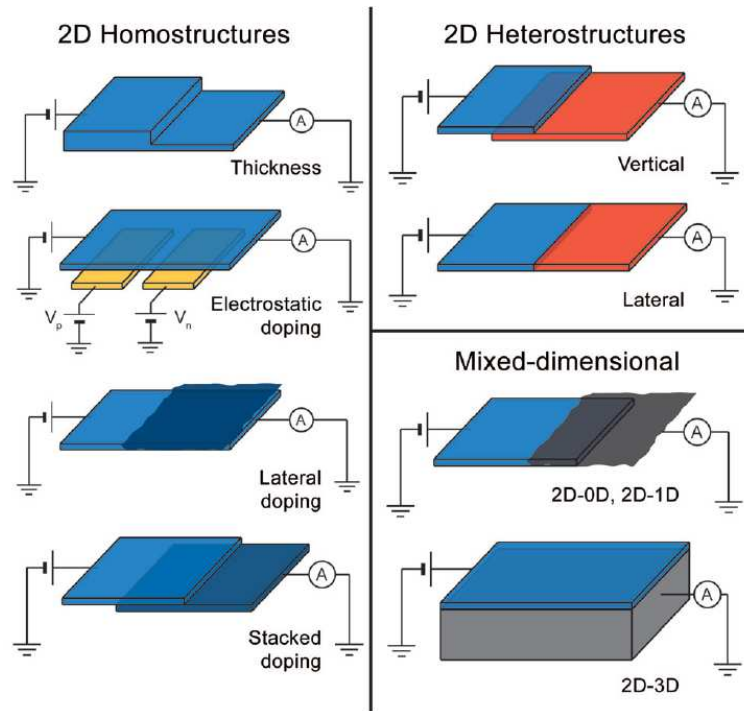


Figure 1.18: Scheme of the main PN junction architectures based on 2D semiconductors. Three main "families" have been distinguished: homostructures which are formed of only one active material with different doping, heterostructures which are formed of different active materials and mixed-dimensional structures which are based on the association of 2D-0D, 2D-1D or 2D-3D materials. Figure extracted from [59].

and electroluminescence from negative trions (negatively charged excitons) is detected [64]. Mixed-dimensional structures have also been demonstrated, for instance with a n-type MoS_2 monolayer deposited on a p-type bulk silicon substrate, as illustrated in Fig 1.19 (b). These vertical structures gave similar efficiencies as the lateral ones, around 1%. This value is also similar to the PL quantum yield at the equivalent excitation rate. This low efficiency is probably related to important non-radiative processes due to bad sample quality. Aiming to improve this yield is one of the main research targets, for example by using samples with less defects grown by the flux method [65] or acid treatments for defect passivation [66].

According to Fig 1.4, due to their bandgap in the near infrared and visible range and high absorption in the solar spectral region, TMD monolayers appear as potential candidates for photovoltaics or more generally as photodetectors. The development of 2D photovoltaics could lead to a future generation of efficient, ultrathin, portable and ultralight solar cells. To obtain a sizeable photovoltaic effect it is important to have a material with good absorption and also where separation of photogenerated carriers is necessary. To separate photocarriers, several structures have been studied. Like previously, lateral PN junctions have been used to demonstrate photovoltaic effect in atomically thin monolayers [68, 62, 63]. Vertical structures have also been tested, relying on type-II band alignment composed for instance of MoS_2 and WSe_2 monolayers stacked together.

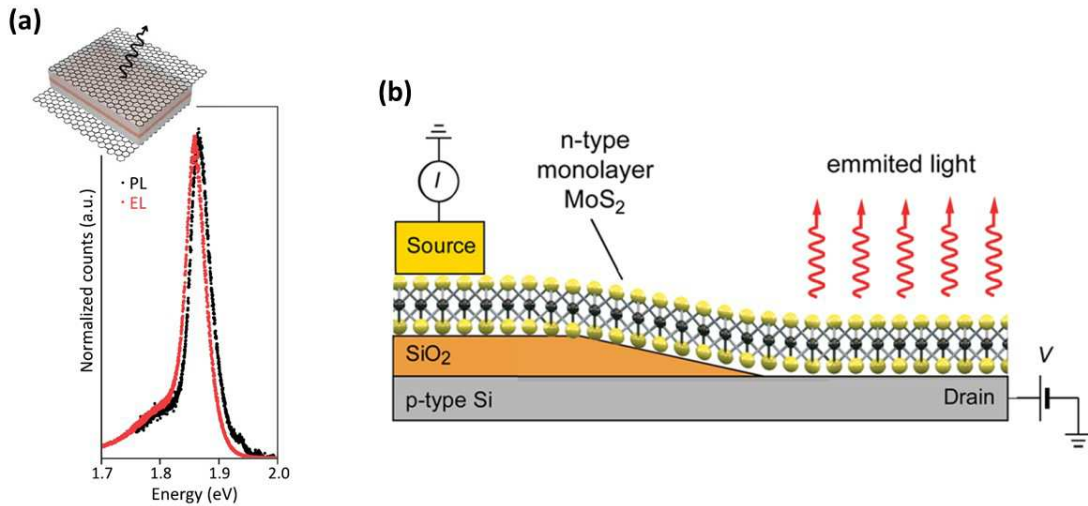


Figure 1.19: **(a)** Graphene/hBN/*MoS*₂ monolayer/hBN/Graphene vertical structure and the corresponding electroluminescence from negative trion. Figure extracted from [40]. **(b)** N-doped *MoS*₂ monolayer on p-doped Si electroluminescent device. Figure extracted from [67].

With this band alignment, the electron goes in a monolayer and the hole goes in the other one, facilitating carrier separation. For 2D TMDs, this is particularly important because excitons have large binding energies and are therefore difficult to "break". Another challenge is that TMD monolayer absorb $\sim 10\%$ of the light which is indeed a large value taking into account the thickness of the material ($\sim 6.5\text{\AA}$) but still low for photovoltaic applications. That is why the development of efficient light trapping methods is considered, like the use of backreflecting substrates or resonators to enhance light-matter coupling [69].

In addition, TMD-based devices have been used in photoconductive mode, that is as photodetectors. TMD monolayers exposed to photons undergo a change of conductivity which can be detected by applying an external bias [70].

Finally, it is important to mention again one of the most exotic properties of TMD monolayers: their valley properties. As shown in section 1.2.4, inequivalent valleys with different valley indices can give rise to a valley polarization which can be detected optically, or electrically through the valley hall effect [71]. Valley polarization can be manipulated with different techniques: optically with polarized light, electrically, injecting spin-polarized charge carriers, or applying magnetic fields... This new degree of freedom, in addition to spin and charge, allows to study new physics also in hybrid devices. For instance to use a TMD monolayer for optical spin or valley polarization and to use an adjacent graphene layer for spin-transport [72].

The development of new optoelectronic devices based on TMD monolayer must be accompanied by improvements on the side of sample fabrication which will be detailed in the next chapter.

1.4 Conclusions

Since 2010 Transition Metal Dichalcogenide monolayers have established themselves as being key materials of the "2D family". Their direct bandgap and unique optical properties governed by strongly bound excitons and valley selection rules makes them interesting materials both for fundamental research and potential applications. In this chapter we gave a brief overview of the main properties of the TMD materials like MoS_2 and WSe_2 that we will study in more detail in the following chapters in novel, high quality van der Waals heterostructures fabricated as part of this thesis work.

Chapter 2

Sample fabrication and experimental setups

This chapter focuses on the experimental techniques implemented for sample fabrication and characterization using optical spectroscopy. In part one, emphasis is placed on the deterministic transfer methods developed at the LPCNO. Comparison with other methods is also presented. Part two highlights the main spectroscopy techniques we implemented to analyse our samples.

2.1 An overview of fabrication techniques

It has already been pointed out in chapter one that the materials studied in this thesis are layered materials. They are comprised of stacks of atomic monolayers with strong covalent bonds in the monolayer plane and weak van der Waals forces between the monolayers ensuring the cohesion of the stacking.

Due to these weak van der Waals forces, it is possible to isolate one atomic monolayer. Here a prominent example is the isolation of graphene [73]. Exfoliation is a very simple technique which only requires a piece of the bulk layered material (graphite for instance), a piece of adhesive tape and a substrate. The simple process of mechanical exfoliation is illustrated in Fig 5.9. In practice, we put small pieces of bulk material on the adhesive tape, then we fold and unfold the tape several times to obtain many pieces of material at the surface of the adhesive tape. Afterwards we transfer the layers on a substrate. As many pieces of bulk are at the surface of the tape, we eventually maximize our chances to obtain monolayers when transferring the material on the substrate.

This very simple technique gave very good results to launch the research on layered materials. However it is easily understandable that such a procedure is very hazardous as it only relies on coincidence. Furthermore, one of the main disadvantages is that the position of the layer transferred on the substrate cannot be controlled. That is why in the following section, improved exfoliation techniques are presented. These methods enable deterministic transfer of layers at precise locations on a substrate. This evolution made it possible to stack layers of different materials, fabricating van der Waals heterostructures.

The fabrication of van der Waals heterostructures using such transfer methods is based

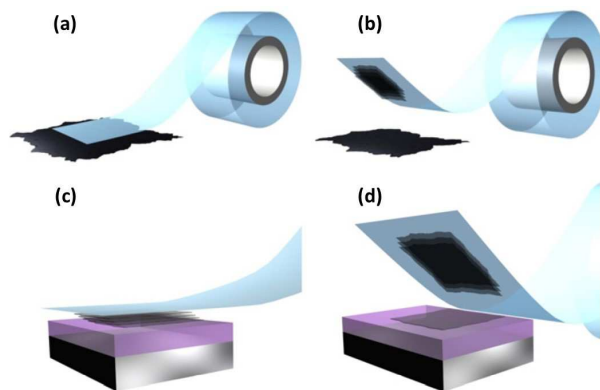


Figure 2.1: Figure extracted from [74] illustrating the basic process of mechanical exfoliation of a 2D material. **(a)** Adhesive tape is stuck on a piece of a bulk layered material (graphite for instance). **(b)** The adhesive tape is detached from the bulk and layers of the material remain on the tape. **(c)** The tape is then stuck on a substrate (silicon for instance). **(d)** Finally the tape is detached from the substrate and some layers of the material are transferred on the substrate (maybe monolayers if we are lucky!).

on layer by layer deposition. One advantage compared to MBE is that layers of van der Waals materials can be stacked without problems of lattice matching which are very important in epitaxy. As a consequence, it is possible to stack a large variety of different materials contrary to MBE which was mainly used for III-V and II-VI semiconductors. In the following sections we will also see that deterministic transfer methods enable obtaining atomically-sharp interfaces between different materials whereas for MBE transition regions are in general present between two different materials, which exist due to mixing and interdiffusion. However, MBE is industrially viable for large area samples and is performed under ultra-high vacuum and high cleanliness conditions contrary to methods derived from exfoliation which present some problems of cleanliness, especially about polymer residues as it will be explained in section 2.2.3.

In the following section, emphasis is put on one type of deterministic transfer method using polydimethylsiloxane (PDMS), which is mainly used at the LPCNO. Even if it is difficult to make a quantitative study, other techniques are also presented in a latter section for a qualitative comparison.

2.1.1 The PDMS deterministic transfer method

In order to fabricate van der Waals heterostructures, that is to stack different layered materials one on top of each other, it is essential to be able to deposit layers at precise locations on a substrate. In the previous section, it has been shown that the basic mechanical exfoliation process cannot reach such a goal as the layers are transferred at random locations onto the substrate.

The method presented here relies on the use of a polydimethylsiloxane (PDMS) viscoelastic stamp [58]. The different steps of the technique are illustrated in Fig 5.10. We still use scotch tape to split bulk materials in a multitude of small pieces of material. Then, instead of transferring the layers from the scotch directly on a substrate, we transfer them on a viscoelastic polymer stamp, which is PDMS in our case. Finally, it is possible to

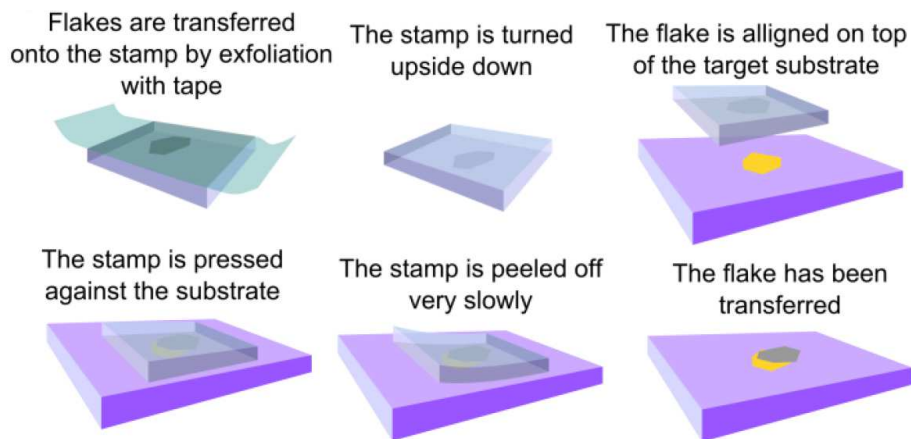


Figure 2.2: The different steps of the deterministic transfer technique with a viscoelastic stamp. Figure extracted from [58].

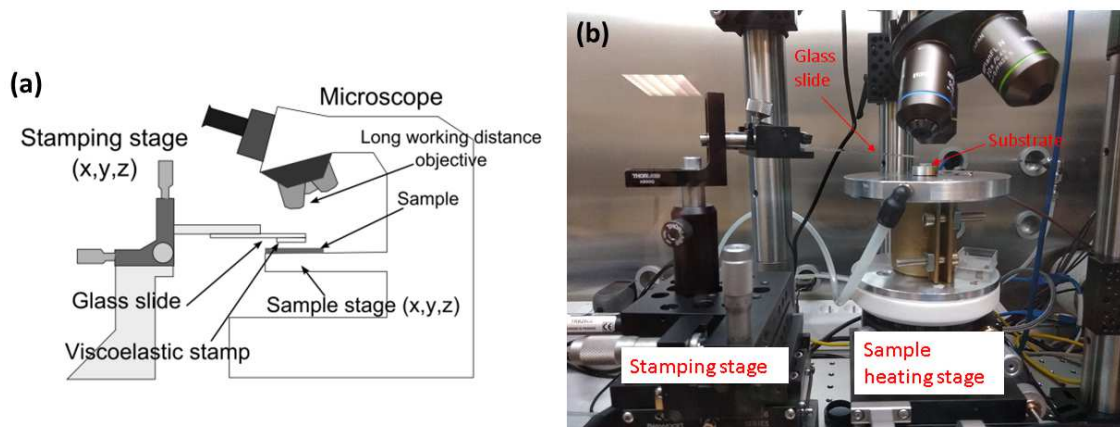


Figure 2.3: (a) Schematic illustrating an experimental setup used for deterministic transfer of layers. The glass slide with the viscoelastic stamp is held by the stamping stage. The substrate onto which we want to transfer the layers is on the sample stage. A microscope with a long working distance objective is used. Figure extracted from [58]. (b) Photography of one of our corresponding setup in a glovebox.

stick this transparent stamp on a desired location on a substrate and then by removing it slowly the layers are transferred from the stamp on the substrate.

In practice, the PDMS stamp, in our case commercial one from GelPack[®], is on a glass slide and the material layers are transferred from the scotch onto this PDMS stamp. Then we use an exfoliation setup as shown in Fig 2.3 which is composed of two main stages: one for the glass slide and one for the substrate. The glass slide with the PDMS stamp is fixed on a stage which can be moved in the XYZ directions using micromanipulators. The PDMS stamp is scanned with an optical microscope to find the appropriate layers that we want to deposit on the substrate. Once an appropriate layer has been found, we place the substrate below the PDMS stamp on another stage which can also be moved in the XYZ directions. Having these two mobile stages makes it possible to align properly the PDMS stamp with the substrate by alternately focusing on the substrate and on the PDMS. We can thus choose with micrometer precision the location of the layer transfer. Once we are well aligned, we lower the PDMS stamp until we come into contact with the substrate.

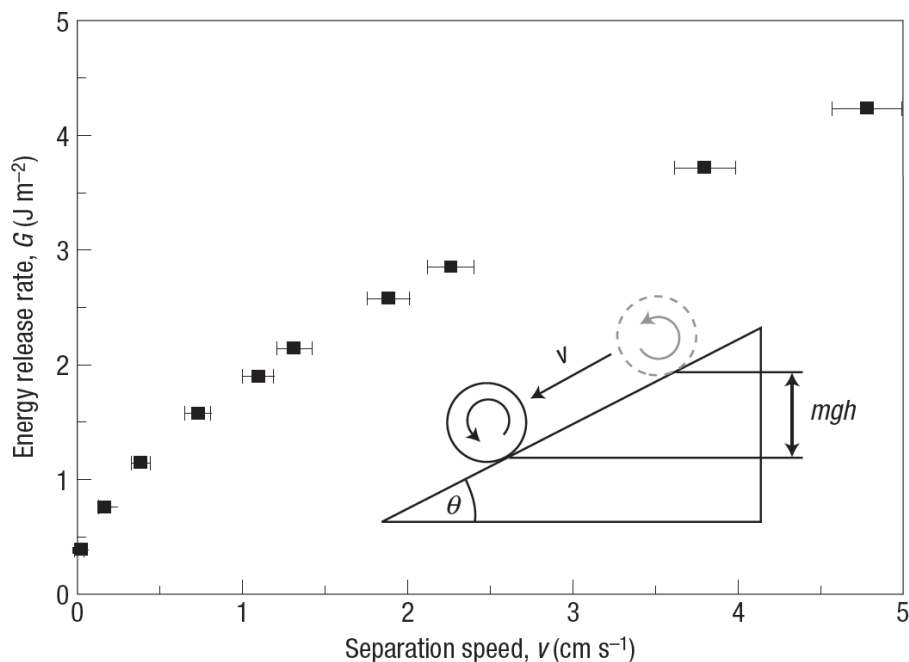


Figure 2.4: Energy release rate G as a function of the separation speed v obtained from a rolling experiment with steel cylinders. Figure extracted from [75].

As noted in Fig 5.10, the peel rate has an important effect during the transfer. Indeed, when the flake is transferred from the PDMS on the substrate, the stamp is peeled off "very slowly", that is at a controlled speed. This effect has been indeed reported by scientists working on micro-transfer-printing [75]. They show that the adhesion properties of polymer stamps are kinetically controllable. That is to say it is possible to make the PDMS very adhesive when it is peeled off very quickly from a substrate or to make it less adhesive when this peel rate is decreased. To show that, rolling experiments have been performed [76, 77, 75]. In this type of experiment, a cylinder of a certain length l and mass m is rolling down a PDMS slope. During the descent, gravitational potential energy is lost. In a first approximation, it is considered that this loss of gravitational potential energy is converted in a separation energy needed to overcome the adhesion forces with PDMS. The separation energy, or energy release rate in $J.m^{-2}$ is noted G . As it is shown in Fig 2.4 when the separation speed is decreased, the energy release rate is smaller, meaning that adhesion forces between the PDMS and the cylinder are smaller.

This property of velocity-dependent viscoelastic response of the elastomeric stamp means that the slower the peeling off rate the better it is if we want to transfer a flake from PDMS on a substrate. The entire process can be performed at room temperature but we noticed that it is easier to transfer flakes when the temperature is increased. However increasing temperature could also impact the problem of polymer residues which will be presented in the following parts.

We applied the PDMS technique to different materials: MoS_2 , WS_2 , $MoSe_2$, WSe_2 , $MoTe_2$, hBN etc... With all these materials we successfully managed to transfer layers. We generally fabricated our van der Waals heterostructures on silicon substrates but also tried to transfer the materials on other substrates such as MgO, bragg mirrors, TEM grids,

sapphire... Transferring TMD monolayers on TEM grids appeared as a very challenging task. Due to the holes of the grid, the contact area between the flake and the substrate was substantially lowered making it difficult for the monolayer to attach to the surface. However, with our experience we can qualitatively claim that the PDMS technique is well adapted for a wide range of layered materials and substrates. This method is particularly attractive because it can be qualified as "all-dry", as it does not need the use of any liquid or solvent, and it is also probably one of the easiest method to implement compared to other techniques which are presented in the following section. The different steps of the method are clearly detailed in [58].

2.1.2 Other techniques to assemble structures on the substrate

In this section we qualitatively present other bottom-up methods which enable deterministic transfer of layered materials on a given substrate. As we will see they also rely on the use of polymer layers to carry the flake that must be transferred.

One approach is to use two different polymers to coat a SiO_2/Si substrate: one water-soluble polymer layer, which can be polyvinyl alcohol (PVA) or the Mitsubishi Rayon *aquaSave*[®], and a PMMA layer. Then on this PMMA layer a flake is exfoliated. The sample is immersed in deionized water to dissolve the water-soluble polymer. As a result, the PMMA layer with the flake is detached from the SiO_2/Si and is floating at the water surface. This PMMA layer is then placed on a glass slide which is clamped to a stage with micromanipulators, like in Fig 2.3. Like for the PDMS technique, the PMMA layer with the flake is brought into contact with a substrate and is slowly peeled off to transfer the flake. If the flake does not detach from the PMMA, it is possible to increase temperature to around 100 °C during the contact. In this case, not only the flake but also the PMMA layer are deposited on the substrate. The final step is to dissolve the PMMA layer using a solvent such as acetone.

This technique was used for the first graphene samples prepared on hBN as illustrated in Fig 2.5. If properly executed, the flake carried by the PMMA should not be in contact with the water used to dissolve the water-soluble polymer but we cannot exclude totally this eventuality. A fortiori, this technique cannot be qualified as dry when the PMMA layer is dissolved in acetone.

We note that dry methods using PMMA have also been implemented [79] as shown in Fig 2.6. In this case a heating/cooling stage is used to control the temperature during the contact between the PMMA and the substrate. By heating in a first step, the PMMA and the flake conforms well to the surface, following the shape of the target substrate. As the next step, the sample is cooled down to transfer the flake.

Among other methods relying on the control of temperature during contact we can cite the elvacite sacrificial layer technique [80]. As sketched in Fig 2.7, a piece of adhesive tape is stuck on a glass slide, then methyl/n-butyl methacrylate copolymer, also called elvacite 2550 acrylic resin, is dissolved in methyl isobutyl ketone (MIBK) and spin-coated on the glass slide and tape. After annealing at 120 °C during 10 minutes to evaporate the remaining MIBK solvent, exfoliation of a material is performed on this elvacite layer. The

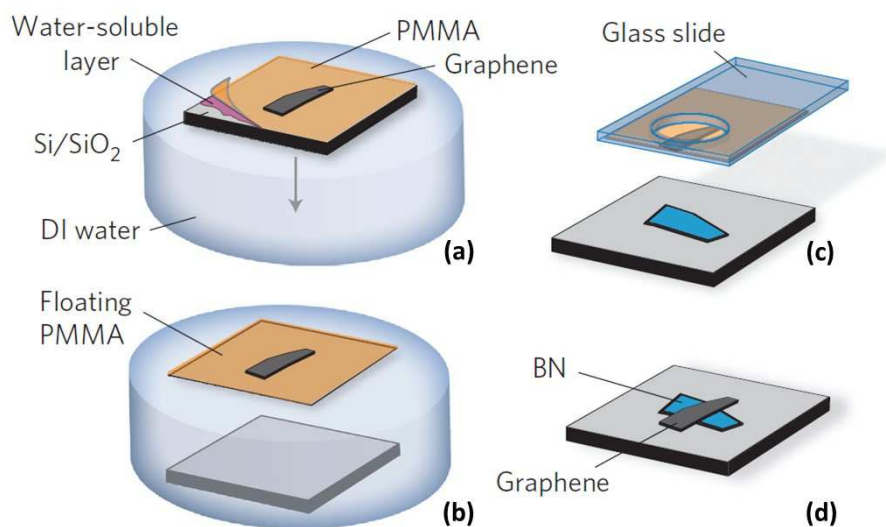


Figure 2.5: Example of a PMMA carrying layer technique used in [78] for transferring graphene on boron nitride. (a) The sample is a SiO_2/Si substrate coated with a water-soluble polymer, and a PMMA layer carrying a graphene flake. It is immersed in deionized water. (b) As a result only the PMMA remains, floating at the water surface. (c) The PMMA with the flake is placed on a glass slide. The graphene flake is aligned with a boron nitride (BN) flake. (d) After bringing into contact the PMMA and peeling it off slowly, the graphene is transferred on the BN.

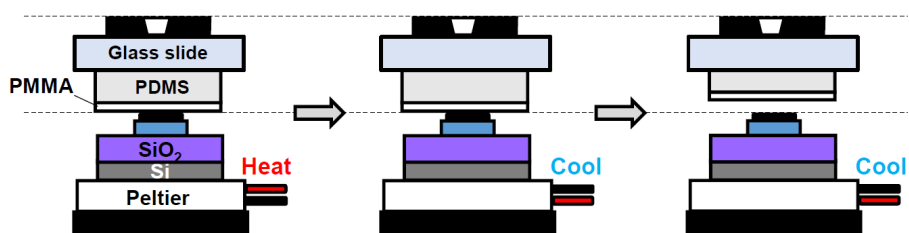


Figure 2.6: PDMS and PMMA layers are on a glass slide. A graphene flake (black layer in contact with PMMA on the figure) is transferred on a hBN layer (blue on the figure). A stage comprising a Peltier module is used to control the temperature. Figure extracted from [79].

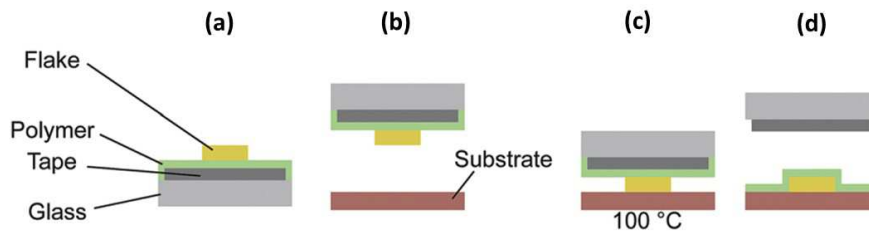


Figure 2.7: (a) A glass slide is prepared with a transparent adhesive tape and an elvacite 2550 acrylic resin spin-coated on it. A 2D material is exfoliated on the elvacite. (b) The glass slide is clamped on a stage with micromanipulators to align the flake with the substrate. (c) The flake is brought into contact with the substrate. (d) At 100 °C the elvacite melts and stays on the substrate with the flake. After this the polymer layer can be dissolved in acetone. Figure extracted from [81].

elvacite layer is scanned with an optical microscope to find an interesting flake. When a flake is found, it is aligned with a substrate and brought into contact. Raising the temperature to around 100 °C, the elvacite layer is melted and deposited on the substrate with the flake. Finally the polymer can be dissolved in acetone.

We can also cite another technique which appears to be one of the best technique to transfer layers on curved surface: the wedging transfer method [82]. However this method also presents disadvantages. First, the flake to transfer is in contact with water, due to capillary forces blisters are induced during the transfer on the substrate in Fig 2.8 (e). Second the alignment in Fig 2.8 (d) is probably quite difficult due to perturbations at the surface of the water. Then the flake is in contact with the solvent used in the final step of Fig 2.8 (f).

All the methods presented in this section are similar in the sense that the different layers are successively deposited on the substrate to fabricate the van der Waals heterostructure: the first layer, the second one etc... In the next part, we present a different approach called pick-up method for which the assembly of the structure is not made on the substrate but on the polymer stamp.

2.1.3 Assembling the structure on the polymer stamp: the pick-up technique

Compared to techniques presented previously, the pick-up technique [83, 84, 85, 86] presents one main difference: the van der Waals heterostructure is assembled on the polymer instead of being assembled on the substrate. As it is explicitly stated in the name of the method, the different layers comprising the van der Waals heterostructure are picked-up one after the other. Therefore, first the layers need to be exfoliated separately on different substrates using the scotch-tape method, and afterwards they can be picked up. The main interest of this technique is to avoid contact of the optically active layers with any stamp that might leave residues. The different steps are represented in Fig 2.9.

So for example if we want to fabricate a top hBN/MoS_2 monolayer/*bottom* hBN heterostructure, we would follow the following steps:

- Exfoliation of hexagonal boron nitride (hBN) with scotch tape on $SiO_2(80nm)/Si$

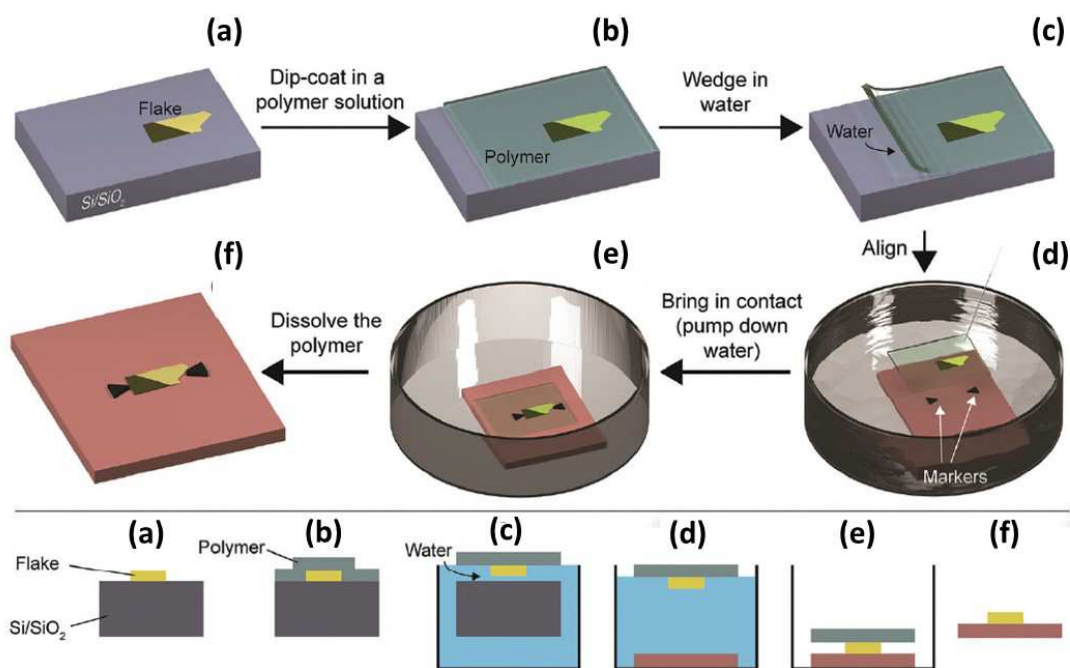


Figure 2.8: (a) The flake is exfoliated on a SiO_2/Si substrate. (b) An hydrophobic polymer layer (cellulose acetate butyrate, 30 mg.mL^{-1} in ethyl acetate, Sigma-Aldrich[®]) is deposited at the surface of the sample by dip-coating. (c) The sample is immersed in water. Water molecules intercalate between the SiO_2 and the polymer, delaminating the polymer layer. (d) The polymer layer with the flake floats at the surface of the water. A target substrate is placed under it. The polymer and flake are aligned with the substrate using a tool such as a needle. (e) Water is pumped from the container and the polymer layer with the flake is deposited on the substrate. (f) The polymer is dissolved in a solvent such as ethyl acetate. Figure extracted from [81].

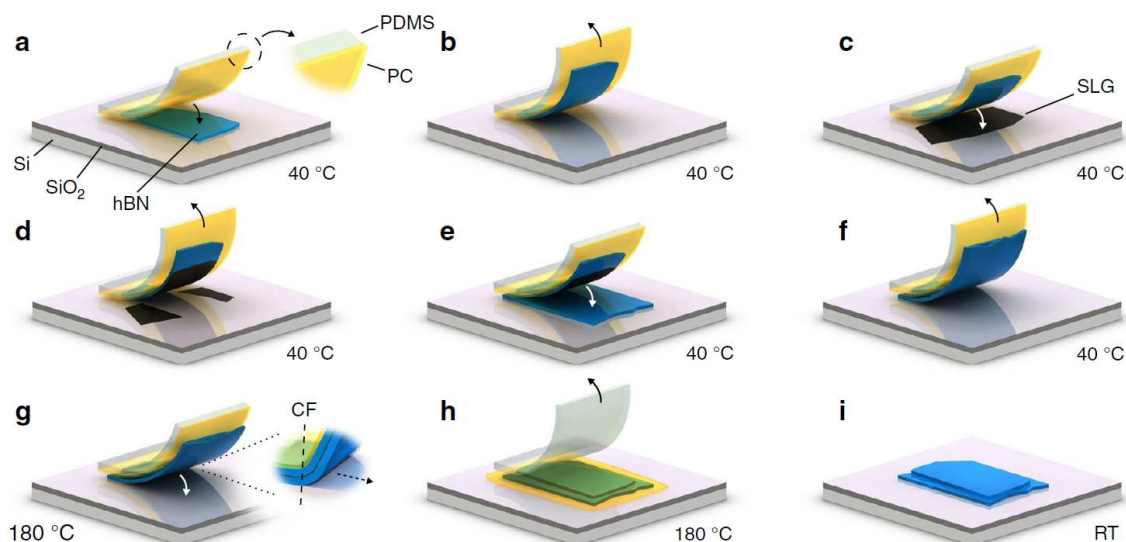


Figure 2.9: Figure extracted from [86] representing the different steps of the pick-up technique to fabricate a top *hBN/graphene* (SLG)/*bottom hBN* heterostructure. From (a) to (f) the different layers of the structure are picked-up with a *PDMS/PC* (polycarbonate) stamp at 40 °C. (g) The final heterostructure which is carried by the polymer stamp is brought into contact with the substrate at 180 °C. (h) Still at 180 °C the stamp is lifted up. The PC has melted and stays on the substrate with the heterostructure. (i) The PC layer is removed by immersing the sample in a solvent, such as chloroform for about 10 minutes.

substrate. This will be the top hBN of the final structure.

- Pick-up of the top hBN with a *PDMS/PC* (polycarbonate) stamp at about 40 °C.
- Exfoliation of *MoS₂* on *SiO₂(80nm)/Si* with scotch tape.
- Pick-up of a *MoS₂* monolayer with the *PDMS/PC/Top hBN* at about 40 °C.
- Exfoliation of hBN on *SiO₂(80nm)/Si* with scotch tape. This will be the bottom hBN of the structure.
- Pick-up of the bottom hBN with the *PDMS/PC/Top hBN/MoS₂* at about 40 °C.
- Transfer of the full heterostructure top *hBN/MoS₂* monolayer/*bottom hBN* on another substrate at about 180 °C.
- Removal of the melted PC layer in a chloroform bath during 10 minutes.

Note that for picking up layers, we sometimes first used higher temperatures to make the PC layer to conform properly with the substrate and the flake during the contact step, and then we decreased the temperature to 40 °C to pick-up the flake when we lifted up the *PDMS/PC* stamp.

In practice, from our experience, this technique can be difficult to set up for several reasons. First we need to exfoliate the layers on silicon substrates before picking them up. With this scotch tape exfoliation, the yield to obtain TMD monolayers is very low from our experience and the monolayers are globally smaller than the ones obtained when

exfoliation is made on a PDMS stamp; only some μm laterally for direct exfoliation on silicon compared to tens or hundreds of μm when exfoliated on PDMS. Increasing the temperature ($\sim 120^\circ\text{C}$) during exfoliation improves the yield of transfer from the scotch to the silicon substrate but still it is lower than the yield of transfer when exfoliation is made on PDMS. Another problem is that the PC is difficult to handle. We need to deposit a thin PC layer on a PDMS stamp. This PC layer is very fragile and folds or breaks easily. Moreover, when we bring the PDMS/PC stamp into contact with substrates, it is more difficult to control the contact compared to PDMS. If the PC is not well stuck on the PDMS, this is even more difficult to control. Maybe for our future trials with this method we need to fabricate thicker PC layers.

Compared to the PDMS deterministic transfer, the pickup method needs the implementation of a lot of different steps which makes it very time consuming. However, we note from our example that except the top hBN which is in contact with the PC, all the other flakes are not in contact with any polymer, which makes this technique attractive to fabricate van der Waals heterostructures with clean interfaces and this pick-up technique is therefore used by many leading groups in the field. We will focus on this problem of polymer residues in section 2.2.3.

2.1.4 Growth and synthesis techniques

So far, all the techniques which have been presented are derived from exfoliation, and the samples fabricated for the present thesis work have been made with such techniques, especially the PDMS deterministic transfer. However, even if this method was of great interest to fabricate samples for fundamental research, it is not adapted to scalable industrial applications. Several limitations prevent exfoliation from being industrially viable: it is too random, the size of monolayers is relatively small with an average size of tens of μm , it is very time consuming and the yield for obtaining monolayers is relatively low. In our experience, we basically obtained one TMD monolayer per PDMS stamp of 1cm^2 . Attempts with chemical and solvent exfoliations made possible to increase the number of exfoliated flakes, but without controlling the layer size and thickness. Furthermore the flakes exfoliated with these techniques are generally contaminated and highly doped.

For these reasons, it is important to implement techniques making 2D materials or van der Waals heterostructures fabrication possible with a better control of physical dimensions, chemical composition, crystallinity. Among them we can cite different growth methods: Physical Vapor Transport (PVT), Physical Vapor Deposition (PVD), Chemical Vapor Deposition (CVD), Molecular Beam Epitaxy (MBE)... Even if the objective of this thesis is not to give a detailed study of growth methods, we present here a very brief overview of this subject.

CVD already gave very good results for the growth of graphene [87, 88, 89]. It was also applied to grow other 2D materials such as members of the TMD family: MoS_2 [90, 91, 92, 93, 94], MoSe_2 [95], WS_2 [96], WSe_2 [97]. One of the main method is the thermal CVD process schematized in Fig 2.10 for the growth of MoSe_2 monolayers. The triangular shapes visible in the optical microscope image of Fig 2.10 (b) are MoSe_2 layers obtained

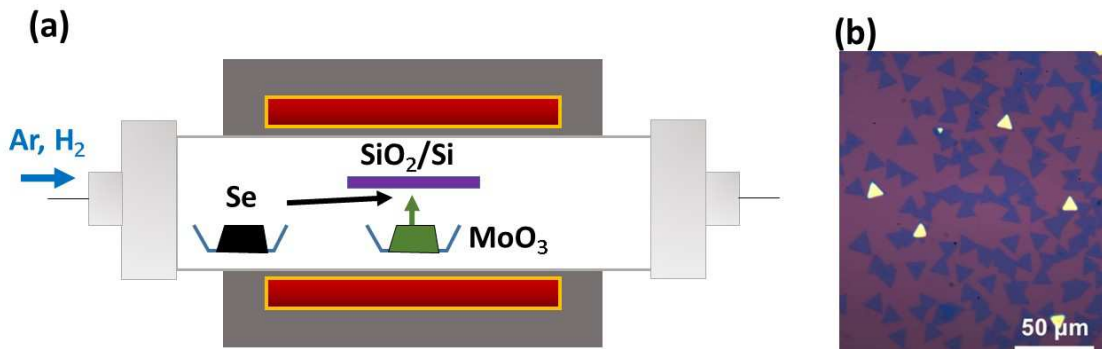


Figure 2.10: (a) Illustration (inspired from [95]) of a thermal CVD furnace used for $MoSe_2$ growth. The precursors used are Se powder and MoO_3 powder. A flow of 65 standard cubic centimeters per minute (sccm) of Ar and 5 sccm of H_2 is used as the carrier gas flow. The substrates onto which the $MoSe_2$ is synthesised are placed in the middle of the furnace, polished face down facing the MoO_3 powder. The red part represents the heating system of the furnace. Temperature is increased to reach $750\text{ }^\circ\text{C}$ and the furnace is kept at this value for 10 to 15 minutes. It is then cooled down to room temperature. (b) Optical microscope image of a silicon substrate after growth. The triangles are $MoSe_2$ layers; some parts are monolayers and other are multilayers. Figure extracted from [95].

after the growth process. This triangular shape comes from the threefold symmetry of TMD monolayers and is due to the fact that edges terminated either by chalcogen or transition metal atoms are thermodynamically favoured.

Not all the layers synthesized are necessarily monolayers. We can easily distinguish them using PL as the monolayers are direct bandgap semiconductors as explained in chapter one. This is shown in Fig 2.11. It is also possible to use Raman spectroscopy to discriminate between different thicknesses [95].

For long, CVD grown monolayers have been neglected by spectroscopists because they presented worse optical quality than exfoliated samples in terms of broadening and defect bound peaks. However recent measurements, also by our group [98], tend to show that by picking up the layers on the initial substrate where they were grown and then depositing them on another substrate like hexagonal boron nitride (hBN), the optical quality is substantially improved [99, 100].

One of the main challenges is to produce uniform large area monolayers. It is also important to control if the growth will be in-plane (2D) or vertical (3D). Studies have shown that increasing the growth temperature lowers the density of thick layers and increasing the super-saturation of the precursors increases the density of thick layers. Metalorganic CVD (MOCVD) has been used to produce large scale monolayers with a certain success [101, 102], but due to the large number of domains, the films produced are polycrystalline.

Beyond the growth of isolated TMD monolayers, heterostructures can be synthesised. These structures can be lateral [103, 104, 105, 106] or vertical [107, 105, 108]. Among the different types of structures which are grown, efforts are also focused on the synthesis of 2D $TMDs/hBN$ heterostructures [109, 110]. As it will be explained in detail in this thesis, hBN revealed excellent properties as a substrate and encapsulation material for 2D TMDs.

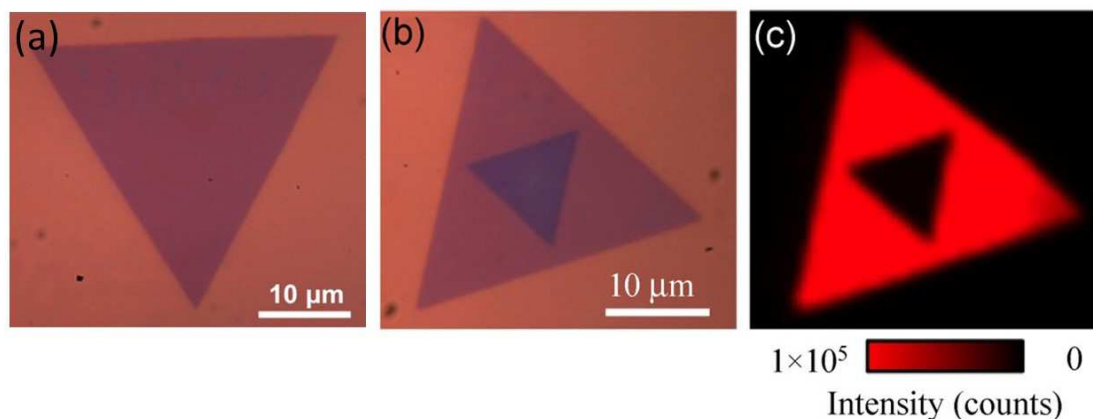


Figure 2.11: (a) A $MoSe_2$ monolayer on a $SiO_2(300\text{ nm})/Si$ substrate. (b) Monolayer/bilayer nanosheet. (c) PL mapping of the flake. The red part corresponds to the zone with the highest intensity which is the monolayer part. Images extracted from [95].

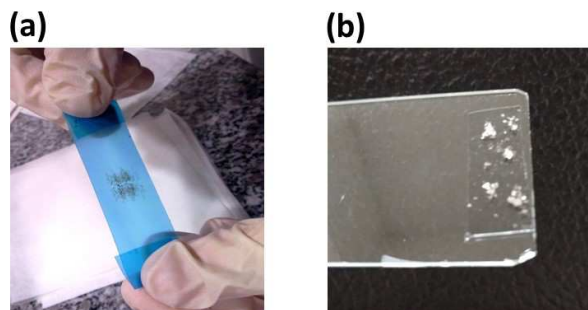


Figure 2.12: (a) Pieces of TMD bulk are placed on a scotch tape which is folded and unfolded several times. (b) After sticking the scotch tape of (a) on a PDMS stamp which is on a glass slide.

2.2 Sample fabrication

The previous section has given a general presentation about different fabrication techniques used in the field of 2D TMD research. In this part, we now focus more precisely on the different steps used in our laboratory to fabricate van der Waals heterostructures, especially hBN/2DTMD/hBN samples as the techniques used at the LPCNO represent the state of the art in this field [111]. The main technique employed is the PDMS deterministic transfer presented previously in section 2.1.1. Concerning the sources of bulk material, we thank our collaborators from the NIMS Tsukuba for high purity hBN and Sef Tongay's group at Arizona State University for TMD bulk, in addition to commercial suppliers 2D semiconductors[®] and HQ Graphene[®] for TMD bulk.

2.2.1 TMD monolayer identification

As explained previously, to obtain TMD monolayers we use mechanical exfoliation with adhesive tape and exfoliate the TMD flakes on a PDMS stamp which is on a glass slide as illustrated in Fig 2.12.

After exfoliation on the PDMS stamp. We clamp the glass slide on a stamping stage

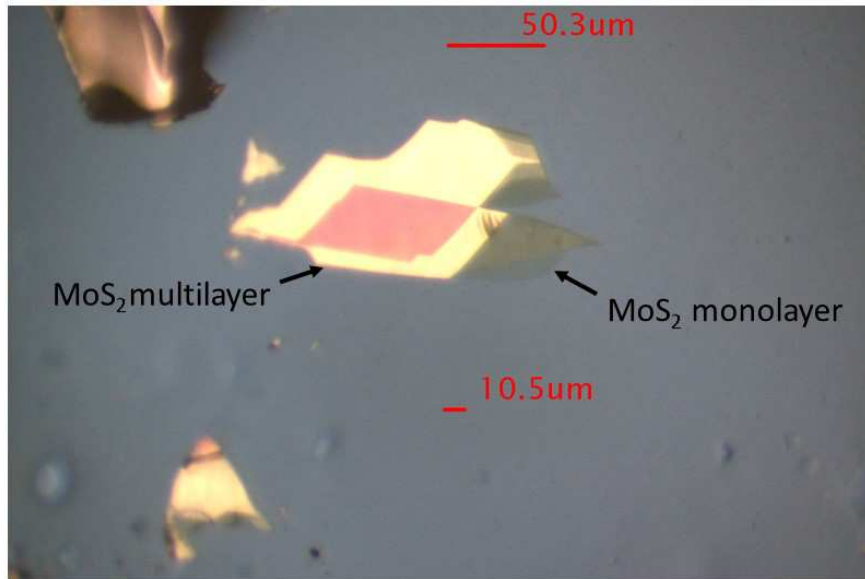


Figure 2.13: Optical microscope image of MoS_2 on a PDMS stamp. Both monolayer and multilayer areas are visible. Due to high absorption, the monolayer appears in light grey by optical contrast.

as the one in Fig 2.3. Then, the PDMS stamp is scanned with an optical microscope with a long working distance objective (in our case we use an Olympus[®] objective MPLFLN $\times 10$ with a working distance of 11 mm).

During the scan we can distinguish between multilayer flakes or monolayer flakes only by optical contrast as shown in Fig 5.11.

In case of doubt, we can check in PL at room temperature if the flake is a monolayer. If it is thicker than a monolayer we do not expect any PL signal or very low in intensity. Note that Raman spectroscopy can also be used to discriminate between bulk and monolayer [112] as E_{2g}^1 and A_{1g} mode shifts in 2D compared to 3D. However, in general, for the principal members of the TMD family (MoS_2 , WS_2 , $MoSe_2$, WSe_2 , $MoTe_2$), we gained enough experience to be able to simply identify monolayers by optical contrast [113]. Furthermore, if the monolayer is standing on the PDMS and is not protected, we fear that laser exposure could damage or influence optical properties of the flake (especially if a high power is used) [114].

2.2.2 Selecting hBN layers

In addition to TMD monolayers, in most of the work presented in this thesis, the van der Waals heterostructures are also composed of hexagonal boron nitride (hBN) layers. It is therefore important to acquire a certain control on the hBN flakes we use to fabricate samples. Moreover, it will be shown in chapter 3 that hBN thickness can play an important role in the optical response of the samples.

We note here that the hBN we use in our structures is highly pure, synthesised from Ba-BN solvent at 4.5 GPa and 1500 °C at the NIMS Tsukuba, Japan [115]. So far, this hBN has been considered as the purest which can be found in the international community

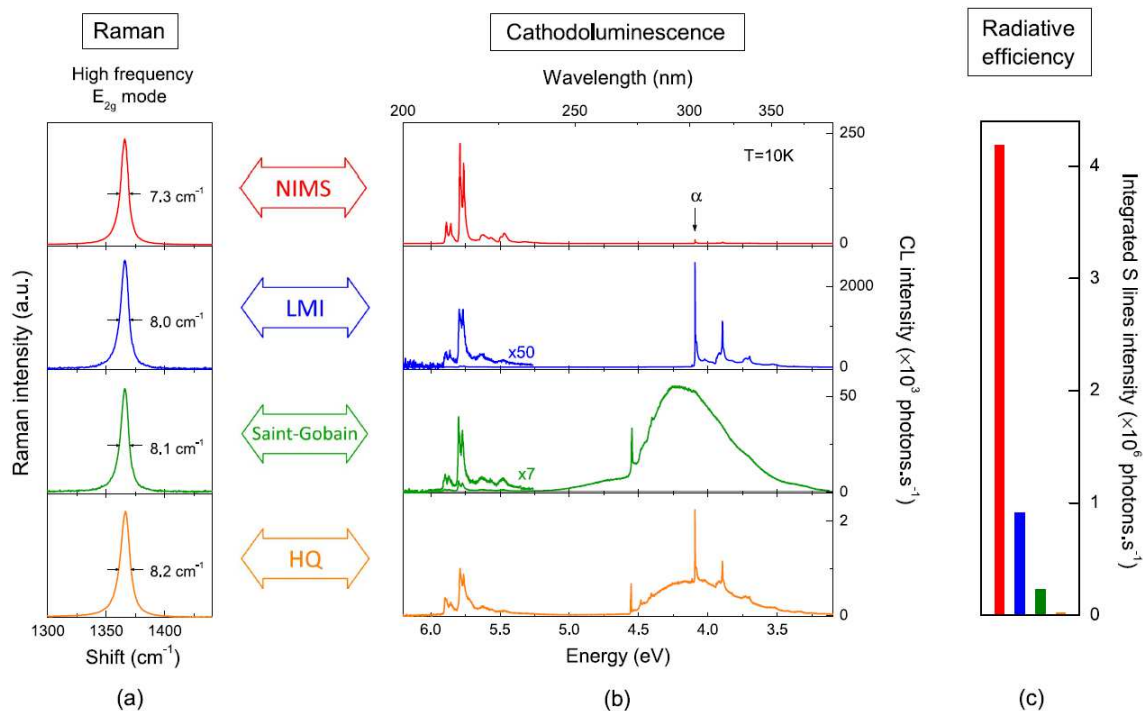


Figure 2.14: Comparison of nanometer-thick hBN from different sources. (a) Hexagonal boron nitride from NIMS presents the narrowest linewidth in raman spectra. (b) It is characterized by an absence of peaks related to defects at energies smaller than 5.0 eV contrary to hBN coming from other sources (HQ Graphene, Saint-Gobain, or "the Laboratoire Multimatériaux et Interfaces" LMI). (c) NIMS' hBN also has the highest radiative efficiency. Figures extracted from [116].

as illustrated in 5.12.

As hBN is also a layered material, we use exfoliation and PDMS deterministic transfer like for TMDs. Similarly, we scan the PDMS stamp to find hBN layers that we select according the following main criteria: their size, their flatness and their thickness. We use hBN both as a substrate and also as a capping layer. Used as a substrate for TMD, the hBN flake must be atomically flat to avoid creating strain in the TMD monolayer which is deposited on its surface. It must be thick enough to avoid transmitting the roughness of the underlying substrate which can be SiO_2 for instance. Used as a capping layer, the hBN flake must be homogeneous and thin enough (in general ~ 10 nm) to mould to the surface of the TMD and bottom hBN.

A first way to assess the thickness of a hBN flake is its color and I have developed a deeper understanding of this problem during my thesis for the group. Indeed, due to interferences, hBN thin films exhibit different colors depending on their thickness. To make the identification easier, we simulated colors as a function of thickness using a transfer matrix approach. The transfer matrix approach, described in detail in chapter 3 to analyze our reflectivity spectra, enables simulating reflectivity of thin films. Once the reflection coefficient $R(\lambda)$ is calculated, we can get a color from the R spectrum. This can be done by adopting the CIE XYZ color space. Analogously to RGB (Red, Green, Blue) system, XYZ is a coordinate system for describing colors. To describe a color it is interesting to understand how it is perceived by the human eye. The retina contains two main types

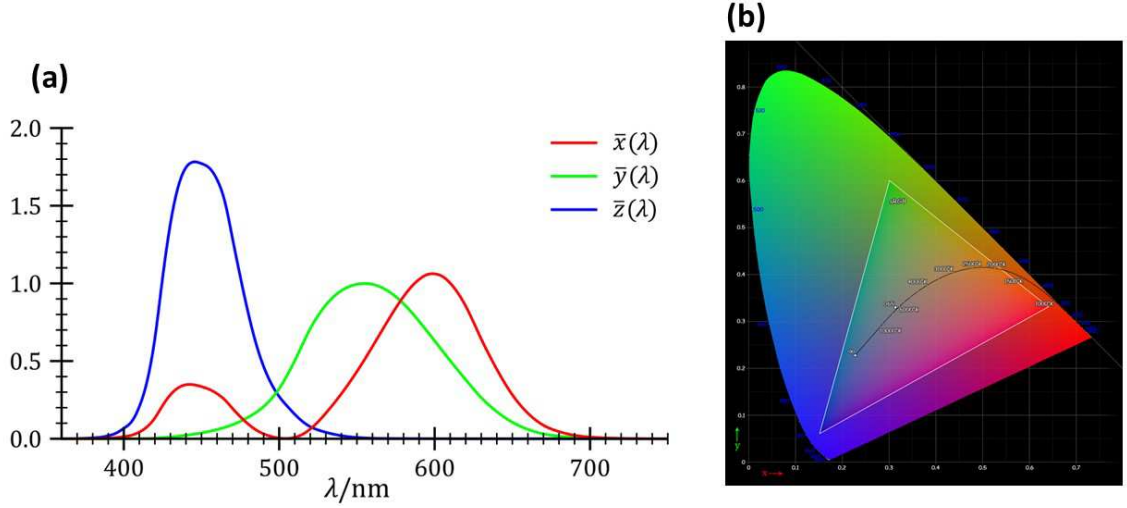


Figure 2.15: **(a)** Color matching functions $\bar{x}(\lambda)$, $\bar{y}(\lambda)$ and $\bar{z}(\lambda)$. Figure extracted from [117]. **(b)** The CIE 1931 xy chromaticity diagram. The triangle represents the gamut for the RGB color space. Figure extracted from [118].

of sensors called rods and cones. The rods are sensitive to luminance whereas cones are sensitive to colors. The cones are divided into three categories which are mimicked in the XYZ system by the color matching functions $\bar{x}(\lambda)$, $\bar{y}(\lambda)$ and $\bar{z}(\lambda)$. To each of this function is associated a sensitivity which depends on the wavelength as shown in Fig 2.15 (a).

From a reflectance spectrum $R(\lambda)$, the tristimulus values X, Y and Z are defined as:

$$X = \int R(\lambda)\bar{x}(\lambda)d\lambda \quad Y = \int R(\lambda)\bar{y}(\lambda)d\lambda \quad Z = \int R(\lambda)\bar{z}(\lambda)d\lambda \quad (2.1)$$

Then, X, Y and Z are normalized:

$$x = \frac{X}{X+Y+Z} \quad y = \frac{Y}{X+Y+Z} \quad z = \frac{Z}{X+Y+Z} = 1 - x - y \quad (2.2)$$

It means that z can be deduced from x and y. So we can describe a color with x and y parameters. This is illustrated with the CIE 1931 xy chromaticity diagram in Fig 2.15 (b). A python class named "ColourSystem" is available online [119]. If needed, these xyz parameters can be converted in the RGB color system.

To simulate the color of an object, the illuminant, that is the type of light illuminating the object must be taken into consideration. In theory we should take the light used in our microscope to scan the PDMS stamps but using the standard illuminant D65 gave results in agreement with the observed colors.

Results for computed colors of hBN flakes on PDMS are given in Fig 5.13.

This tool is experimentally very useful as we know now that controlling hBN thickness is important for optical spectra for enhancing absorption in the TMD monolayer and even for controlling the exciton lifetime. In addition to color we can measure reflectivity of an hBN flake and compare this spectrum with the simulated reflectivity.

The precise determination of hBN thickness can be particularly delicate when considering ultra-thin hBN flakes (~ 1 nm). This is the case for example if we want to fabricate

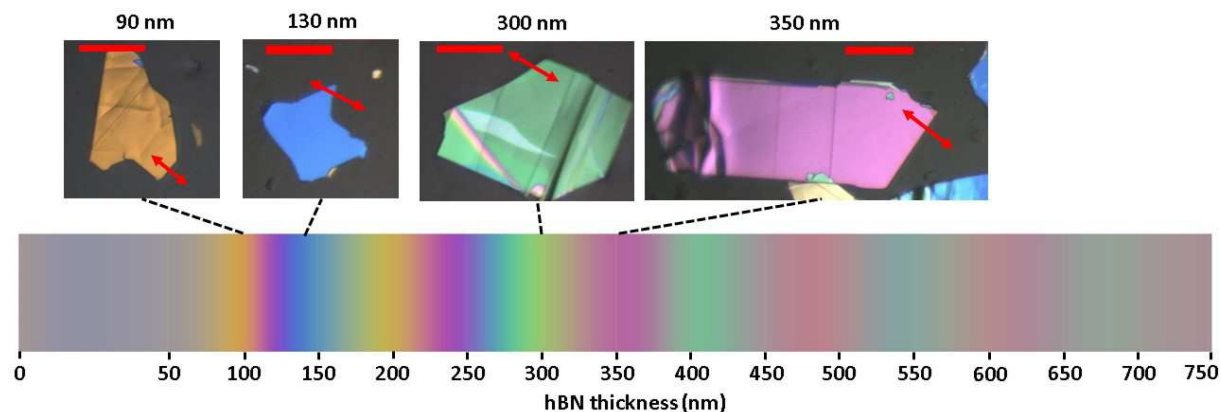


Figure 2.16: Computed colors of hBN on a PDMS stamp as a function of thickness. For comparison some hBN flakes are shown with the corresponding thicknesses measured with AFM. The red arrows indicate the approximate positions of the AFM measurements. The red scale bars on the optical microscope images correspond to $50.3 \mu\text{m}$.

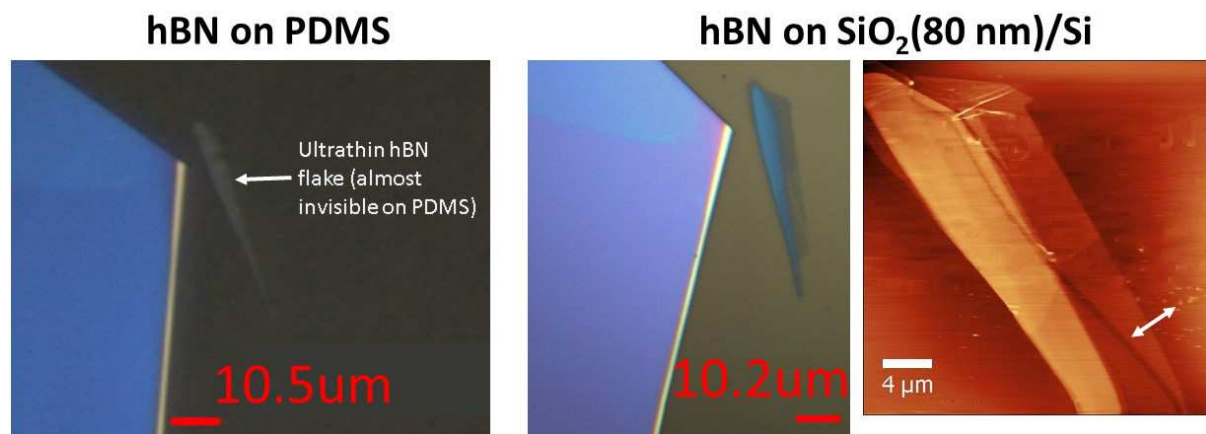


Figure 2.17: On the left an image of a thin hBN flake on PDMS. On the right, the same hBN flake after transfer on a silicon substrate with a SiO_2 thickness of 80 nm. The corresponding AFM image is shown. A thickness of about 2 nm is measured at the position of the white arrow.

a tunnel barrier with hBN. Finding ultra-thin flakes is challenging as they are transparent on PDMS below a certain thickness (~ 5 nm). To enhance optical contrast, hBN can be deposited on a silicon substrate with a certain SiO_2 thickness enabling optical identification of thin hBN. Gorbatchev et al. have shown that it is possible to identify hBN monolayers by optical contrast when the flakes are deposited on an adequate substrate with a 90 nm SiO_2 layer [120]. In Fig 2.17, an example of a thin hBN flake is shown on PDMS and after transfer on a $\text{SiO}_2(80 \text{ nm})/\text{Si}$ substrate. On PDMS the thin hBN has a grey color whereas it appears more clearly with a blueish contrast on the silicon substrate. Furthermore, when deposited on SiO_2 thinner parts are distinguishable on the right side of the flake and were invisible on the PDMS. For the given example, the thinnest parts measured with AFM are about 2 nm thick.

This technique can be used to find hBN monolayers, but our experience shows that this is still a challenging work and most of the thinnest flakes found had a thickness of

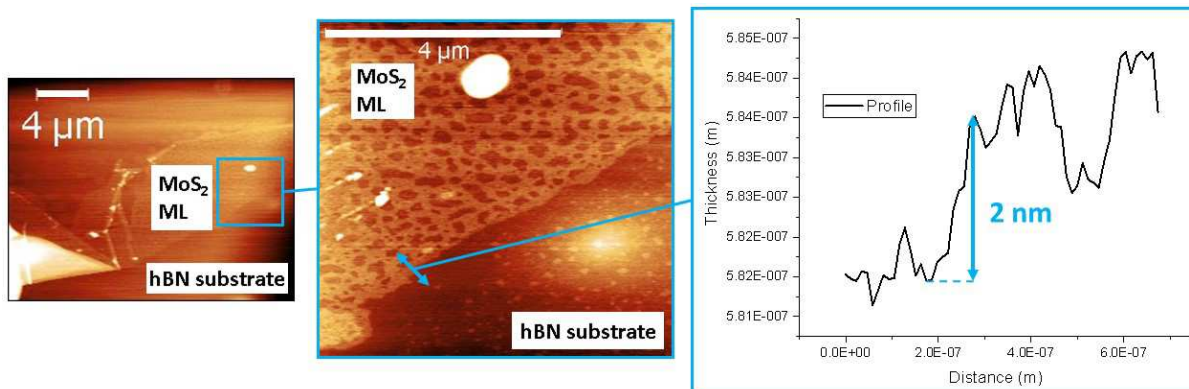


Figure 2.18: Two AFM images of a MoS_2 monolayer/hBN heterostructure. The scale bars correspond to $4 \mu\text{m}$. The position of the AFM profile is indicated with a blue arrow.

about 1 nm instead of the 3 \AA expected for a hBN monolayer.

The work is not finished when a thin hBN is found. The next step is to be able to incorporate the given flake in a van der Waals heterostructure. As the hBN flake has been deposited on SiO_2 , it must then be picked up from this substrate. To do this a method such as the PC pick-up technique presented in the previous section can be implemented. We developed at LPCNO a simple technique which does not require to use any solvent. This pick up technique relies again on PDMS and temperature dependent pick-up.

2.2.3 The problem of polymer residues

For the different deterministic transfer techniques presented before one of the recurrent problems is the issue of polymer residues on the semiconductor layers we want to investigate. In our case, the flakes deposited during the fabrication process of van der Waals heterostructures are in contact with a PDMS stamp. In this part, some methods used to solve or minimize the problem of polymer residues that were optimized during this thesis work are presented.

Atomic Force Microscopy (AFM) measurements performed on van der Waals heterostructures can reveal the presence of polymer residues at the sample surface. Fig 5.14 shows AFM measurements performed on a MoS_2 monolayer/hBN heterostructure. At the surface of the sample, especially on the MoS_2 monolayer, a large area is covered with polymer residues giving a "leopard pattern". Due to this, it is not possible to measure the right thickness of the MoS_2 monolayer which should be $\sim 6.5 \text{ \AA}$. Instead the profile gives thickness of several nm ($\sim 2 \text{ nm}$ for the points taken in the figure). We note that most of the residues cover the MoS_2 and only a few "grains" are visible on the hBN.

The sample in question was fabricated with a commercial PF PDMS film from Gelpack[®] with a retention level $\times 4$. We also tried to use a PF PDMS film with a retention level $\times 8$ to observe the effect on polymer residues (see Fig 2.19). AFM measurements on a MoS_2 multilayer/hBN structure revealed the presence of a lot of polymer residues covering almost all the surface of the sample. Compared to the case of the PDMS $\times 4$, for a retention level of $\times 8$ the PDMS covers even the hBN. The AFM profiles give larger residue thickness

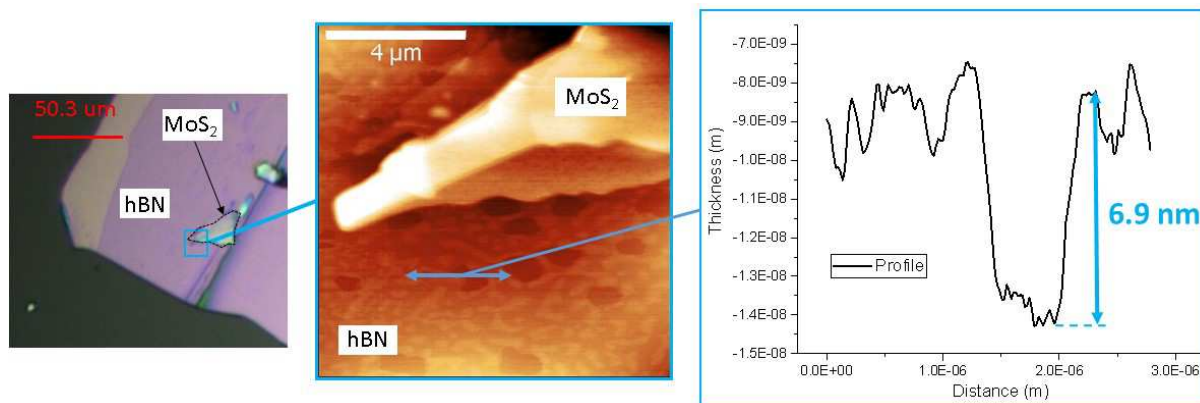


Figure 2.19: Optical microscope and AFM images of a MoS_2 multilayer/hBN structure. The position of AFM profile is indicated with a blue arrow.

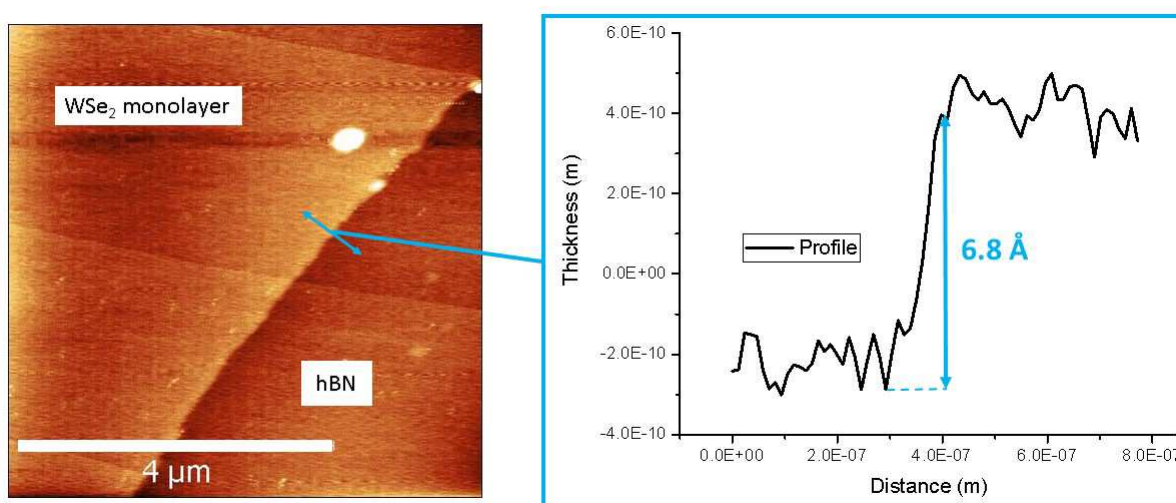


Figure 2.20: AFM image of a WSe_2 monolayer deposited on a hBN substrate with a cleaner PDMS stamp. The profile gives the right thickness expected for a TMD monolayer (between 6 and 7 Å).

of several nm (~ 6.9 nm for the example of Fig 2.19). We expected this result as Gelpack PDMS films with retention levels $\times 8$ are more sticky.

For the next samples, we use another PDMS, the highly purified DGL film from Gelpack with a retention level $\times 4$. Fig 5.15 shows an AFM measurements of a WSe_2 monolayer/hBN heterostructure. It is now possible to measure the thickness of a TMD monolayer which is comprised between 6 and 7 Å. We do not observe the "leopard pattern" related to polymer residues.

However, further measurements made with scanning electron microscope (SEM) revealed the presence of PDMS residues even when the cleaner PDMS was used (see Fig 2.21). The samples of panels (a) and (b) have been prepared differently. The one in panel (a) has been deposited on silicon with PDMS whereas the one in panel (b) has been deposited on silicon only using scotch tape and without any polymer. In panel (a) white areas related to polymer residues are visible whereas in panel (b) these residues are not present

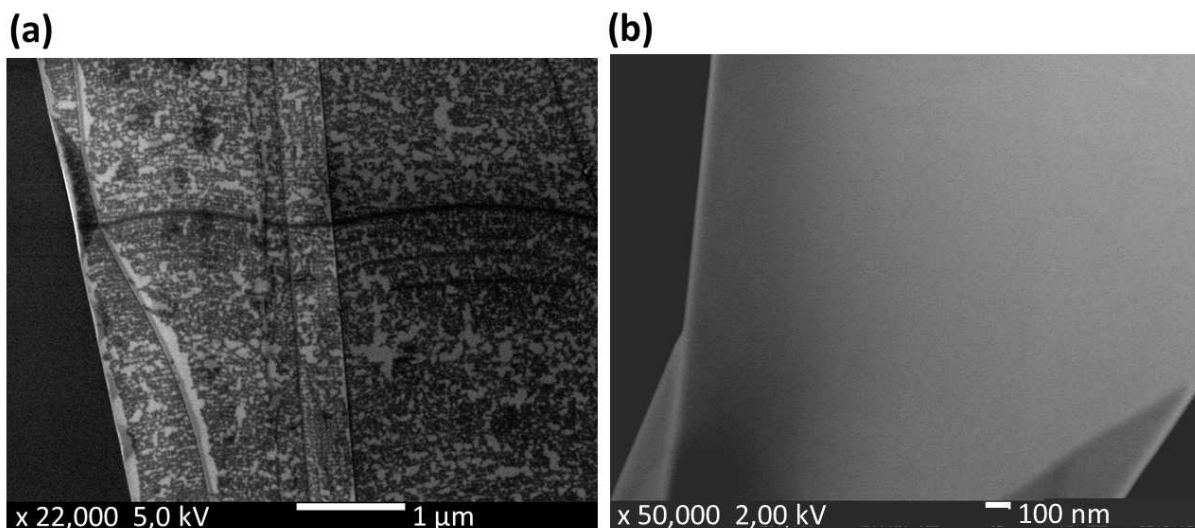


Figure 2.21: **(a)** This panel shows a SEM image of a hBN flake deposited on silicon with "clean" PDMS. The white areas correspond to PDMS residues. The horizontal stripes have been produced by the AFM tip during the scan even if we used tapping mode. **(b)** This panel shows a SEM image of a hBN flake deposited on silicon only with scotch. As no polymer has been used, the smooth surface of hBN appears without any residue.

and the hBN surface looks smooth. Another interesting information to add concerning panel (a) is that the corresponding sample has been submitted to AFM measurements in tapping mode before doing the SEM measurements. In this case AFM did not reveal the presence of the residues contrary to SEM and we observe that even if we used tapping mode the AFM tip interacted with the PDMS residues, producing a pattern of horizontal lines where the scan was made. We believe that the PDMS residues are probably very thin compared to the ones of Fig 5.14 and Fig 2.19. In fact, in contact mode interaction of the AFM tip with polymer residues has previously been used to clean 2D materials like graphene whose electronic properties were improved after this kind of process [121].

The problem of PDMS residues was already highlighted in micro-contact printing experiments [122, 123, 124]. It was shown that an UV/ozone treatment of the PDMS stamp can considerably improve the situation by reducing the residues transferred [123]. The same technique has been applied to the fabrication of van der Waals heterostructures. With supporting AFM measurements, it has been shown that the treatment of commercial PDMS stamps from Gelpack improved the quality of the transfer by drastically reducing the amount of polymer contaminants [125]. The UV/ozone treatment breaks organic species present at the surface of the stamp. In addition a thin oxidized layer SiO_x of about 20-30 nm forms at the surface. This layer does not contain carbon and acts as a barrier preventing the diffusion of oligomers from the PDMS to the substrate onto which the stamp is brought into contact. Among the disadvantages of such a method we note that this kind of treatment must be optimized because it can also change strongly the adhesion properties of the PDMS making exfoliation of flakes on its surface very difficult. On our side we conducted a few experiments by treating PDMS stamps with O_2 plasma with preliminary results showing that it can indeed be very challenging to exfoliate flakes

on the polymer when it has been treated. We also used O_2 plasma to treat hBN flakes after their transfer with untreated PDMS. Consecutive SEM measurements have shown that the hBN surface after plasma treatment is clean. However, if treatment of hBN flake is possible, it is not possible to treat TMD monolayers without impacting their properties and creating structural defects.

Another way to avoid the problem of residues between layers in a van der Waals heterostructure is to adopt the pick-up method presented in 2.1.3. In this case only the top layer is in contact with a polymer such as PC. All the layers have been deposited only with scotch so they are not covered with residues like the hBN flake of Fig 2.21 (b).

However we will see in the next section that with a simple annealing process it is possible to induce the aggregation of contaminants present between layers in van der Waals heterostructures. As a consequence some areas of the structures are clean and homogeneous but others are covered with blisters and bubbles which form between the layers. In our confocal microscope for optical spectroscopy, the excitation/detection spot diameter is $<1 \mu\text{m}$, a clean sample structure residue free over several μm is therefore sufficient for our work.

2.2.4 Interlayer contaminants

During the fabrication of van der Waals heterostructures, different thin layers or 2D materials are brought into contact. During the process, contaminants can be trapped between layers, especially when the fabrication process is made in an ambient environment. Among the effects induced by interlayer contaminants we find strain, inhomogeneous dielectric environment and also charge transfer doping.

Evidence is already visible in the optical microscope images where bubbles form when van der Waals layers are deposited one on top of the other. Particularly we observe the formation of such blisters when we deposit the top hBN in our encapsulated van der Waals heterostructures (hBN/TMD monolayer/hBN). A simple annealing on a hot plate leads to the coalescence of the contaminants forming larger bubbles as illustrated in Fig 2.22.

Another way to observe clearly these blisters is in dark field images, where scattered light is collected making blisters and layer edges appear brighter as illustrated in Fig 2.23.

These bubbles are also clearly visible in AFM measurements in Fig 5.16, where they appear as round shapes. After annealing, the blisters aggregate to give larger bubbles. In general the bubbles preferably aggregate at crack or wrinkle locations like the blister framed on the image of the sample after annealing in the figure.

The shape and size of bubbles have been precisely studied using AFM in [126]. The main shapes observed are round, triangular or pyramidal as a result of the competition between van der Waals and elastic forces. AFM indentation experiments of the bubbles have shown that the pressure inside is of the order of the MPa for bubbles with a radius $R=250-800 \text{ nm}$, and could in principle reach 1 GPa for smaller bubbles with $R=1 \text{ nm}$. These high pressures can locally strongly modify the properties of materials as it has been shown in the case of graphene for which enormous pseudo-magnetic fields greater than 300 Tesla have been induced [127]. In our work we still treat bubbles as undesirable features that we want to eliminate.

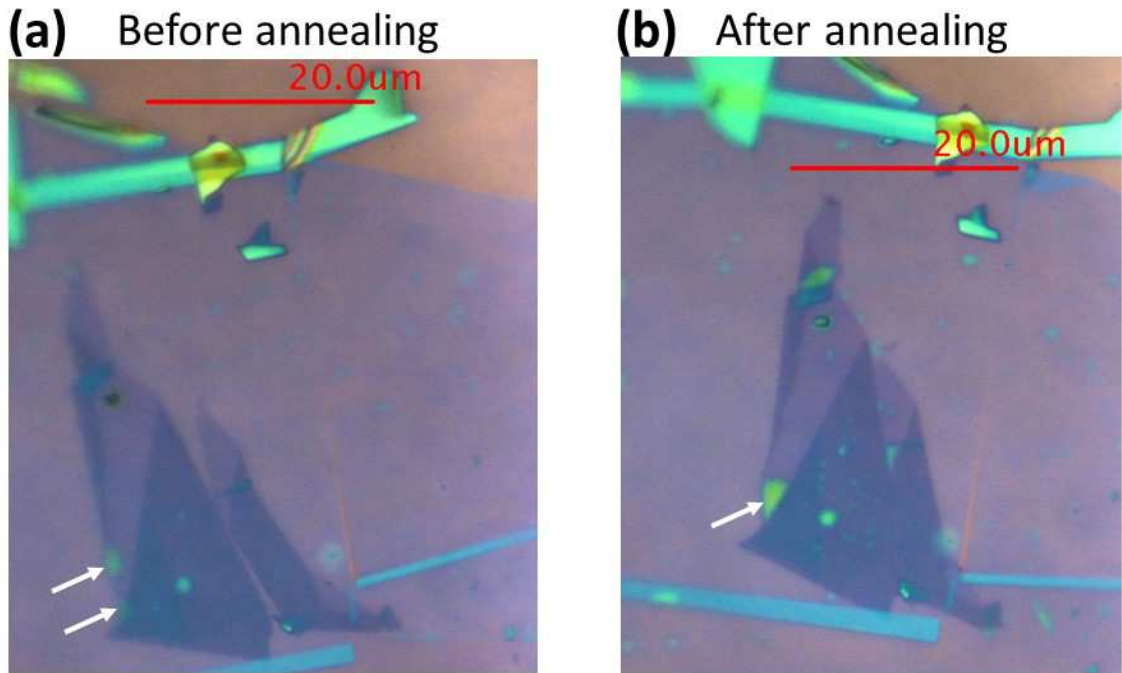


Figure 2.22: (a) and (b) Two optical microscope images of a same hBN/ MoS_2 /hBN sample before and after annealing on a hot plate. The red scales correspond to 20 μm . The white arrows designate blisters before and after coalescence due to annealing.

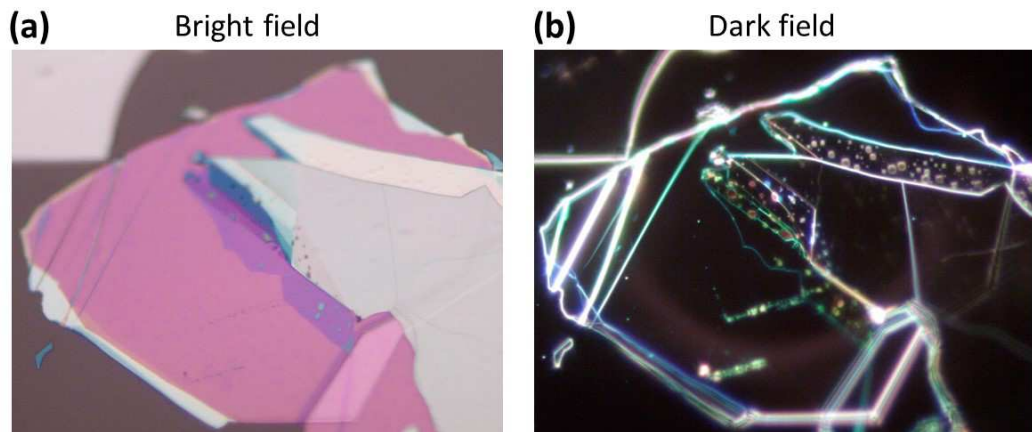


Figure 2.23: Two microscope images of a TMD monolayer deposited on an hBN flake in bright and dark field. (a) In the bright field image, some blisters appear with a blueish color. (b) In dark field, the light is scattered by bubbles. A lot of blisters which were invisible in dark field appear clearly now.

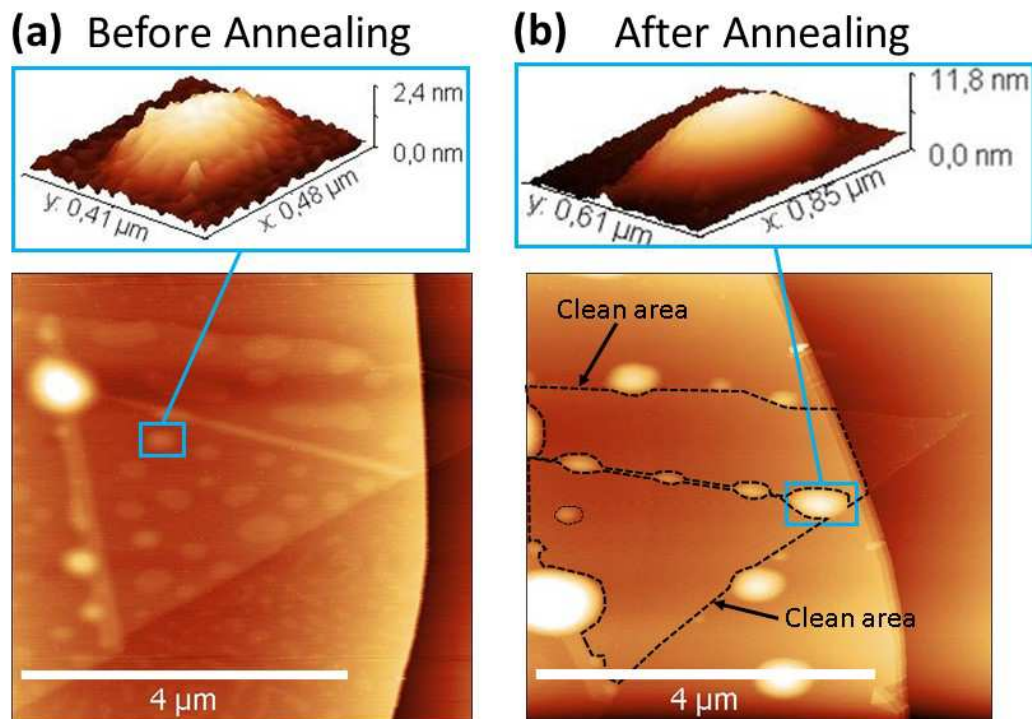


Figure 2.24: Two AFM images of a hBN/ WSe_2 monolayer/hBN van der Waals heterostructure. The bubbles visible here appeared after the deposition of the top hBN. **(a)** A multitude of blisters between top hBN and WSe_2 and between top hBN and bottom hBN are visible. **(b)** After annealing, the blisters aggregate to form larger bubbles and leave behind clean areas surrounded with black dotted lines.

We undoubtedly have areas with blisters where the van der Waals materials are not in contact due to trapped contaminants. However, a simple annealing can greatly improve the situation by aggregating contaminants in larger pockets, leaving apparently clean larger surfaces. Now the following question could be asked: are these "clean" surfaces really clean? Are the interfaces between the different layers of the van der Waals heterostructure really atomically sharp, without any contaminants?

One way to bring an experimental answer to this question is to take cross-sectional images with a Transmission Electron Microscope (TEM) of van der Waals heterostructures. These measurements have indeed confirmed that pocket of trapped contaminants aggregate and leave atomically sharp interfaces [128]. This effect is called the self-cleansing mechanism. It is induced by the affinity between two van der Waals materials which can be higher than the affinity with contaminants. In [129], 2D materials (MoS_2 , WS_2 , WSe_2 , $MoSe_2$ and $NbSe_2$) encapsulated between hBN layers have been investigated with cross-sectional TEM. The samples have been fabricated using a technique similar to the one illustrated in Fig 2.5 either in air or in an inert atmosphere in a glovebox. For encapsulated MoS_2 and WS_2 prepared in air, the interlayer spacing between them and hBN was found to agree well with their DFT calculations. For WSe_2 however, samples prepared in air revealed larger values than expected for interlayer spacing, which could be an experimental evidence of trapped contaminants between WSe_2 and hBN. In contrast, an encapsulated WSe_2 was also prepared in an inert argon environment and the right WSe_2 /hBN spacing was measured.

We carried our own cross-sectional TEM experiments in collaboration with the CEMES laboratory in Toulouse, I give here a very brief summary of this ongoing experiments. We fabricated a hBN/ MoS_2 monolayer/hBN van der Waals heterostructure with the PDMS transfer technique in a glovebox, in a nitrogen atmosphere. After each layer deposition thermal annealing was performed. Once the van der Waals structure was complete, we brought it to CEMES and prepared the sample for TEM observation. The sample preparation procedure, shown in Fig 2.25, is summarized below:

- The area where we want to take a cross-section is covered with platinum to protect the sample.
- A focused ion beam (FIB) is used to cut a "slice" of the sample around the zone where platinum was deposited.
- The slice is removed from the sample and brought into contact with a special TEM grid to which it is attached by depositing Pt.
- The slice is thinned down some tens of nm with FIB.

Once the sample is ready, TEM experiments through the cross-section can be performed. Fig 2.26 shows a TEM image of our hBN/ MoS_2 monolayer/hBN van der Waals heterostructure. The interfaces between hBN and MoS_2 are atomically sharp with no clear trace of interlayer contaminants. Measurement of the interlayer spacing between hBN and Mo planes gives the expected value of ~ 6.5 Å. This is experimental evidence

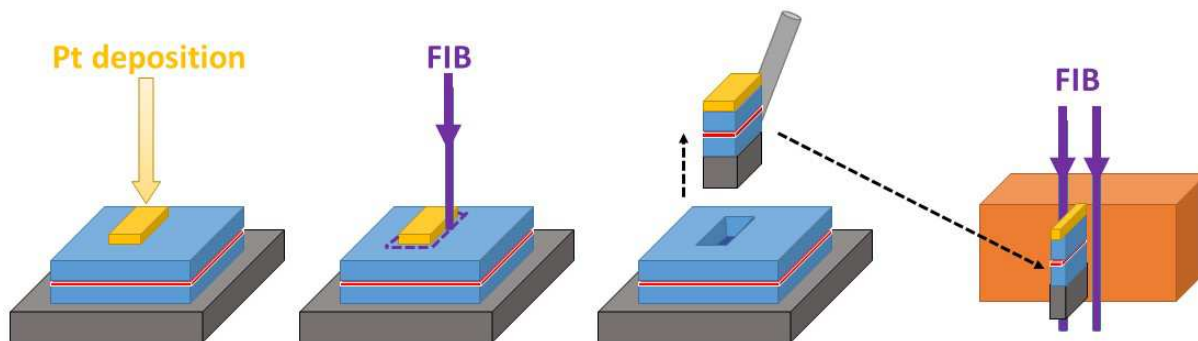


Figure 2.25: Schematics illustrating the sample preparation for our cross-sectional measurement. Blue volumes are hBN layers, red correspond to MoS_2 monolayer, dark grey to a conductive substrate, light grey to a micro-manipulator and brown volume represents a TEM grid for cross-sectional imaging. In our case we deposited platinum to protect locally the sample, with FIB we cut a slice of the sample. The area protected with platinum is not damaged by FIB. The slice is taken out from the sample to attach it on a TEM grid by soldering. With FIB we thin down the slice to some tens of nm. [CEMES and LPCNO, Toulouse, unpublished]

of the quality of interfaces we can obtain by using the simple PDMS deterministic transfer method. Note that the zone scanned is blister-free. Of course, we could argue that the image is very localized, about $38 \times 38 \text{ nm}^2$, but while scanning the sample it seemed that most of the zones presented these atomically sharp interfaces. Nevertheless, some bubbles were visible in other areas of the sample in optical microscope images. Further experiments are ongoing to compare different fabrication techniques such as our PDMS transfer with the PC pick-up method. Another challenge is to analyse more precisely the composition of contaminants pockets, which have so far been identified as hydrocarbons [128].

Our results confirm that a self-cleansing mechanism enables obtaining van der Waals heterostructures with atomically sharp interfaces. The contaminants aggregate, generating clean areas within the van der Waals stack.

Still, the problem is that these blisters can reduce the clean area available. As it has been highlighted in Fig 2.22 and 5.16, raising temperature has an important effect on bubbles which become mobile and can aggregate into larger bubbles. In the example shown the annealing was performed after stacking. However other experiments have underlined that temperature must be controlled during the fabrication procedure. In [86], Purdie et al. used a PC pick-up method, underlining the importance of temperature when the final heterostructure is transferred on a substrate. When the heterostructure is brought into contact with the substrate (see Fig 2.9 (g)) blisters can be pushed away from the interfaces if the temperature is around $180 \text{ }^\circ\text{C}$. They clearly show that if this temperature is lowered to $110 \text{ }^\circ\text{C}$ for this fabrication step, the amount of blisters present in the final sample is higher.

As illustrated in Fig 2.27, another method which can be implemented to solve the problem of bubbles is a post-processing surface treatment using AFM in contact mode [130, 131]. After the fabrication of the sample, AFM tip is used to push the bubbles out

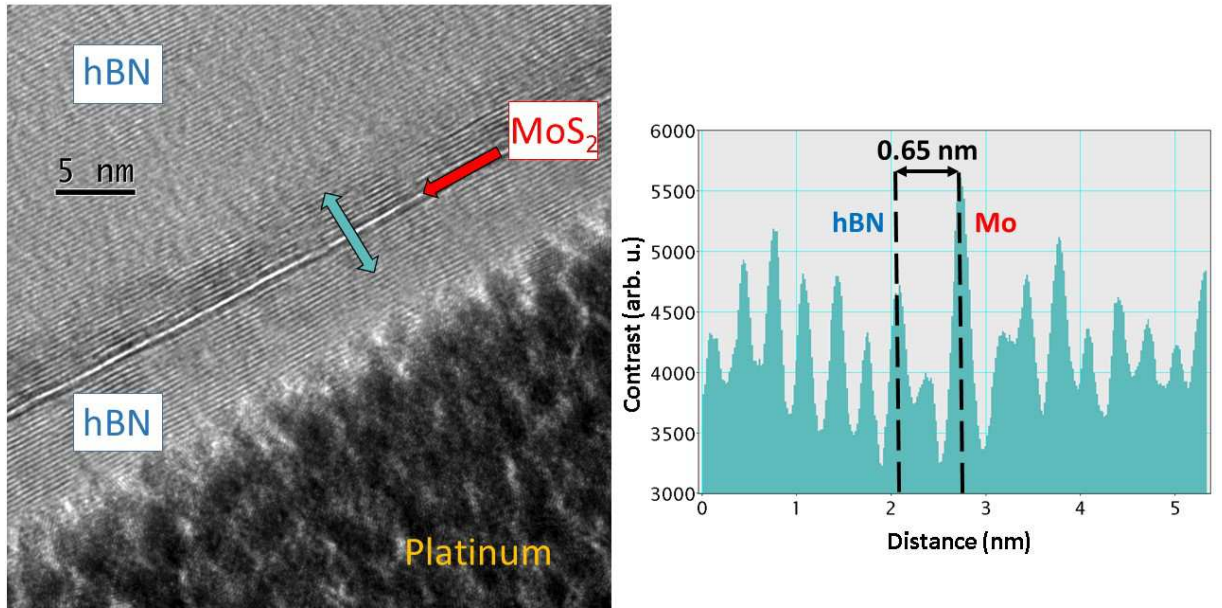


Figure 2.26: TEM cross-sectional image of a hBN/ MoS_2 monolayer/hBN van der Waals heterostructure. hBN and MoS_2 layers are visible. By taking a profile we find the expected interlayer spacing between Mo and hBN planes of ~ 6.5 Å. Also we can check that ~ 3 Å separate two hBN planes. [CEMES and LPCNO, Toulouse, unpublished]

of, or towards the edges of the van der Waals heterostructure.

This technique, also called AFM ironing, enables the displacement of interlayer contaminants at the buried interfaces by applying forces generally in the range of tens to hundreds of nN. Experiments have demonstrated that corrugations initially present are ironed away. However, we note that such a method is not adapted to larger bubbles as it is very difficult to move micrometer size blisters, even by applying thousands of nN. In this situation the risk is to damage the structure by perforating the top layer above the bubble and ripping the surface apart.

To summarize, blistering is still a real issue in the field of 2D materials which can prevent obtaining clean van der Waals heterostructures and can be particularly detrimental

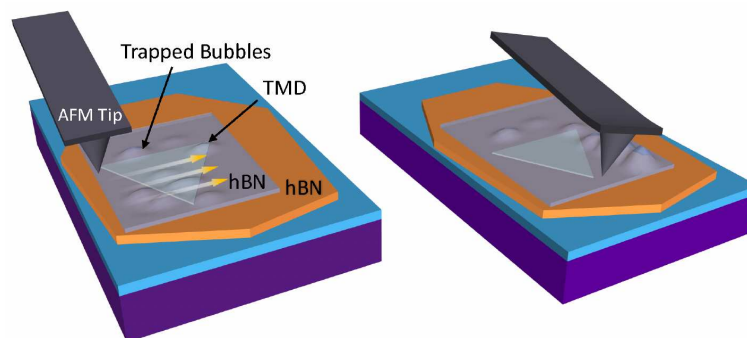


Figure 2.27: Illustration of AFM ironing. The trapped bubbles are pushed away by the AFM tip. Figure extracted from [130].

when proximity between layers is important, for example to observe interlayer excitons in type II heterostructures [132]. We can distinguish between two main kind of methods to tackle the problem of blisters in van der Waals heterostructures: the ones which are implemented during the fabrication process and the post-processing ones.

During the fabrication process it is possible to reduce blistering by playing with different parameters such as the temperature during layers stacking and the speed at which they are brought into contact. The reduction of polymer residues is also a key factor to decrease the amount of contaminant susceptible to aggregate into bubbles. Moreover, a controlled environment is preferable. That is why we decided to build an exfoliation setup in a glovebox in a nitrogen atmosphere with well controlled moisture and O_2 levels kept under 0.1 parts per million (ppm). For a better control of the lamination process manual micro-manipulators have been replaced by motorized actuators from Newport[®] TRB25CC and LTA-HL, which have minimum incremental motions of 0.1 and 0.05 μm respectively. With this new equipment we hope that the next generations of samples will present less defects. We also note that working in an inert environment is necessary for some materials such as black phosphorous or ferromagnetic materials like $CrBr_3$.

We have also seen that post-processing techniques can be performed such as annealing or AFM ironing to obtain larger areas exploitable for our physical studies.

2.3 Introduction to optical spectroscopy techniques

This section is dedicated to the presentation of the main optical setups I had the opportunity to use during my thesis. After introducing the setup, I explain the working principles of the main optical characterization techniques I used to study the van der Waals heterostructures I fabricated.

2.3.1 Optical spectroscopy setup

In a simple view, our optical setup can be divided into the following main parts: a light source, the sample to characterize, a spectrometer and a detector. This simple view is illustrated in Fig 2.28.

We note that the sample is in a cryostat, under vacuum. I used during my thesis so called low vibration closed-cycle He cryostats: the attoDRY 700 from Attocube[®] and the Optidry from My Cryo Firm[®]. These cryostats do not require liquid helium filling and present several advantages such as low mechanical vibrations and good temperature stability. With such equipment, we typically reach temperatures as low as 4K, but this temperature can be slightly higher (~ 10 K) depending on the quality of the thermal contact with the sample via a cold finger (no exchange gas is present).

Inside the cryostat, the sample is glued with silver paint on a stage which is attached to piezo-nanopositioners from Attocube[®]. The silver paste ensures good thermal contact with the sample. The nanopositioners are designed to work at low temperature and are made from non-magnetic materials to operate in magnetic fields if necessary. They can move in three directions (xyz) with a precision down to 10 nm and a travel range of 5 mm.

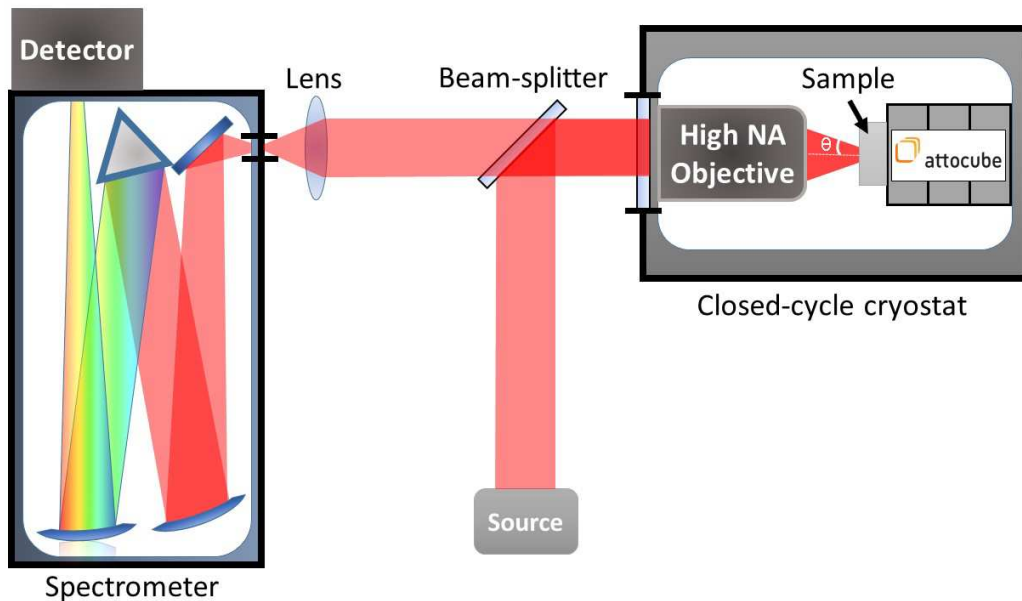


Figure 2.28: This simple schematics illustrates the main elements of our setup designed for optical spectroscopy experiments at low temperature. The light from the source (laser or white light) is reflected by a beam-splitter and goes through the cryostat window to be focused on the sample by an objective with a high numerical aperture. The signal is then collected by the same objective and goes through the beam-splitter to finally reach a spectrometer which disperse the light which is then recovered by a detector.

Another important element found in the cryostat is the objective. In our configuration, it focuses the light on the sample from a collimated beam and also collects the signal from it. To reach a high spatial resolution, a high numerical aperture is required. With the Rayleigh criterion we can roughly calculate the beam spot diameter D in the focal plane of our objective:

$$D = 1.22 \times \frac{\lambda}{N.A.} \quad (2.3)$$

where λ is the wavelength of light and N.A. is the numerical aperture of the objective given by: $N.A. = n \sin(\theta)$ where n is the refractive index of the medium between the objective and the sample (in our case this is vacuum so $n=1$) and θ is the maximum half-angle of the cone of light exiting the objective, as shown in Fig 2.28.

For the work presented in this thesis, we mainly used an achromatic objective from Partec[®] with a numerical aperture $NA=0.82$. By using equation 2.3 and $\lambda=632.8$ nm (HeNe laser wavelength) we evaluate the beam spot diameter $D=9.4 \times 10^{-7}$ m, roughly 1 μm . Combined with the precise positioning system, this micro-photoluminescence ($\mu\text{-PL}$) setup was initially implemented for the study of single nano-objects, especially quantum dots which require a high spatial resolution.

We note that in confocal geometry the excitation light path is the same as the detected light path, collected by the same objective. This apparatus is very similar to the one of a confocal microscope, whose principle illustrated in Fig 2.29 was patented in 1957 by Marvin Minsky [133]. The simple idea is to reject the beam of light coming out of the focal plane by using a pinhole. In our setup, the path of the detected light from the

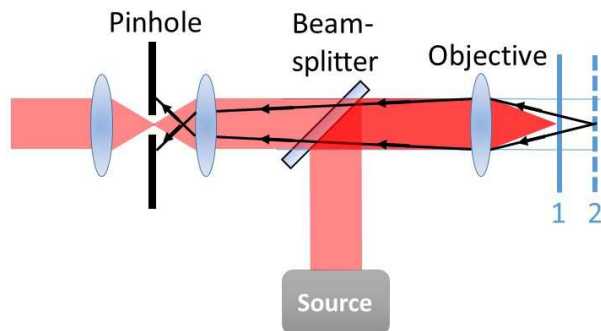


Figure 2.29: Schematic illustrating the principle of a confocal microscope. Path of the light coming from the focal plane is shaded in red whereas the path from the out-of-focus light is represented with black lines and arrows. The pinhole blocks these black beams of light.

objective to the spectrometer is long enough so that the beams which are not coming from the focal plane diverge and are lost, thus we do not need to use a pinhole to stop them. When using a shorter detection path, the spectrometer slit plays the role of the pinhole.

Even if we do not need a spatial resolution as high as the one required for the study of quantum dots, this high resolution is also very beneficial for the optical characterization of TMD monolayers. Indeed, TMD monolayers are generally subject to spatial inhomogeneities, for example because of the problem of blisters presented previously. It is therefore important to be able to scan the TMD monolayer to find the areas which have the best optical quality. Having a high spatial resolution is also required if we want to perform mapping (for example PL mappings) of the TMD monolayer, some of which are only a few μm in diameter.

Now, to analyse the light coming from the sample, it is focused on an entrance slit to go through a spectrometer coupled to a detector. In my case, I mostly used a 500 mm focal length Acton SP2500i spectrometer from Princeton Instruments[®]. The characteristics of the spectrometer for different gratings are given in table 2.1.

Grating (lines/mm)	Wavelength coverage (nm)	Dispersion in nm/mm	Pixel resolution (at 700 nm) in μeV
300	174	6.5	290
600	85	3.2	72
1200	41	1.52	38

Table 2.1: Wavelength coverage, dispersion and resolution for the SP2500i spectrometer with different gratings.

The spectrometer is coupled to a Charged-Coupled Device (CCD) cooled with liquid nitrogen to increase the signal-to-noise ratio. The photoactive region of the CCD is an array of photodiodes which are p-doped metal-oxide semiconductors (MOS) capacitors. When photons impinge on the array, electrons are excited and accumulate at the semiconductor-oxide interface of the capacitors. The electric charge accumulated is proportional to the light intensity impinging on the capacitor. These accumulated charges are then transferred to a read-out zone which converts these charges into a digital signal.

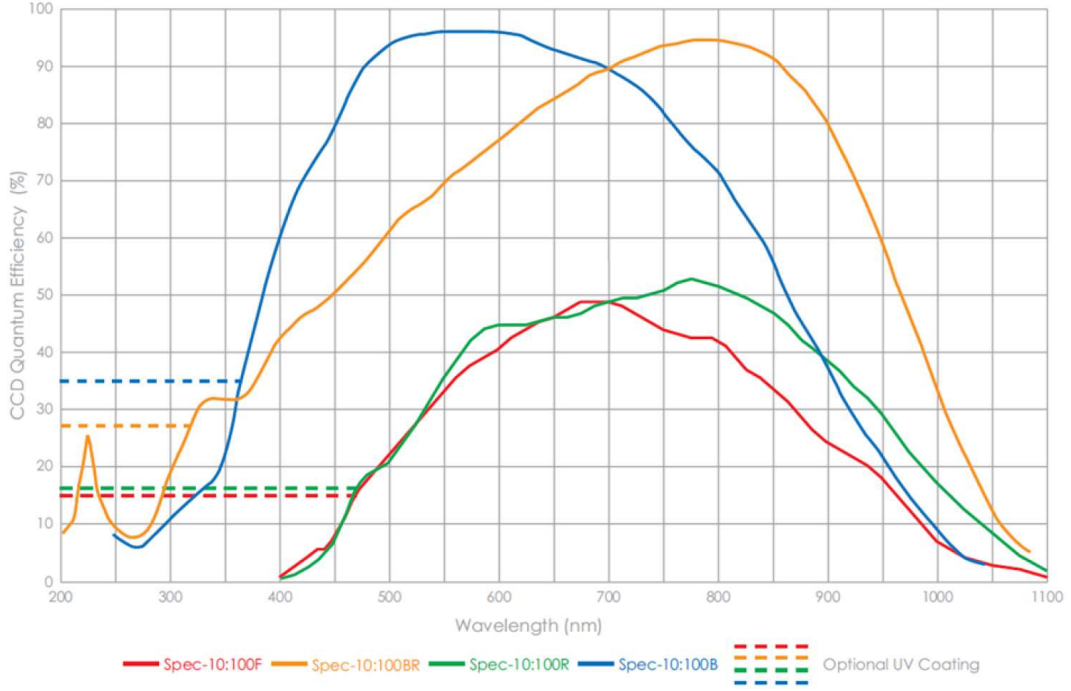


Figure 2.30: Quantum efficiency of different detectors. The yellow curve corresponds to our CCD camera.

The array of our CCD is made of 1340×100 pixels which measure $20 \mu\text{m} \times 20 \mu\text{m}$ each. To improve its quantum efficiency (up to 95% at 800 nm) the CCD has been designed in a back-illuminated geometry. As show in Fig 2.30, our camera is sensitive to radiation in the visible range and in the near infrared (NIR). It is therefore adapted to the main members of the TMD family. As an example the wavelengths of the main excitonic transitions at low temperature (4 K) of encapsulated TMD monolayer samples are: 603 nm for WS_2 , 642 nm for MoS_2 , 719 nm for WSe_2 and 756 nm for $MoSe_2$. I also worked on $MoTe_2$ monolayers during my thesis (see chapter conclusions), in this case I used another detector, with higher sensitivity in the infrared range, the PyLon IR InGaAs camera, however, if not stated explicitly, the results presented in this manuscript were acquired with the silicon CCD.

Another experimental challenge in the study of TMD monolayers is to find the flake positioned on the substrate (typically $5 \text{mm} \times 5 \text{mm}$). That is why our spectroscopic setup has also an imaging part, as shown in Fig 2.31, which enables us obtaining images of our sample in real time inside the cryostat. To this end, an imaging source emits light which is collimated and sent on a first beam splitter (BS2 on the schematic) which reflects the imaging light to another beam splitter (BS3 on the schematic) which is mounted on a flip mount adapter. This convenient flip mount adapter enables removing BS3 when we want to perform spectroscopic measurements (see panel (a)). Then, the imaging light is reflected by BS3 towards the sample in the cryostat, itself reflecting the light which comes back to BS3 and then goes through BS2 towards an imaging camera similar to a webcam. Note that the imaging light is in reality not perfectly collimated in order to have a image of the sample larger than only the beam spot diameter focused by the objective.

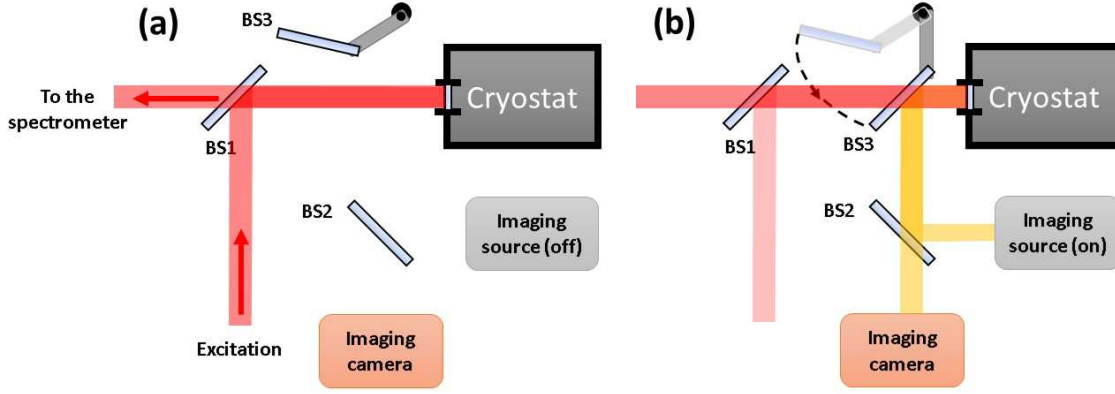


Figure 2.31: **(a)** When we acquire experimental data, the setup is in this configuration. The beam splitter BS3, mounted on a flip mount adapter is removed. **(b)** When we want to look at the sample, we switch on the imaging source reflected by BS2 and BS3 is flipped to direct the imaging light towards the sample in the cryostat. Then this light is reflected by the sample surface, reflected by BS3 and comes through BS2 to finally reach the imaging camera giving an image in live of the sample surface. These versatile systems are designed by my colleague Delphine Lagarde at the LPCNO.

Now that we have presented some of the crucial elements of the spectroscopic setups, emphasis will be put on the main techniques used to characterize optical properties of TMD monolayer samples. At the same time, different excitation sources (not described so far) will be presented and other optical equipment such as polarization elements used to conduct our polarization dependent experiments.

2.3.2 Reflectivity experiments

Among the standard interaction processes of light with matter we find absorption, transmission and reflection. That is why we begin here by presenting one of the most basic types of measurements we performed during my thesis: reflectivity. Reflectivity probes the linear optical properties of semiconductors. In a first approach the classical Lorentz model gives good results in agreement with experimental results. The optical properties of a material can be seen as the interaction between light (electromagnetic radiation), and various types of oscillators. In a semiconductor, many different type of oscillators can be found, like phonons, or excitons for example. The interaction between light and these different oscillators is taken into account in the complex dielectric function $\epsilon(\omega) = \epsilon_1(\omega) + i\epsilon_2(\omega)$ which can be modelled as a superposition of Lorentzian oscillators [19]:

$$\epsilon(\omega) = 1 + \sum_j \frac{f_j}{\omega_{0j}^2 - \omega^2 - i\omega\gamma_j} \quad (2.4)$$

where ω_{0j} is the resonant frequency of the oscillator, ω is the angular frequency of the incident field, γ_j is the damping of the j^{th} oscillator and f_j is the oscillator strength, a quantity without dimensions giving the coupling strength between the incident electromagnetic field and the j^{th} oscillator. Note that the oscillator strength is not determined classically, however in quantum mechanics, this quantity is proportional to the dipole ma-

trix element $|H_{ij}^D|^2 = |\langle j|H^D|i\rangle|^2$ with i and j the initial and final states of the optical transition. In [19] for a given oscillator, the oscillator strength f is defined as:

$$f = \frac{2N\omega_0}{\epsilon_0\hbar}|H_{ij}^D|^2 \quad (2.5)$$

The complex dielectric function is related to the complex refractive index $\tilde{n}^2 = \epsilon(\omega)$. Then the real and imaginary parts of \tilde{n} which correspond to the refractive index n and the extinction coefficient κ are given by:

$$\begin{aligned} n &= \frac{1}{\sqrt{2}}(\epsilon_1 + (\epsilon_1^2 + \epsilon_2^2)^{\frac{1}{2}})^{\frac{1}{2}} \\ \kappa &= \frac{1}{\sqrt{2}}(-\epsilon_1 + (\epsilon_1^2 + \epsilon_2^2)^{\frac{1}{2}})^{\frac{1}{2}} \end{aligned} \quad (2.6)$$

The reflectivity depends on these two parameters. For a normal incident field, R is given by:

$$R = \frac{I_r}{I_i} = \frac{(n(\omega) - 1)^2 + \kappa^2(\omega)}{(n(\omega) + 1)^2 + \kappa^2(\omega)} \quad (2.7)$$

where I_i and I_r are the intensities of the incident and reflected light respectively.

Finally the Kramers-Kronig relations relate n and κ and it is possible to deduce ϵ_1 and ϵ_2 from reflectivity data as it has already been done for TMD monolayers [134].

In our case, reflectivity was more adapted to our samples compared to transmission measurements. Indeed, we generally used opaque silicon as a substrate onto which the TMD monolayers or van der Waals heterostructures were deposited. In addition, the architecture of our spectroscopic setup, illustrated in Fig 2.28, was adapted to confocal reflectivity measurements, not to transmission. For this type of measurements we used a commercial halogen lamp as a broadband white light source with a stabilized power supply. In order to consider only the signal related to the TMD monolayers, we performed so called differential reflectivity measurements, as schematically represented in Fig 2.32 for a hBN/MoS_2 monolayer/ hBN van der Waals heterostructure. Even if some transitions already appear in raw data, calculating differential reflectivity strongly enhances their visibility, showing sharp peaks. The differential reflectivity is calculated as:

$$\frac{DR}{R} = \frac{R_{vdwTMD} - R_{vdw-TMD}}{R_{vdw-TMD} - background} \quad (2.8)$$

where R_{vdwTMD} is the reflectivity spectrum of the full van der Waals heterostructure comprising the TMD (hBN/MoS_2 monolayer/ hBN in the example of the figure). However, $R_{vdw-TMD}$ is the reflectivity spectrum of the van der Waals heterostructure without the TMD monolayer. In addition, we also measure a "background" signal. That is we block the excitation light (white light for reflectivity) and acquire a spectrum with same acquisition time as R_{vdwTMD} and $R_{vdw-TMD}$. We thus obtain a spectrum of noise which can have different origins: unexpected light noise in the dark experimental room but also some thermal noise affecting the CCD camera, though the camera is cooled with liquid nitrogen. Moreover the baseline is never exactly at zero intensity so acquiring a background

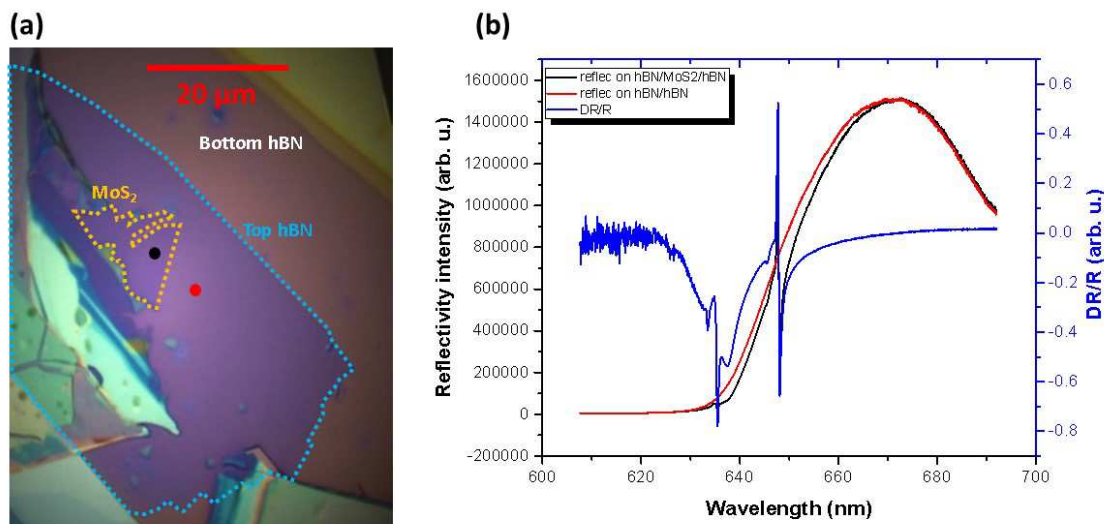


Figure 2.32: **(a)** Optical microscope image of a $hBN/MoS_2/hBN$ van der Waals heterostructure. The black and red spots correspond to two different locations where we took reflectivity spectra. **(b)** The reflectivity spectra in black and red associated to the black and red spots in (a) are plotted as a function of wavelength. By applying the differential reflectivity formula: $(R_{black}-R_{red})/(R_{red}-background)$ we obtain the blue curve. The blue curve contains several spectrally narrow exciton transitions in MoS_2 monolayer, discussed in detail in chapter 3. The background corresponds to the noise which could come unexpectedly from other light sources present in the dark room where we perform experiments or could be due to thermal noise influencing the detector response.

enables solving this problem. We note that acquiring a background is not critical in the case of reflectivity experiments, but it can be especially important for PL measurements. Furthermore to reduce spectral noise in reflectivity, we accumulate a certain number of spectra.

With this technique, excitonic transitions such as the A:1s and B:1s appear which reveal the spin-orbit splitting between these two excitons. In addition, it is also possible to distinguish the Rydberg series of A exciton: 1s, 2s, 3s ... making it possible to deduce the binding energy of the exciton and the energy position of the free particle bandgap [27]. Reflectivity experiments give information about transitions which have a sufficient oscillator strength, but other transitions coming from defect-assisted recombination, bound-excitons, charged excitons, biexcitons etc... are more difficult to observe with this method. That is why we present in the next section another class of experiments, photoluminescence (PL), which brings supplementary information.

2.3.3 Photoluminescence (PL)

In addition to light absorption, a material can emit light by different processes. Among the main physical processes associated to light emission by a semiconductor we can cite electroluminescence (EL) which is used for the operation of LEDs, cathodoluminescence (CL) which consists in the excitation of the material with an electron beam followed by the emission of light by the given material, and photoluminescence (PL) when the material is excited with light. PL is a sensitive, non-destructive technique valuable for the study

of optoelectronic properties of semiconductors. While reflectivity is sensitive to states with a high oscillator strength and a high density of states (DOS), PL emission depends on fast-relaxation processes and is sensitive to transitions with the lowest energies and shortest radiative lifetime. PL probes therefore rather occupation of states rather than their oscillator strength.

Firstly, the material is excited by a photon which creates an electron-hole pair. To excite the material, different light sources can be used. I performed a lot of experiments with a HeNe laser excitation at 632.8 nm. This wavelength was adapted to most of the encapsulated TMD monolayers (see chapter 3) but not to encapsulated WS_2 monolayer which has its main excitonic transition around 600 nm. For this material, a green laser at 532.8 nm could be used. I also used tunable lasers, such as Ti:sapphire, especially when we had to conduct photoluminescence excitation (PLE) experiments, that is PL with a source exciting at different wavelengths. To reach high precision in the wavelength tuning between 700 and 1000 nm, a SOLSTIS from MSQUARED[®] was used. Basically, the excitation source must be chosen according to the material and its bandgap.

One advantage of PL over reflectivity is that it enables observing optical transitions with small oscillator strengths. It is therefore possible to observe transitions associated to excitons bound to defects or impurities, or charged excitons (trions) as it will be presented in chapter 4. Indeed, the presence of defects generally induces the appearance of energy levels in the forbidden bandgap and PL is sensitive to these lowest energy states. In our samples, the main transitions are usually related to free excitons, but we also observe frequently transitions at lower energy which can be related to defects or other exciton complexes. In fact, PL is a very useful tool to assess the quality of a sample. It can also be used to perform mappings in order to study sample inhomogeneities. For example, we obviously do not expect the same PL signal on a clean van der Waals heterostructure and on a sample full of blisters.

Compared to reflectivity, we need to add some optical elements in our setup to properly perform PL. One problem in PL can be that the light from the laser can perturb our measurements, especially if the laser wavelength is close to the signal we want to study. For instance, the case of MoS_2 is particularly sensitive if we excite the material with the HeNe laser. The MoS_2 main transition is visible around 640 nm and the HeNe laser emits light at 632.8 nm, so the signal and the excitation are very close. It means that we must use a filter (a long-pass) to stop the light from the laser going to the spectrometer and let the MoS_2 signal passing through. We use such a filter and position it somewhere before the spectrometer. We always place such a filter to ensure a clean signal (not only in the case of MoS_2). Actually a filter must also be placed in the excitation path, before the excitation light goes in the cryostat. This is necessary to "clean" the laser (that is spectrally narrow) which can present some small additional features or a tail extending at wavelengths different from its main wavelength. The necessity to use filters is illustrated in Fig 2.33.

A variant of PL is photoluminescence excitation (PLE) which consists in varying the excitation wavelength and keeping fixed the detection wavelength. For instance, in the

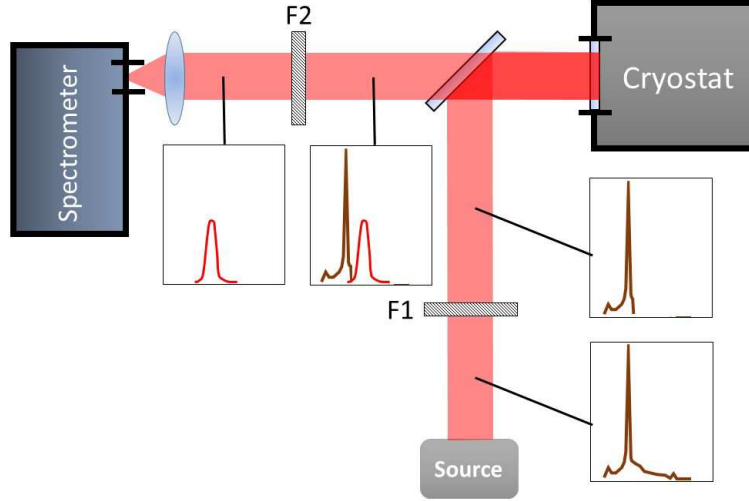


Figure 2.33: Schematics illustrating the purpose of using filters to clean the recorded signal from laser. Two filters F1 and F2 have been respectively placed in the excitation and in the detection path of the setup. F1 is a short-pass which removes the tail and all the lines at higher wavelengths compared to the central line of the laser (632.8 nm for the HeNe for instance). F2 is a long-pass which cut the laser and let the PL signal go through.

Fig 3.20 of chapter 3, a PLE spectrum is shown. In this example, the PL intensity is detected at the neutral A:1s exciton energy and the laser energy is varied in the range where excited states of the exciton are present (2s, 3s etc...) and also the B exciton. When the excited states are excited resonantly by the laser, the A:1s state PL emission shows a strong increase in intensity. The PLE intensity I_{PLE} measured at the energy E_{det} can be written as [135]:

$$I_{PLE}(E_{ex}, E_{det}) = P_{abs}(E_{ex}) \cdot P_{rel}(E_{ex}, E_{det}) \cdot P_{em}(E_{det}) \cdot I_{ex}(E_{ex}) \quad (2.9)$$

where E_{ex} is the excitation energy, $P_{abs}(E_{ex})$ is the absorption probability at the energy E_{ex} , $P_{rel}(E_{ex}, E_{det})$ is the probability that the photogenerated electron-hole pair relaxes from E_{ex} to E_{det} , $P_{em}(E_{det})$ is the emission probability of photons at the energy E_{det} after relaxation, and $I_{ex}(E_{ex})$ is the excitation intensity at the energy E_{ex} . During PLE spectroscopy, only the excitation energy E_{ex} is varied and the excitation intensity I_{ex} is kept fixed. It means that during a PLE experiment, the parameters which will change are $P_{abs}(E_{ex})$ and $P_{rel}(E_{ex}, E_{det})$. Thus to observe an intense PLE intensity we must be exciting a state with strong absorption of incoming photons and then the relaxation from E_{ex} to E_{det} must be efficient too. That is why, coming back to our TMD monolayers, we observe intense PLE when we excite excitonic states such as A:2s or A:3s and detect the signal at A:1s. It is indeed for these two reasons: absorption is efficient at A:2s and A:3s and then the relaxation to A:1s is also efficient via phonon emission.

PL measurements can be enriched by varying different parameters during the measurements such as excitation power, temperature, electric or magnetic field... In the next part we focus on the optical setup which enables us conducting polarization-resolved measurements.

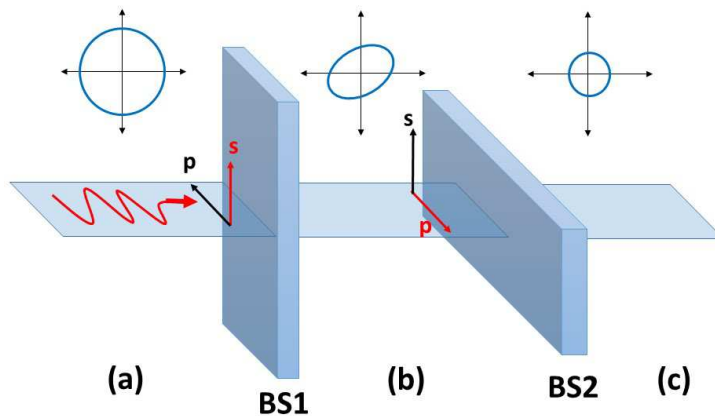


Figure 2.34: (a) Incoming light is circularly polarized and is coming on the first beam splitter BS1. A coordinate system with red and black arrows is associated to BS1. In this case, relatively to the plane of incidence the red arrow corresponds to the s polarization and the black one to the p polarization. (b) After passing through BS1, the polarization of light has changed. It is now elliptical because the coefficients of transmission through BS1 for s and p are not the same. The light goes on a second beam splitter labelled BS2 which is identical to BS1 and just rotated by 90° around the light propagation axis. As BS2 is rotated, the coordinate system associated to it is also rotated and now the red arrow corresponds to p polarization and the black one to s polarization. It is inverted compared to BS1. (c) After passing through BS2, the polarization is circular.

2.3.4 Polarization-resolved experiments

In chapter one, emphasis has been put on the unusual valley properties and optical selection rules in TMD monolayers. It has been shown that inequivalent K valleys exist in 2D TMDs and that these valleys can be selectively excited with σ^+ or σ^- polarized light. In addition, linear excitation of these materials gives rise to valley coherence [56].

It is thus of primary importance to build an appropriate setup to perform polarization-resolved measurements. One first problem to solve comes from the beam splitter we place in front of our cryostat. Indeed the transmission/reflection coefficients are different for s and p polarization. It basically means that if a circular polarization passes through this beam splitter, it will become elliptical. An elegant solution, clearly presented by Louis Bouet in his thesis [136] is to add another beam splitter rotated by 90° around the light propagation axis. This effect of compensation is illustrated in 2.34. In the example of the figure, an incident circularly polarized light goes through a first beam splitter BS1. As the transmission coefficients are not identical for s and p components of the polarization, the light is elliptically polarized after going through BS1. Then a second beam splitter BS2 is placed, identical to BS1 but rotated by 90° around the light propagation axis. Its s and p components are inverted compared to BS1. After going through BS2, the light recovers a circular polarization, though the intensity has been lowered by a factor $T_s \times T_p$.

Once this problem due to the beam splitter is solved. We must use the appropriate waveplates in the spectroscopy setup. The different optical elements used to excite the sample with circularly polarized light are represented in Fig 2.35.

In the excitation path, a Glan Taylor linear polarizer GT1 has its axis aligned with the

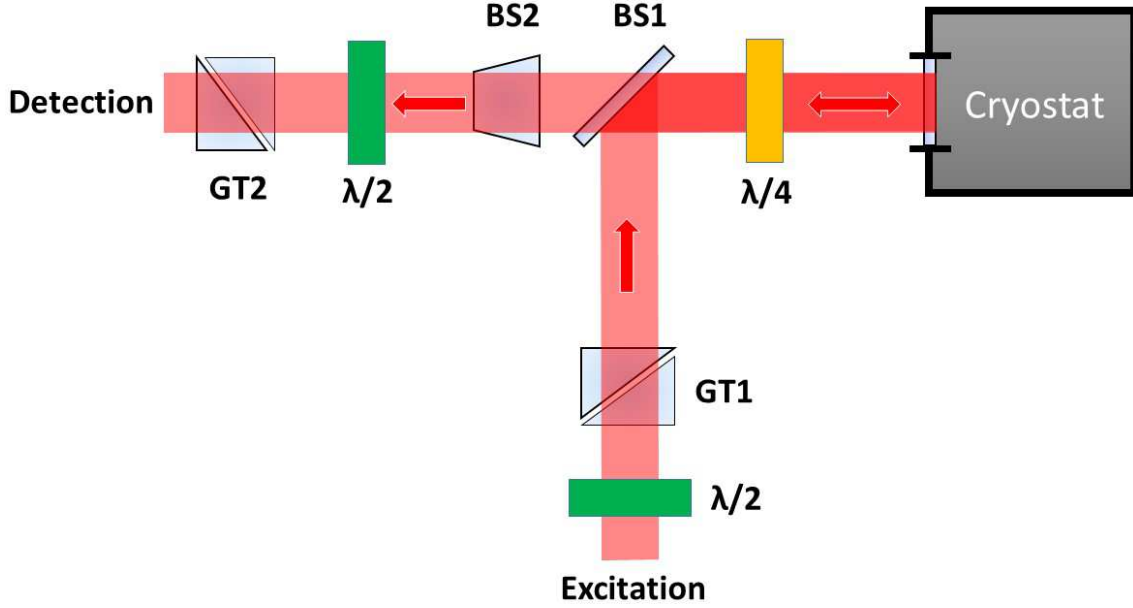


Figure 2.35: Optical setup for polarization resolved measurements. GT1 and GT2 are Glan-Taylor linear polarizers. BS1 and BS2 are beam splitters. $\lambda/2$ and $\lambda/4$ are half-wave and quarter-wave plates respectively.

s polarization of the beam splitter BS1, both to maximize excitation power and to avoid polarization degradation. Before GT1 a half-wave plate $\lambda/2$ on a rotation mount is placed to maximize the light transmitted through GT1. The linear polarized light reflected by BS1 then passes through a quarter-wave plate $\lambda/4$, making an angle of 45° with a neutral axis to transform the linear polarization into a circular one. This circularly polarized light goes into the cryostat to excite the sample.

In the detection path, due to the confocal geometry, the PL signal goes back through the $\lambda/4$ plate. It then goes through the two beam splitters BS1 and BS2 to finally reach a $\lambda/2$ in a rotation mount and a Glan-Taylor polarizer GT2 which are both used to analyse the polarization.

In practice we first analyse the reflection of the laser without the sample to determine which angles of the $\lambda/2$ in detection correspond to the co- and cross-polarized position. For example if the excitation laser is σ^+ polarized, the angle of the $\lambda/2$ for which the intensity on the spectrometer is maximized enables measuring the co-polarized signal, that is the signal which has also a σ^+ polarization. When we rotate the $\lambda/2$ of 45° , we now measure the cross-polarized signal which corresponds actually to a σ^- polarization. This should correspond to the minimum of intensity. We then note the two angles for the co- and cross-polarizations. After this calibration procedure, we can study our sample by detecting both σ^+ and σ^- polarized PL. These intensities enable defining the circular polarization degree:

$$P_{degree} = \frac{I_{co} - I_{cross}}{I_{co} + I_{cross}} \quad (2.10)$$

where I_{co} and I_{cross} are the co- and cross-polarized signal intensities.

The same analysis as before holds in the case of linear polarization. The only difference in the optical setup is that the $\lambda/4$ is removed. It means that the laser which excites the

sample is linearly s-polarized by GT1 and then the $\lambda/2$ in the detection path is rotated to analyse either co- or cross-polarized PL signals, that is the signals which are s-polarized like the laser or which are p-polarized.

We note that the rotation of waveplates we evoked can be manual. However it is also possible to use Liquid Crystal Retarders (LCR) which are tuned by applying a voltage to measure the polarization. Experimentally using LCR can be very useful if we want to automate the procedure and make it more reproducible instead of changing the angles manually, as done in [111].

2.4 Conclusions

In this section, an overview of our fabrication techniques and experimental setups has been presented. Emphasis has been put on fabrication techniques derived from the well-known mechanical exfoliation method. So far, these manual methods have been the most used by the scientific community working on TMD monolayers. However the reader should keep in mind that growing efforts are made to automate the fabrication process and make it more adapted to possible future industrial applications.

In our laboratory, the deterministic transfer technique with PDMS has been used extensively to fabricate the quasi totality of our van der Waals heterostructures. It remains a technique with many attractive aspects: cheap, applicable to many materials and quick compared to other methods... Nevertheless we discussed some potential drawbacks of the technique such as the problem of PDMS contaminants on the layers or the presence of blisters between the layers of a van der Waals heterostructure. We are still working on improving the technique, believing that at this stage it remains a competitive approach.

Finally, we presented the main optical setups which have been used to obtain the experimental results presented in this thesis work, focusing on reflectivity and PL. However, this quick presentation does not pretend to cover the entirety of this vast subject but gives to the reader the key elements necessary for a good comprehension of this work. Further details can be found here [19, 135].

Chapter 3

Optical spectroscopy of TMD monolayers encapsulated in hexagonal boron nitride

It has been shown in the previous chapter that it is possible to stack layers from different layered materials in order to obtain a van der Waals heterostructure. This chapter focuses on hBN/TMD monolayer/hBN van der Waals heterostructures which revealed an improved optical quality as compared to TMD monolayers directly transferred on SiO_2 , as the effects of disorder are largely suppressed [137].

After explaining the main motivations which led the scientific community to study this kind of samples, optical spectroscopy results from measurements such as photoluminescence and reflectivity will be presented. It will be emphasized that hBN encapsulation has enabled reducing greatly the inhomogeneous broadening by placing TMD monolayers in this new dielectric environment. We will detail that the SiO_2 /hBN/TMD monolayer/hBN structures with atomically sharp interfaces show thin layer interference effects and these variations in electric field amplitude impact samples with different hBN spacer thickness. This allows to tune the optical response as light absorption and the visibility of excitonic transitions in the spectra is varied.

3.1 Motivations for hBN encapsulation

3.1.1 Inhomogeneous broadening of TMD monolayers on SiO_2

Since 2010 [1, 2], TMD monolayers have been widely studied, however, for several years most of the experimental work focused on TMD monolayers directly deposited on SiO_2 substrates. This choice was in part motivated by compatibility for microelectronics following the demonstration of a transistor device based on a MoS_2 monolayer [11]. Though these samples gave a first good insight of the main properties of these materials, detailed analysis of optical spectroscopy experiments was hindered by broad linewidths due to inhomogeneous broadening [138, 49, 50, 139, 48, 51, 140, 141, 56, 28].

The most prominent effect was visible for MoS_2 , with excitonic linewidths which could

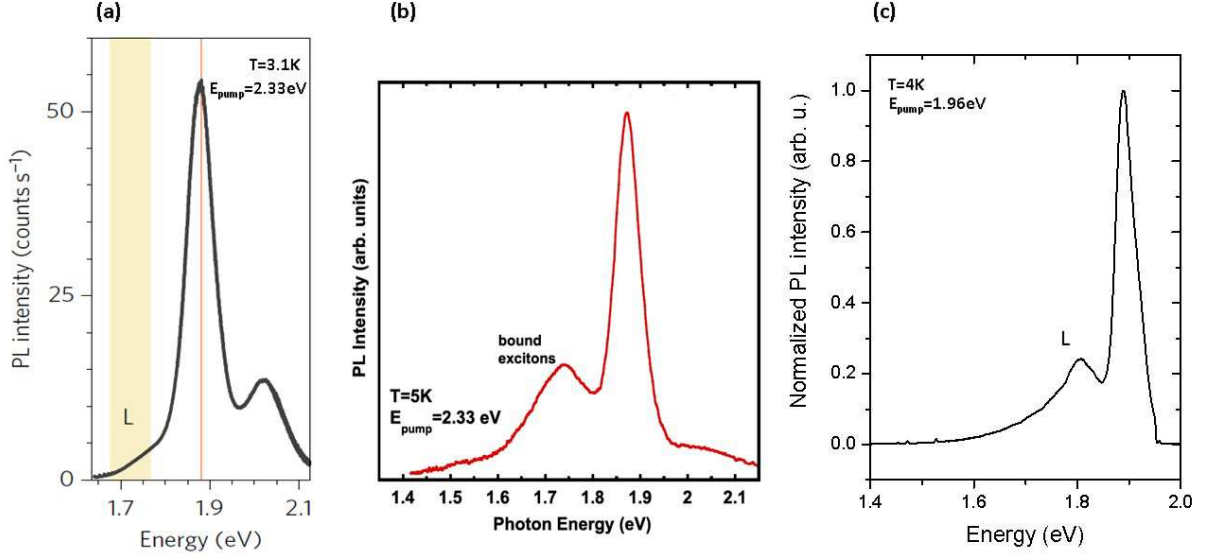


Figure 3.1: Photoluminescence spectra of MoS_2 from different groups at cryogenic temperatures. (a) PL signal from MoS_2 monolayer grown by chemical vapour deposition on SiO_2 . Figure extracted from [50] (b) PL signal from MoS_2 monolayer on SiO_2 prepared by mechanical exfoliation from a bulk crystal. Figure extracted from [139]. (c) Our own experimental data from a MoS_2 monolayer deposited on SiO_2 by using mechanical exfoliation from a bulk crystal.

reach ≈ 50 meV even at cryogenic temperatures. Fig 5.17 shows MoS_2 monolayer photoluminescence spectra at cryogenic temperatures from different groups. Fig 5.17 (a), extracted from [50], shows a PL spectrum from a CVD grown MoS_2 on a SiO_2 substrate, whereas Fig 5.17 (b) (extracted from [139]) and Fig 5.17 (c) show PL spectra from MoS_2 monolayers prepared using mechanical exfoliation techniques such as the ones presented in chapter 2. Even though sample preparations were quite different, the three spectra are very similar. Three main features appear: a dominant transition around 1.880 eV which was at this time mistakenly ascribed to A-exciton, a broad peak at lower energy between 1.75 and 1.8 eV labelled "L" associated to bound excitons [138], and another broad peak at higher energy around 2 eV which was ascribed to B-exciton transition (not visible in Fig 5.17 (c) due to filter used to cut laser excitation).

Transition linewidth is affected by two main contributions called homogeneous and inhomogeneous broadening. As explained in [142, 44] homogeneous broadening γ is given by:

$$\gamma = \Gamma/2 + \gamma^* \quad (3.1)$$

where Γ is the population relaxation rate due to radiative and nonradiative recombinations and γ^* is linked to pure dephasing mechanisms such as exciton-exciton or exciton-phonon scattering.

In addition, due to local potential fluctuations and disorders, the exciton transition energy can vary. The combination of all the different shifted transition energies will give rise to an inhomogeneous distribution of exciton energies as illustrated in Fig 3.2.

Therefore, observing so broad transitions in PL suggested that inhomogeneous broad-

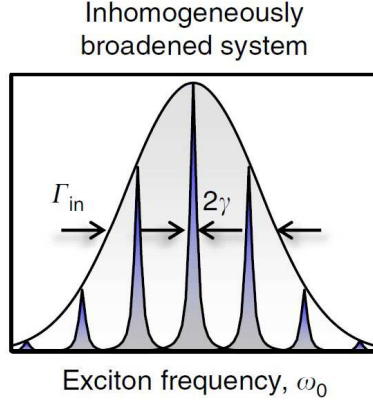


Figure 3.2: Illustration of inhomogeneous broadening effect.

ening plays an important role in these samples. This was confirmed by four-wave mixing (FWM) experiments and Multidimensional coherent spectroscopy (MDCS) which discriminate between the homogeneous and inhomogeneous contribution to the linewidth [142, 44, 143, 144, 145]. Even if homogeneous broadening depends on excitation density and temperature due to exciton-exciton and exciton-phonon interactions [142], the homogeneous linewidth should be only a few meV, which is much smaller than the tens of meV observed for TMD monolayers deposited on SiO_2 . This large discrepancy is an argument in favour of optical transition linewidth being dominated by inhomogeneous broadening.

In addition to infer values for homogeneous broadening and compare with the global linewidth, the inhomogeneous broadening contribution can be deduced from time-resolved FWM experiments where a photon echo behaviour can be observed. Fig 3.3 (b) shows a time-resolved FWM amplitude spectrum as a function of delay τ_{12} between the 2 pump pulses E_1 and E_2 for a $MoSe_2$ monolayer on SiO_2 from [142]. The photon echo behaviour appears along the diagonal on this color plot. The narrower the echo in time, the larger the inhomogeneous broadening and conversely the broader the echo in time, the smaller the inhomogeneous broadening. Fig 3.3 (c) shows similar spectra in the frequency domain, after 2D Fourier Transform Spectroscopy, for a WSe_2 monolayer on sapphire. The inhomogeneous broadening assessed along the diagonal is larger as compared to homogeneous broadening γ in the cross-diagonal direction. This large inhomogeneous broadening is a signature of local spatial inhomogeneity, which is typically due to the substrate supporting the TMD monolayer, and charge puddles and strain variations impact the optical transitions in the monolayer.

3.1.2 Unstable emission characteristics of TMD monolayers on SiO_2

When SiO_2 is used as a substrate, it has been shown that TMD monolayers are subject to changeable optical properties depending on sample history and experimental conditions particularly for MoS_2 monolayer. Indeed, for a given sample, energy position of the A-exciton in PL can vary after several cooldown cycles in a cryostat [139]. It was attributed to changes in dielectric environment at different temperatures, for instance due to water molecules or other species adsorbed at the surface [138].

Furthermore, power-dependent experiments have also clearly highlighted the problem

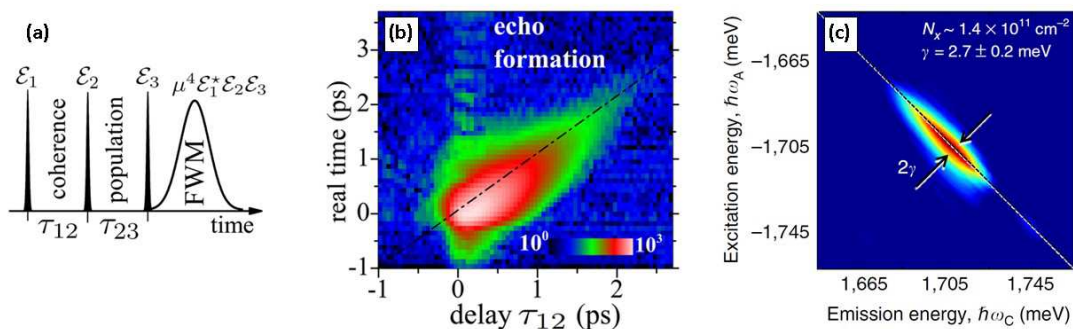


Figure 3.3: **(a)** Pulse sequence for FWM experiment extracted from [44]: three pulses E_1 , E_2 and E_3 are sent on the sample at different times. Pulses 1 and 2 are separated by a time τ_{12} and pulses 2 and 3 by time τ_{23} . A photon echo signal E_s is detected in transmission in the phase-matching direction $k_s = -k_1 + k_2 + k_3$. **(b)** Time-resolved FWM amplitude as a function of τ_{12} for a $MoSe_2$ monolayer deposited on SiO_2 . The formation of a photon echo is visible: a Gaussian signal with a maximum for $t = \tau_{12}$. The narrower the echo in time, the larger the inhomogeneous broadening. Figure extracted from [44]. **(c)** 2D Fourier-transform spectrum of the bright valley exciton for a CVD-grown WSe_2 monolayer on sapphire. Along the diagonal the inhomogeneous broadening can be deduced from photon echo. Homogeneous broadening γ can be deduced in the cross direction. Figure extracted from [142].

of photodegradation [114, 146, 147]. This effect was undoubtedly demonstrated by Cadiz et al. in our group: Fig 3.4 (a) shows an hysteresis behaviour at low temperature when the sample is exposed to different excitation laser powers while we monitor the PL emission. Under laser exposure, photodoping is visible in PL through a decrease of neutral exciton emission and an increase of trion emission, appearing as a shift of the main PL peak. Fig 3.4 (b) shows similar behaviour at $T = 300$ K under vacuum for PL before (black) and after (red) laser exposure with a power of $24.5 \mu W$. It also brings another interesting result by showing that exposition to air can bring back the sample to the initial situation (blue), drawing attention to the impact of ambient environment on the optical response. Although these effects are interesting, they mask the intrinsic optical properties which we need to access.

3.1.3 Hexagonal Boron Nitride as a new substrate

Inhomogeneous broadening and instability of samples were among the main reasons which brought scientists to transfer TMD monolayers on different substrates [148, 149, 150, 151]. Several substrates were tested such as few-layer graphene, gold, Mica, Gel-films, sapphire, Teflon, polystyrene... Among all the candidates, hexagonal boron nitride (hBN) attracted the most the interest of the TMD community.

In fact, this material had already interested the graphene community some years ago. Indeed, scientists working on graphene were struggling with similar problems. At first, 300 nm SiO_2/Si was used as a substrate because single-layer graphene can be visualized by optical contrast. However, it is known now that transport properties are affected by this substrate.

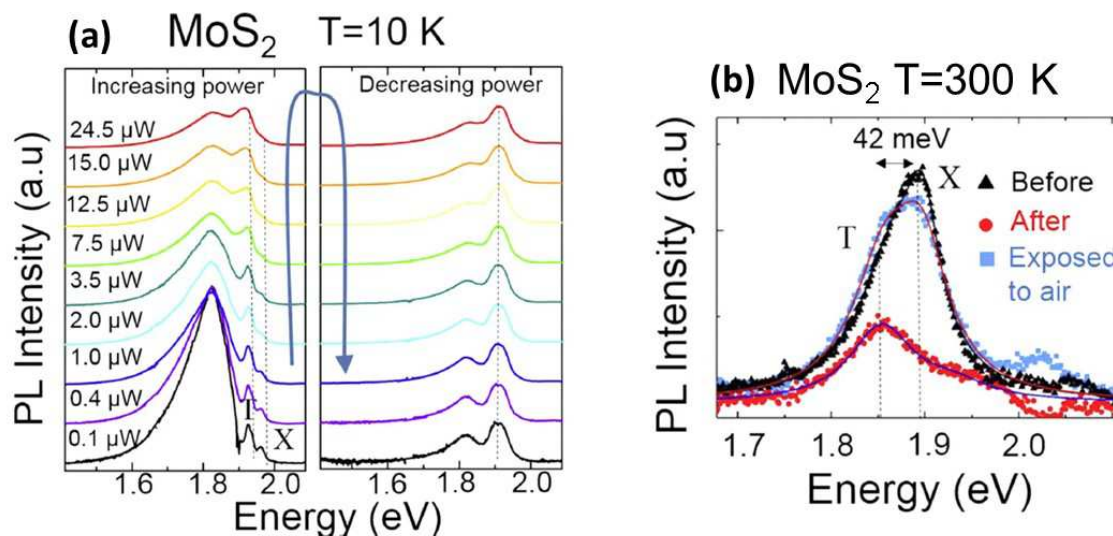


Figure 3.4: (a) PL spectra of MoS_2 monolayer on SiO_2 substrate submitted to pulsed excitation (1.5 ps) at 400 nm for different averaged powers. (b) PL spectra taken at $T=300$ K. Black curve corresponds to PL under $0.1 \mu W$ excitation under vacuum, red one is after $24.5 \mu W$ excitation during several minutes under vacuum, and blue one is after exposure to ambient environment. The spot diameter is $\approx 1 \mu m$. X labels the neutral exciton transition whereas T labels the charged exciton (trion) transition. Figures are extracted from [114].

The doping level of graphene is different according to fabrication details and substrate morphology [152]. Molecules can adsorb onto SiO_2 , forming hydroxyl groups (-OH) which can induce some charge transfer influencing doping of graphene giving rise to hysteresis behaviour under ambient conditions [153]. Not only adsorbates but also scattering from trapped charges inside SiO_2 [154], electron-phonon interaction [4, 155] and SiO_2 roughness [152, 156, 157] limit the mobility, preventing from reaching the expected intrinsic properties of graphene.

To tackle these problems, hexagonal boron nitride has proven to be an excellent substrate. hBN presents several main advantages compared to silicon:

- It has the same structure as graphite (see Fig 3.5) and their lattice parameter only differs by about 1.7 %.
- It is crystalline and atomically flat compared to amorphous SiO_2 which is rough.
- It has a low defect density thanks to optimized growth by our collaborators at NIMS [115] and is free of dangling bonds and charge traps.
- It is a high-bandgap semiconductor with $E_g \sim 6$ eV.

After deposition on hBN, graphene revealed higher mobilities, up to three times larger than on SiO_2 [78]. Used as a tunnel barrier, conductive AFM measurements show a "high level of uniformity in the tunnel current" [159], an evidence of the fact that hBN from NIMS is a highly pure, comparatively defect-free material.

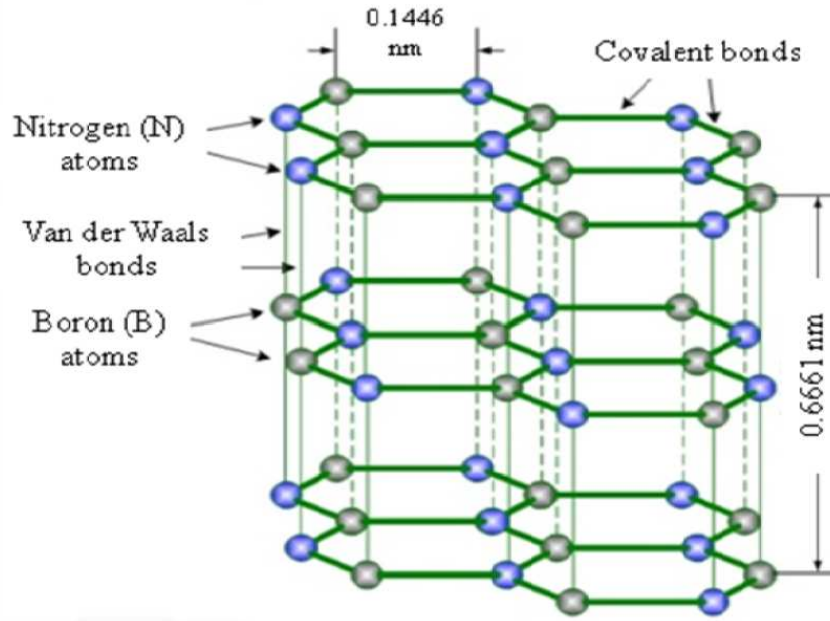


Figure 3.5: Structure of hexagonal boron nitride, extracted from [158]

All these arguments lead the TMD community to follow the path of their graphene community predecessors, by choosing hexagonal boron nitride as a new substrate material to study TMD monolayers.

In optical spectroscopy, especially photoluminescence, a strong effect is the change of the ratio of the charged exciton or trion (electron-hole pair + 1 extra carrier) to neutral exciton emission noted T/X. The trion (T) PL versus neutral exciton (X) PL is a basic optical tool to probe if the monolayer is charge neutral [114]. As shown in Fig 3.6 (a) and (b), the T/X ratio for a fresh $MoSe_2$ monolayer exfoliated on SiO_2 changes drastically, from about 1/3 to 1 after 120 s of exposure to a continuous wave laser at 532 nm and 230 μ W. This is the photodoping effect presented in section 3.1.2. Now, however, if we first transfer a few-layer hBN flake on SiO_2 and then transfer the $MoSe_2$ monolayer on this hBN flake, the behaviour is very different, and only a slight change of T/X ratio is visible as shown in Fig 3.6 (c). The typically 100 nm thick hBN now separates the TMD monolayer from the charge puddles in the SiO_2 and the charge transfer probability is considerably lowered.

3.1.4 HBN capping: protecting TMD monolayers from environment

Using hBN as a substrate indeed eliminates several problems such as SiO_2 roughness, oxide trapped charges which can induce inhomogeneous broadening and strong photodoping. However, it has also been underlined that ambient environment and adsorbed molecules can influence TMD monolayer optical properties. For this reason, in addition to an hBN substrate (that is bottom layer), hBN has also been used as a capping layer (that is top layer) to protect TMD monolayers from the environment and adsorbates.

In the following section, optical properties of hBN-encapsulated samples will be stud-

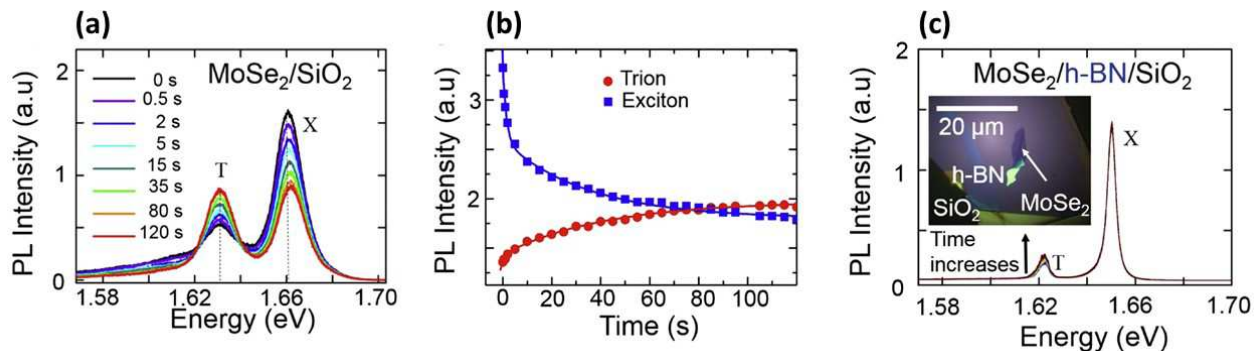


Figure 3.6: (a) Evolution of PL spectrum, for a $MoSe_2$ monolayer (exfoliated from VPT-grown bulk) on SiO_2 , after different exposure times to a continuous wave laser excitation at 532 nm and 230 μW . (b) Evolution of Trion and Exciton integrated intensities corresponding to PL spectra shown in (a). (c) Evolution of PL spectrum, for a $MoSe_2$ monolayer (exfoliated from Ti-doped VPT-grown bulk) on a few-layer hBN flake after exposure to a continuous wave laser at 633 nm and 40 μW . Figures extracted from [114]



Figure 3.7: Schematic representation of a hBN-encapsulated sample.

ied.

3.2 hBN-encapsulated samples: an optical study

3.2.1 Sample fabrication

Using the all-dry transfer technique presented in section 2.1.1 of chapter 2, an hBN bottom flake, TMD monolayer and hBN top flake are subsequently transferred on a SiO_2 (80 nm)/Si substrate giving a structure illustrated in Fig 3.7. The exact impact of hBN flake thicknesses (order of magnitude: tens of nm) is not investigated in this section but will be studied in section 3.3, later in the chapter.

3.2.2 Approaching homogeneous linewidth

The main representatives of the TMD family (MoS_2 , $MoSe_2$, WS_2 and WSe_2) were studied by using photoluminescence spectroscopy (see Bo Han et al. for our work on encapsulated $MoTe_2$ [160] and also the conclusion chapter of this thesis). The different

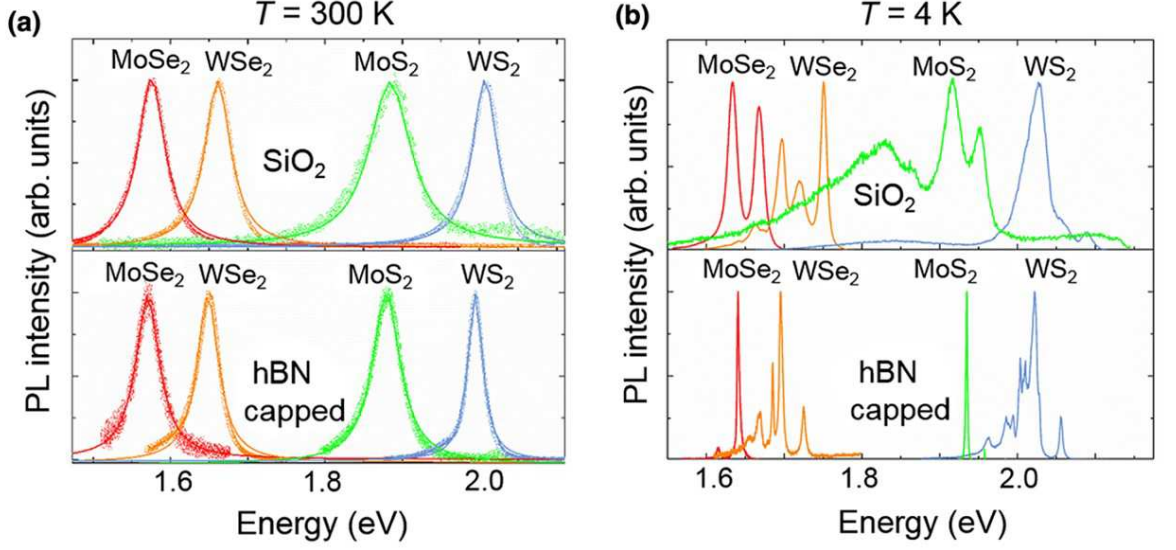


Figure 3.8: (a) Comparison of PL spectra for TMD monolayers deposited on SiO_2 and encapsulated between hBN at $T=300$ K. (b) Same as (a) but at $T=4$ K. Figures extracted from [111].

spectra at room temperature $T=300$ K and cryogenic temperature $T=4$ K are presented in fig 5.18.

It is important to note the different transition energies of the A-exciton for samples on SiO_2 and encapsulated ones. For all TMD materials, encapsulated monolayers present excitonic transitions shifted towards lower energies as summarized in table 3.1.

Material	X_A energy on SiO_2 (eV)	X_A energy, encapsulated (eV)	ΔE (meV)
MoS_2	1.951	1.931	20
WS_2	2.089	2.056	33
$MoSe_2$	1.668	1.641	27
WSe_2	1.751	1.725	26

Table 3.1: Neutral A-exciton energy at 4 K from PL measurements in fig 5.18 (b)

This shift of tens meV in energy is the result of two considerably larger energy renormalization effects which almost compensate each other. Indeed, the different dielectric environment with hBN surrounding the monolayer induces a shift of both the exciton binding energy and the free carrier bandgap up to several hundreds of meV [25, 27, 161]. In our experiments, the neutral exciton energy corresponds to what is called the optical bandgap E_{opt} , with $E_{opt}=E_g-E_B$, where E_g is the free carrier bandgap and E_B is the exciton binding energy. Both E_g and E_B are redshifted for encapsulated samples, so the result is only a small shift between 20 and 30 meV at lower energies of E_{opt} .

In addition to this energy shift, a clear improvement of optical quality is visible. Already at 300 K, for the four materials, transition linewidths are reduced as shown in table 3.2.

Material	Linewidth non-encapsulated (meV)	Linewidth Encapsulated (meV)
MoS_2	66	44
WS_2	39	23
$MoSe_2$	43	38
WSe_2	41	34

Table 3.2: Linewidths measured from PL measurements in Fig 5.18 (a) at 300K

This improvement is even more drastic when we go to cryogenic temperatures. Linewidths are decreased as summarized in table 3.3. Please that for our best samples the PL linewidth is now down to 1 meV FWHM [98, 162].

Material	Linewidth non-encapsulated (meV)	Linewidth Encapsulated (meV)
MoS_2	26	4
WS_2	18	4.5
$MoSe_2$	12	3.4
WSe_2	9	5.3

Table 3.3: Linewidths measured from PL measurements in Fig 5.18 (b) at 4K

Moreover, the shape and number of peaks in the PL spectra is different. This is especially the case for disulfide compounds MoS_2 and WS_2 .

For WS_2 , hBN-encapsulation enables distinguishing different peaks which were not visible for samples on SiO_2 . Samples on SiO_2 presented a PL response with one main broad peak which was in fact the convolution of different transitions.

For MoS_2 , encapsulated sample PL mainly shows one very well defined intense peak at 1.935 eV corresponding to the neutral A-exciton, whereas on SiO_2 , several broad transitions corresponding to bound excitons (~ 1.83 eV), trions (~ 1.917 eV), A (~ 1.951 eV) and B (~ 2.1 eV) excitons are covering a large energy range from 1.5 to 2.2 eV.

Reflectivity measurements brought similar results showing a clear improvement of the optical quality with sharper transitions obtained for encapsulated samples as shown in Fig 3.9.

These very encouraging results, with linewidths as low as 1 meV, show that hBN encapsulation enables approaching the homogeneous limit by reducing the contribution from the inhomogeneous broadening. This was confirmed by other groups' work [163, 146, 164, 165]. In particular, four wave mixing experiments have confirmed that inhomogeneous broadening is reduced when monolayers are encapsulated [165, 164]. Figure 3.10 shows that photon echo along the diagonal $\omega_\tau = -\omega_t$ is reduced for encapsulated samples, which is a clear evidence of the decrease of inhomogeneous broadening contribution.

3.2.3 Temperature-dependent measurements

The same samples as in Fig 5.18 and 3.9 were investigated by using PL and reflectivity as a function of temperature between 4 and 300 K. These experiments bring new useful information such as the evolution of optical bandgap, linewidth or emission intensity with temperature.

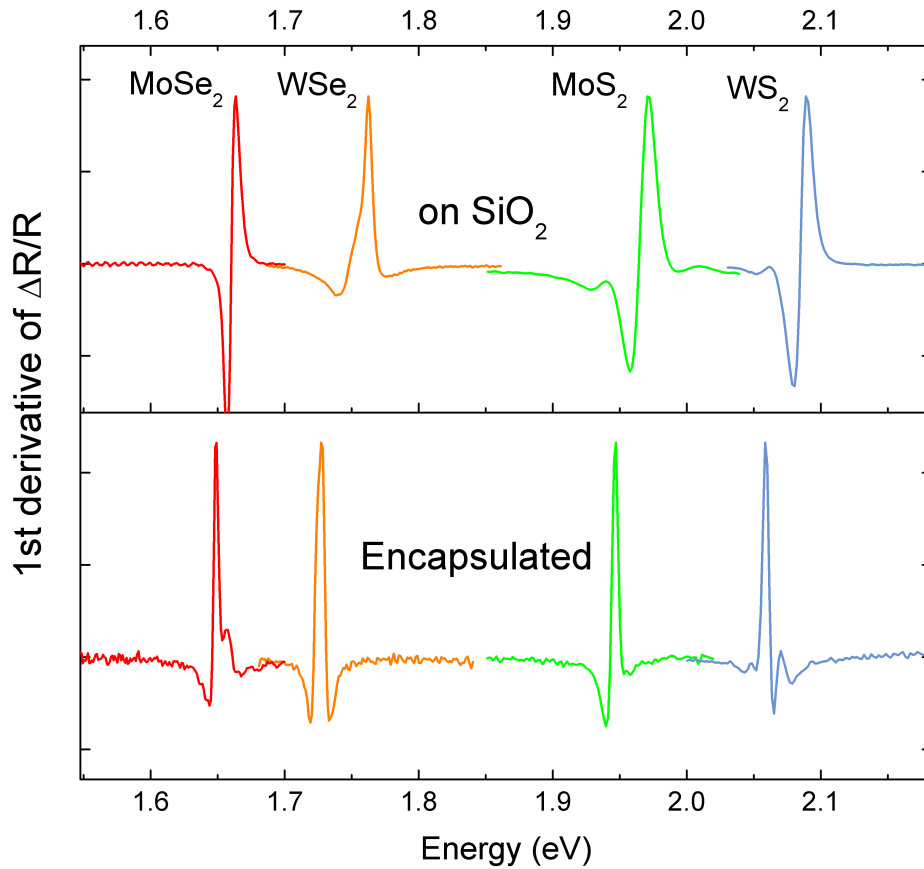


Figure 3.9: First derivative of differential reflectivity measurements for $MoSe_2$, $MoSe_2$, WS_2 and WSe_2 , on SiO_2 and encapsulated, at $T=4$ K.

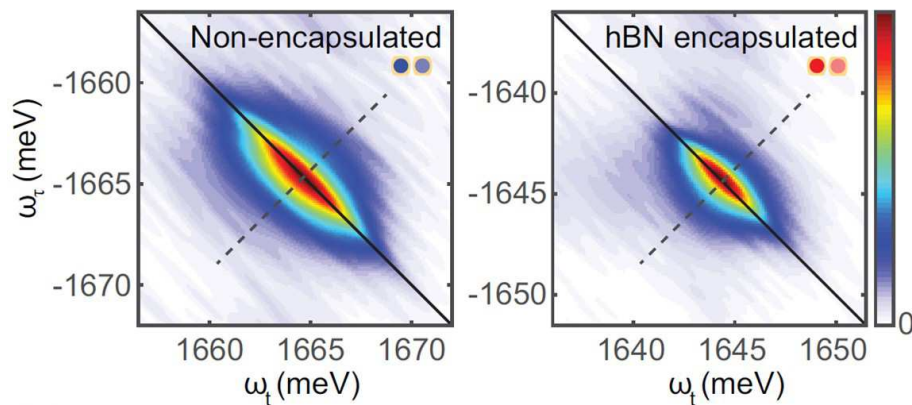


Figure 3.10: Low-power multidimensional coherent spectra of non-encapsulated $MoSe_2$ monolayer on sapphire and of hBN-encapsulated $MoSe_2$ monolayer. ω_τ is the absorption energy and ω_t is the emission energy. Figure extracted from [165].

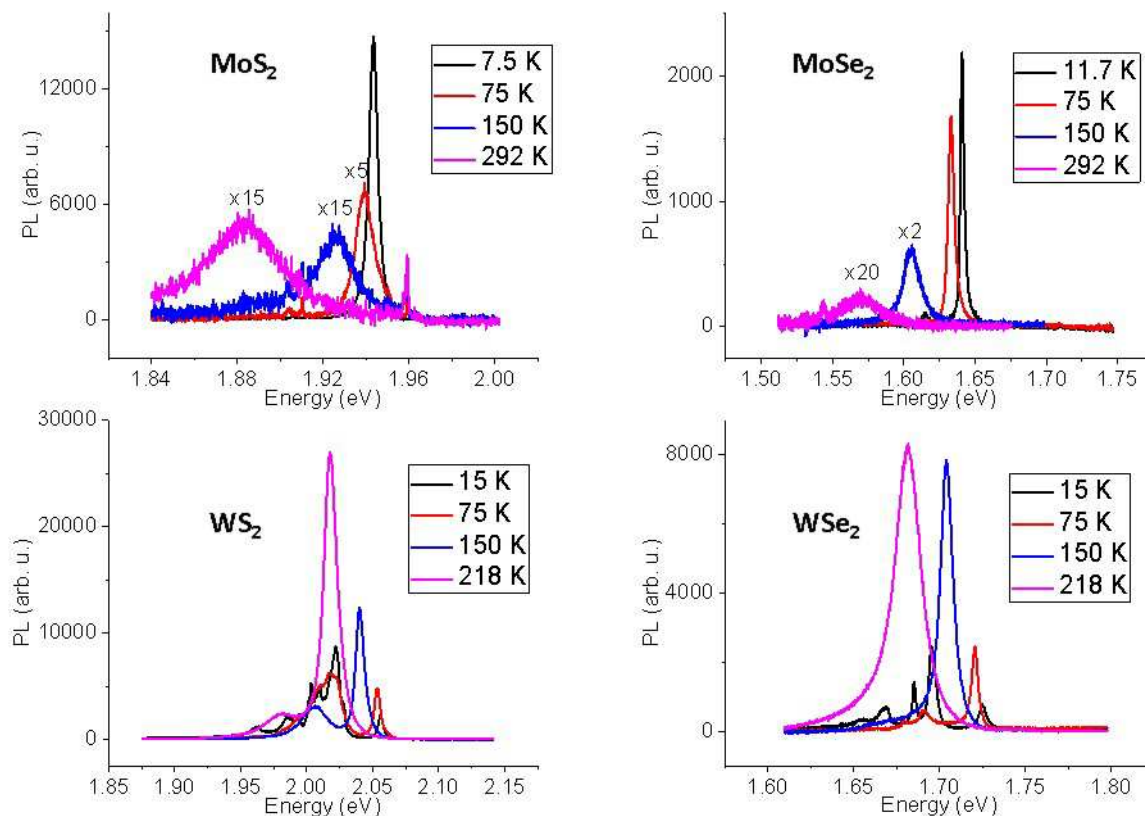


Figure 3.11: PL spectra at different temperatures between 4 and 300 K for encapsulated monolayer MoS_2 , $MoSe_2$, WS_2 and WSe_2 .

Fig 3.11 shows 4 PL spectra at 4 different temperatures for the 4 monolayer materials MoS_2 , $MoSe_2$, WS_2 and WSe_2 .

For all the materials, the optical bandgap is redshifted when temperature is increased. This is a well-known behaviour of the temperature dependence of semiconductor bandgaps which shifts due to a combined effect from thermal expansion and thermal vibration inducing temperature-dependent electron-lattice and electron-phonon interactions [166].

From reflectivity and PL, the evolution of the neutral exciton transition energy for each material is plotted in fig 3.12 and fitted with the following empirical law [167]:

$$E_G(T) = E_G(0) - S\Omega \coth[\Omega/(2k_B T)] - 1 \quad (3.2)$$

where $E_G(0)$ is the optical bandgap at $T=0$ K, S is a dimensionless coupling constant, Ω is an average phonon energy and k_B is the Boltzmann constant.

Fig 3.12 gives the parameters $E_G(0)$, S and Ω after fitting with equation 3.2. The fitting parameters found are in good agreement with previous work [168, 169, 170, 141]. We note that PL and reflectivity give the same energy evolution, indicating that effects of exciton localization are negligible (no Stokes shift).

With a similar approach, we analyze the change of linewidth in PL with temperature. We can fit the temperature evolution of linewidth with the phenomenological equation [145, 143]:

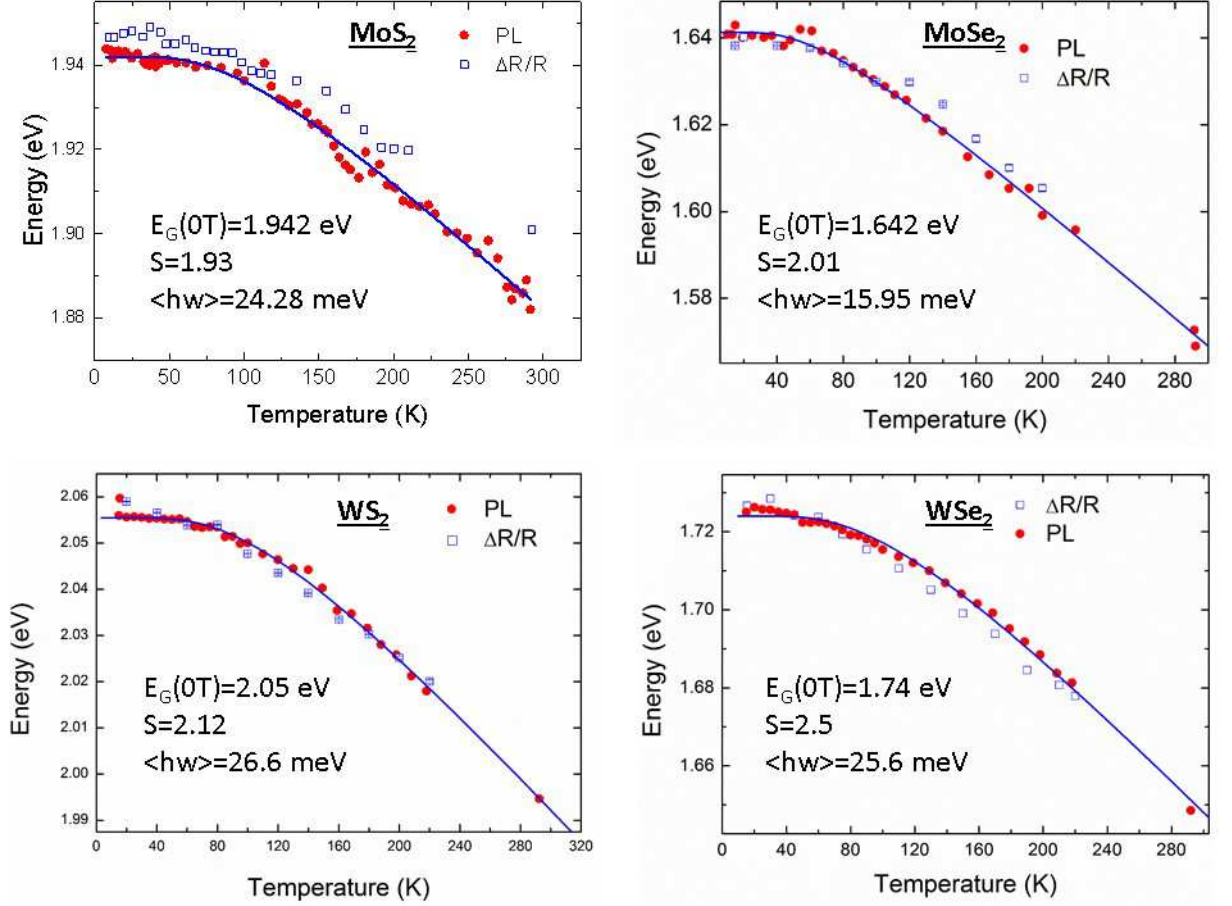


Figure 3.12: Neutral A exciton energy extracted from PL and reflectivity measurements at different temperatures between 4 and 300 K for MoS_2 , $MoSe_2$, WS_2 and WSe_2 . Blue lines correspond to fits with equation 3.2.

$$\gamma = \gamma_0 + c_1 T + \frac{c_2}{e^{\Omega/k_B T} - 1} \quad (3.3)$$

where γ_0 is the linewidth at $T=0$ K. Due to hBN encapsulation, γ_0 can be down to 1 meV in the best samples, but can be as high as tens of meV due to inhomogeneous broadening in non-encapsulated monolayers. c_1 in $\mu\text{eV}/\text{K}^{-1}$ describes the linear increase due to interactions with acoustic phonons, c_2 is a measure of the strength of the coupling to optical phonons and Ω is the averaged energy of the relevant phonon. Experimental points for $\gamma(T)$ and their fits are given in fig 3.13.

We notice that the four materials exhibit low FWHM < 5 meV at cryogenic temperature but at room temperature the linewidths differ a lot with, for instance, emission FWHM ~ 50 meV for MoS_2 and FWHM ~ 25 meV for WS_2 . Even if the origin of this difference still needs to be studied more systematically, larger linewidth at 300 K for MoS_2 is an indication of a stronger coupling with optical phonons. On a practical note, the impact of hBN encapsulation on the optical transition linewidth is therefore most clearly visible at $T=4$ K, whereas at $T=300$ K spectrally broad (tens of meV) transitions are observed due to broadening by scattering with phonons.

Coming back to Fig 3.11, it is noticeable that tungsten-based compounds and molybdenum-

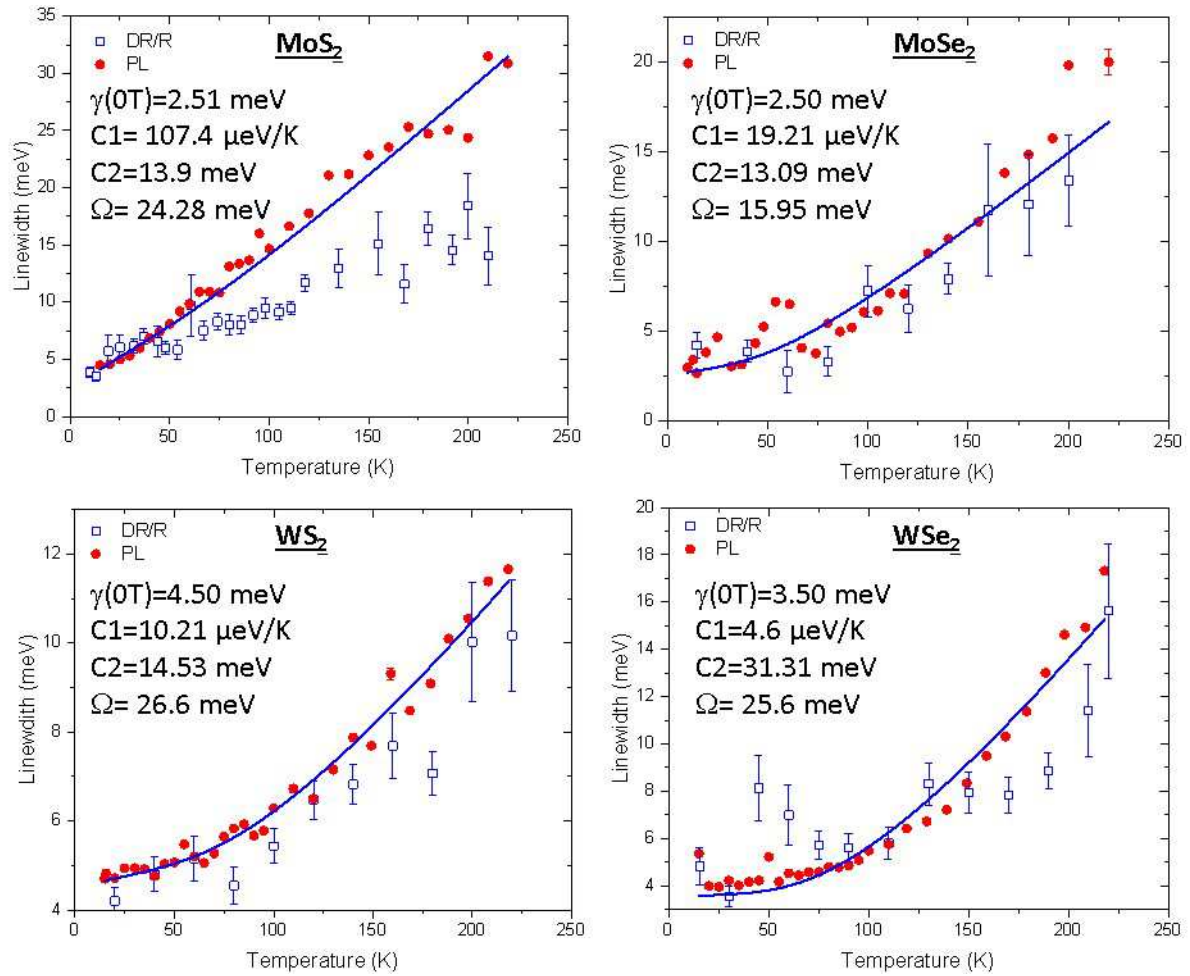


Figure 3.13: Neutral A exciton linewidth extracted from PL and reflectivity measurements at different temperatures between 4 and 300 K for MoS_2 , MoSe_2 , WS_2 and WSe_2 . Blue lines correspond to fits with equation 3.3.

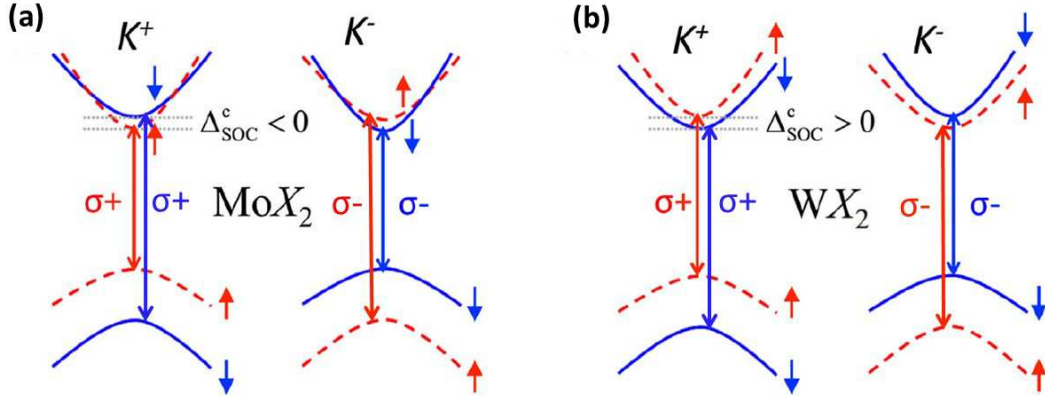


Figure 3.14: Representation of K^+ and K^- valleys for Mo- and W-compounds. The valleys can be selectively excited with $\sigma+$ and $\sigma-$ polarized light. Electron spins notations for both conduction and valence bands. Figure extracted from [24]

based compounds have an opposite emission intensity evolution with temperature. Intensity increases with temperature for WS_2 and WSe_2 whereas it decreases with temperature for MoS_2 and $MoSe_2$. This can be understood by considering the energetic order of dark and bright exciton species. Due to spin-orbit coupling, the conduction band splits into two sub-bands which are spin-polarized. The transition from one sub-band to the top valence band (also spin-polarized due to spin-orbit splitting) is called bright if it is spin-allowed or dark if it is spin forbidden. As it is represented in Fig 3.14 (reproduced from chapter 1), the sign of splitting in the conduction band between Mo- and W- compounds is reversed. For Mo- compounds, the bright transition is associated to the lowest lying conduction sub-band and the sub-band at higher energy is associated to the dark exciton. When temperature is increased, the sub-band associated to the bright exciton is depopulated to populate the dark exciton states and non radiative processes start to be competitive, also depending on the TMD monolayer intrinsic quality (defect density). This explains the lower intensity observed for Mo- compounds at higher temperatures. On the contrary, in the case of W-compounds, increasing temperature depopulates the dark exciton band to populate the bright one which is about 30-40 meV higher in energy [13, 34]. Note that the exact energy separation between bright (spin-allowed) and dark (spin-forbidden) exciton transitions depends in addition to the spin-orbit splitting also on Coulomb exchange terms and different effective mass values. It therefore results in an increase of the PL intensity for W-compounds with temperature, see also discussion on bright and dark excitons in chapter 5.

3.2.4 Valley polarization measurements

It has been shown in chapter 1 that due to inversion symmetry breaking TMD monolayers have unequivalent K valleys at the corners of the Brillouin zone see Fig 3.15. Chiral optical selection rules give rise to valley polarization which can be tracked in optical spectroscopy experiments. Due to the bad optical quality of MoS_2 monolayers deposited on SiO_2 , valley polarization of this material was not studied in detail until recently. However, as shown in

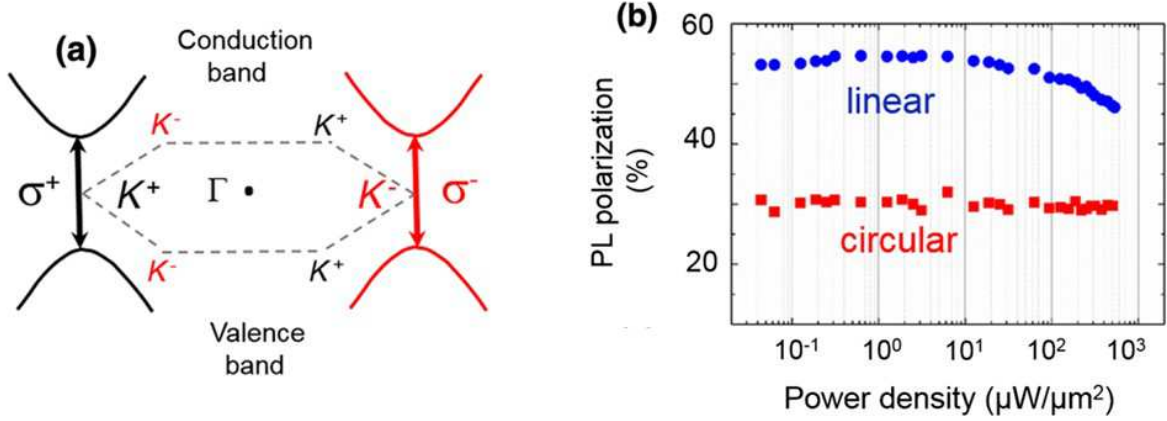


Figure 3.15: (a) Circular dichroism in TMD monolayers with inequivalent valleys K^+ and K^- which can be respectively excited with σ^+ and σ^- polarized light. (b) Linear and circular polarization degree as a function of excitation power density for hBN/ MoS_2 monolayer/hBN. Laser energy=1.96 eV and $T=4$ K. Figures extracted from [111].

section 3.2.2, encapsulation in hBN reduces drastically spectral contributions from defect states and inhomogeneous broadening. This leads to narrow linewidths and clear excitonic transitions which enable studying valley properties of hBN/ MoS_2 monolayer/hBN with unprecedented detail.

As explained in chapter 1, to measure valley polarization, we excite the sample with a continuous wave circularly polarized laser, σ^+ or σ^- , to excite σ^+ or σ^- polarized excitons. We then detect σ^+ and σ^- polarized PL emission due to exciton recombination using a setup as presented in chapter 1. Finally, by comparing the intensities I_{σ^+} and I_{σ^-} of these two photoluminescence signals, we can calculate the circular polarization degree given by:

$$P_c = \frac{I_{\sigma^+} - I_{\sigma^-}}{I_{\sigma^+} + I_{\sigma^-}} \quad (3.4)$$

Similarly, we can measure the linear polarization degree:

$$P_{lin} = \frac{I_X - I_Y}{I_X + I_Y} \quad (3.5)$$

where I_X and I_Y are the linearly polarized intensities along X and along Y. Here X and Y axis are arbitrarily chosen and have no particular orientation with respect to the monolayer crystallographic axis.

Fig 3.15 (b) shows circular and linear polarization degree as a function of power density, measured for an encapsulated MoS_2 at $T=4$ K, excited with a continuous wave HeNe laser (1.96 eV).

The value for $P_c \sim 30\%$ does not change with laser power. Valley coherence reaches a value up to $P_{lin} \sim 55\%$ and then decreases for power $> 50 \mu W/\mu m^2$. This can be due both to many-body effects such as exciton-exciton interactions which begin to be non-negligible and also sample heating. This idea is corroborated by Fig 3.16, which shows that for power $> 100 \mu W/\mu m^2$ linewidth is broadened, an indication for dephasing at the origin of

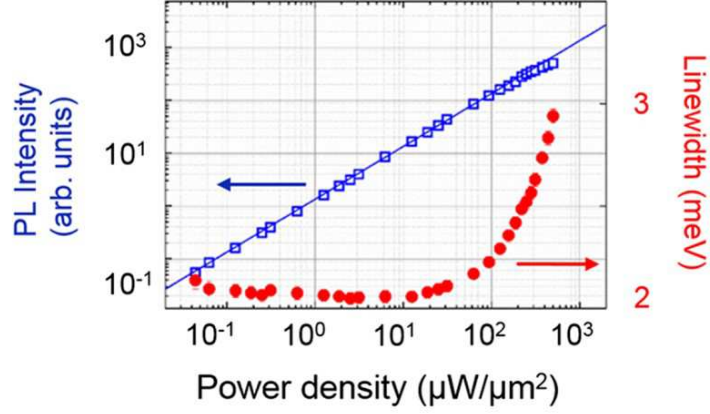


Figure 3.16: (a) PL intensity and linewidth as a function of power density. Laser energy=1.96 eV and $T=4$ K. Figure extracted from [111].

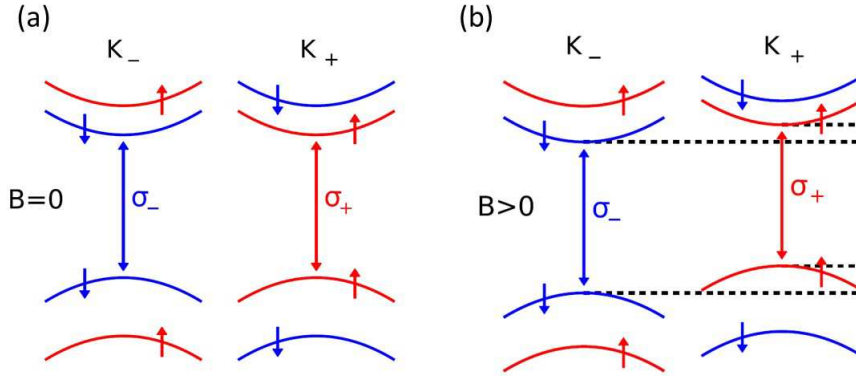


Figure 3.17: (a) Valleys K_+ and K_- at zero magnetic field. (b) Sketch of possible valley Zeeman splitting with $B>0$. Figures extracted from [171].

the loss of valley coherence.

Besides these power dependent measurements, magneto-optics experiments can be performed in order to change polarization properties and lift valley degeneracy as illustrated in Fig 3.17.

For a deeper theoretical approach about the Zeeman effect in two-dimensional crystals, readers are advised to refer to [172, 173]. In our experiment, a magnetic field is applied perpendicularly to the hBN/ MoS_2 monolayer/hBN heterostructure (z -direction) in a Faraday geometry. As a consequence, transition energies for σ_+ excitons and σ_- excitons are now different and we can resolve them spectrally by detecting σ_+ and σ_- polarized light. The Zeeman splitting measured is thus given by:

$$\Delta_Z = E_{\sigma_+}^{PL} - E_{\sigma_-}^{PL} = g\mu_B B_z \quad (3.6)$$

where $E_{\sigma_+}^{PL}$ and $E_{\sigma_-}^{PL}$ are respectively the PL signals coming from splitted K_+ and K_- valleys, g is the Landé factor of the exciton, μ_B is the Bohr magneton and B_z is the applied magnetic field. Results are summarized in Fig 5.19. Panel (a) shows that we are able to resolve Zeeman splitting at moderate fields of ± 9 T, where earlier studies

on samples with broad linewidth needed pulsed magnetic fields up to 63 T [140, 169]. Here again, the narrow excitonic linewidth are obviously a key parameter to achieve if we want to be able to resolve a Zeeman splitting of the order of 1 meV at ± 9 T. For different values of B we extract Δ_Z and plot them in fig 5.19. Using equation 3.6, we can extract a value for the exciton Landé g -factor of $g_X = -1.7 \pm 0.1$. This value is small compared to the few previously reported values in [140, 169] which gave g -factors between $g_X = -4$ and $g_X = -4.5$. However more recent works also found smaller values of the 1s A-exciton g -factor of $g_X \approx -3.0$ [174]. Even if the origin of these discrepancies is not yet understood, it seems that there is a correlation between the quality of the samples investigated and the g -factor. Higher quality samples, with narrow linewidths and less inhomogeneous broadening exhibit smaller g -factors for the 1s A-exciton in MoS_2 . At this stage we can only speculate that the different g -factors in different samples are due to sample-to-sample variations in strain, dielectric environment and the possible proximity of dark (spin-forbidden) states. Further studies are needed to clarify this.

In addition to the Zeeman splitting, Fig 5.19 (c) shows that applying a magnetic field also changes the circular polarization degree P_c of the emission, a trend observed for linear, circular $\sigma+$ and $\sigma-$ polarized laser excitation. Indeed, it is more favorable to populate the lowest energy valley, so for instance at positive magnetic fields, the $\sigma+$ exciton transition shifts to lower energy, is more favorably populated, and thus $I_{\sigma+}$ is higher in photoluminescence. So even with an initial linear excitation, by applying a magnetic field it is possible to create valley population imbalance and to observe circular polarization [175].

Another effect is visible in our magneto-optics experiments: rotation of linear polarization. Such effect has already been observed in past experiments in monolayer WSe_2 by our group [176]. First the sample is excited with a linearly-polarized laser, thus creating a superposition of the two exciton states $|+1\rangle$ and $|-1\rangle$ which can be expressed as $|X\rangle = \frac{1}{\sqrt{2}}(|+1\rangle + |-1\rangle)$, which is called exciton alignment. Then a magnetic field is applied, generating precession of this pseudospin at a frequency Ω around the magnetic field B_Z , inducing rotation of the PL polarization.

This effect is illustrated in Fig 3.19 for our MoS_2 encapsulated sample. The sample is excited with HeNe laser with polarization σ_X , a magnetic field B_Z is applied perpendicularly to the monolayer. In detection, a liquid crystals polarizer enables measuring PL intensity for different polarization angles, the data are plotted in Fig 3.19 (b) for $B_Z = 0$ and ± 9 T. Without magnetic field we measure a PL maximum at an angle $\theta = 0^\circ$, that is at the same polarization as the laser, σ_X . However, when a magnetic field is applied, this maximum shifts to an angle $\theta \neq 0^\circ$. At +9 and -9 T the measured angles are respectively $+5^\circ$ and -5° . This is a signature of a rotation of the PL linear polarization. Please note that we carefully eliminated all other sources that could change the linear polarization axis, such as Faraday rotation in the microscope objective. In summary, we optically initialize a superposition of valley states, we rotate this superposition by a finite angle that we tune with the magnetic field B_Z and we subsequently detect the new superposition state through its polarization in PL emission. This is an important step towards complete control of exciton states, see also related work of the group of Tony Heinz (Stanford) [177].

Valley polarization

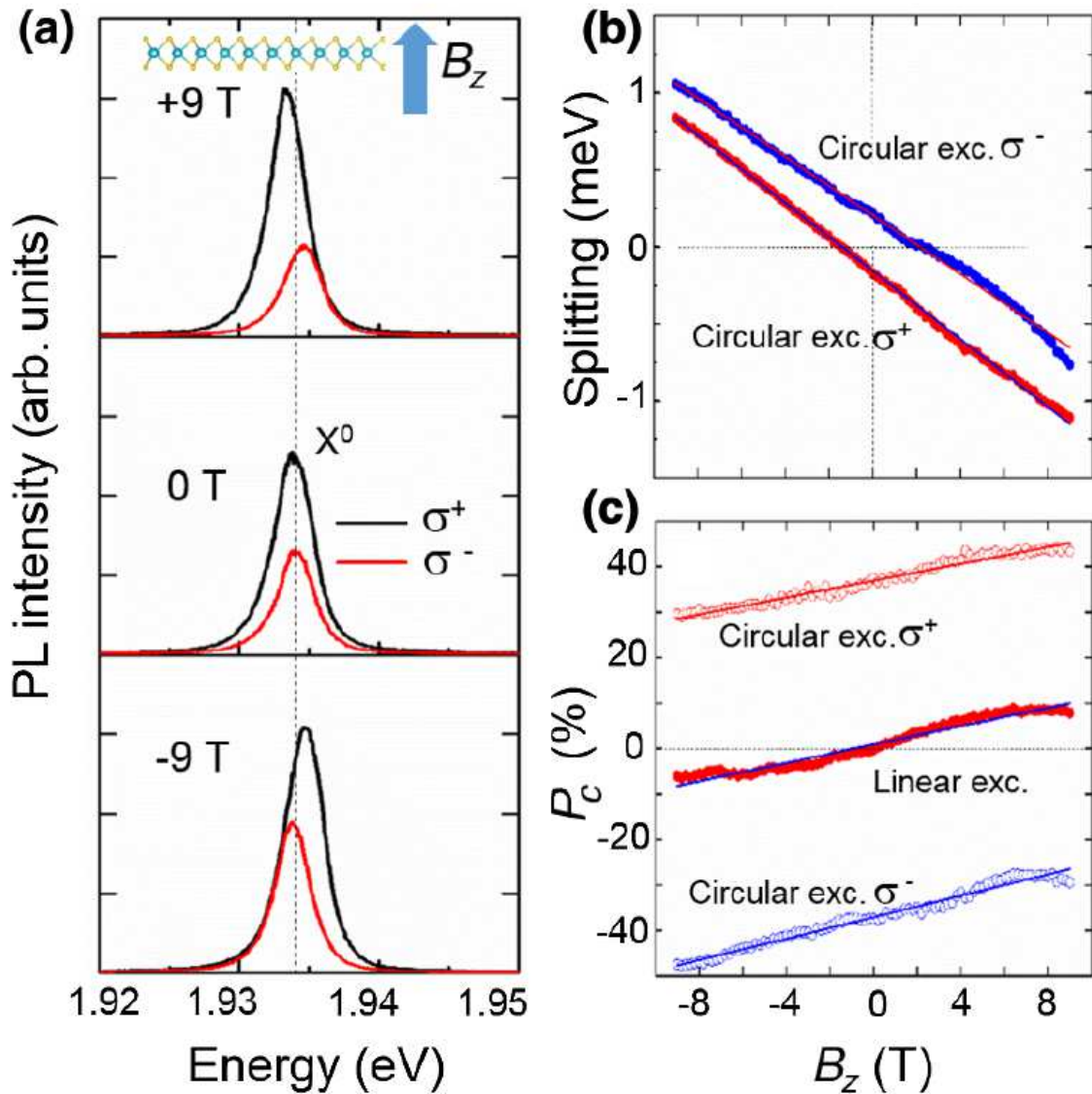


Figure 3.18: (a) PL spectra at -9, 0 and +9 T for σ^+ (black curves) and σ^- (red curves) detections and σ^+ excitation. (b) Zeeman splitting as a function of magnetic field B for σ^+ and σ^- excitations. (c) Measurements of circular polarization degree P_c for σ^+ , σ^- and linear excitations. Figures extracted from [111].

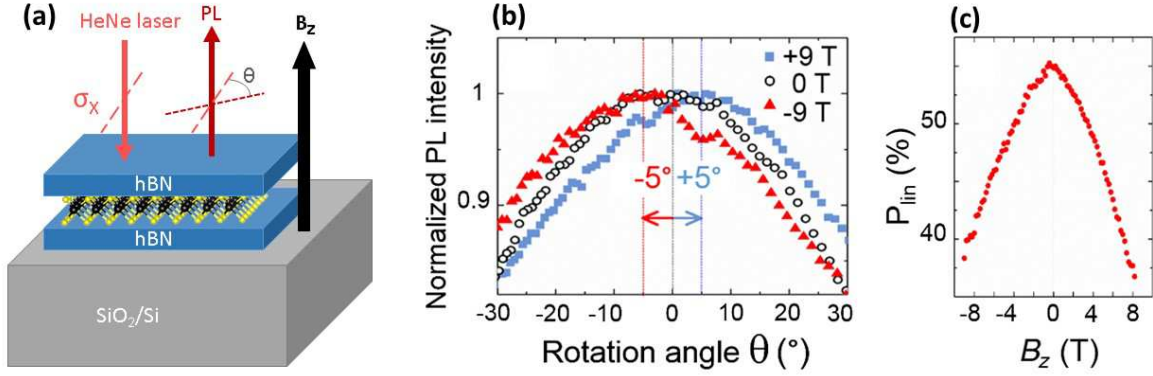


Figure 3.19: **(a)** Schematic of the experiment. σ_X linearly polarized laser is used to excite the hBN/ MoS_2 monolayer/hBN heterostructure. A magnetic field B_Z is applied perpendicularly to the sample. As a result rotation θ of linearly polarized PL is measured. **(b)** Measurements of PL intensity at different magnetic fields as a function of the linear detection angle θ made with the initial linear excitation polarization, extracted from [111]. **(c)** Linear polarization degree as a function of magnetic field, extracted from [111].

Keeping the detection angle of the liquid crystals polarizer at 0° and measuring the linear polarization degree P_{lin} as a function of magnetic field B_Z , it is clearly noticeable that the P_{lin} decreases with B as shown in Fig 3.19. We have just seen that, due to rotation of linear polarization, we expect a loss of the linear polarization degree for fixed linear detector. However, here, the loss is quite large; P_{lin} drops from 55% at zero field to about 35% at $B_Z = \pm 9$ T. The rotation angle of $\pm 5^\circ$ cannot explain by itself such a loss, so it is believed that dephasing induced processes during the PL lifetime could come into play, impacting the coherent superposition.

3.3 Excitonic states in hBN-encapsulated MoS_2 monolayers

In the previous section we focused on the 1s state of the neutral A-exciton, which is the only transition we see in PL for MoS_2 monolayer, as in Fig 5.18. Here we are going to study more precisely the Rydberg series of A-exciton (see section 1.2.3 and Fig 1.9 (b) chapter 1), with its excited states 2s, 3s etc... in addition to the 1s state. This work is going to show that for a precise analysis of the optical properties of encapsulated samples, we have to consider interferences in the multilayer system constituting the van der Waals heterostructure and also the effect of hexagonal boron nitride as a new dielectric environment surrounding excitons present in the TMD monolayer.

3.3.1 Optical spectroscopy of excited exciton states

To study excited exciton states in our sample, we perform reflectivity and photoluminescence excitation (PLE) at cryogenic temperature. The main results of the experiments are summarized in Fig 5.20. In Fig 5.20 (a), the main transition at 1.926 eV corresponds to the A:1s exciton. About 150 meV above, the broader B exciton transition is visible, in agreement with previous measurements [178, 72] and theoretical calculations which predict that the splitting between A and B excitons should be dominated by the spin-orbit

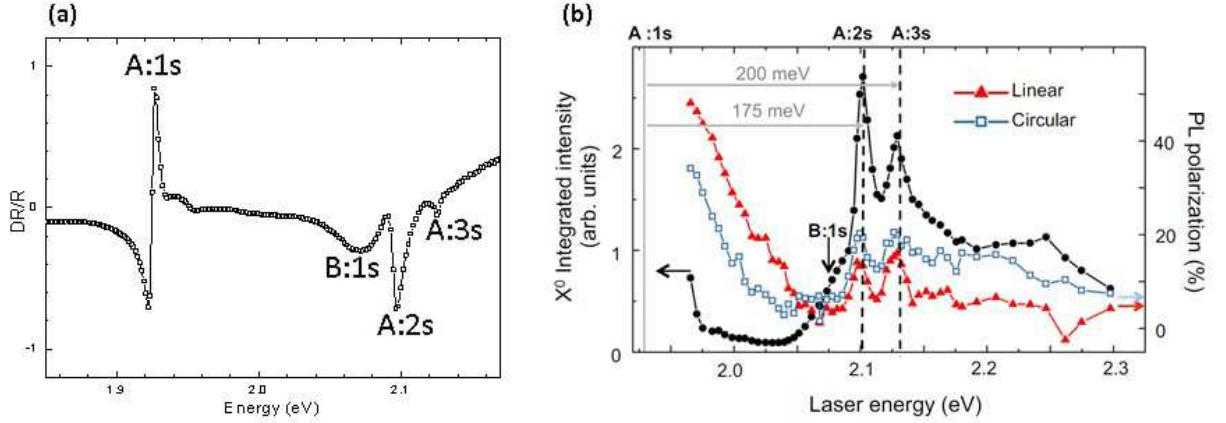


Figure 3.20: **(a)** Differential reflectivity DR/R at low temperature performed with a power-stabilized white halogen lamp. **(b)** PLE experiment. The PL of A:1s exciton is detected while the excitation laser energy is scanned across B, A:2s and A:3s excitonic states. Intensity in black, linear polarization degree in red (under linear excitation) and circular polarization degree in blue (under circular excitation) are measured. Figure extracted from [181].

splitting in the valence band [179, 14, 180]. Moreover, two other transitions appear at ~ 2.097 and ~ 2.126 eV, ascribed to A:2s and A:3s excitonic states. PLE measurements in Fig 5.20 (b) show clear resonances in intensity when the excitation laser is scanned across these energies, a signature of coupling between these states and A:1s state. Furthermore, the A:1s PL emission is strongly linearly and circularly polarized when these excited states are respectively excited with linearly and circularly polarized light. These measurements show that A:1s and these states are coupled (that is there is efficient relaxation from A:2s to A:1s), an evidence in favour of identifying them as A:2s and A:3s exciton excited states. Finally, recent investigations at high magnetic fields with our collaborators at the Los Alamos National Laboratory by measuring Zeeman splitting and diamagnetic shift of these states has confirmed their identification [174].

When looking more into details of Fig 5.20 (a), the relative oscillator strengths f_2/f_1 (between A:2s and A:1s) and f_3/f_1 (between A:3s and A:1s) are quite surprising. Indeed, if we apply the simple 2D hydrogenic model presented in section 1.2.3 of chapter 1, we would expect an oscillator strength f_n varying with principal quantum number n as follows [19]:

$$f_n \propto \left(n - \frac{1}{2}\right)^{-3} \quad (3.7)$$

With such an approach, we would expect $f_2/f_1 \approx 0.037$ and $f_3/f_1 \approx 0.008$. In figure 5.20 (a) we rather measure $f_2/f_1 \approx 0.40$ and $f_3/f_1 \approx 0.09$. These values are basically one order of magnitude larger than what we would expect using equation 3.7. In the following sections, we analyse these discrepancies, first by considering interferences in the van der Waals heterostructures and then by taking into account the effect of dielectric environment on exciton binding energies and oscillator strength.

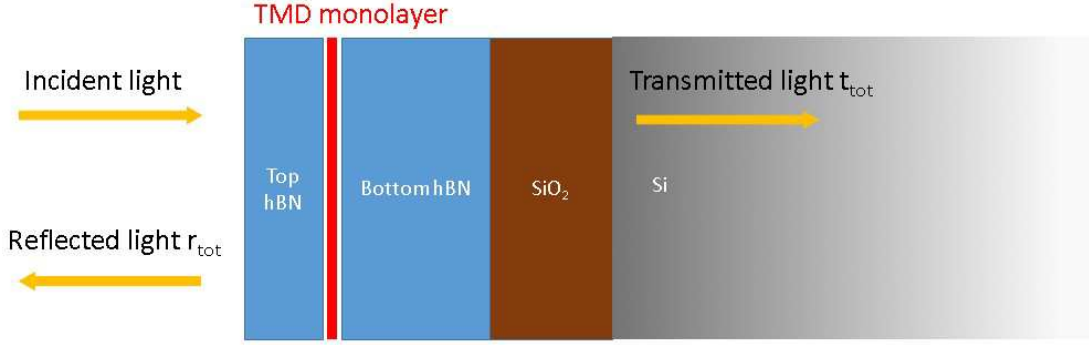


Figure 3.21: Multilayer structure for our transfer matrix approach. In our case, we can consider light propagating perpendicularly to the monolayer plane. We checked numerically that using a microscope objective with high numerical aperture and therefore not strictly normal incidence, does not considerably impact the validity at this approach. The aim is to calculate the reflection coefficient r_{tot} .

3.3.2 Interferences in the van der Waals heterostructure

Our target is to model the full optical response of the multilayer structure, to check if the exciton resonances, separated in energy by more than 100 meV, vary in amplitude in the spectra not just due to differences in oscillator strength but also due to interference effects. In this section, we use a transfer matrix approach developed with our collaborators M. Glazov and M. Semina (Ioffe Institute, St-Petersbourg) in order to calculate reflectance of our structures: hBN/ MoS_2 monolayer/hBN/ SiO_2 (83nm)/Si. The idea of transfer matrix approach is illustrated in figure 5.21.

We must calculate the following matrices:

- Matrices at the interfaces: $T_{vacuum \rightarrow Top hBN}$, $T_{hBN \rightarrow SiO_2}$, $T_{SiO_2 \rightarrow Si}$.
- Matrices accounting for the phase shift in each medium: $T_{Top hBN}$, $T_{Bottom hBN}$ and T_{SiO_2} .
- The matrix for the 2D MoS_2 monolayer: T_{MoS_2} .

The transfer matrix at an interface between two dielectric slabs of indices n_1 and n_2 is given by:

$$T_{n_1 \rightarrow n_2} = \frac{1}{2n_1} \begin{pmatrix} n_1 + n_2 & n_2 - n_1 \\ n_2 - n_1 & n_2 + n_1 \end{pmatrix} \quad (3.8)$$

Then to calculate the matrices accounting for the phase shift in a medium, we must know the thickness t of each layer:

$$T = \begin{pmatrix} e^{i\frac{\omega n}{c}t} & 0 \\ 0 & e^{-i\frac{\omega n}{c}t} \end{pmatrix} \quad (3.9)$$

where ω is the angular frequency of light, n is the refractive index of the medium and c is the speed of light in vacuum.

Finally to calculate the matrix accounting for the monolayer:

$$T = \frac{1}{t} \begin{pmatrix} t^2 - r^2 & r \\ -r & 1 \end{pmatrix} \quad (3.10)$$

with t the transmission coefficient and r the reflection coefficient.

Following a similar approach as the one exposed in [182] for quantum wells, we can express the coefficient r for the MoS_2 monolayer as [181]:

$$r(\hbar\omega) = \sum_{n=1}^3 \frac{i\Gamma_{0,A:ns}}{E_{A:ns} - \hbar\omega - i(\Gamma_{0,A:ns} + \Gamma_A)} + \frac{i\Gamma_{0,B:1s}}{E_{B:1s} - \hbar\omega - i(\Gamma_{0,B:1s} + \Gamma_B)} \quad (3.11)$$

where Γ_0 and Γ are the radiative and nonradiative dampings of the excitons. We consider 1s, 2s and 3s states for the A-exciton and only 1s state for B-exciton in order to reproduce our data of Fig 5.20.

The total transfer matrix for the full structure is thus given by:

$$T_{tot} = T_{SiO_2 \rightarrow Si} T_{SiO_2} T_{bottomhBN \rightarrow SiO_2} T_{bottomhBN} T_{MoS_2} T_{tophBN} T_{vacuum \rightarrow tophBN} \quad (3.12)$$

We have the following relation to obtain r_{tot} and t_{tot} :

$$T_{tot} \begin{pmatrix} 1 \\ r_{tot} \end{pmatrix} = \begin{pmatrix} t_{tot} \\ 0 \end{pmatrix} \quad (3.13)$$

Therefore it is possible to calculate r_{tot} and to compare the simulated reflectance with our data from Fig 5.20. We performed the calculations by varying the bottom hBN and SiO_2 thicknesses to evaluate the effect on the reflectivity spectrum. Comparison between simulations and measured data is shown in Fig 5.22. The best fit of the data is found with the red graph, corresponding to the real layer thicknesses: $t_{SiO_2}=93$ nm, $t_{bottomhBN}=130$ nm (AFM value) and $t_{tophBN}=7$ nm (AFM value). Changing the thickness parameters can change the observable relative intensities of the exciton transitions considerably. For instance, taking the green curve, calculated for the following thicknesses $t_{bottomhBN}=155$ nm, $t_{SiO_2}=83$ nm and $t_{tophBN}=7$ nm, it is noticeable that the shape of the A:1s transition is different but has a similar intensity as the A:1s transition of the red curve. However, B:1s and the excited states A:2s and A:3s are less intense for the green curve compared to the red one.

It is thus important to take into account all the layers composing the heterostructure when we consider the optical response of these samples. The intensities of the excitonic states in reflectivity is indeed modulated by the reflectivity of the whole heterostructure. The visibility of the A:2s state compared to the A:1s can therefore be enhanced due to these thin layer interference effects. Since performing these first simulations, we carefully choose for each project the hBN layer thickness, in order to enhance the visibility of the excitonic transition we want to study. Nevertheless, this effect cannot explain by itself the relative intensities visible in fig 5.20 (a). In the next section we highlight the additional effect of the dielectric environment on exciton binding energy and oscillator strength.

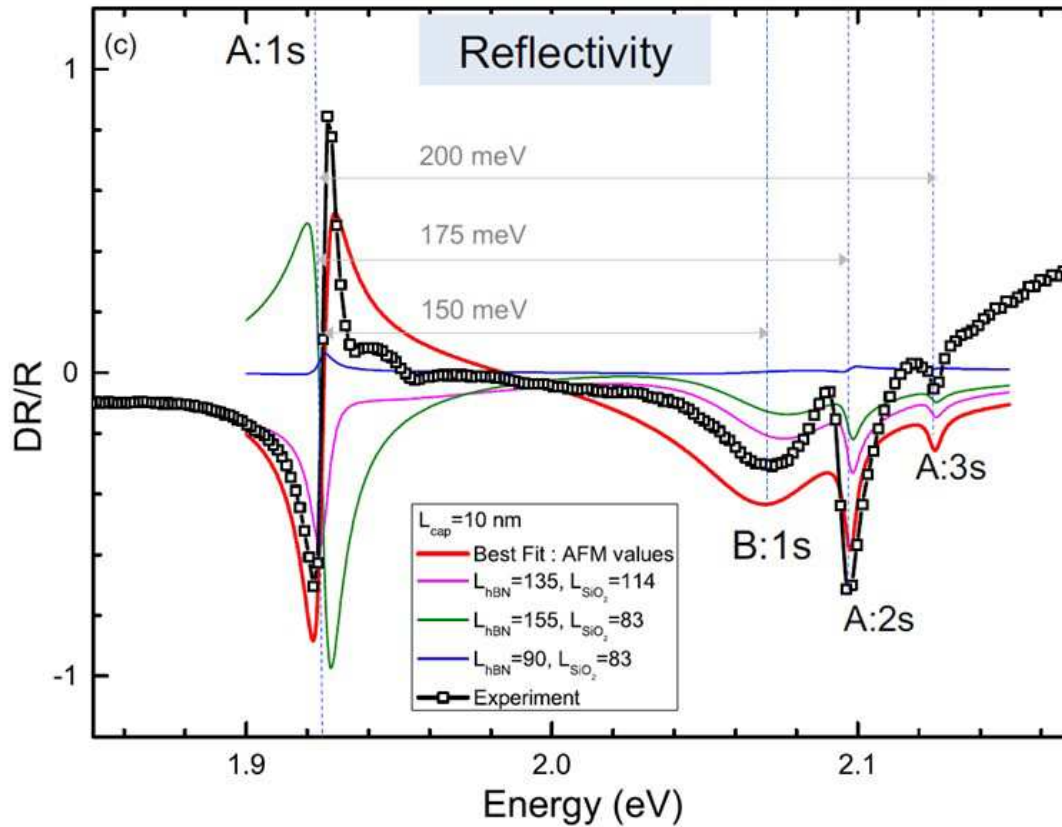


Figure 3.22: In black, same DR/R data as in Fig 5.20 (a). The colored spectra are obtained using the transfer matrix method for different bottom hBN thicknesses, top hBN is kept at 7 nm (value measured with AFM). SiO_2 is always 83 nm apart for the magenta curve where it is set to 114 nm. Red curve is the best fit, obtained with a bottom hBN thickness of 130 nm as measured with AFM. Figure extracted from [181].

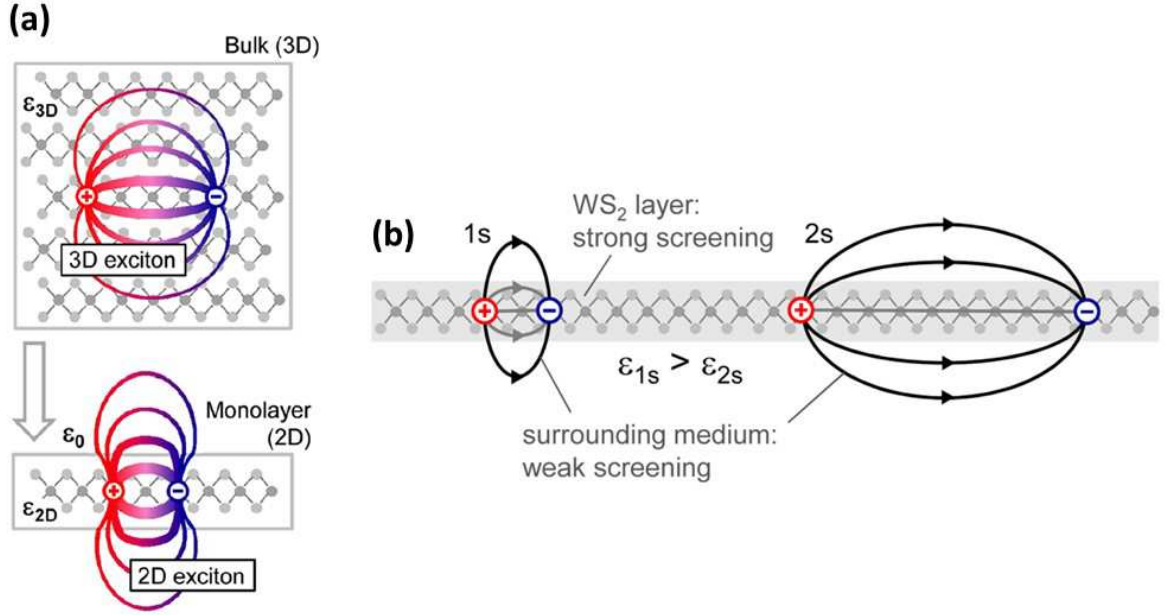


Figure 3.23: (a) Representation of an electron-hole pair in real space, for a 3D crystal and a 2D crystal. The electric field lines are also drawn. Dielectric environment changes are taken into account through the different dielectric constants ϵ_{3D} and ϵ_{2D} ; ϵ_0 is the vacuum permittivity. (b) Illustration of the excitons in 1s and 2s states in a WS_2 monolayer. Their interaction is drawn through the electric field lines. Figures extracted from [27].

3.3.3 Influence of dielectric environment on excitons

We have just seen that interferences in the multilayer system play a non negligible role in the visibility of excitonic transitions in our reflectivity spectra. However, in addition the effect of the dielectric environment on more intrinsic excitonic properties has to be taken into account. Experimental proofs show that the hydrogenic model used to describe the 2D Wannier exciton is not adapted to describe excitonic states in our systems [27]. Going from 3D to 2D, the influence of dielectric environment outside the monolayer on excitons becomes more important. As schematically shown in Fig 5.23 (a) we cannot consider a perfect 2D exciton; E -field lines of the interaction between the electron and the hole go out of the monolayer plane, thus experiencing the influence of the surrounding dielectric environment.

In addition, Fig 5.23 (b) illustrates with 1s and 2s states, the fact that for higher principal quantum numbers n , the exciton radius increases and the field lines are more influenced by the dielectric environment. As a consequence, the potential felt by the exciton depends on its principal quantum number n . Actually, as also demonstrated in [27] the effective dielectric constant "felt" by the exciton changes with n : for lower n the electron-hole interaction is more screened than for higher n . Therefore, if $n=1,2$, the binding energies deviate from the hydrogen model, however at $n > 2$ the effective dielectric constant is roughly constant and hydrogen model works. In order to model properly this behaviour, the Rytova-Keldysh potential [32, 33] is generally used [183, 184, 185]:

$$V(r) = \frac{-e^2}{8\epsilon_0 r_0} \left(H_0 \left(\frac{\kappa r}{r_0} \right) - Y_0 \left(\frac{\kappa r}{r_0} \right) \right) \quad (3.14)$$

where e is the electron charge, ϵ_0 is the vacuum permittivity, r_0 is the screening length, κ is an average dielectric constant and H_0 and Y_0 are the Struve and Neumann functions. The screening length is given by $r_0=2\pi\chi_{2D}$ with χ_{2D} is the 2D polarizability of the monolayer. The average dielectric constant is given by $\kappa=\frac{1}{2}(\epsilon_{top}+\epsilon_{bottom})$ with ϵ_{top} and ϵ_{bottom} the dielectric constants of the top and bottom dielectric layers surrounding the monolayer.

The same model was used with our hBN/MoS₂ monolayer/hBN sample. We solved the Schrödinger's equation $H\psi_{ns}(r)=E_{ns} \psi_{ns}(r)$ for radially s-type exciton states using the Rytova-Keldysh potential. We then compared the calculated binding energies with the values found using a Coulomb potential $V(r)=-e^2/\epsilon r$, as shown in Fig 5.24 (a) and (c). The parameter r_0 was varied in order to fit the experimental values as well as possible. Rytova-Keldysh potential gives results in excellent agreement with experiments for $r_0=2.95$ nm: exciton binding energy $E_B \approx 222$ meV, separation A:1s-A:2s ≈ 174 meV, A:2s-A:3s ≈ 28 meV. The r_0 value also agrees well with theory [184]. The value for E_B is confirmed in recent magneto-optics work on our samples [174].

Fig 5.24 (b) also demonstrates that relative oscillator strengths are quite different for $n > 1$ using either Rytova-Keldysh or Coulomb potential. The values plotted in Fig 5.24 (b) are shown in the table below:

Principal quantum number n	f_n/f_1 Keldysh	f_n/f_1 Coulomb
1	1	1
2	0.09813	0.03704
3	0.02707	0.008
4	0.01099	0.00292
5	0.00549	0.00137
6	0.00313	0.00075
7	0.00195	0.00046
8	0.00129	0.00030
9	0.00090	0.00020
10	0.00065	0.00015

Table 3.4: Numerical values of relative oscillator strengths plotted in fig 5.24 (b).

In summary, the oscillator strength for 2s and 3s is considerably higher using the more realistic Keldysh potential as compared to the ideal 2D Coulomb potential. We can therefore explain the visibility of the A:2s and A:3s in reflectivity in Fig 5.20 and 5.22 by the combined effect of thin layer interference and intrinsically higher oscillator strength.

3.4 Hybrid heterostructure with bottom hBN grown by MBE

This section presents additional results on encapsulated TMD monolayers. However the difference here is that the bottom hBN used as a substrate has been grown by our collaborators S. Nakhaie, L. Geelhaar and J.M.J. Lopes, in the Paul-Drude-Institut in Berlin, from elemental precursors B and N by molecular beam epitaxy (MBE) [186, 187]. Compared to other techniques such as Chemical Vapor Deposition (CVD), MBE offers a good

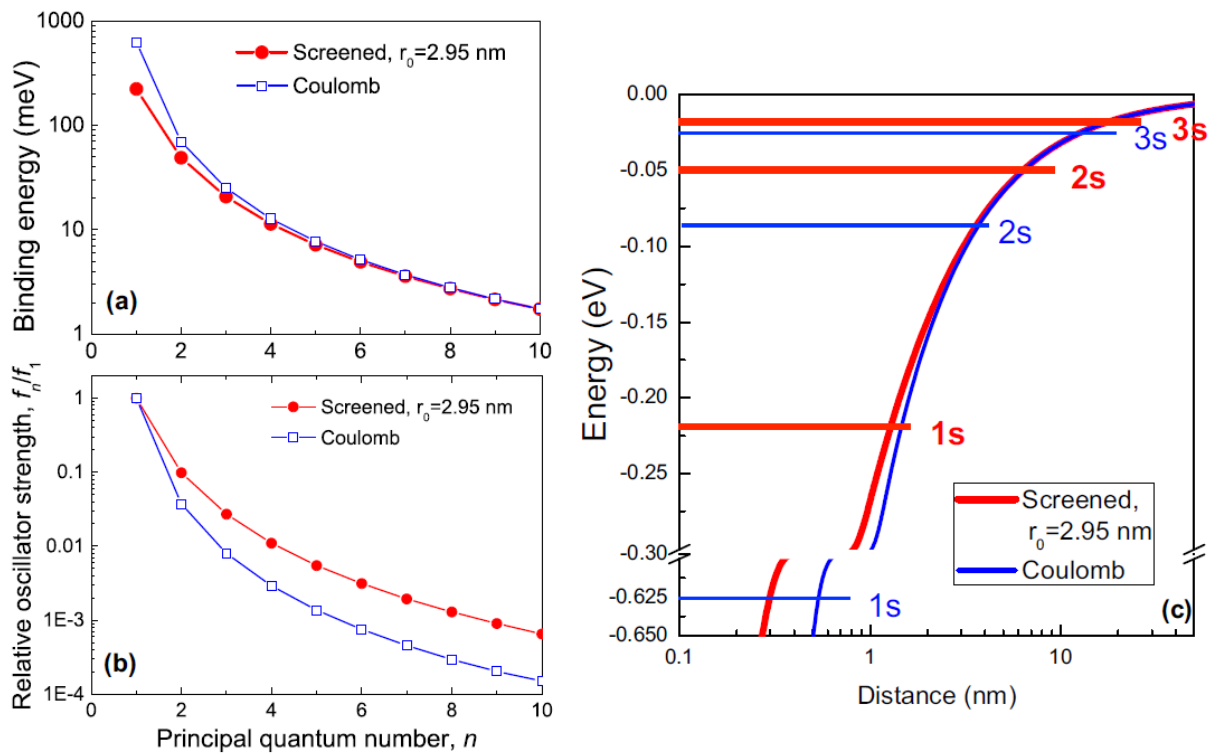


Figure 3.24: Comparison of calculations obtained with two different potentials $V(r)$: screened (Rytova-Keldysh) and Coulomb. (a) Calculated values of binding energies as a function of principal quantum number n . (b) Calculated values of relative oscillator strength f_n/f_1 as a function of principal quantum number n . (c) Comparison of the bound states as a function of exciton radius. Figures extracted from [181].

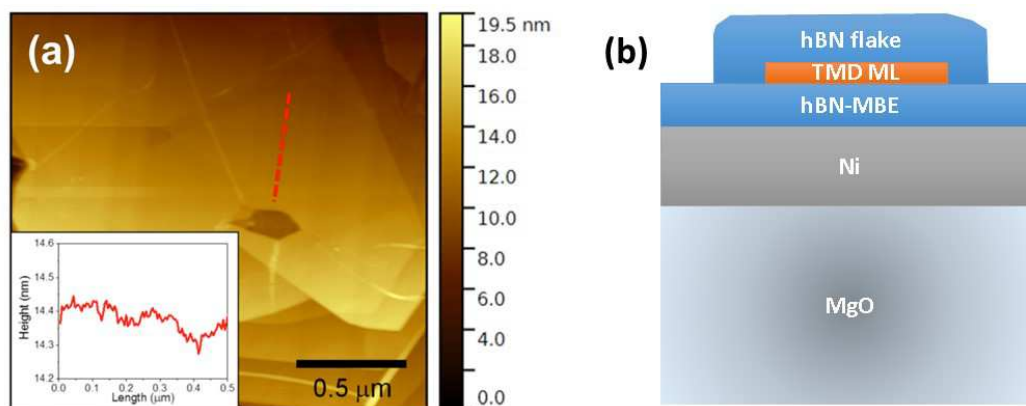


Figure 3.25: (a) AFM image of the hBN film grown by MBE on Ni/MgO(111). The red dashed line shows the location of the AFM profile given in inset. Figure extracted from [188]. (b) Schematics representing our TMD monolayer encapsulated structure.

control of crystal growth making possible to grow monolayer thick materials. Contrary to CVD, it does not rely on the decomposition of a molecular precursor which depends on the catalytic properties of the substrate.

The hBN is synthesized on a template consisting of MgO (111) covered by a 300 nm polycrystalline nickel (Ni) layer. Such a template was previously used for the growth of hBN/graphene vertical heterostructures [187]. The average hBN film thickness is 1 nm, which corresponds to 3 hBN monolayers. It is relatively smooth with a root-mean-square roughness of about 0.3 nm and presents flat terraces of $1 \mu\text{m}^2$ as shown in Fig 3.25 (a). The surface is however inexorably influenced by the underlying Ni polycrystalline substrate. Wrinkles form in hBN during the cooling after the growth due to the unequal expansion coefficients of hBN and Ni. Contrary to exfoliated hBN of several hundred μm lateral size, the hBN-MBE layer covers the entire $1\text{cm} \times 1\text{cm}$ substrate. On the top of this ultrathin layer, MoS_2 and MoSe_2 monolayers are deposited using the PDMS deterministic transfer technique. The TMD monolayers are finally covered with a top hBN flake from NIMS [115] of thickness ~ 11 nm according to AFM measurements. An heterostructure as the one of Fig 3.25 (b) is obtained.

The MoS_2 and MoSe_2 samples were placed in the cryostat of our optical spectroscopy setup in order to perform PL and reflectivity measurements at low temperature $T=10$ K. For PL, the MoS_2 was excited with a 532 nm continuous wave laser and MoSe_2 was excited with continuous wave HeNe laser at 632.8 nm. A broadband stabilized white light is used to perform reflectivity. The main results obtained for the MoS_2 monolayer sample are summarized in Fig 3.26. In PL we observe clearly the A-exciton transition X_A which exhibits a linewidth down to 6 meV. Comparison with reflectivity (Fig 3.26 (b)) shows X_A at the same energy around 1.97 eV. This negligible Stokes shift is an evidence in favour of a negligible localization of excitons, showing the good quality of the sample at the location where the spectra have been taken. The B-exciton noted X_B also appears, about 150 meV at higher energy than X_A , a value in agreement with previous measurements [178, 72]. Panel (c) shows two PL spectra taken under $20 \mu\text{W}$ excitation taken before and after exposure up to $50 \mu\text{W}$. A small hysteresis is measured, possibly a consequence of

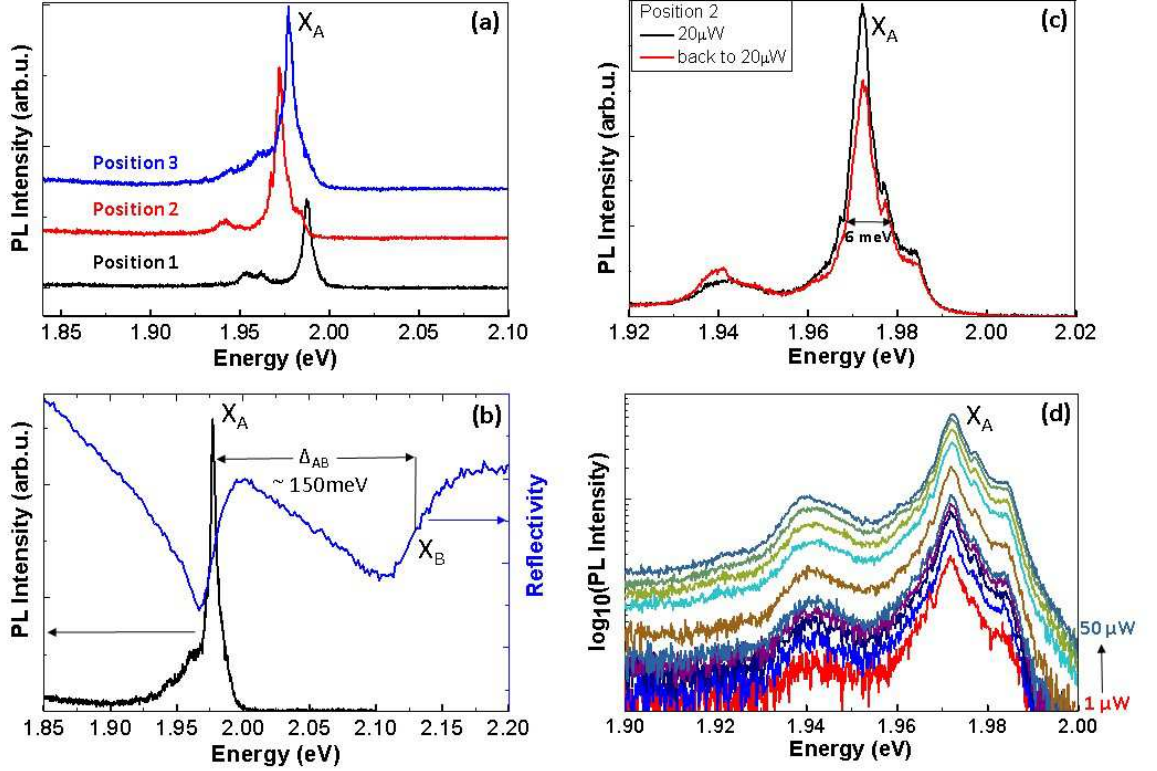


Figure 3.26: Different measurements performed on the hBN/*MoS*₂ monolayer/hBN-MBE van der Waals heterostructure. (a) PL spectra taken at different positions. X_A denotes the A-exciton transition. (b) Comparison between reflectivity and PL at a given position on the sample. X_B indicates the transition associated to B-exciton. Δ_{AB} is the splitting between A and B excitons. (c) PL spectra recorded under 20 μ W excitation before (black curve) and after (red curve) exposure up to 50 μ W. (d) Power-dependent PL measurements with an excitation power from 1 to 50 μ W.

weak photodoping. However panel (d) shows that when increasing power up to 50 μ W, the overall spectral shape is not affected. This is in stark contrast with what has been presented in Fig 3.4 for *MoS*₂ samples deposited directly on *SiO*₂ without coverage by a top hBN layer. Also the linewidth compared to Fig 3.4 of several tens of meV is vastly improved here.

Concerning *MoSe*₂, similar trends are observed in Fig 3.27 as for the material *MoS*₂. Panel (a) shows negligible Stokes shift and reveals a splitting $\Delta_{AB} \sim 210$ meV. For *MoSe*₂, contrary to *MoS*₂ we also observe trion T in PL. Like for *MoS*₂, we observe a weak photodoping effect which is visible in panel (b) through the small changes in intensities of X_A and T. Note also in this figure that the X_A transition linewidths as low as 3 meV are measured. In panel (c), it is also shown that the increase of the excitation power up to 50 μ W does not generate important change of the spectral shape.

These experimental results converge towards similar conclusions as the ones which were given about hBN encapsulation in the previous sections. A clear improvement of the spectral quality is revealed and inhomogeneous broadening is strongly lowered compared to samples on *SiO*₂ [188]. However we note that still the surface of the hBN-MBE of these samples presented some inhomogeneities, mainly due to inhomogeneities of the underly-

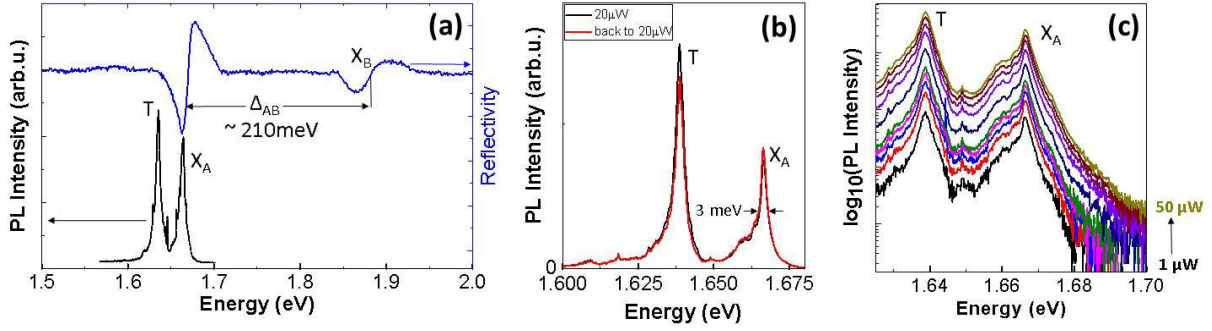


Figure 3.27: Different measurements performed on the hBN/*MoSe*₂ monolayer/hBN-MBE van der Waals heterostructure. **(a)** Comparison between PL and reflectivity measurements of the encapsulated *MoSe*₂. X_A and X_B denote the A and B-excitons and T denotes the trion, visible only in PL. **(b)** PL spectra recorded under 20 μW excitation before (black curve) and after (red curve) exposure up to 50 μW . **(c)** Power-dependent PL measurements with an excitation from 1 to 50 μW .

ing Ni layer which is polycrystalline with crystalline domains with typical micrometer-size diameters. Therefore the growth of homogeneous wafer-scale ultra-thin hBN films is still a challenge to be addressed in future experiments.

3.5 Conclusions

Optical spectroscopy experiments of hBN/TMD monolayers/hBN have shown that encapsulation in hexagonal boron nitride improves greatly the sample optical quality. Several major observations can be underlined.

Firstly, the inhomogeneous broadening is strongly reduced, even approaching the homogeneous limit of excitonic transitions. This allows to distinguish different excitonic transitions which overlap within broad peaks in non-encapsulated samples studied previously by the 2D community. It has also enabled us to measure valley Zeeman splitting of the order of 1 meV at moderate B fields of ± 9 T for *MoS*₂, where pulsed magnetic fields were needed before due to larger linewidth. The improvement of the spectral quality is especially visible for *MoS*₂ which presented spectrally broad features associated to localized states and bound excitons when deposited directly on *SiO*₂ [138, 49, 139, 48, 51, 140]. These broad peaks have now disappeared and the spectra are cleaner showing one intense main excitonic transition corresponding to the A:1s state.

Encapsulation also protects the samples from the environment and degradation. They are more stable, even after several cooldown cycles in cryostats or storage for several months. They also do not present the same photodoping behaviour which was observable for previous samples without encapsulation.

Encapsulated monolayers do not have the same doping level. The Fermi level is effectively lowered. For example, the effect is particularly clear for *MoSe*₂ monolayers. At this point, we speculate that a thick (>100 nm) bottom hBN layer prevents charge transfer from the *SiO*₂ to the monolayer.

All these improvements made possible the experiments shown in this chapter, especially the results obtained for exciton states in MoS_2 . Beyond that, it enabled us studying and identifying excitonic transitions such as trions [189] or dark excitons [34, 36], presented in the next chapters.

It has also been shown that we have to consider the influence of this new dielectric environment on the excitons in the TMD monolayer or on the overall samples optical response, through interferences in the heterostructure. Recently, some of our results have also shown that more intrinsic properties are impacted by hBN-encapsulation such as the exciton radiative lifetime [162]. By controlling the hBN thickness, we can tune the radiative lifetime from less than 1 to 10 ps.

Finally, it is also important to underline that progress is made in order to replace the widely used mechanical exfoliation with more industrially viable techniques such as Molecular Beam Epitaxy (MBE) [188]. We can imagine that in the future, the hBN/TMD monolayer/hBN will be grown with industrial techniques such as Chemical Vapor Deposition (CVD) [190], which would be highly desirable for future applications.

Chapter 4

Charge Tunable structures (MoS_2 , $MoSe_2$, WSe_2)

In this section we investigate charge tunable structures with different 2D TMDs as active materials. These samples enable changing the doping level of the semiconductor monolayer in order to investigate different regimes: intrinsic, p-doped and n-doped.

We will see that charge tunable structures bring additional information enabling the identification of excitonic states. Among these excitonic transitions, one of the clearest signatures of 2D TMD doping is the observation of charged excitons in the optical spectra.

Due to the different order of spin states in the conduction band for Mo-based as compared to W-based monolayers, the charged excitons (trions) observed in MoS_2 and $MoSe_2$ will be different from WSe_2 . This is due to a multitude of trion configurations as electrons can have different spin but also different valley quantum numbers.

4.1 Trions: three-particle bound states

In the previous chapters, the existence of two-particle bound states, excitons, has been highlighted on many occasions. The concept of these bound quasiparticles can be expanded to more complex bound states. Among them, we can cite trions. As it is explicit in their name, trions are composed of three particles: two electrons and one hole (X^-), or two holes and one electron (X^+) as shown in Fig 4.1. In contrast to excitons which are neutral quasiparticles, trions are charged quasiparticles.

Exciton binding energies in TMD monolayers are typically of the order of 200-400 meV, depending on the dielectric environment. The optical transitions associated with trions are typically 20 to 40 meV below the neutral exciton transitions. This energy difference is termed trion binding energy and we will present a detailed calculation in section 4.5.1.

We note that the trion picture is valid at low doping as it reproduces most of our experimental observations. At higher carrier densities the trion quasiparticle picture is replaced by the polaron picture [191]. In this many-body approach, excitons are immersed in a Fermi sea of electrons, interactions between excitons and these carriers lead to attractive or repulsive polarons as illustrated in Fig 4.1 for n doping.

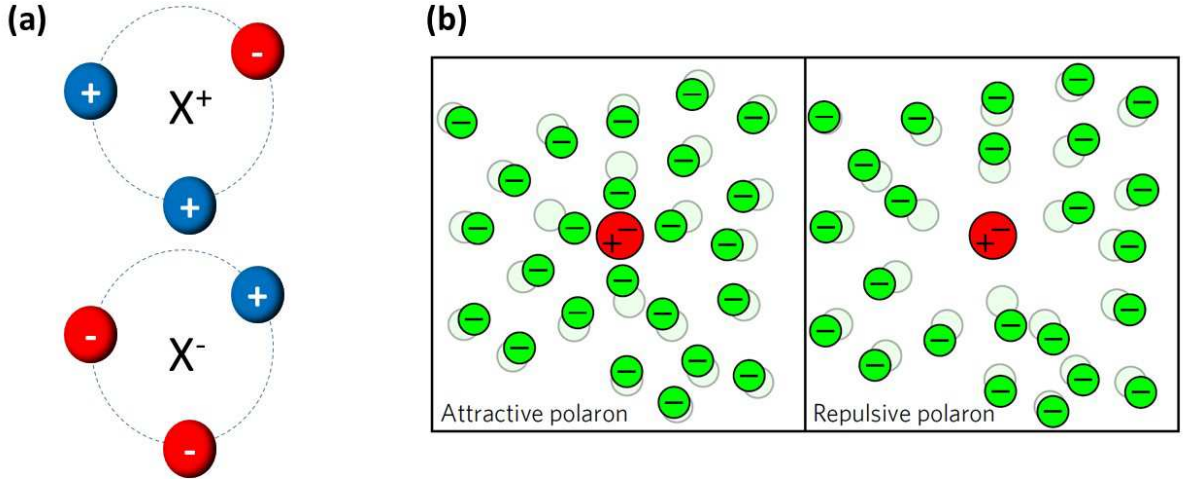


Figure 4.1: (a) X^+ is the positively charged trion. X^- is the negatively charged trion. (b) Excitons interacting with a cloud of electrons can lead to attractive or repulsive polarons. Figure extracted from [192].

4.2 Fabrication of charge tunable structures

To observe trions in TMD monolayers, it is possible to fabricate devices to control doping in the semiconductor. The fabrication and testing of devices with different designs and TMD materials were an important part of this thesis work. Basically, charge tunable structures enable injecting carriers in the semiconductor to change the doping level through application of a bias voltage. An example of such a structure is schematically represented in Fig 5.25 (a) with the corresponding optical microscope image of a real, working device in panel (b). In this case gold electrodes are pre-patterned on a SiO_2/Si substrate. Then layers can be transferred on the substrate using dry deterministic transfer methods presented in chapter 2. First bottom hBN is deposited, then the TMD monolayer (WSe_2 in the example of Fig 5.25), then a graphite layer is transferred to connect the WSe_2 to the gold electrode, and finally the top hBN is deposited on the WSe_2 . Like for samples in chapter 2, thermal annealing is performed between each layer deposition. In the example the silicon is used as a backgate but we can also use another pre-patterned electrode and a bottom graphite under the bottom hBN. We concentrate in this chapter on the samples that showed a clear optical response to the applied bias.

In the configuration of Fig 5.25, the electrodes were prepatterned and then the van der Waals heterostructure was fabricated. However it is also possible to fabricate the heterostructure in the first place and to pattern afterwards the electrodes as illustrated in Fig 4.3. We suspect that using such a method the contacts obtained are better than with pre-patterned electrodes. According to our experiments, this technique seems to increase stability of the samples. Indeed, we did not observe major fluctuations of trions intensity with time whereas for samples with pre-patterned electrodes the trion intensity decreases with time (especially in the p-doped regime). To understand and improve the quality of the devices, deeper studies of stability must be carried out, in the following we focus on the new physics that could be gleaned from working devices.

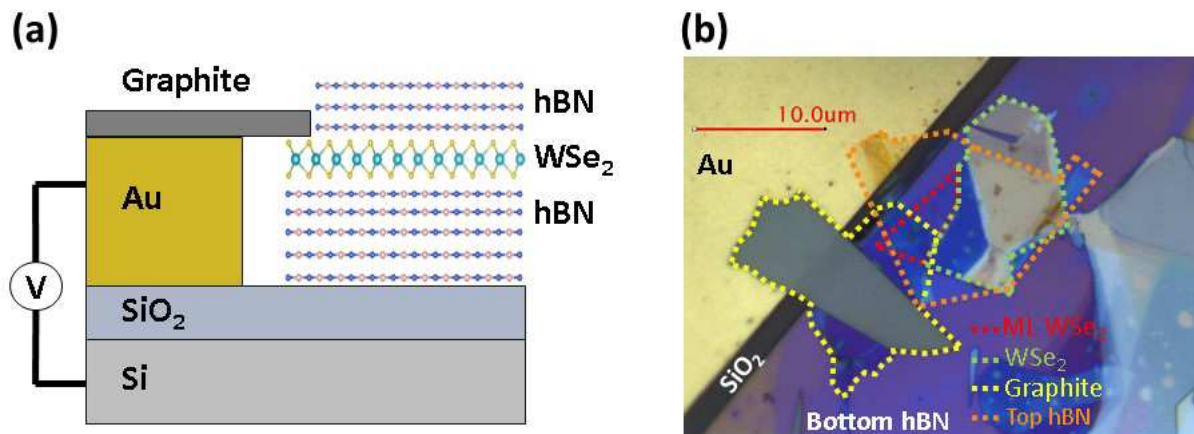


Figure 4.2: (a) Schematics of a hBN/ WSe_2 monolayer/hBN charge tunable structure. The WSe_2 monolayer is connected to the gold electrode with a graphite layer. The silicon serves as a backgate. Figure extracted from [189]. (b) Corresponding microscope image of the structure. Difference is made between the monolayer part highlighted by red dashed lines and the multilayer WSe_2 in green dashed lines.

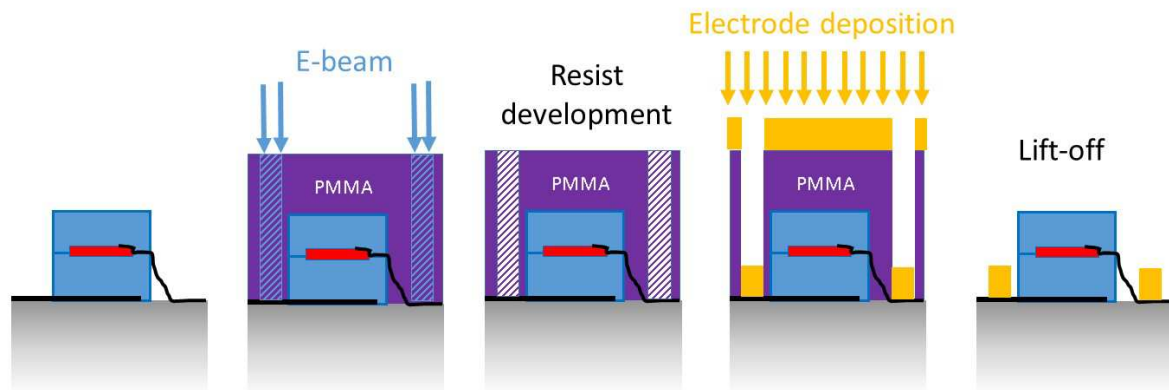


Figure 4.3: The different steps of a device fabricated using e-beam lithography. First the van der Waals heterostructure is fabricated using dry transfer methods as presented in chapter 2. Then PMMA is deposited on the structure by spin-coating and the PMMA is exposed to an electron beam (E-beam). After exposition the resist is developed; the parts exposed to the e-beam are dissolved in MIBK/IPA developer. The electrodes are deposited by metal evaporation. The remaining PMMA layer is removed during lift-off using acetone.

4.3 MoS_2 charge tunable structure

From the different TMD materials, MoS_2 monolayers showed particularly broad linewidth in non-encapsulated samples, with optical transitions with FWHM of 50 meV. This is why, following narrowing of the linewidth to a few meV in hBN, we processed the MoS_2 monolayer into a charge tunable structure. The device structure is as follows. Like in chapter 3, a MoS_2 monolayer was encapsulated in hBN with the techniques described in chapter 2. In addition the monolayer is connected to an electrode to inject carriers in the semiconductor and, therefore, to change its doping level.

In Fig 5.26 (a), a colorplot of the differential reflectivity is shown. The bias voltage is changed to tune the doping level between the neutral and n-doped regime. Fig 5.26 (b) shows two differential reflectivity spectra corresponding to the two regimes. In the neutral regime, neutral exciton A:1s, A:2s transitions and B:1s exciton are visible, with an energy separation of 155 meV between A:1s and B:1s which roughly corresponds to the spin-orbit splitting in the valence band (see Fig 1.16 in chapter 1). When electrons are injected into the structure, oscillator strengths of transitions associated to neutral A exciton decrease strongly. Even if A:1s state is still visible, the higher excited state A:2s totally disappears. This confirms further that A:2s is indeed a transition associated to neutral excitons, which was not clear at the beginning of this thesis work. Two transitions shifted to lower energies compared to A:1s and B:1s appear for n-doping. They are separated by 155 meV, which coincides with the A:1s-B:1s splitting. Thus, these two peaks are associated with negative trions of A and B excitons noted A^- and B^- .

Some earlier work from other groups also focused on studying different doping regimes of MoS_2 monolayers. Either with a same approach as the one exposed here, relying on electrodes [193] or using chemical dopants [194]. However, as pointed out in chapter 3, the optical quality of the non-encapsulated monolayers was not good enough to clearly distinguish between neutral and charged excitons. Deconvolution of the main photoluminescence peak around 1.9 eV was challenging as excitons, trions and defects transitions overlapped. Again, encapsulation in hBN improved the optical quality and was a crucial step forward.

Now, trion and exciton peaks are clearly resolved in our reflectivity experiment. The trion binding energy measured is 35 ± 10 meV, that is the energy difference between exciton and trion transitions. This can be compared to the neutral exciton binding energy of 220 meV measured for these structures. This trion binding energy is larger than the 20 meV measured in previous experiments on samples with considerably larger linewidth [193]. This large trion binding energy indicates that trions can still be addressed at room temperature. Recent measurements from other groups have also revealed the presence of negative trions in hBN-encapsulated MoS_2 [195]. Results on charge tunable MoS_2 monolayers confirmed for us that our samples with thick hBN bottom layers and without contacts are essentially charge neutral, as charge transfer from SiO_2 is suppressed and intrinsic doping seems to be negligible.

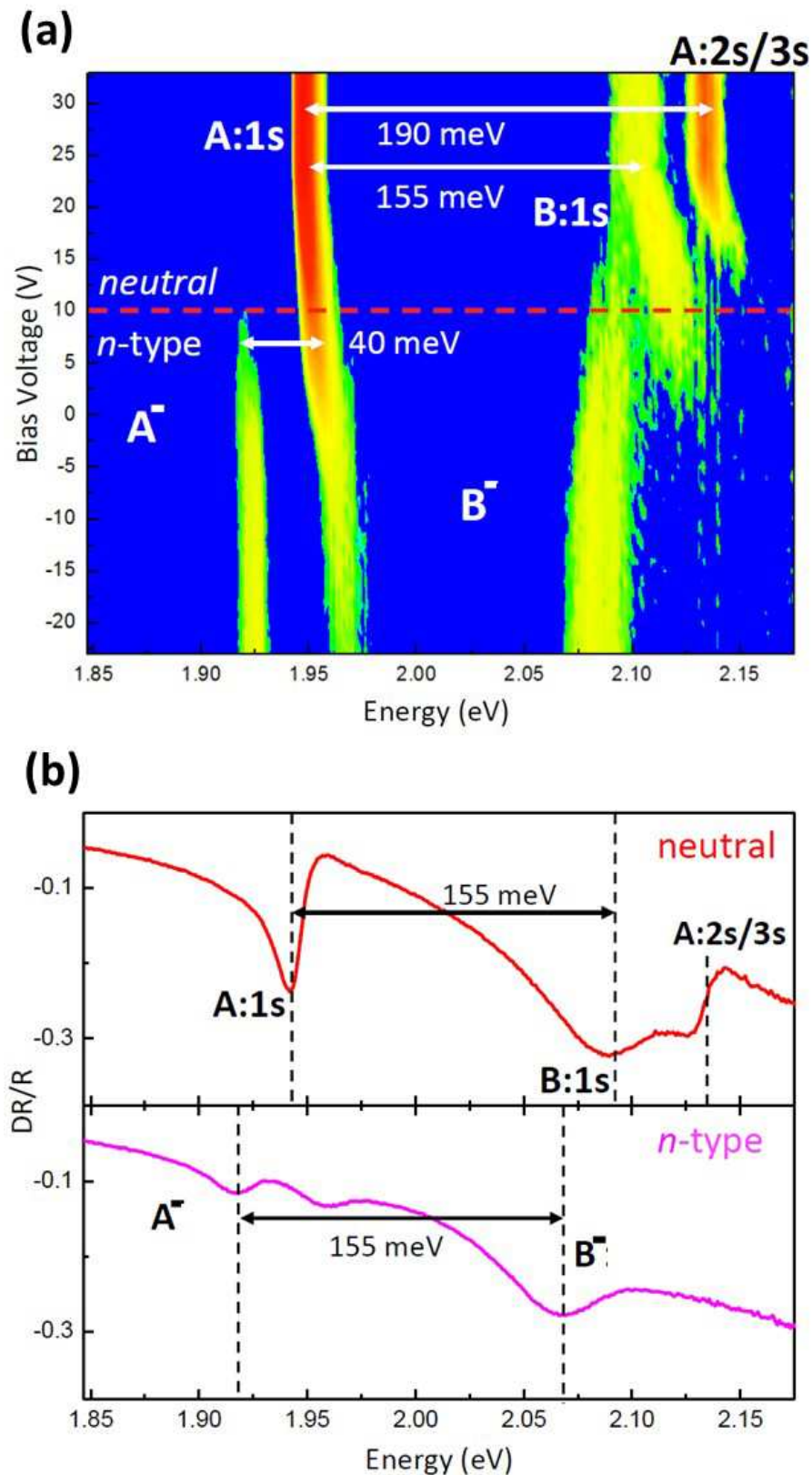


Figure 4.4: Encapsulated MoS_2 charge tunable sample at cryogenic temperature. (a) Colorplot of differential reflectivity DR/R as a function of bias voltage and energy. (b) Spectra of DR/R at two different voltages corresponding to two different doping levels. Figures extracted from supplement material of [181].

4.4 $MoSe_2$ charge tunable structure

As it was shown in chapter 3 in fig 3.8 (b), $MoSe_2$ monolayer PL spectrum at low temperature already presents two transitions which can be resolved. It was indeed one of the materials showing the best spectral quality even when the monolayer was deposited on SiO_2 without encapsulation. The lowest-energy transition was ascribed to negatively charged trions X^- due to intrinsic doping. Electrical control of doping confirmed the nature of this transition visible in PL. In Fig 5.27 (a) and Fig 4.6, at 0 V both trion (≈ 1.612 eV) and neutral exciton (≈ 1.638 eV) are visible. When we increase voltage (either positive or negative), the neutral exciton disappears and new transitions associated to positive trion X^+ and negative trion X^- appear clearly, showing that we access the p- and n-doped regimes. The binding energies measured are very close for X^+ and X^- : 26.6 and 26 meV respectively. At 0V, a peak at the same energy as the negative trion X^- suggests that the sample is n-doped, even when we don't apply any voltage. Note that for this sample we did not manage to reach a purely neutral regime as trion features never disappeared totally, which hints at intrinsic background doping in the layer.

Additional reflectivity measurements shown in Fig 5.27 (b) have also revealed the presence of X^+ and X^- with a similar binding energy around 27 meV. In comparison with PL data, at 0 V the neutral exciton A:1s exhibits a large oscillator strength whereas no trion feature is visible at this voltage, corresponding to the neutral regime. X^+ and X^- appear at positive and negative voltages respectively, but in our voltage range the neutral exciton A:1s never disappears fully in contrast to PL measurements of panel (a). Reflectivity shows transitions with large oscillator strength. This is not the case of PL where lower energy states are preferentially populated. That could explain why the trion transition which is at lower energy appears intense in PL but not in reflectivity.

As the so-called trion peak appears in PL even at (close to) zero doping, it can be questioned if this peak is indeed associated to charged excitons. Another scenario taking into account phonon replica could explain this high intensity of PL peak below the exciton, even at 0 V [196]. As shown in Fig 4.7 (a) and as initially hypothesized by Dery and Song, momentum-dark neutral excitons can be formed by associating a valence state in the K^+ valley (denoted K in the figure) and an electron in the opposite K^- valley (denoted K' in the figure) [197]. As illustrated in Fig 4.7 (b), it is possible to imagine different phonon-assisted radiative processes with different energies. In Fig 4.7 (c), a PL spectrum of neutral $MoSe_2$ is considered. In the absence of electron-hole exchange, the energy of the momentum-dark K_u^i exciton is resonant with the bright X exciton. By emitting an appropriate optical phonon A_1 , a phonon-assisted radiative process could explain the existence of the lower energy peak which is generally ascribed to trion even at 0 V in charge tunable structures. Using this model relying on phonon-assisted transitions, the fit in red is obtained, giving good agreement with the data. This simple scenario can be revised once the electron-hole Coulomb exchange terms are known in sign and amplitude, which is not the case at the moment.

We find similar trion binding energies of 26-27 meV in PL and reflectivity. This is close

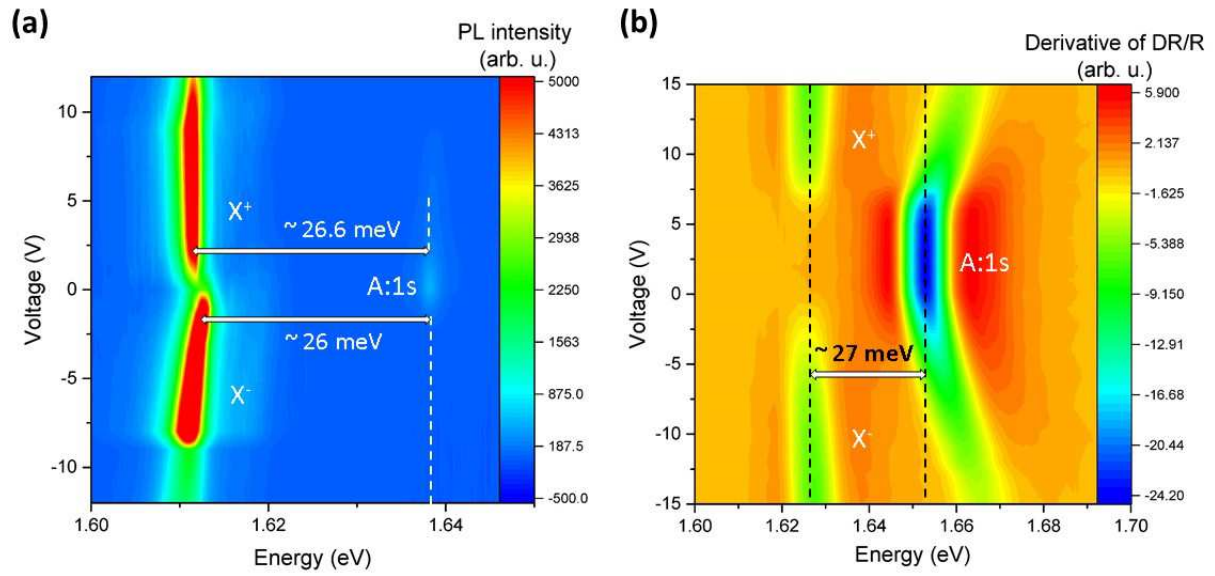


Figure 4.5: Encapsulated $MoSe_2$ monolayer charge tunable structure at cryogenic temperature. At positive voltage holes are injected in the monolayer whereas electrons are injected at negative voltages. (a) Photoluminescence as a function of energy and voltage. Trions X^+ and X^- are marked and the comparatively weak neutral exciton A:1s emission. (b) Derivative of differential reflectivity DR/R as a function of energy and voltage.

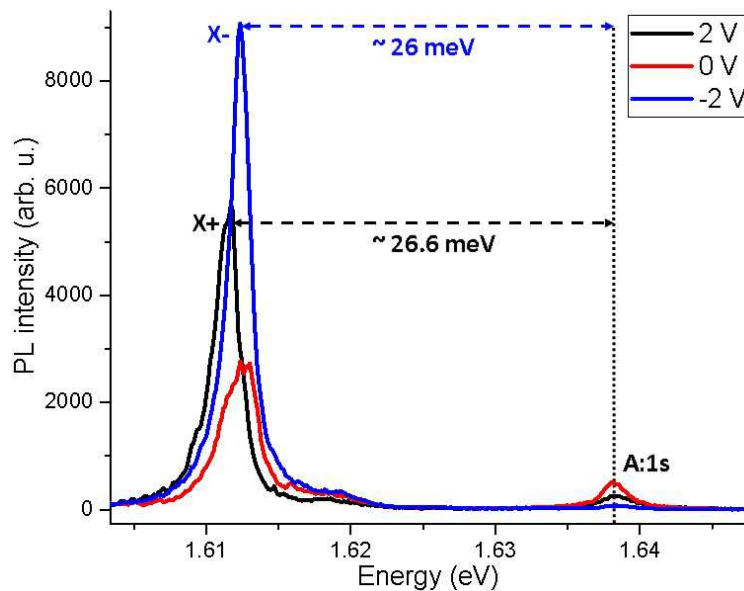


Figure 4.6: PL spectra at three different voltages: 2 V, 0 V and -2 V. The neutral exciton A:1s and both positive X^+ and negative X^- trions are visible.

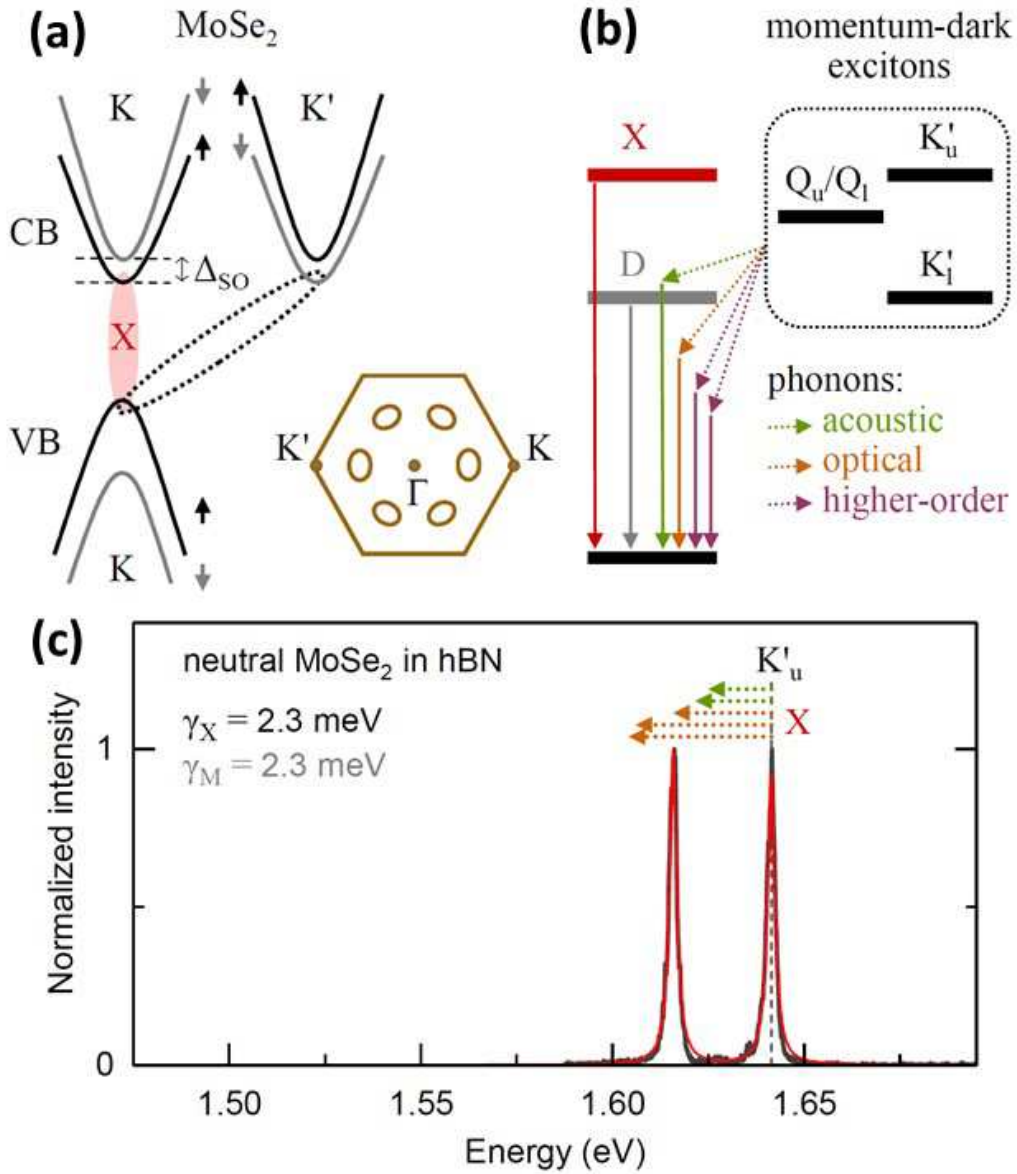


Figure 4.7: (a) Single-particle picture illustrating the possible momentum-dark transition between K (K^+) and K' (K^-) valleys, at opposite corners of the Brillouin zone. The bright exciton transition is represented in red. (b) Illustration of different transitions which could arise from phonon replicas of momentum-dark excitons from Q or K' valleys. The subscripts u and l mean "unlike" and "like" and refer to the spin-unlike or spin-like transitions. For instance, a K'_u transition is represented in (a) in dashed lines. (c) PL spectrum of an encapsulated $MoSe_2$ monolayer. In dashed lines are represented the energies of different phonons (acoustic and optical) which could explain the existence of a phonon replica of dark momentum transitions K' on the lower energy side of X transition. Figures extracted from [196].

to the one measured for unencapsulated samples [141] and identical values were measured in $MoSe_2$ encapsulated between hBN by other groups [198]. This can be compared to the neutral exciton binding of hBN encapsulated $MoSe_2$ that we measured to be about 190 meV [160]. At higher doping in Fig 5.27 (b), A:1s is blue-shifted and the energy separation between A:1s and trions increases. This can be explained by the many body effects evoked previously; we cannot consider anymore an exciton alone but an exciton in a 2D electron gas giving rise to repulsive polarons.

4.5 WSe_2 charge tunable structure

In this section we study a charge tunable structure made of an encapsulated WSe_2 monolayer. We will especially focus on the fine structure of trions which is now observable due to the great improvement of optical quality induced by hBN encapsulation.

4.5.1 Calculation of trion binding energies

First we present a model calculation for the X^+ and X^- binding energies, developed by our collaborators M. Semina and M. Glazov [189]. With a similar approach as the one presented for excitons in chapter one, the general wavefunction for a trion can be written [189]:

$$\Psi_{i,j,k}(\vec{K}_{trion}, \vec{R}) = \Omega^{-1/2} e^{i\vec{K}_{trion} \cdot \vec{R}} \phi^{env}(\vec{r}_i - \vec{r}_k, \vec{r}_j - \vec{r}_k) \phi_{ij}^{(2)}(\vec{r}_i, \vec{r}_j) \phi_k^{(1)}(\vec{r}_k) \quad (4.1)$$

where $\Omega^{-1/2}$ is a normalization factor, i, j designate the two identical carriers (two electrons or two holes) and k is the subscript for the third carrier (one hole or one electron). To these particles are associated the two-particles Bloch function $\phi_{ij}^{(2)}(\vec{r}_i, \vec{r}_j)$ and one-particle Bloch function $\phi_k^{(1)}(\vec{r}_k)$. $\phi^{env}(\vec{r}_i - \vec{r}_k, \vec{r}_j - \vec{r}_k)$ is the envelope function of the relative motion of the charge carriers in the trion. \vec{K}_{trion} is the wavevector of translational motion of the trion center of mass. \vec{R} is the position of the trion center of mass given by:

$$\vec{R} = \frac{m_1(\vec{r}_i + \vec{r}_j) + m_2 \vec{r}_k}{2m_1 + m_2} \quad (4.2)$$

with m_1 the mass of the 2 identical carriers and m_2 the mass of the third one.

One difference compared to the exciton wavefunction is that the trion wavefunction must be antisymmetric. The two-particles Bloch function $\phi_{ij}^{(2)}$ can be written as a symmetric or an antisymmetric combination of the two single particle Bloch functions:

$$\phi_{ij}^{(2)}(\vec{r}_i, \vec{r}_j) = \frac{1}{\sqrt{2}} \begin{cases} \phi_i(\vec{r}_i) \phi_j(\vec{r}_j) - \phi_i(\vec{r}_j) \phi_j(\vec{r}_i) \\ \phi_i(\vec{r}_i) \phi_j(\vec{r}_j) + \phi_i(\vec{r}_j) \phi_j(\vec{r}_i) \end{cases} \quad (4.3)$$

For the top line of Eq 4.3, the envelope function ϕ^{env} must be symmetric and it is antisymmetric for the bottom line of Eq 4.3. The trions will be qualified as symmetric if ϕ^{env} is symmetric and inversely they will be qualified as antisymmetric if ϕ^{env} is antisymmetric.

Like for the exciton, by solving the Schrödinger equation for the envelope function ϕ^{env} , it is possible to calculate the trion binding energies. In an effective mass approach, the general form of the Hamiltonian for a trion can be written:

$$H_{tr} = \frac{-\hbar^2 \nabla_i^2}{2m_i} + \frac{-\hbar^2 \nabla_j^2}{2m_j} + \frac{-\hbar^2 \nabla_k^2}{2m_k} + V(|\vec{r}_i - \vec{r}_k|) + V(|\vec{r}_j - \vec{r}_k|) + V(|\vec{r}_i - \vec{r}_j|) \quad (4.4)$$

After transforming the Hamiltonian to its relative coordinates form [199, 200, 189]:

$$H_{tr} = -\frac{\hbar^2}{2\mu} \left(\Delta_1 + \Delta_2 + \frac{2\sigma}{\sigma+1} \nabla_1 \nabla_2 \right) + V(|\vec{\rho}_1|) + V(|\vec{\rho}_2|) - V(|\vec{\rho}_1 - \vec{\rho}_2|) \quad (4.5)$$

where $\vec{\rho}_{1,2} = \vec{r}_{i,j} - \vec{r}_k$ are notations for the relative positions of identical carriers (i and j) compared to the third carrier (k). $\Delta_{1,2}$ and $\nabla_{1,2}$ are the Laplacian and gradient operators acting on functions of relative motions $\rho_{1,2}$. $\mu = m_e m_h / m_e + m_h$ is the reduced mass of the electron-hole pair and $\sigma = m_{i,j} / m_k$ is the ratio of effective mass of one of the identical carriers over the effective mass of the nonidentical one. Therefore, for a positive trion X^+ , $m_{i,j} = m_h$ and $m_k = m_e$ whereas for a negative trion X^- , $m_{i,j} = m_e$ and $m_k = m_h$ with m_e and m_h the effective masses of electrons and holes. The term $\propto \nabla_1 \nabla_2$ accounting for a finite mass ratio σ is known as the Hughes-Eckart term in the theory of atoms and molecules. V is the interaction potential corresponding to the direct electron-hole interaction. As shown in chapters 1 and 3 a Rytova-Keldysh interaction potential V is taken when studying our semiconductor monolayer systems, instead of the ideal 2D Coulomb potential.

To calculate the binding energies of symmetric trions, the following trial function is used for ϕ^{env} [189]:

$$\phi_{sym}^{env}(\vec{\rho}_1, \vec{\rho}_2) \propto \frac{\exp(-|\vec{\rho}_1|/a_1 - |\vec{\rho}_2|/a_2) + \exp(-|\vec{\rho}_1|/a_2 - |\vec{\rho}_2|/a_1)}{1 + d(|\vec{\rho}_1 - \vec{\rho}_2| - R_0)^2} \times (1 + c|\vec{\rho}_1 - \vec{\rho}_2|) \exp(-s|\vec{\rho}_1 - \vec{\rho}_2|) \quad (4.6)$$

where a_1, a_2, c, d, R_0 and s are trial parameters. For antisymmetric trions, the trial function, orthogonal to Eq. 4.6 takes the form [189]:

$$\phi_{antisym}^{env}(\vec{\rho}_1, \vec{\rho}_2) \propto |\vec{\rho}_1 - \vec{\rho}_2| e^{i\theta_{12}} \phi_{sym}^{env}(\vec{\rho}_1, \vec{\rho}_2) \quad (4.7)$$

where θ_{12} is the angle of vector $\vec{\rho}_1 - \vec{\rho}_2$ with an in-plane axis and $\phi_{sym}^{env}(\vec{\rho}_1, \vec{\rho}_2)$ is introduced in Eq. 4.7.

Similarly to the exciton which was modeled, in a first approximation, as an hydrogen atom H , X^+ and X^- trions can be modeled as H_2^+ and H^- ions respectively [201, 202, 203]. The trial wavefunction above comprises these two limiting cases. The part $(\exp(-|\vec{\rho}_1|/a_1 - |\vec{\rho}_2|/a_2) + \exp(-|\vec{\rho}_1|/a_2 - |\vec{\rho}_2|/a_1)) \times (1 + c|\vec{\rho}_1 - \vec{\rho}_2|)$ is the function used to describe H^- ion, called Chandrasekar wave. The factors $\exp(-s|\vec{\rho}_1 - \vec{\rho}_2|)$ and $1 + d(|\vec{\rho}_1 - \vec{\rho}_2| - R_0)^2$ account for the other limiting case corresponding to the H_2^+ molecule.

In the following parts for comparing with our measurements, only symmetric trions are considered. In Fig 4.8, binding energies are plotted as a function of screening radius r_0 and the electron-to-hole effective mass ratio $\sigma = m_e/m_h$.

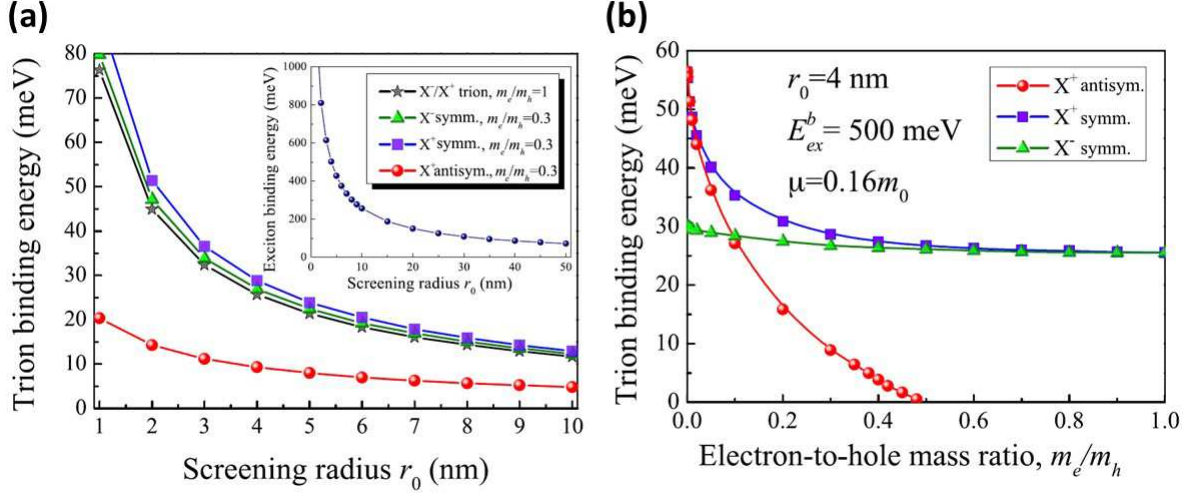


Figure 4.8: (a) Binding energies of the X^+ and X^- trions for several effective mass ratios at a fixed reduced mass $\mu=0.16 m_0$, $\epsilon^*=1$ (the effective dielectric constant taken in the Rytova-Keldysh potential). Inset shows the exciton binding energy as a function of the screening radius r_0 . (b) Trion binding energies as a function of the effective mass ratio σ at a fixed reduced mass $\mu=0.16 m_0$ and the screening radius $r_0=40 \text{ \AA}$, $\epsilon^*=1$ (the effective dielectric constant taken for simplicity in the Rytova-Keldysh potential), E_{ex}^b is the exciton binding energy. Figures extracted from [189].

We note in panel (a) that the screening radius r_0 has a big influence both on the trion binding energy and on the exciton binding energy (see inset). However, the orders of magnitude of binding energies are clearly different between the two quasiparticles. In agreement with previous works [27, 184, 204, 205], calculations give binding energies in the range of 100 to 1000 meV for excitons and 10 to 100 meV for trions. In panels (a) and (b), we see that when $\sigma=1$ binding energies for negative and positive trions are identical, however for $\sigma < 1$, we expect higher binding energies for the positive trion X^+ which is composed of holes, heavier particles compared to electrons in standard semiconductors like GaAs. Therefore in our experiments we would expect X^+ to be at lower energy compared to X^- . We will see that it is not the case and will try to explain why. Please note that at the time of writing only very few experimental values for m_e and m_h are reported, which is why we calculate for completeness the energies as a function of m_e/m_h .

Note also that this calculation does not reflect the trion fine structure which will be studied in the following paragraphs.

4.5.2 Spectroscopy and charge tuning

Optical spectra of WSe_2 monolayers reveal a very rich structure with different peaks which need to be identified. This is highlighted in Fig 4.9, which shows a PL spectrum of a WSe_2 monolayer. Using a charge tunable structure, we will try to identify trion features in this forest of peaks.

In order to identify optical transitions associated to trions, a charge tunable structure has been designed and fabricated. The Fig 4.10 shows voltage dependent PL spectra with a color plot in panel (a) and in panel (b) three spectra illustrating neutral, p- and n-doped

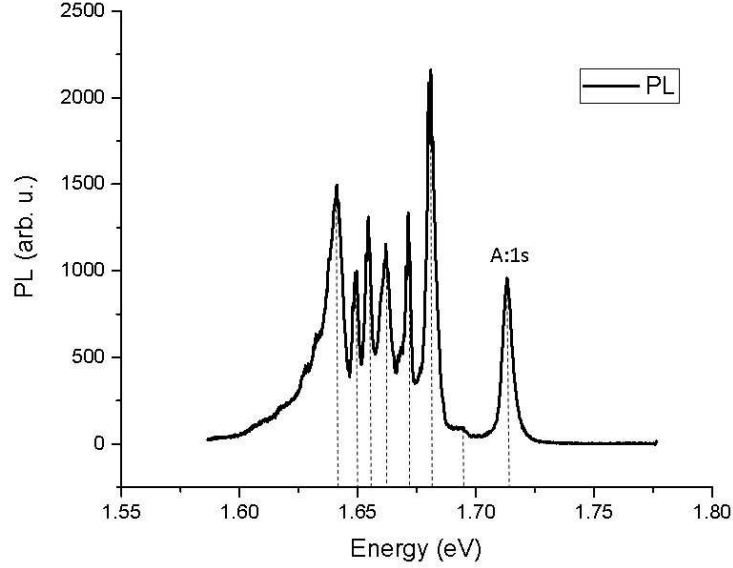


Figure 4.9: A PL spectrum of an encapsulated WSe_2 monolayer excited with a HeNe laser (1.96 eV) at an averaged power of $2 \mu W$. The excitation spot diameter is about $1 \mu m$. Integration time of 10 s. Temperature $T=10$ K.

regimes. In panel (b), energy difference between A:1s and trion peaks are indicated. These energies correspond to the trion binding energies. For the positive trion, one peak appears, the binding energy is $E_B^{tr}(X^+) \approx 24$ meV. For the negative trion, we have two different peaks with different binding energies: $E_B^{tr}(X_1^-) \approx 30.5$ meV and $E_B^{tr}(X_2^-) \approx 37$ meV.

We also observe the trions in reflectivity measurements. Please note that as soon as we see transitions in reflectivity or absorption in the n-type regime, the polaron concept is more powerful than the simple 3-particles trion description, which we can use for very low doping as stated before. The data shown in Fig 5.28 are from another WSe_2 charge tunable sample. They confirm the results presented in PL measurements in Fig 4.10. In the p-doped regime, only one additional peak appears corresponding to the positive trion X^+ ; its measured binding energy is $E_B^{tr}(X^+) \approx 21$ meV. In the n-doped regime, a doublet is visible with two different binding energies of $E_B^{tr}(X_1^-) \approx 29$ meV and $E_B^{tr}(X_2^-) \approx 35$ meV.

Analysing this consistent data from different samples obtained in small step voltage scans, and focusing on trions, two main observations deserve our attention. Two peaks appearing in the n-doped regime separated by 7 meV can be ascribed to negative trions. The positive trion has a lower binding energy than the negative one, in contrast to theoretical predictions of part 4.5.1. In the following paragraphs we analyse these experimental observations.

4.5.3 Trion fine structure

Trions are composed of three particles. To get a deeper understanding of trions, it is relevant to consider which valleys in momentum space are occupied by the different particles.

First we consider X^+ trions at the K-valleys which are composed of two holes and one electron. Due to the large spin-orbit splitting in the valence band (~ 500 meV) for WSe_2 monolayers, the two holes relevant here occupy the highest valence bands in K^+ and K^-

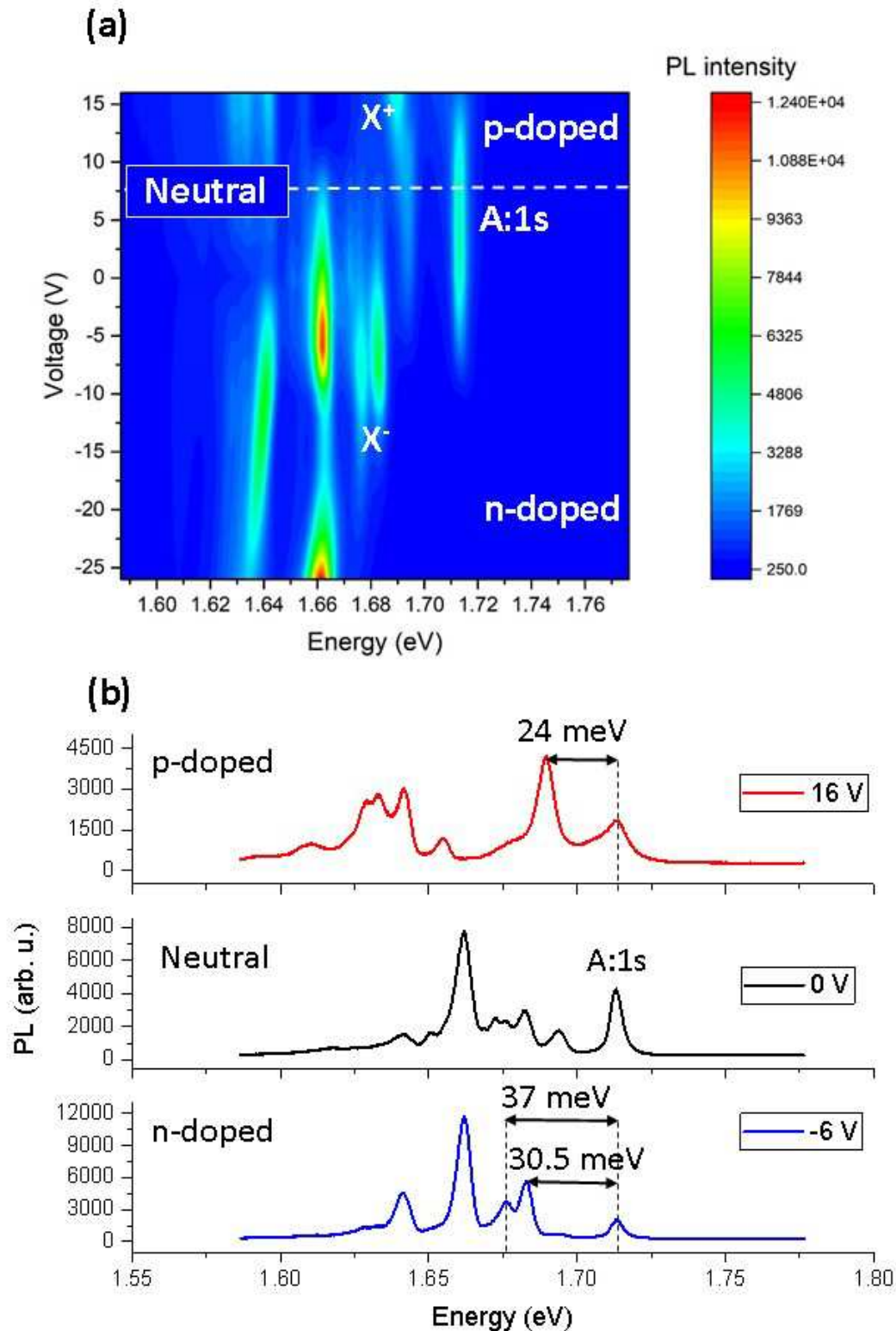


Figure 4.10: PL spectroscopy with HeNe laser as excitation source. Excitation spot diameter of $50 \mu\text{m}$. Averaged excitation power of $50 \mu\text{W}$. Temperature $T=10 \text{ K}$. **(a)** Color plot of PL spectra as a function of energy in abscissa and voltage in ordinate. The three doping regimes (neutral, n-doped and p-doped) are visible. A:1s is the neutral exciton transition. X^+ and X^- are respectively positive and negative trion transitions. **(b)** Three line cuts of the color plot at three different voltages showing the three doping regimes. Energy differences between neutral exciton A:1s and trions (positive and negative) are indicated.

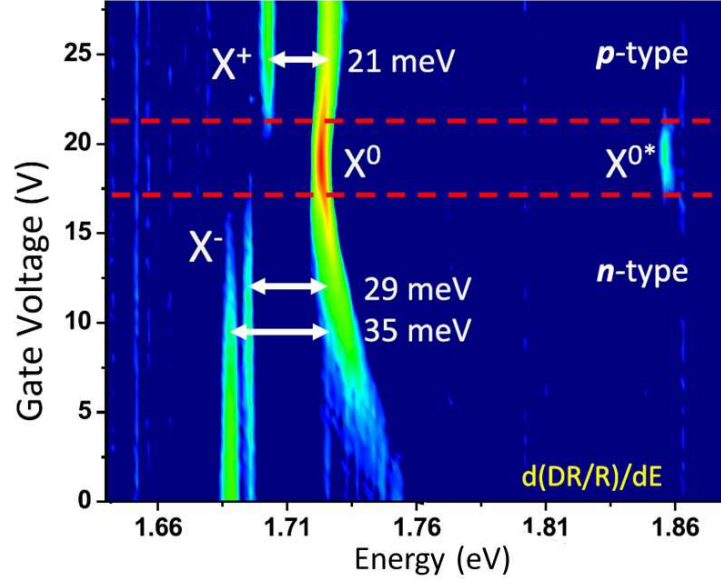


Figure 4.11: Derivative of differential reflectivity (DR/R) as a function of Energy in abscissa and Gate Voltage in ordinate for an encapsulated WSe_2 charge tunable structure at cryogenic temperature. X^0 is the neutral exciton (A:1s), X^{0*} is an excited state of neutral exciton. X^+ and X^- are respectively positive and negative trions. Figure extracted from [189].

valleys. However, as the spin-orbit splitting is smaller in conduction band (~ 40 meV), the electron has four different possibilities. Fig 5.29 illustrates two positive trions: one configuration is spin-forbidden and therefore is optically dark and another configuration is spin-allowed and is optically active (bright).

If the electron of the bright trion is in the K^+ valley, it emits σ^+ -polarized light, but it emits σ^- -polarized light when the electron occupies the K^- valley. The different configurations possible for X^+ are summarized in table 5.3, as the electrons are characterized by two quantum numbers, the spin index s_e and the valley index τ_e .

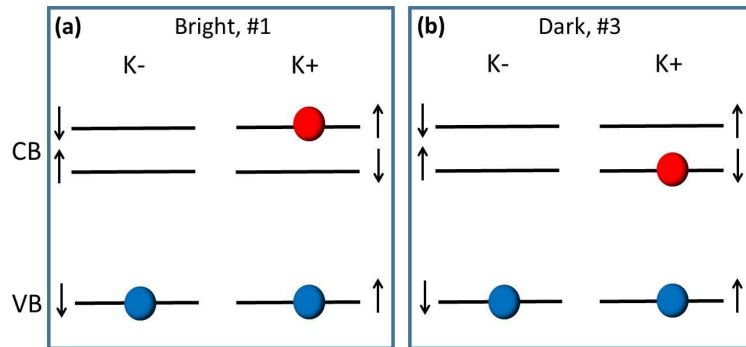


Figure 4.12: WSe_2 positive trions X^+ . (a) Bright trion (spin-allowed) with electron in K^+ valley. (b) Dark trion (spin-forbidden) with electron in K^+ valley. Only spin-conserving transitions are optically active.

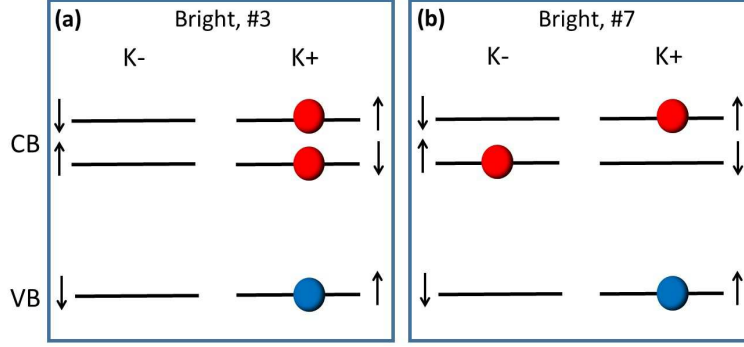


Figure 4.13: WSe_2 negative trions X^- . (a) Schematics representing an intravalley trion. (b) Schematics representing an intervalley trion.

#	s_e	τ_e	Bright/Dark
1	+1/2	+1	Bright (σ^+)
2	-1/2	-1	Bright (σ^-)
3	-1/2	+1	Dark
4	+1/2	-1	Dark

Table 4.1: Symmetric X^+ trion states. The electron state is characterized by its spin index (s_e) and its valley index (τ_e).

For negative trions X^- the situation is more complicated. It is composed of one hole and two electrons. Basically, the hole has two possibilities, it can be in K^+ or in K^- in the upper valence band corresponding to $\tau_h = \pm 1$. Then the two electrons have $\binom{2}{4} = 6$ possibilities for s_e/τ_e combinations. In total there are $2 \times 6 = 12$ different configurations for the negative trion. Four of them are represented in Fig 5.30.

The 12 different configurations are summarized in the table 5.4.

#	s_1	τ_1	s_2	τ_2	τ_h	Bright/Dark
1	+1/2	+1	-1/2	-1	+1	Bright (σ^+)
2	+1/2	+1	-1/2	-1	-1	Bright (σ^-)
3	+1/2	+1	-1/2	+1	+1	Bright (σ^+)
4	+1/2	-1	-1/2	-1	-1	Bright (σ^-)
5	+1/2	+1	-1/2	+1	-1	Dark
6	+1/2	-1	-1/2	-1	+1	Dark
7	+1/2	-1	+1/2	+1	+1	Bright (σ^+)
8	-1/2	-1	-1/2	+1	-1	Bright (σ^-)
9	+1/2	-1	+1/2	+1	-1	Dark
10	-1/2	-1	-1/2	+1	+1	Dark
11	-1/2	+1	+1/2	-1	+1	Dark
12	-1/2	+1	+1/2	-1	-1	Dark

Table 4.2: Symmetric X^- trion states. The two electrons e_1 and e_2 are characterized by their spin indices (s_1 and s_2) and their valley indices (τ_1 and τ_2). The hole state is given by its valley index τ_h (its spin index is deduced immediately).

Situations for X^+ and X^- are very different. Considering the two bright states for X^+ , we understand easily that these two states are equivalent energetically, the only difference is that in one case the electron is in K^+ and in the other case it is in K^- . For X^- , bright states can be intrinsically quite different, like panels (a) and (b) in Fig 5.30. We can distinguish between intravalley negative trions for which all particles are in the same valley and the intervalley negative trions for which particles occupy both valleys K^+ and K^- . These two kinds of trions have different binding energies and give rise to the two negative trion transitions observable in Fig 4.10 and 5.28, separated by 7 meV.

The existence of these two types of trions in WSe_2 was discussed for the first time by Yu et al. [206]. Experimental observations in PL [207] or in pump-probe measurements [208] already reported these two trion states. Similarly in broad PL spectra of WS_2 monolayers [209]. However these older studies needed deconvolution and fitting procedure to deduce the existence of the two trion peaks from the spectra. In the present experiment described in this section, the two trion peaks are resolvable in PL and reflectivity without any deconvolution procedure. Again, we take advantage of the great optical quality of TMD monolayers encapsulated in hBN heterostructures as explained before in chapter 3.

Now, the question is: how can we explain that we have two negative trion transitions separated by 7 meV? The idea is summarized in Fig 4.15. To explain the difference of binding energy between inter and intravalley trions, the short-range electron-electron and electron-hole exchange interaction must be taken into account. As explained in [189], an effective hamiltonian needs to be used to model the exchange interaction. Unfortunately, at this point we do not know the sign of the Coulomb exchange terms separating inter- and intravalley trions, we can therefore not determine which of these transitions is at lower or higher energy, respectively. The full inclusion of the Coulomb exchange interaction in binding energy calculations should also bring an answer to the question concerning the lower binding energy of the positive trion.

We note that we only observed one negative trion in the case $MoSe_2$ monolayer, see our measurements in Fig 5.27 and 4.6. In this material the sign of the spin-orbit splitting in the conduction band is opposite to WSe_2 . As illustrated in Fig 4.14 when a photon excites the material an electron-hole pair is generated between the top of the valence band and the lowest energy state in the conduction band. At low temperature the electrons injected by applying a voltage occupy the lowest energy states in the conduction band. So only intervalley trions form as the electron states at higher energies in the conduction band are not occupied. This is indeed different from WSe_2 in which we populate these higher energy states when the material is excited with light.

4.5.4 Neutral and charged biexcitons

In this chapter we focused on trions, but higher order bound complexes have been reported and can be seen in our measurements. Indeed if we consider reflectivity spectra in Fig 5.28, the different transitions have been identified, however in PL shown in Fig 4.10, spectra are richer and several peaks still need to be identified. Under strong excitation ($\sim 4 \times 10^3 \text{ W.cm}^{-2}$) optical signatures of four- and five-particle complexes have been reported [210, 211]. They are respectively called biexcitons XX^D and charged biexcitons

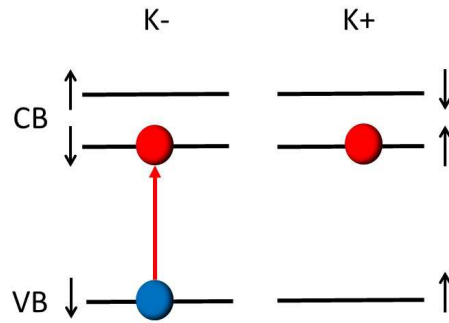


Figure 4.14: Illustration of an example of a trion in a $MoSe_2$ monolayer. A resident electron is present in the $K+$ valley, in the lowest energy state available. A photon generates an electron-hole pair in the other valley ($K-$). A trion is then created by these 3 particles.

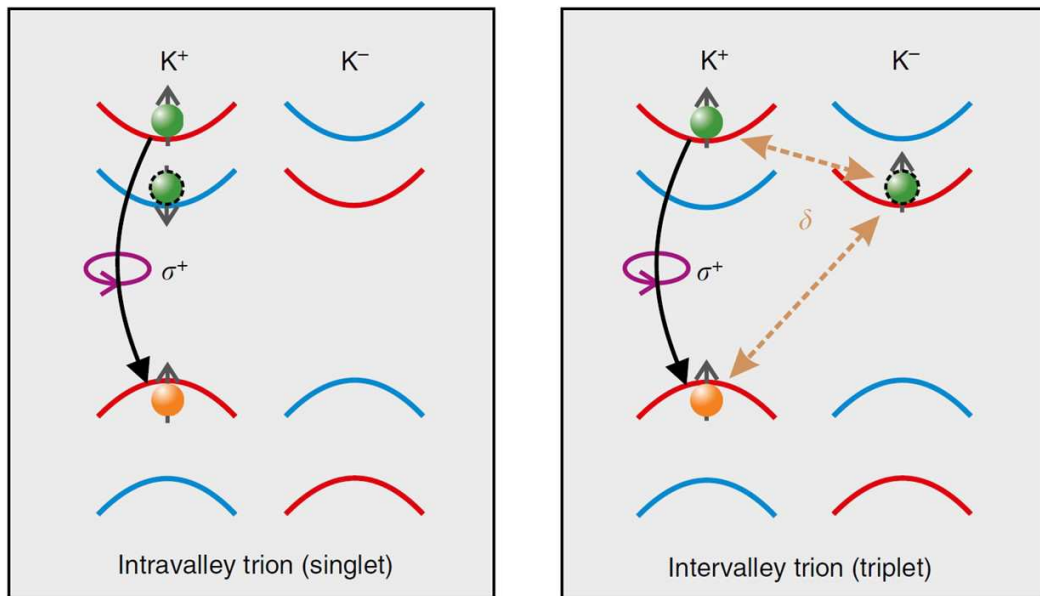


Figure 4.15: Representation of inter- and intravalley negative trions (two electrons and one hole) in tungsten compounds, also named singlet and triplet configurations. Dashed arrows schematize the intervalley electron-hole interaction giving rise to a splitting δ between intervalley and intravalley trions. Figure extracted from [209].

XX^- or quintons. Comparison of our data with [210] is presented in Fig 4.16.

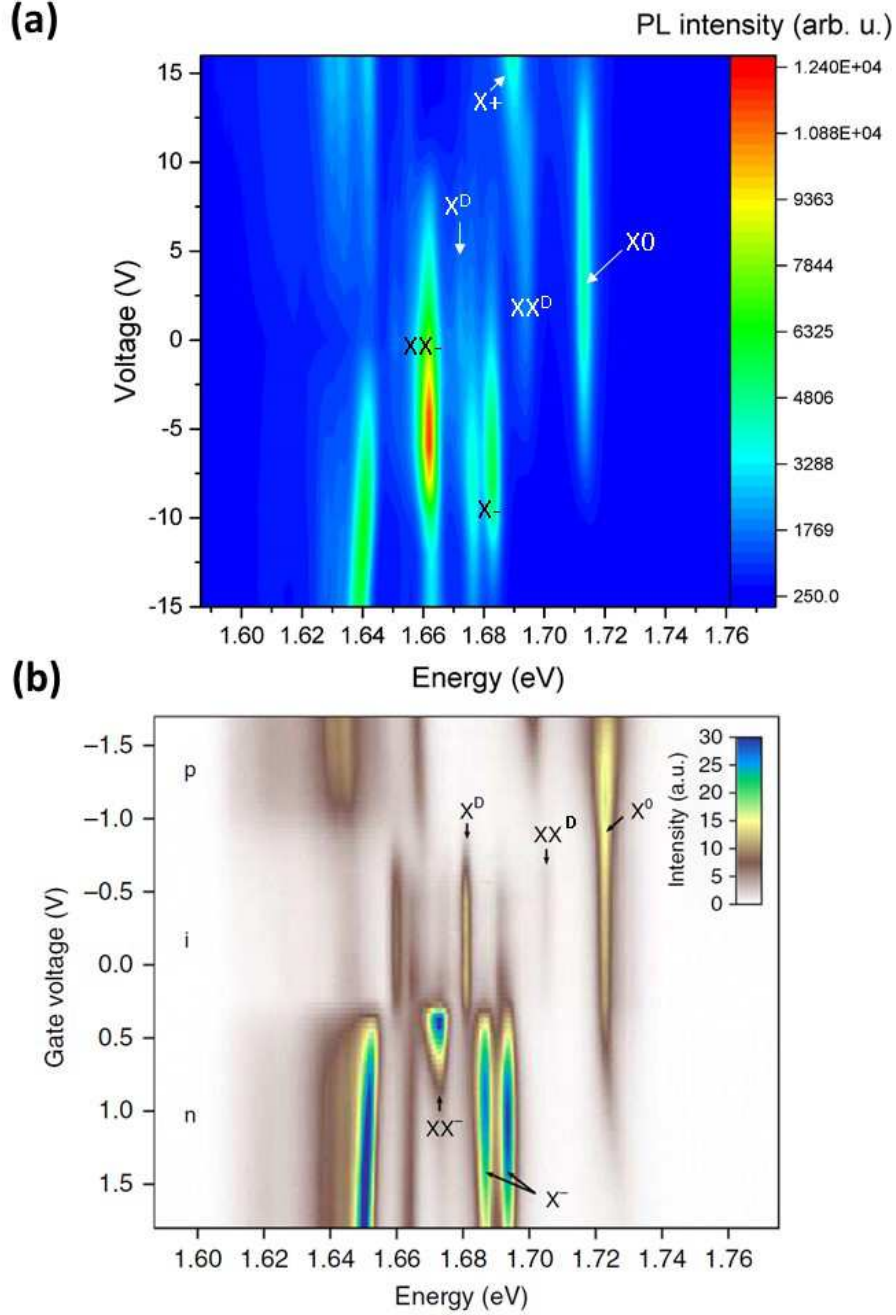


Figure 4.16: (a) Data obtained with one of our charge tunable structure at cryogenic temperature [LPCNO, unpublished]. (b) Data from [210]. The spectra are very similar even if our sample already shows some n-doping signatures at 0 V.

Our data also show signatures of XX^D and XX^- . The identity of these features has been confirmed in power dependent PL measurements which have shown that the XX^D peak increases quadratically with power [210, 211], as it is expected for such quasiparticles [212]. The charged biexciton XX^- also shows a superlinear increase with power. This contrasts with the linear behaviour of neutral excitons X^0 . Fig 4.17 shows power dependent PL measurements performed with our own sample. The neutral exciton X^0 (A:1s), biexciton XX^D and quinton XX^- are labelled. Panel (b) presents the evolution of the

integrated intensity as a function of power for these three species. We indeed find a superlinear behaviour for XX^D and XX^- and the X^0 is closer to a linear behaviour. As was the case of trions, also a multitude of biexciton states exist due to different valley and spin combinations. Biexcitons can be formed by different combinations of bright and dark excitons. The biexcitons observed in our experiment are formed from the association of a dark exciton X^D with a bright one X^0 . Moreover, the biexciton transition XX^D is only visible when both bright exciton X^0 and dark one X^D exist in the spectra. Due to the long lifetime of X^D of 100 ps compared to 1 ps for the bright, the formation of XX^D is more likely. The configuration of a bright-bright biexciton is unlikely because of the short lifetime of bright excitons. The configuration dark-dark also does not fit with experimental results as a negative binding energy (anti-binding) would be expected for such a configuration. Further analysis using strong out-of-plane magnetic fields have confirmed that bright and dark excitons constitute XX^D . This can be gleaned from the different g-factor we measured for bright (-4.25 ± 0.01) and dark (-9.4 ± 0.1) excitons [36].

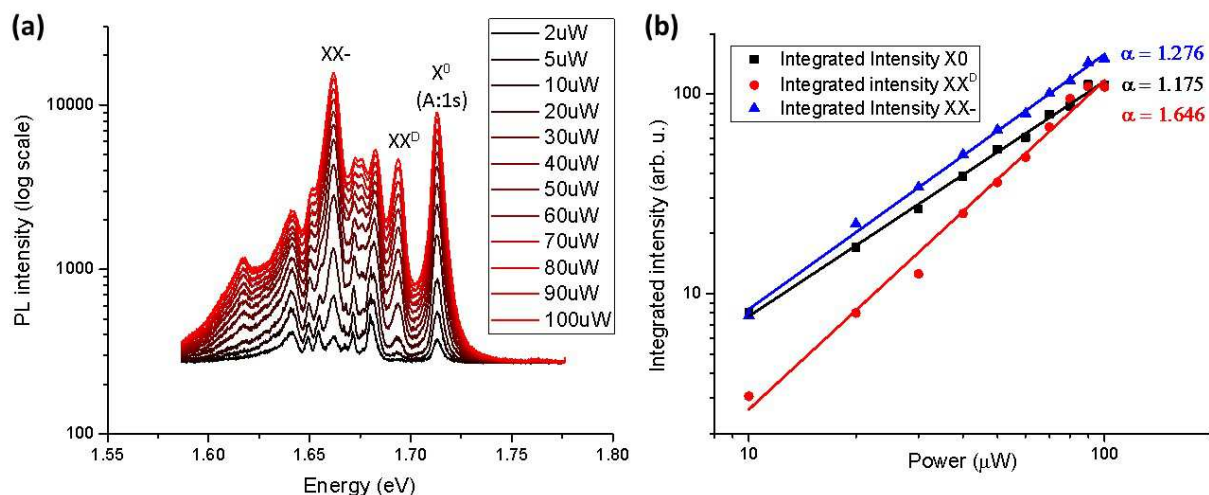


Figure 4.17: **(a)** PL spectra with increasing powers at cryogenic temperature. Some of the peaks saturate while others dominate the spectra. The neutral exciton X_0 (A:1s), biexciton XX^D and charged biexciton XX^- are labelled. **(b)** Different evolution of intensity with power (logarithmic scales) for the A:1s exciton, the biexciton XX^D and the negatively charged biexciton XX^- .

If the biexciton can be seen as the association of a dark exciton with a bright one, the quinton XX^- is formed from a trion and a neutral exciton. Due to the high spin-orbit splitting in the valence band, no positively charged biexciton XX^+ was observed. As can be seen from the results on charge tunable samples, still many exciton complexes and their dynamics need to be studied and our group at the LPCNO is now performing measurements on charge tunable devices stable in time for many days of measurements in magneto-optics and time-resolved PL setups.

4.6 Conclusions

Table 4.3 below gives a summary of the binding energies of the charged excitons measured from the data reported in this chapter. Comparatively, the binding energies measured for the neutral exciton are also indicated.

Material	E_B negative trion	E_B positive trion	E_B neutral exciton
MoS_2	40 meV	-	220 meV [181]
$MoSe_2$	26 meV	27 meV	190 meV [160]
WSe_2	29 and 35 meV	21 meV	161 meV [213]

Table 4.3: Table summarizing binding energies measured for trions from the data reported in this chapter. For comparison, values measured for the neutral exciton are also given.

The fabrication of charge tunable devices led us to the study of doping regimes in different 2D materials: MoS_2 [181], $MoSe_2$ [196] and WSe_2 [189]. The improvement of spectral quality by encapsulation has a strong impact on our measurements, especially in the case of MoS_2 and WSe_2 . In addition to excitons, we have seen that three-particle complexes can form in these semiconductor nanostructures. These quasiparticles, called trions, have optical signatures visible in PL. Positive X^+ and negative X^- trions appear in p-doped and n-doped regimes respectively. For encapsulated MoS_2 we only observed negative trions due to technical limitations in our device, whereas for WSe_2 and $MoSe_2$ we observed both X^+ and X^- . Surprisingly, the X^+ trion has a lower binding energy compared to X^- whereas we would expect that the trion comprised of heavier particles should exhibit a higher binding energy. This could mean that electrons in this material have larger effective masses than holes. Recent measurements have shown that the effective masses are indeed large [214, 215] however, such an approach is not sufficient to explain the difference in binding energy between X^+ and X^- . A more complete theoretical approach taking into account the details of the Coulomb exchange terms needs to be developed in the future.

For MoS_2 , observation of both A^- and B^- trions associated to A and B excitons was clearly evidenced for the first time. The disappearance of A:2s/3s in doped regime accompanying the reduction of the A:1s intensity is another argument underpinning their identification as excited states of the neutral A exciton in addition to our recent confirmation in magneto optics [174].

Concerning WSe_2 , charge tunable structures made possible the clear identification of positive trion X^+ and also of negative intervalley and intravalley trions X^- . This situation is different from $MoSe_2$ for which only intervalley trions form due to the spin order in the conduction band. The three doping regimes (p-doped, neutral and n-doped) are observable both in reflectivity and in PL. Higher order bound complexes such as biexcitons XX^D and quintons XX^- have been distinguished thanks to charge tuning. Still several transitions need to be clearly identified in the complex WSe_2 emission spectrum, especially at lower energies [216], which serves as a motivation for future experiment.

Conclusion

In the preceding chapters I have detailed several examples of new physics on excited exciton states and charged exciton states, that we were able to study at the LPCNO largely due to the improved optical quality of our samples fabricated during my thesis. In addition I have performed and contributed to other experiments, which are summarized concisely below.

MoTe₂ and upconversion.

In addition to the materials $MoSe_2$, WSe_2 and MoS_2 studied in this thesis, encapsulation also allowed detailed new insight on high quality $MoTe_2$ samples. This material has an optical gap at 1.17 eV in the near infrared region of the optical spectrum, so detection with an InGaAs device and not only an Si-CCD camera was necessary. In the figure, we can see the sharp PL emission with 3 meV FWHM of the exciton groundstate A:1s. In reflectivity and also absorption we observe the excited exciton state A:2s, 120 meV above the A:1s exciton. This allowed us to roughly extrapolate an exciton binding energy of 160 meV for $MoTe_2$ monolayer encapsulated in hBN.

In the lowest panel of the $MoTe_2$ spectroscopy results we report a very surprising observation : laser excitation at low energy at the A:1s resonance results in emission of high excited states A:2s. This observation is summarized for four different materials in the next figure. For reasons of energy conservation, this upconversion emission is clearly a non-linear optical process. Together with M. Glazov and L. Golub from the Ioffe institute we developed the following scenario : we interpret the upconversion emission as being the result of exciton-exciton scattering. These Auger-type processes where one exciton is annihilated as the second one absorbs its energy are usually observed for experiments using pulsed laser excitation generating considerable exciton densities. We observe upconversion emission for continuous laser excitation and therefore need a scenario that makes exciton-exciton scattering efficient even at moderate densities. First, we find experimentally that upconversion is a resonant process, we need to be within the absorption FWHM of the A:1s exciton with the excitation laser to observe any signal. Second, the power dependence of the upconversion PL has twice the slope of the standard PL, hinting at a 2 excitons process. We therefore propose resonant Auger scattering to be at the origin of the upconversion emission. We take into account the particular conduction band structure of TMD monolayers, which makes a promotion of the electron to a high energy state more likely. After exciton-exciton scattering, as the remaining high energy exciton relaxes towards the A:1s state, we observe hot PL emission from the intermediate states such as the B:1s or the A:2s. From an experimental point of view, upconversion allows a clear

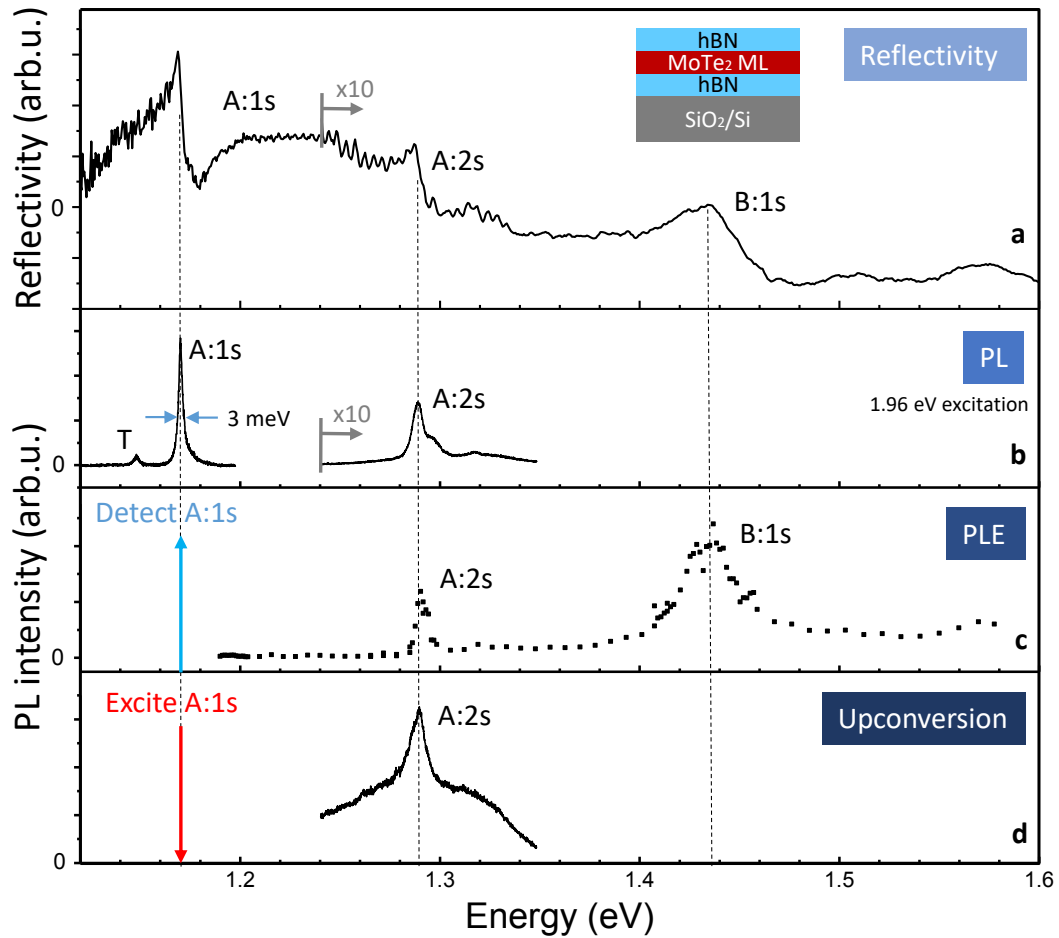


Figure 4.18: **Exciton spectroscopy in $MoTe_2$ monolayers encapsulated in hBN.** T=4 K. (a) Differential reflectivity spectrum, the energy positions of the exciton transitions A:1s, A:2s and B:1s are marked. (b) Excitation with a HeNe Laser at 1.96 eV results in hot PL of the A:2s and PL for the A:1s state. The low energy peak labeled T might be related to the trion or phonon replica. (c) Photoluminescence excitation measurements detecting the emission from the A:1s exciton. Peaks related to the resonant excitation of the A:2s and B:1s are marked. (d) Upconversion PL, the laser tuned into resonance with the A:1s state results in emission about 120 meV higher energy, Figure extracted from [160].

observation of excited state energies, which gives us information on the exciton binding energy. Our work was for example the first report on the energy position of excited exciton states in $MoTe_2$.

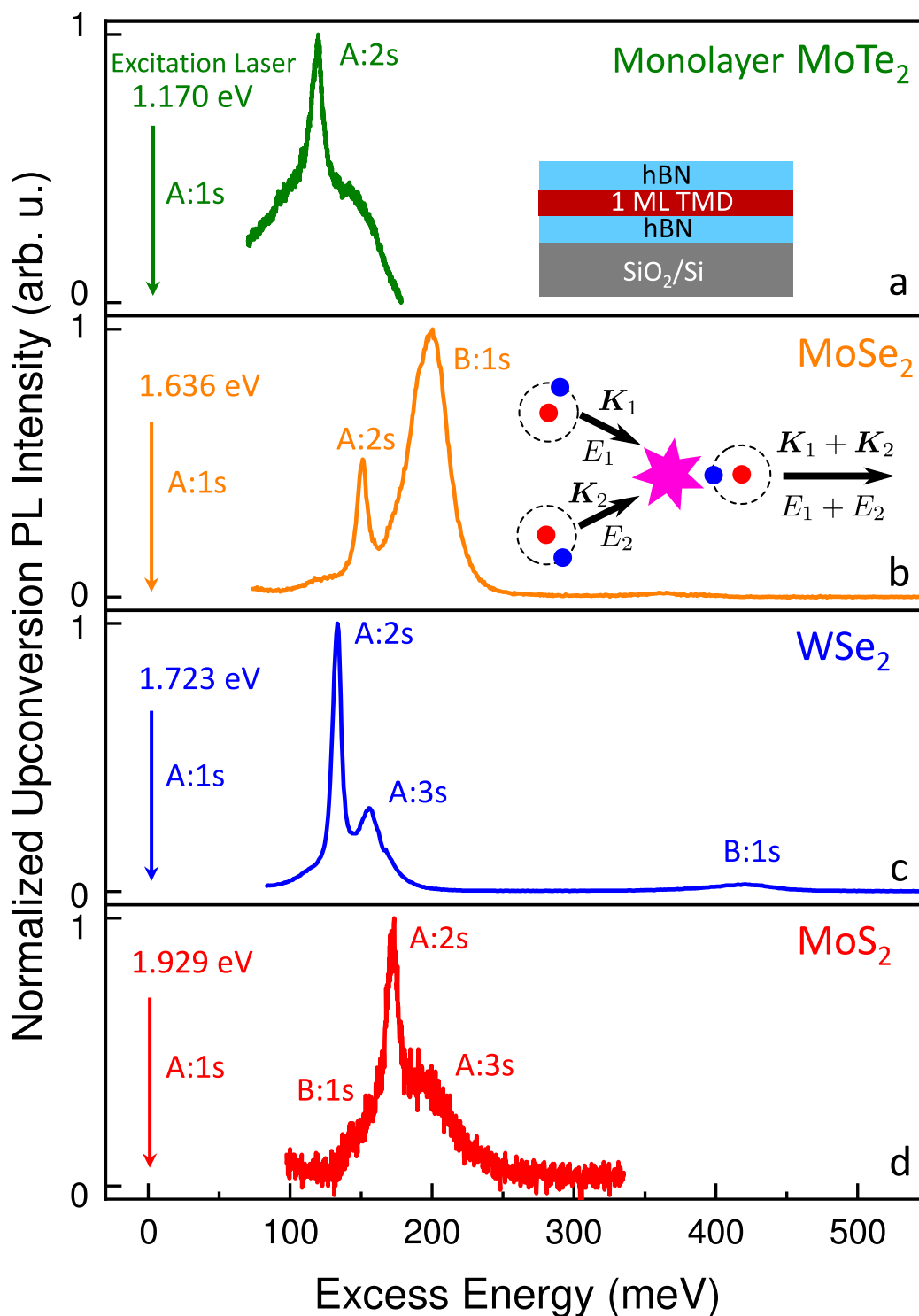


Figure 4.19: **Upconversion spectroscopy in TMD monolayers.** We present for four different monolayer materials resonant excitation experiments of the A:1s exciton at $T=4$ K, that result in PL emission at higher energy. The laser energy – equal to the A:1s transition energy – is marked by a vertical arrow. The upconversion emission peaks are labeled A:2s and B:1s, where the origin of these peaks is confirmed in complementary experiments such as reflectivity and PLE. Inset in (a) shows the sandwich structure of all the samples. Inset in (b) shows the exciton-exciton Auger process where one exciton annihilates and another one acquires total momentum and energy of the two particles. Figure extracted from [160].

Dark and Bright excitons in WSe_2 monolayer. Before hBN encapsulation was used for WSe_2 monolayer, the PL spectrum below the main neutral exciton transitions contained broad, not-reproducible peaks. For charge-tunable samples we have discussed in detail the appearance of trion lines. But even in the neutral regime there are several lines we can now clearly spectrally resolve in high quality samples and we will see that one of the very prominent lines about 40 meV below the bright neutral exciton is the dark exciton. It is in principle spin forbidden and with an optical dipole out of plane, so our target here is to argue briefly how it can be observed in experiments.

The sign of the spin splitting in the conduction band is crucial for the energetic order of bright (spin-allowed) versus dark (spin-forbidden) transitions, see Fig 4.20(c). From symmetry analysis (collaboration M. Glazov) we learn that the spin forbidden transition has its optical dipole out of the monolayer plane. This motivated experiments in Fig 4.20(a) using side excitation and detection, in contrast to the usual experiments with excitation and detection normal to the monolayer plane in reflection geometry. These experiments brought to light a new peak shown in the PL measurements in Fig 4.20(b) 40 meV below the bright neutral exciton X^0 and polarized indeed out of plane, which we therefore ascribe to the dark exciton X^D . The fact that we see this line in emission tells us that the spin-states are mixed, no signal is expected in the absence of spin-mixing of the conduction states. Our attribution of this line to an exciton with lower oscillator strength is confirmed in time resolved measurements, where we observe PL emission times of the order of 100 ps, as compared to 1 ps for the bright exciton shown in Fig 4.20(d).

The dark exciton line is not only observed through side excitation, but also in the standard experimental geometry sketched in Fig 4.21(a) for top excitation and detection normal to the monolayer plane. Most monolayer samples only have a lateral size of micrometers, which is why we perform micro-PL with microscope objectives with high numerical aperture NA=0.82 in our case. As a consequence, we do not just collect light emitted normal to the monolayer plane, but also z-components, that is from excitons with out-of-plane optical dipoles. Therefore, when integrating over the full angle for detection, we see in our spectrum the in-plane polarized, bright and spin allowed exciton, but also the z-polarized dark exciton in Fig 4.21(b). As we close a pinhole in the Fourier plane of the objective, we effectively reduce the NA, that is the detection angle and the z-polarized emission is not detected anymore in panel (c) of Fig 4.21. We find similar results for WS_2 monolayers, which have the same order of conduction spin states. For $MoSe_2$ and MoS_2 the exact position of the spin-forbidden, dark exciton states still needs to be determined, which is more challenging as they are in principle above the bright exciton in energy.

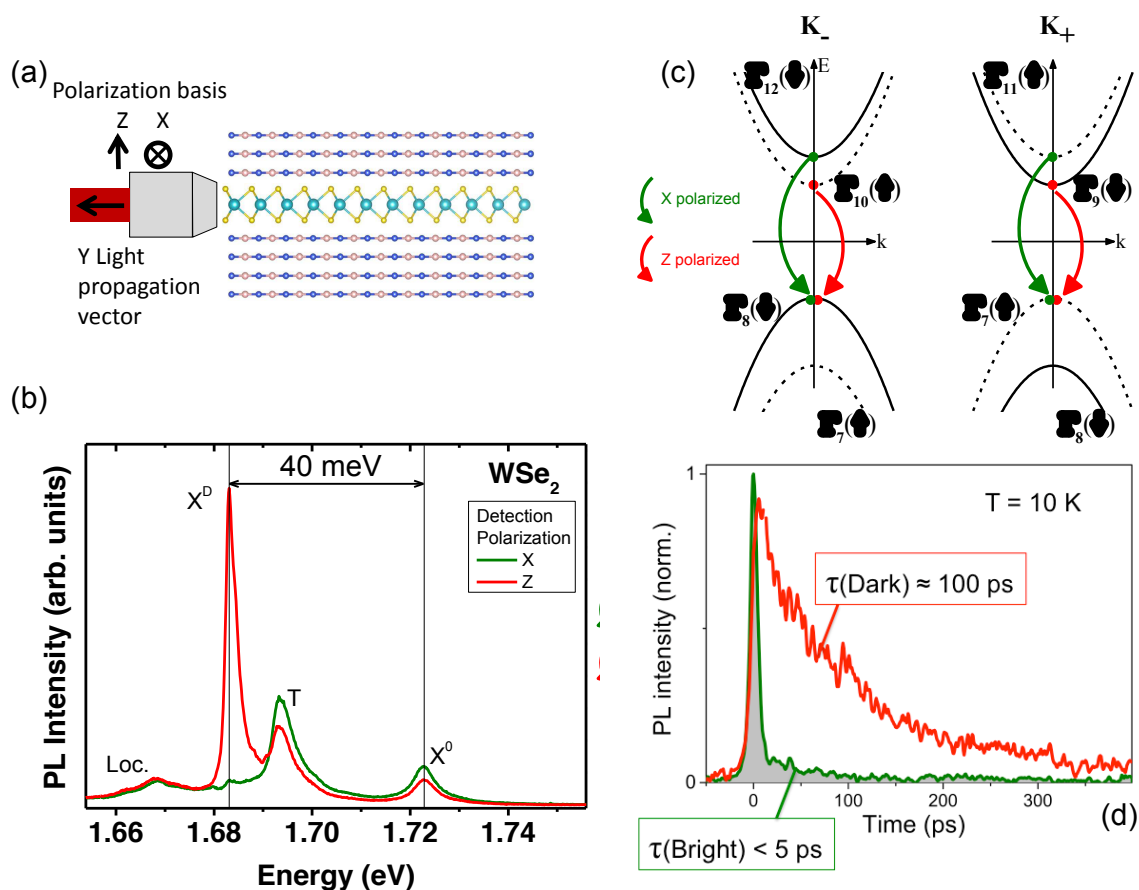


Figure 4.20: **Out-of plane and in-plane polarized excitons in WSe_2 monolayer.** (a) sketch of the experiment : excitation and detection from the side, not the monolayer top. (b) Linear detection basis in detection and excitation can be varied. For z-polarization out of the monolayer plane we observe a new transition X^D about 40 meV in energy below the bright, spin-allowed X^0 . (c) Spin-allowed and spin-forbidden transitions at K_+ and K_- points and underlying symmetries for WSe_2 monolayer. (d) Measurement of PL emission time for X^D (≈ 100 ps) and X^0 (< 5 ps) using a streak camera system. (a) to (d) adapted from [34] and [36].

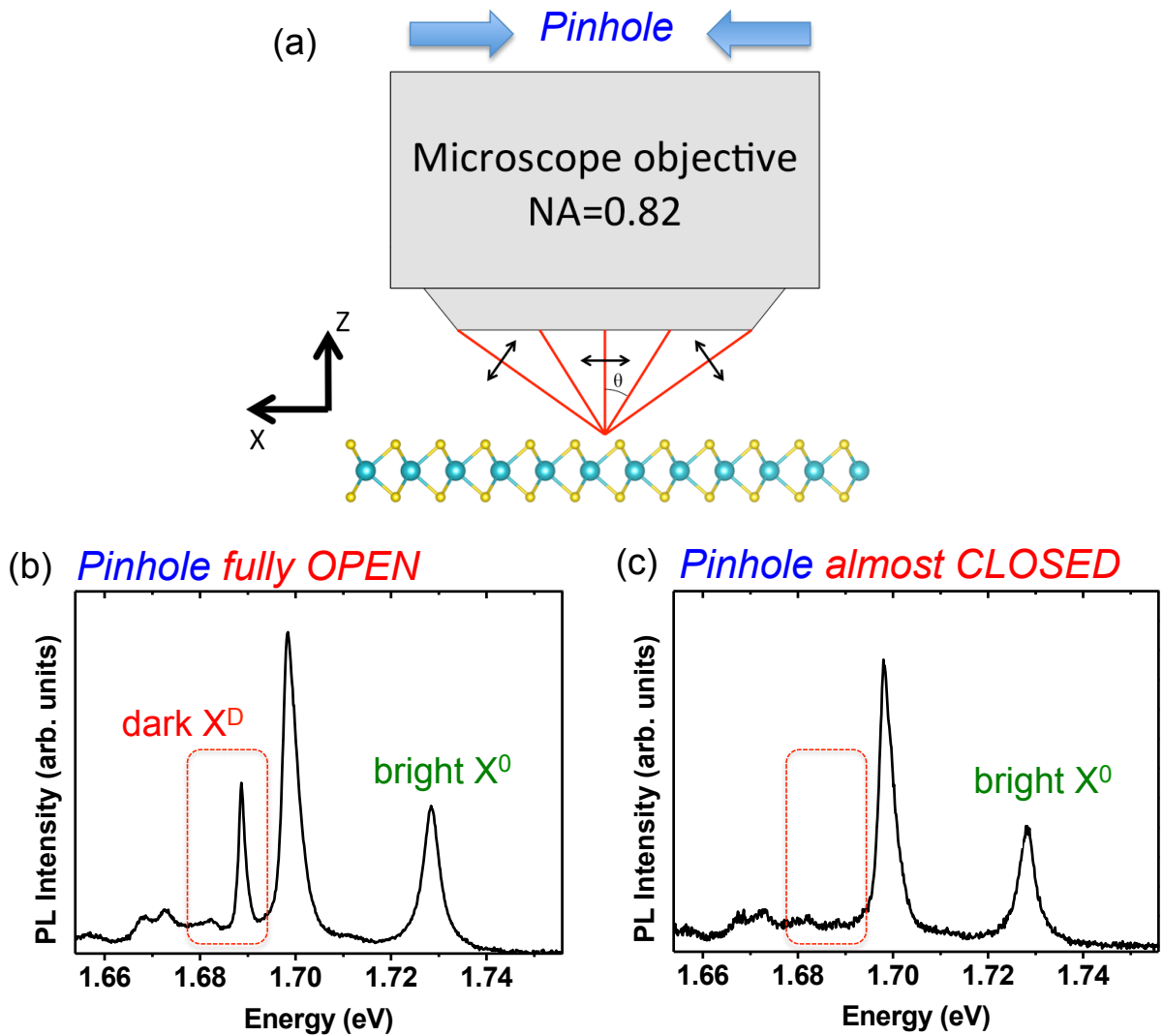


Figure 4.21: **Large NA objective for observation of out-of-plane and in-plane excitons.** (a) Sketch of typical experimental geometry, using microscope objective with high numerical aperture (NA), necessary to have high spatial resolution, but also introducing out-of-plane for excited/detected radiation. (b) PL spectrum with fully open pinhole, integrating over all angles. (c) By closing the pinhole, we eliminate z-polarized emission X^D . Adapted from [34].

Perspectives.

During this thesis work our understanding of optical transitions of TMD monolayer materials has greatly improved, as we can distinguish between dark and bright neutral excitons, charged excitons and biexcitons and their different combinations. As future research directions we aim to couple these optical transitions with high oscillator strength to other structures through simple exfoliation or dry-stamping. Two prominent examples pursued in the community and by us are shown in Fig 4.22.

For example, we started investigating the general field of so-called proximity effects. Here the target is to modify the optical and polarization properties of the excitons in the TMD monolayer by placing the ML on a magnetic substrate, for example a magnetic van der Waals materials such as CrI_3 or $CrBr_3$, see work of the Seattle group in Fig 4.22(a,b). The idea is to induce a valley Zeeman splitting in WSe_2 monolayer already at zero applied magnetic field due to proximity effects, as has been shown in [217]. These magnetic materials have only been discovered very recently and the field of hybrid semiconductor/magnetic layer devices is just starting.

Another pathway of modifying the light-matter interaction in WSe_2 monolayer for example is to couple the exciton resonance to a photonic cavity mode. Here the group of Hui Deng in Michigan, where I worked for one month during my thesis, proposed planar photonic crystals and the TMD monolayer active region is simply exfoliated on top. This simple device allowed to observe strong coupling of excitons and photonic crystal modes, see the characteristic anti-crossing in Fig 4.22(d).

In addition to coupling monolayers to magnetic or photonic structures, another emerging research field is the study of TMD multilayers. Also here the experimental parameters and the expected physical phenomena are vast. For example, in MoS_2 homobilayer, we have found a new type of exciton with an electron localized in one layer and a hole state delocalized over both layers. This interlayer exciton has high optical oscillator strength (high visibility in absorption) a built-in electric dipole and is interesting for future experiments on exciton-exciton interactions [221]. When 2 different materials, for example $MoSe_2$ and WSe_2 monolayers, are brought together by dry stamping or direct CVD growth, the different lattice constants will result in moiré effects in the structure, which have shown to induce periodic variations of the bandstructure [222], with first promising reports [223]. In general TMD heterostructures allow studying a multitude of exciton complexes, for example spatially indirect excitons with considerably longer PL emission time compared to the intralayer excitons with recombination times of only 1 ps. As for the project on proximity effects, bringing 2 TMD monolayers in contact at a controlled angle is a real challenge in terms of clean fabrication, which needs again to be improved in terms of precision and reproducibility. As perspectives, well controlled periodic moiré potentials can capture individual excitons if the barriers are high enough, in this case a periodic array of single photon emitters would be created, as predicted by [224] with first claims that need to be confirmed [225].

We hope these brief examples give a feel of the many open challenges in the field, in terms of sample fabrication, optical spectroscopy and magnetic characterization.

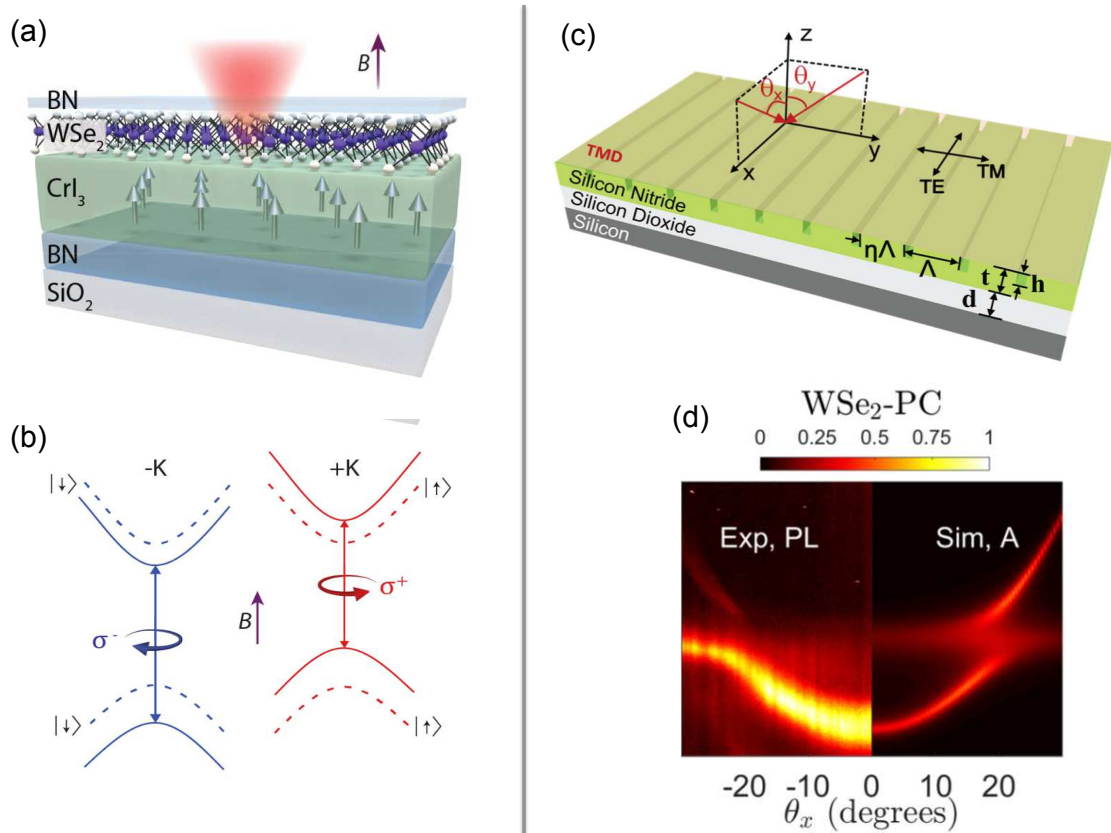


Figure 4.22: **Perspectives on proximity effects and photonic structures.** (a) Schematic of WSe_2 monolayer on the 2D ferromagnet CrI_3 . (b) Emission of the WSe_2 monolayer shows a Zeeman splitting in the absence of external magnetic fields, simply due to the proximity of the ferromagnet. Adapted from [217]. (c) Photonic structure on top of which a WSe_2 monolayer can be directly exfoliated. (d) strong coupling between excitons and photonic cavity modes (anticrossing). Adapted from [218]

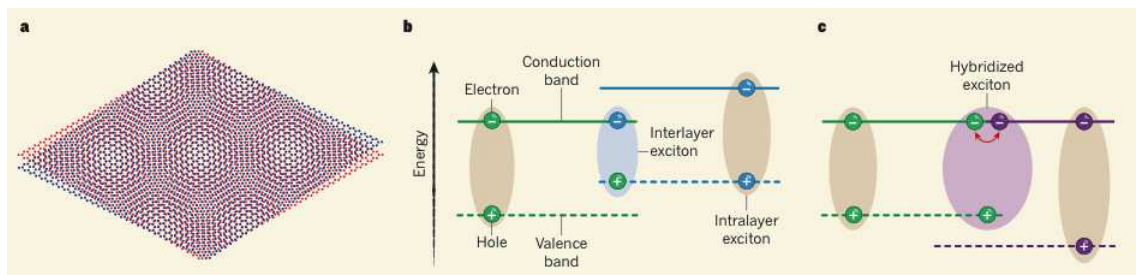


Figure 4.23: **Perspectives on TMD multilayers.** (a) Sketch of TMD crystals stacked with a slight twist angle, giving rise to Moire patterns and hence periodic potentials. (b) In hetero-bilayers different exciton species can be investigated, for example in $MoSe_2/WSe_2$ with type II alignment. (c) Excitons with hybridized states, delocalized over 2 layers can also be investigated, here $MoSe_2/WSe_2$ is shown where the conduction band is aligned [219, 220].

List of publications

- M. Manca, M.M. Glazov, C. Robert, F. Cadiz, T. Taniguchi, K. Watanabe, **E. Courtade**, T. Amand, P. Renucci, X. Marie, G. Wang and B. Urbazek (2017). Enabling valley selective exciton scattering in monolayer WSe 2 through upconversion. Nature communications, 8, 14927. [Link](#)
- F. Cadiz, **E. Courtade**, C. Robert, G. Wang, Y. Shen, H. Cai, T. Taniguchi, K. Watanabe, H. Carrere, D. Lagarde, M. Manca, T. Amand, P. Renucci, S. Tongay, X. Marie and B. Urbaszek (2017). Excitonic Linewidth Approaching the Homogeneous Limit in MoS 2-Based van der Waals Heterostructures. Physical Review X, 7(2), 021026. [Link](#)
- **E. Courtade**, M. Semina, M. Manca, M.M. Glazov, C. Robert, F. Cadiz, G. Wang, T. Taniguchi, K. Watanabe, M. Pierre, W. Escoffier, E.L. Ivchenko, P. Renucci, X. Marie, T. Amand, and B. Urbaszek (2017). Charged excitons in monolayer WSe 2: Experiment and theory. Physical Review B, 96(8), 085302. [Link](#)
- G. Wang, C. Robert, M.M. Glazov, F. Cadiz, **E. Courtade**, T. Amand, D. Lagarde, T. Taniguchi, K. Watanabe, B. Urbaszek and X. Marie (2017). In-plane propagation of light in transition metal dichalcogenide monolayers: optical selection rules. Physical review letters, 119(4), 047401. [Link](#)
- C. Robert, T. Amand, F. Cadiz, D. Lagarde, **E. Courtade**, M. Manca, T. Taniguchi, K. Watanabe, B. Urbaszek and X. Marie (2017). Fine structure and lifetime of dark excitons in transition metal dichalcogenide monolayers. Physical Review B. 96, 155423. [Link](#)
- C. Robert, M. A. Semina, F. Cadiz, M. Manca, **E. Courtade**, T. Taniguchi, K. Watanabe, H. Cai, S. Tongay, B. Lassagne, P. Renucci, T. Amand, X. Marie, M. M. Glazov, and B. Urbaszek (2018). Optical spectroscopy of excited exciton states in MoS 2 monolayers in van der Waals heterostructures. Physical Review Materials, 2(1), 011001. [Link](#)
- F. Cadiz, C. Robert, **E. Courtade**, M. Manca, L. Martinelli, T. Taniguchi, K. Watanabe, T. Amand, A.C. H. Rowe, D. Paget, B. Urbaszek and X. Marie (2018). Exciton diffusion in WSe2 monolayers embedded in a van der Waals heterostructure. Applied Physics Letters, 112(15), 152106. [Link](#)

- S. Shree, M. Semina, C. Robert, B. Han, T. Amand, A. Balocchi, M. Manca, **E. Courtade**, X. Marie, T. Taniguchi, K. Watanabe, M. M. Glazov and B. Urbaszek (2018). Observation of exciton-phonon coupling in MoSe2 monolayers. Physical Review B 98, 035302. [Link](#)
- **E. Courtade**, B. Han, S. Nakhaie, C. Robert, X. Marie, P. Renucci, T. Taniguchi, K. Watanabe, L. Geelhaar, J.M.J. Lopes, and B. Urbaszek (2018). Spectrally narrow exciton luminescence from monolayer MoS2 and MoSe2 exfoliated onto epitaxially grown hexagonal BN. Applied Physics Letters 113, 032106. [Link](#)
- B. Han, C. Robert, **E. Courtade**, M. Manca, S. Shree, T. Amand, P. Renucci, T. Taniguchi, K. Watanabe, X. Marie, L.E. Golub, M.M. Glazov and B. Urbaszek (2018). Exciton states in monolayer MoSe2 and MoTe2 probed by upconversion spectroscopy. Physics Review X 8, 0311073. [Link](#)
- I. C. Gerber, **E. Courtade**, S. Shree, C. Robert, T. Taniguchi, K. Watanabe, A. Balocchi, P. Renucci, D. Lagarde, X. Marie and B. Urbaszek (2019). Interlayer excitons in bilayer MoS2 with strong oscillator strength up to room temperature. Physics Review B 99, 035443. [Link](#)
- M. Goryca, J. Li, A. V. Stier, S.A. Crooker, T. Taniguchi, K. Watanabe, **E. Courtade**, S. Shree, C. Robert, B. Urbaszek and X. Marie (2019). Revealing exciton masses and dielectric properties of monolayer semiconductors with high magnetic fields. arXiv:1904.03238. [Link](#)
- H.H. Fang, C. Robert, M.A. Semina, D. Lagarde, **E. Courtade**, T. Taniguchi, K. Watanabe, T. Amand, B. Urbaszek, M.M. Glazov and X. Marie (2019). Control of the exciton radiative lifetime in van der Waals heterostructures. Accepted for publication as a Letter in Physical Review Letters. Available on the arXiv: [Link](#)

Conferences

- Presentation of a poster at the International school on Nanosciences in Etioilles (91), France. June, 25 to 30, 2017.
- Best poster award at the conference Flatlands beyond Graphene in Lausanne, Switzerland. August 29 to September 1, 2017.
- Presentation *Fine structure of excitonic states in hBN/TMD monolayer/hBN van der Waals heterostructures* at the GDR Graphene and Co in Aussois, France. October 15 to 19, 2017.
- Presentation *Optical spectroscopy of excited exciton states in MoS₂ monolayers in van der Waals heterostructures* at the Journées de la Matière Condensée (JMC) in Grenoble, France. August 27 to 31, 2018.
- Presentation *Towards control of the homogeneous exciton linewidth in transition metal dichalcogenide monolayers* at the Rank Prize Meeting, Symposium on two-dimensional semiconductors for Optoelectronics in Grasmere, England. April 8 to 11, 2019.

Chapter 5

Résumé en Français

Introduction: les monocouches atomiques de dichalcogénures de métaux de transition

Un intérêt grandissant pour les matériaux 2D

Avec l'essor des nanotechnologies, des systèmes aux dimensions nanométriques ont été développés et étudiés: puits quantiques (2D), nanofils (1D), boîtes quantiques (0D)... Au delà des puits quantiques qui sont d'ores et déjà utilisés dans l'industrie des semiconducteurs, nous nous intéressons dans ce travail de thèse à la limite extrême des monocouches atomiques semiconductrices.

L'intérêt pour ces monocouches atomiques a connu un véritable essor à travers le graphène. En 2010 Andre Geim et Konstantin Novoselov reçurent the prix Nobel de Physique pour leur travail et expériences pionnières sur ce matériau en 2D. Le graphène est une monocouche d'atomes de carbone arrangés dans une structure hexagonale. Il peut être obtenu simplement à partir de graphite qui est un matériau de van der Waals composé de monocouches atomiques faiblement liées entre elles par des liaisons de van der Waals. A l'aide d'un simple bout de scotch, il est possible de mettre en oeuvre un simple procédé d'exfoliation mécanique pour parvenir à retirer une monocouche atomique. Ce matériau est stable et présente des propriétés physiques fascinantes parmi lesquelles: des mobilités intrinsèques atteignant $2 \times 10^5 \text{ cm}^2 \text{V}^{-1} \text{s}^{-1}$ à température ambiante [4], des conductivités thermiques importantes [5], des propriétés mécaniques imbattables qui ont amené les scientifiques à qualifier le graphène de "matériau le plus dur jamais mesuré" [6]. Cependant, le graphène est un semimétal et non un semiconducteur. Il n'a donc pas de bande interdite, ce qui peut compliquer son utilisation pour de nombreuses applications.

Heureusement, quoique le graphène soit un illustre représentant de la famille des matériaux en 2D, il est loin d'en être l'unique représentant. Tel qu'illustré dans la figure 5.1, cette famille est vaste et englobe différents types de matériaux: semiconducteurs, métaux, isolants, supraconducteurs...

Parmi ces matériaux, nous nous intéressons dans cette thèse aux Dichalcogénures de Métaux de Transition (TMD en anglais pour "Transition Metal Dichalcogenide") du groupe

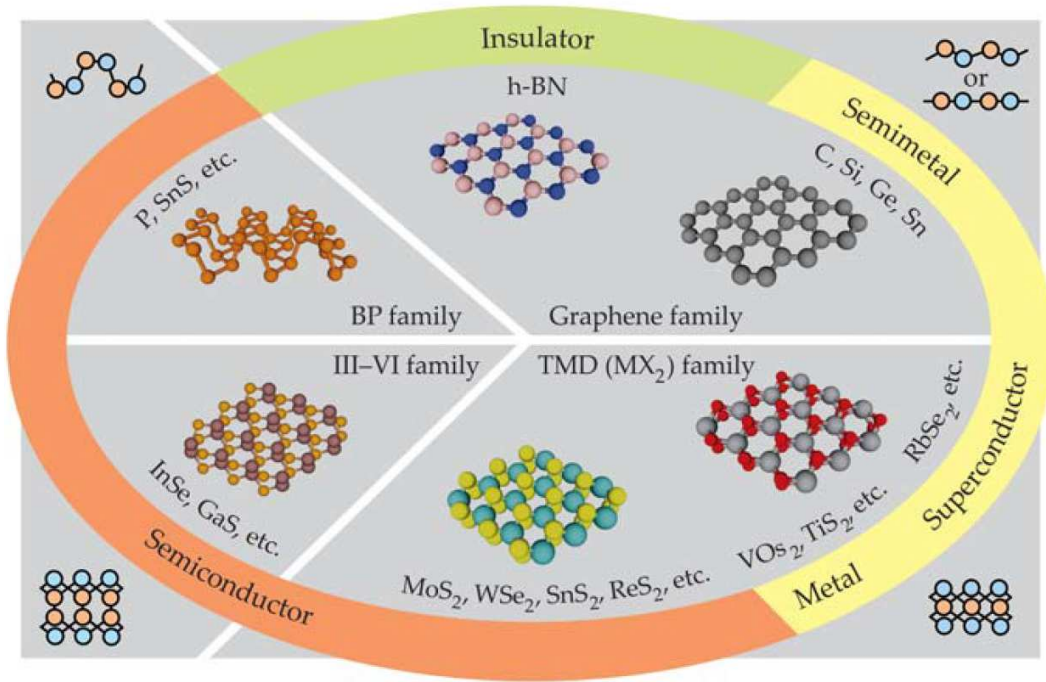


Figure 5.1: La vaste famille des matériaux en 2D. Figure extraite de [8].

VIB. Ce sont des semiconducteurs ayant un gap compris entre 1.0 et 2.0 eV pour les principaux représentants de cette famille qui ont été étudiés au cours de mon travail de thèse (MoS_2 , WS_2 , $MoSe_2$, WSe_2 , $MoTe_2$). Tout comme le graphène, ils présentent l'avantage de pouvoir être fabriqués facilement en utilisant la technique de l'exfoliation mécanique [7]. Cette technique, très économique et facile à mettre en oeuvre explique aussi pourquoi les matériaux en 2D ont été un sujet de recherche accessible pour beaucoup d'équipes scientifiques.

Par ailleurs, il est possible d'empiler des couches de différents matériaux grâce à des méthodes dérivées de l'exfoliation mécanique. De cette manière des hétérostructures de van der Waals ayant de nouvelles propriétés physiques peuvent être fabriquées tel qu'illustré par la figure 5.2.

La structure cristalline des TMD

Les dichalcogénures de métaux de transition (TMD pour "Transition Metal Dichalcogenide" en anglais) étudiés dans cette thèse ont la formule chimique MX_2 avec M un métal de transition (Mo, W) et X un atome de chalcogène (S, Se ou Te).

Ce sont des matériaux de van der Waals composés d'un empilement de monocouches atomiques, tel qu'illustré dans 5.3 (a). Par de simples procédés d'exfoliation mécanique il est donc possible d'isoler une monocouche atomique.

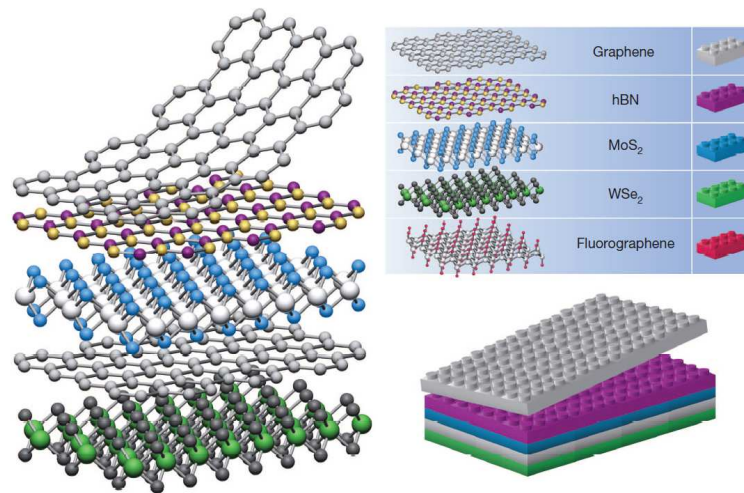


Figure 5.2: Représentation de l'assemblage d'une hétérostructure de van der Waals, aussi représenté dans une visi très simplifié avec des pièces Lego[®]. Figure extraite de [9].

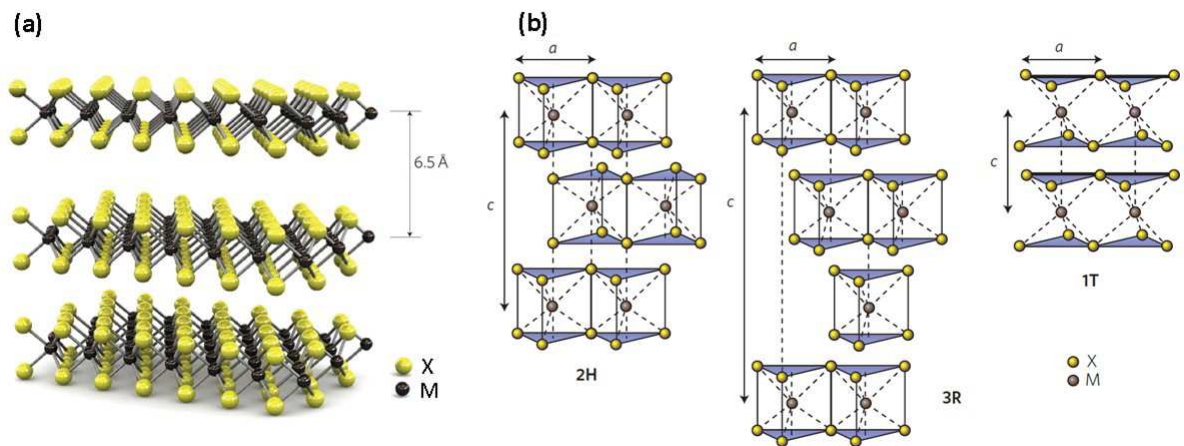


Figure 5.3: **(a)** Représentation 3D d'une tricouche d'un TMD avec un empilement 2H. L'espace entre les couches est d'environ ~ 6.5 Å. Figure extraite de [11]. **(b)** Différents types de structure: a est le paramètre de maille compris entre 3.1 et 3.7 Å pour différents matériaux et c est l'indice d'empilement. L'empilement 2H est celui qui est étudié dans cette thèse, étant d'ailleurs le type d'empilement de la molybdenite naturelle. Figure extraite de [12].

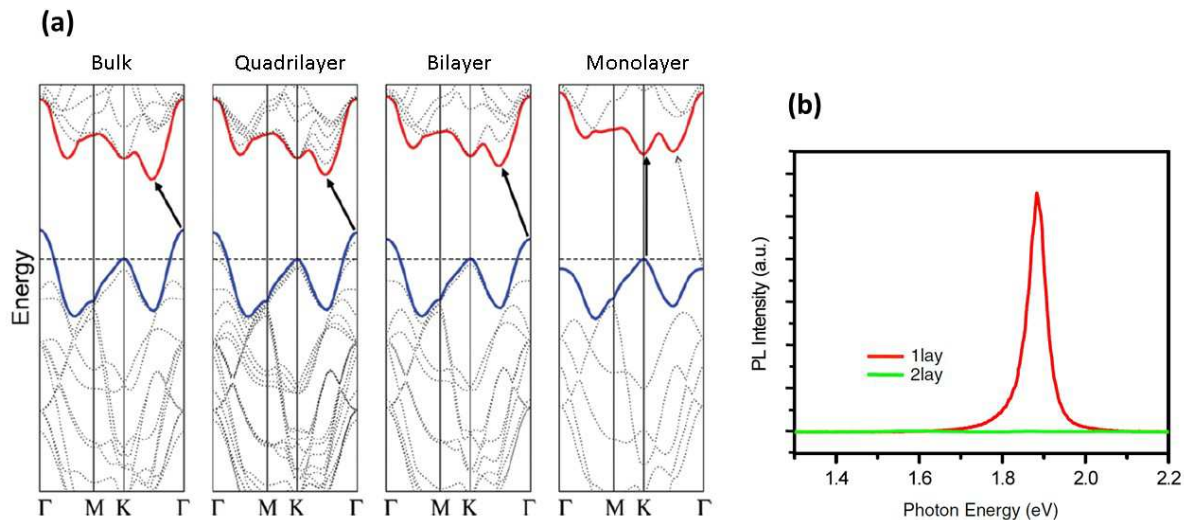


Figure 5.4: (a) Calculs DFT pour un matériau bulk, quatre couche, trois couches, deux couches et une couche atomique de MoS_2 . Dans le cas de la monocouche atomique, le gap est direct. Figure extraite de [2]. (b) Spectres de photoluminescence d'une bicouche (en vert) et une monocouche atomique (en rouge) de MoS_2 . Figure extraite de [1].

	MoS_2	$MoSe_2$	WS_2	WSe_2	$MoTe_2$	WTe_2
Δ_{SO}^{VB} (HSE,LDA) en meV	148	186	429	466	219	484
Δ_{SO}^{VB} (PBE,PBE) en meV	148	184	425	462	213	480
Valeur expérimentale moyenne	≈ 145	≈ 191	≈ 394	≈ 440	-	-

Table 5.1: Valeurs du splitting spin-orbite Δ_{SO}^{VB} calculés en utilisant la méthode de la DFT. A titre de comparaison les valeurs expérimentales moyennes sont indiquées. Toutes ces valeurs sont extraites de [13].

Structure de bande

Une des propriétés notables des monocouches de TMD est leur gap direct. Les résultats théoriques et expérimentaux montrent que lorsqu'on passe d'un TMD en 3D à un TMD en 2D, le gap au départ indirect devient direct. La figure 5.4 montre bien cette transition vers un gap direct au point K de la zone de Brillouin, qui se traduit expérimentalement par un rendement quantique accru.

A noter également, que la structure de bande des monocouches de TMD est caractérisée par un splitting spin-orbite important dans la bande de valence tels qu'indiqué par les valeurs du tableau 5.1.

La bande de conduction est également splitté dû au couplage spin-orbite, quoique les valeurs soient beaucoup plus faibles que dans la bande de valence.

	MoS_2	$MoSe_2$	WS_2	WSe_2	$MoTe_2$	WTe_2
Δ_{SO}^{CB} (HSE,LDA) en meV	3	22	-32	-37	36	-52
Δ_{SO}^{CB} (PBE,PBE) en meV	3	20	-31	-37	32	-54

Table 5.2: Valeurs du splitting spin-orbite Δ_{SO}^{CB} calculées en utilisant la méthode de la DFT. Valeurs extraites de [13].

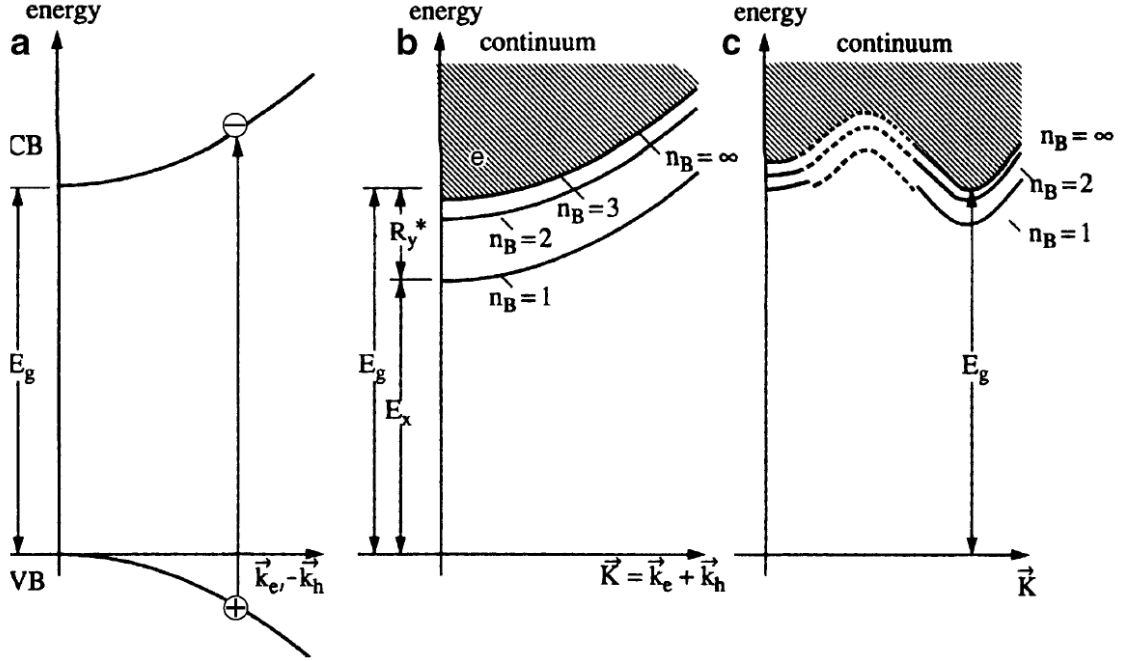


Figure 5.5: Différentes représentations d'un exciton: (a) dans le schéma des bandes de valence et de conduction, dans la représentation de l'exciton pour un exciton direct (b) et un exciton indirect (c). Figure extraite de [19].

Les excitons dans les monocouches de TMD

Les propriétés optiques des monocouches de TMD sont dominées par des paires électron-trou liées par l'interaction de Coulomb, appelées excitons. Comme un atome d'hydrogène, les excitons ont différents niveaux d'énergie formant la série Rydberg de l'exciton. A ces niveaux d'énergie, représentés schématiquement dans la figure 5.5 (b), sont associés différents nombres quantiques principaux n_B .

Dans un modèle hydrogénoïde simple, la résolution de l'équation de Schrödinger pour la fonction enveloppe du mouvement relatif permet d'extraire les niveaux d'énergie de l'exciton: 1s, 2s, 3s... [23]:

$$E_{n_B} = R_y^* \frac{1}{n_B^2} \quad (5.1)$$

avec n_B le nombre quantique principal et R_y^* l'énergie Rydberg de l'exciton donnée par:

$$R_y^* = 13.6 \frac{\mu}{m_0} \frac{1}{\epsilon^2} \quad (5.2)$$

avec m_0 la masse de l'électron au repos, et μ la masse réduite de l'exciton.

Dans un système en deux dimensions, cette formule donnant les énergies de liaison des

niveaux de la série de Rydberg devient:

$$E_B = R_y^* \frac{1}{(n_B - \frac{1}{2})^2} \quad (5.3)$$

Le confinement quantique en 2D induit donc des énergies de liaison supérieures à ce qui est attendu pour un modèle 3D.

En effet, dans nos monocouches atomiques de TMD, les excitons sont fortement liés. L'énergie de liaison d'un exciton est de l'ordre de plusieurs centaines de meV. C'est considérable si l'on considère d'autres semiconducteurs bien connus tels que les puits quantiques de GaAs (≈ 10 meV) ou le ZnO (≈ 60 meV). Outre l'effet du confinement 2D, la diminution du écrantage diélectrique en 2D mène aussi à des énergies de liaison plus élevées. De plus, la masse réduite μ des excitons dans une monocouche de TMD est élevée ($\mu \approx 0.25$).

L'étude des propriétés excitoniques dans les TMD en 2D est un des axes principaux des recherches présentées dans cette thèse. Une grande partie du travail se concentre en effet sur l'exciton A dans les monocouches de TMD qui est à l'origine des transitions ayant les plus grandes forces d'oscillateur dans ces matériaux.

Les règles de sélection optique

Lorsque l'on considère un TMD en 2D, la symétrie d'inversion est brisée. Cela donne lieu à des vallées K inéquivalentes aux angles de la zone de Brillouin hexagonale. Les deux différents types de vallée sont nommés K^+ et K^- , tel qu'illustré dans la figure 5.6.

Par ailleurs, il est possible d'exciter sélectivement soit les vallées K^+ soit les K^- soit les deux. Pour cela il faut exciter le matériau avec la bonne polarisation: respectivement σ^+ , σ^- ou linéaire.

Dans des expériences de photoluminescence (PL), la polarisation de la lumière émise est ensuite étudiée à travers le degré de polarisation circulaire:

$$P_c = \frac{I_{\sigma^+} - I_{\sigma^-}}{I_{\sigma^+} + I_{\sigma^-}} \quad (5.4)$$

ou linéaire:

$$P_c = \frac{I_X - I_Y}{I_X + I_Y} \quad (5.5)$$

La figure 5.7 illustre ce type de mesure.

Les règles de sélection optique sont illustrées schématiquement dans la figure 5.8.

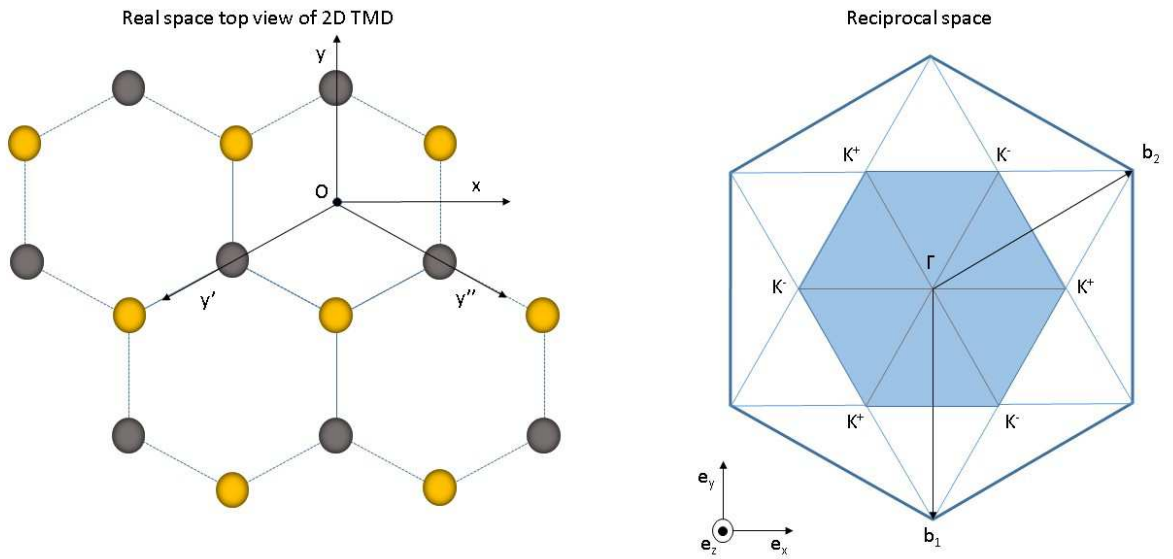


Figure 5.6: Espaces réel et réciproque d'un TMD en 2D. La zone ombrée correspond à la première zone de Brillouin. Dans l'espace réel, le groupe ponctuel du cristal est D_{3h} avec un axe de rotation d'ordre 3 (Oz), 3 axes d'ordre 2 (Oy , Oy' , Oy''), une symétrie miroir σ_h définie par le plan (xOy) et 3 symétries miroirs ($\sigma_v, \sigma_v^i, \sigma_v''$ définies par les plans (yOz), ($y'Oz$), ($y''Oz$)). Dans l'espace réciproque, aux angles de la zone de Brillouin (K^+ et K^-), le groupe ponctuel est C_{3h} ; du fait des vallées K inéquivalentes la symétrie est abaissée (les axes d'ordre 2 et les symétries miroirs associées σ_v, σ_v^i et σ_v'' sont supprimées).

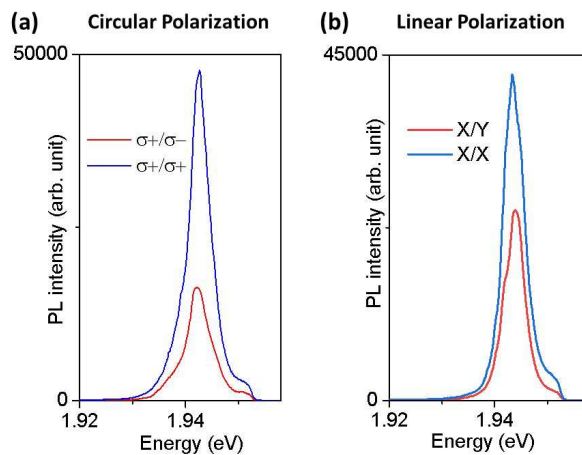


Figure 5.7: Mesure de polarisation en PL avec un monocouche de MoS_2 à température cryogénique. **(a)** Exemple de mesure de polarisation circulaire. En bleu, co-circulaire ($\sigma + / \sigma +$) et en rouge, circulaire croisé ($\sigma + / \sigma -$). **(b)** Exemple de mesure de polarisation linéaire. En bleu, co-linéaire (X/X) et en rouge, linéaire croisé (X/Y).

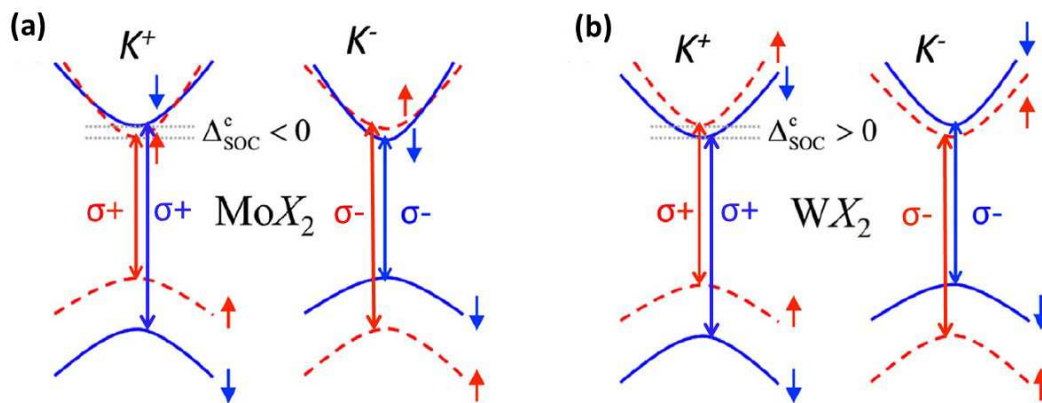


Figure 5.8: Représentation des vallées K^+ et K^- pour des composés à base de Mo et de W. Les vallées peuvent être excitées sélectivement avec de la lumière polarisée σ^+ et σ^- . Notations avec le spin électronique pour les bandes de conduction et de valence. Figure extraite de [24]

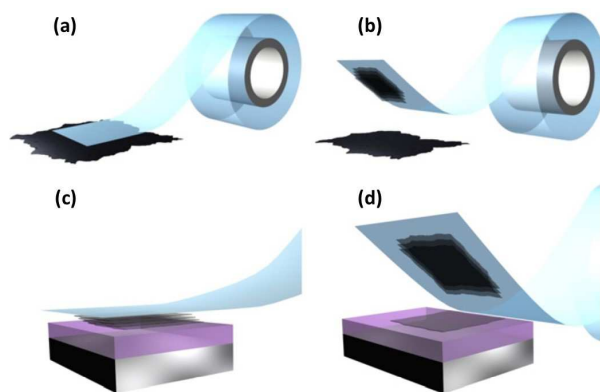


Figure 5.9: Figure extraite de [74] illustrant le procédé basique de l'exfoliation mécanique d'un matériau 2D.

La fabrication d'échantillons et les dispositifs expérimentaux

Les TMD sont des matériaux de van der Waals constitués d'un empilement de couches atomiques. Les liaisons covalentes assurent la cohésion des couches, mais entre les couches les faibles forces de van der Waals rendent possible la fabrication de monocouches atomiques.

La méthode la plus simple est l'exfoliation mécanique. Le procédé, illustré dans la figure 5.9, consiste à déposer quelques fragments du matériau sur un bout de scotch, à plier et déplier à plusieurs reprises le morceau de scotch, à coller ce scotch sur un substrat puis à le décoller de manière à transférer des couches du scotch vers le substrat. Cette technique très simple donna de bons résultats pour lancer la recherche sur les matériaux 2D. Cependant, il est facilement compréhensible qu'une telle procédure est très aléatoire et repose en très grande partie sur la chance. En outre, un des principaux désavantages est que ce simple procédé ne permet pas de contrôler en quel point du substrat la monocouche atomique est déposée.

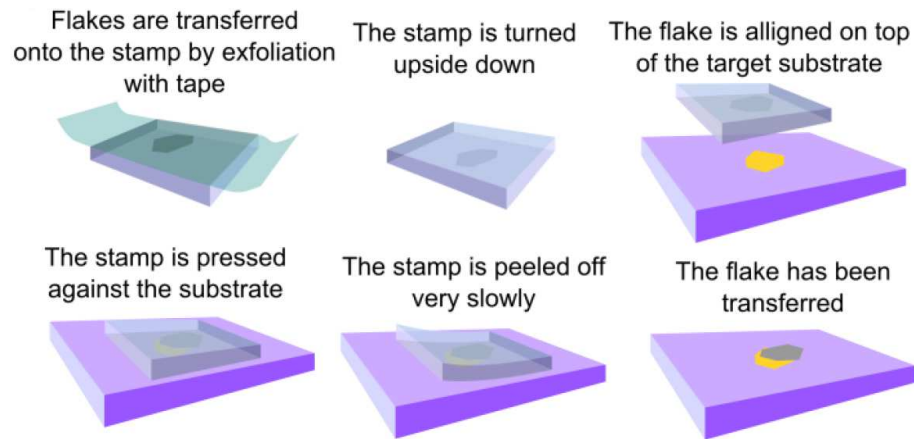


Figure 5.10: Les différentes étapes du transfert déterministe utilisant un polymère viscoélastique. Figure extraite de [58].

La méthode de transfert par PDMS

La méthode basique de l'exfoliation mécanique présentant le gros désavantage d'être trop aléatoire, d'autres procédés qui en dérivent ont été développés. L'une de ces méthodes, se rapprochant du "micro-transfer printing" utilise un morceau de polymère (du PDMS dans notre cas) sur lequel le matériau est transféré avant d'être transféré sur un substrat [58].

Dans l'objectif de fabriquer des hétérostructures de van der Waals, c'est à dire un empilement de différents matériaux de van der Waals, il est essentiel de pouvoir déposer les couches à des positions précises sur le substrat. Les différentes étapes du procédé de fabrication que nous utilisons communément au LPCNO sont illustrées dans la figure 5.10.

En pratique, le morceau de PDMS est déposé sur une lame de verre et le matériau est transféré depuis un morceau de scotch sur le PDMS. Ensuite, le morceau de PDMS couvert de matériau est scanné à l'aide d'un microscope optique pour trouver les couches à déposer sur le substrat. Une fois qu'une couche intéressante est trouvée, le morceau de PDMS est aligné avec un substrat avec une précision de $1 \mu\text{m}$ pour choisir précisément la zone où est transférée la couche. Le morceau de PDMS est amené en contact avec le substrat puis est retiré très lentement afin de transférer le matériau sur le substrat.

En répétant ces étapes pour différents matériaux et différentes couches, on peut empiler ces couches en un endroit précis du substrat pour fabriquer des hétérostructures de van der Waals.

D'autres méthodes existent telles que la technique du "pick-up" mais au LPCNO la technique du PDMS reste pour l'instant la plus utilisée.

Sélection des couches d'une hétérostructure de van der Waals

La première question que l'on peut se poser est comment trouver une monocouche atomique de TMD. Le matériau est exfolié à l'aide de scotch puis déposé sur le morceau de PDMS. Le PDMS en question est ensuite scanné avec un microscope optique. Tel

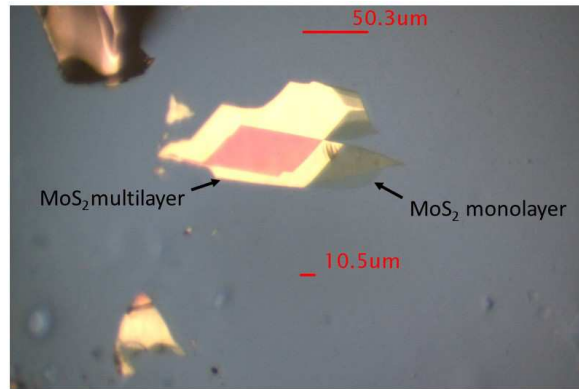


Figure 5.11: Image au microscope optique de couches de MoS_2 sur un morceau de PDMS. Des multicouches ainsi qu'une zone correspondant à une monocouche atomique sont visibles. Du fait de l'absorption importante, la monocouche est visible par simple contraste optique.

qu'illustré dans la figure 5.11, les monocouches des TMD étudiés au cours de ma thèse (MoS_2 , $MoSe_2$, WS_2 , WSe_2 , $MoTe_2$) sont discernables par simple contraste optique.

En cas de doute il est possible de réaliser des mesures de PL à température ambiante pour vérifier qu'il s'agit bien d'une monocouche atomique. Cependant, avec l'expérience, il est possible de détecter par contraste optique des monocouches en ayant très peu de doutes [113]. De plus, lorsque la monocouche est sur du PDMS et n'est donc pas protégé, nous craignons que l'exposition à un laser ne dégrade ses propriétés optiques (en particulier si une puissance trop élevée est utilisée) [114].

Les hétérostructures de type hBN/monocouche de TMD/hBN font partie des échantillons les plus étudiés au cours de ma thèse. Ainsi, outre la sélection du TMD, il faut être choisir les bonnes couches de nitrure de bore hexagonal (hBN) qui seront incorporées aux hétérostructures. Il faut noter que le hBN que nous utilisons au LPCNO est obtenu par croissance par nos collaborateurs du NIMS. Tel qu'illustré par la figure 5.12, il s'agit à l'heure actuelle du hBN le plus pur que l'on puisse trouver.

Outre la pureté du hBN, il est également particulièrement important d'être capable de contrôler l'épaisseur des couches de hBN incorporées dans les hétérostructures. Tout comme pour le TMD, le hBN est déposé sur un morceau de PDMS, puis le polymère est scanné avec un microscope optique pour sélectionner les couches qui seront incorporées dans les échantillons. Sur le PDMS, les flocons de hBN apparaissent sous différentes couleurs qui sont caractéristiques de leur épaisseur. Au cours de mon travail de thèse, j'ai eu l'occasion de développer un programme en Python en me basant sur le formalisme mathématique des matrices de transfert pour simuler la couleur de couches de hBN en fonction de leur épaisseur. Les résultats obtenus par cette méthode sont illustré dans la figure 5.13. Outre les couleurs, pour une précision accrue des mesures à l'AFM peuvent être réalisées. A noter que les couches de hBN ayant typiquement une épaisseur inférieure à 5 nm sont transparentes sur le PDMS et ne sont donc pas visibles en utilisant notre setup d'exfoliation. C'est pourquoi, afin de trouver des couches ultra-fines de hBN, une technique consiste à les déposer sur des substrats avec une épaisseur de SiO_2 adaptée (≈ 90 nm). Grâce aux interférences, il devient alors possible de détecter ces couches par

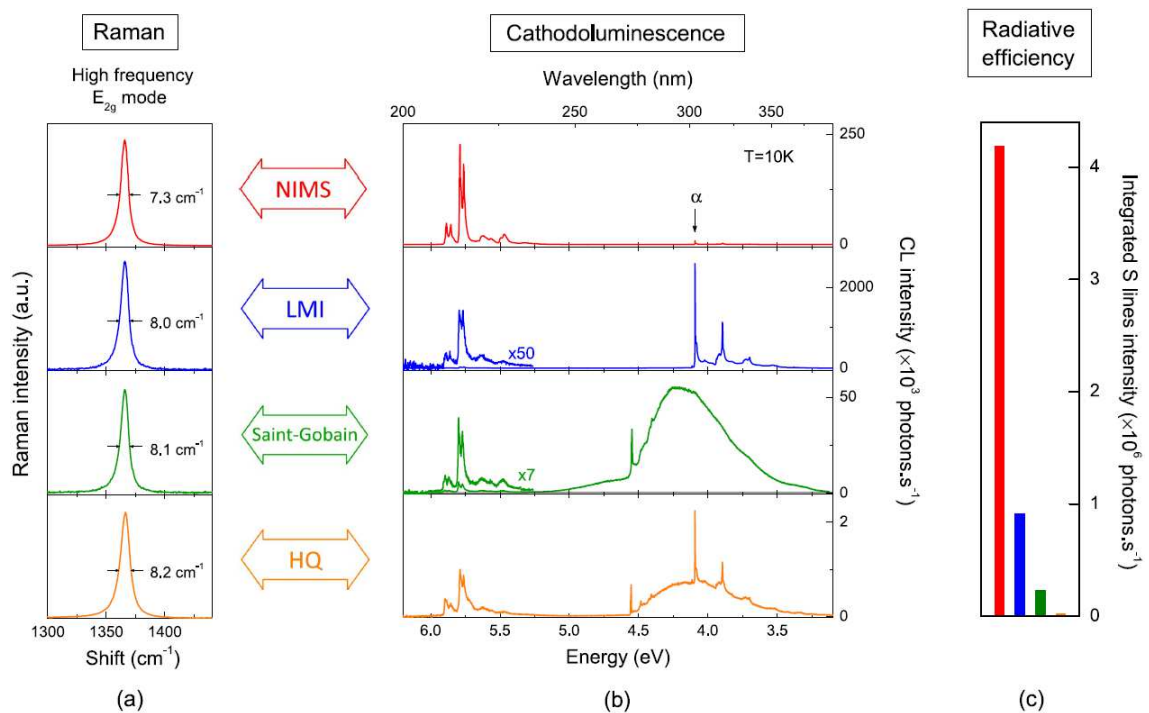


Figure 5.12: Comparaison de couches de hBN d'épaisseur nanométrique provenant de différentes sources. **(a)** Le nitrure de bore hexagonal du NIMS présente la largeur à mi-hauteur la plus fine dans les spectre Raman. **(b)** Il est caractérisé par l'absence de pics de défauts aux énergies inférieures à 5.0 eV contrairement au hBN provenant d'autres sources (HQ Graphene, Saint-Gobain, ou le "Laboratoire Multimatériaux et Interfaces" LMI). **(c)** Le hBN du NIMS présente également la plus grande efficacité quantique. Figures extraite de [116].

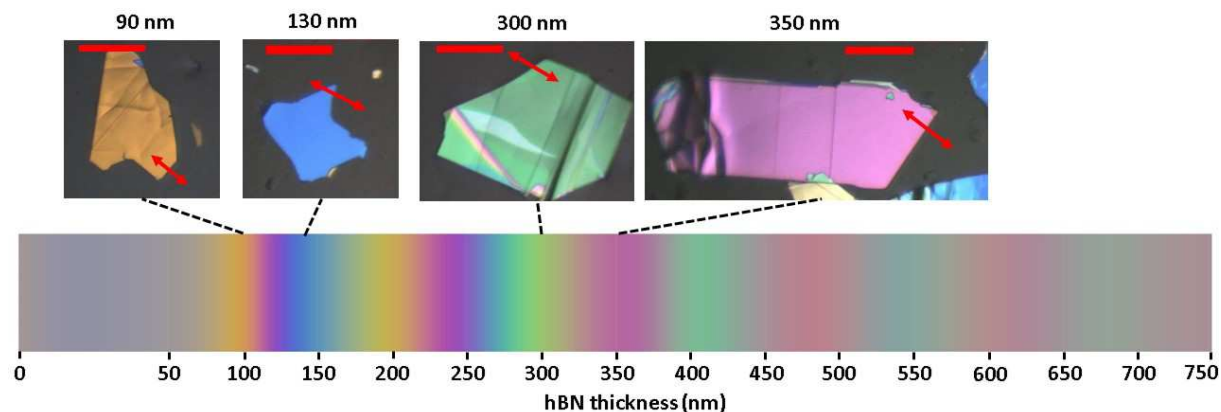


Figure 5.13: Couleurs simulées du hBN sur du PDMS en fonction de l'épaisseur du hBN. A titre de comparaison des images au microscope optique de flocons de hBN sont montrées avec les mesures AFM d'épaisseurs correspondantes. Les flèches rouges indiquent les positions approximatives des mesures AFM. L'échelle rouge sur les images au microscope correspond à $50.3 \mu\text{m}$.

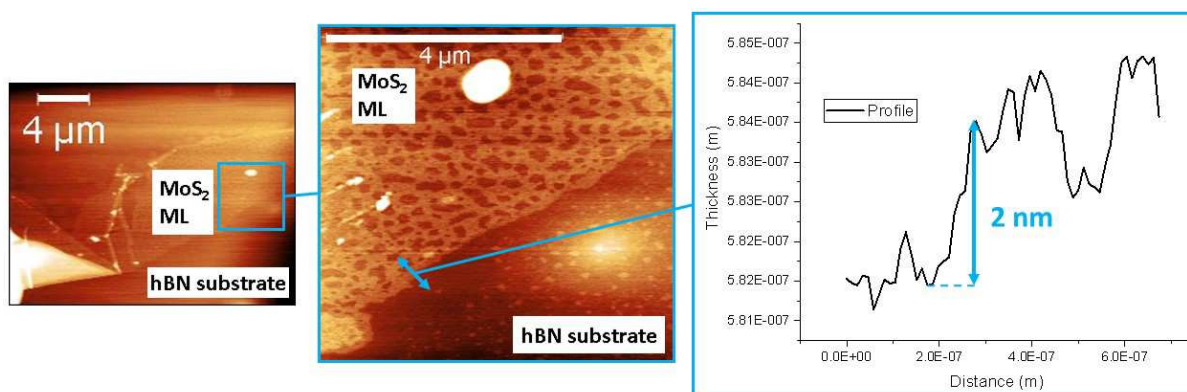


Figure 5.14: Deux images AFM d'une même hétérostructure monocouche de MoS_2/hBN . Les barres d'échelle correspondent à $4 \mu\text{m}$. La position du profil AFM est indiquée par une flèche bleue.

contraste optique [120].

Le problème des résidus et contaminants

La technique de fabrication que nous utilisons implique que les matériaux soient déposés sur du PDMS. Or, ce polymère viscoélastique peut laisser des résidus à la surface des couches après leur dépôt sur un substrat. Les images AFM de la figure 5.14 montrent bien la présence de résidus de PDMS, en particulier à la surface de la monocouche de MoS_2 . Du fait de ces résidus, il n'est pas possible de mesurer la bonne épaisseur pour la monocouche atomique.

Nous utilisons maintenant un autre PDMS qui laisse beaucoup moins de résidus comme le montre la figure 5.15.

En plus du problème des résidus de polymère, d'autres contaminants peuvent être piégés entre les couches au cours du procédé de fabrication d'une hétérostructure. Ces contaminants piégés forment des bulles qui, après un recuit, coalescent pour former des

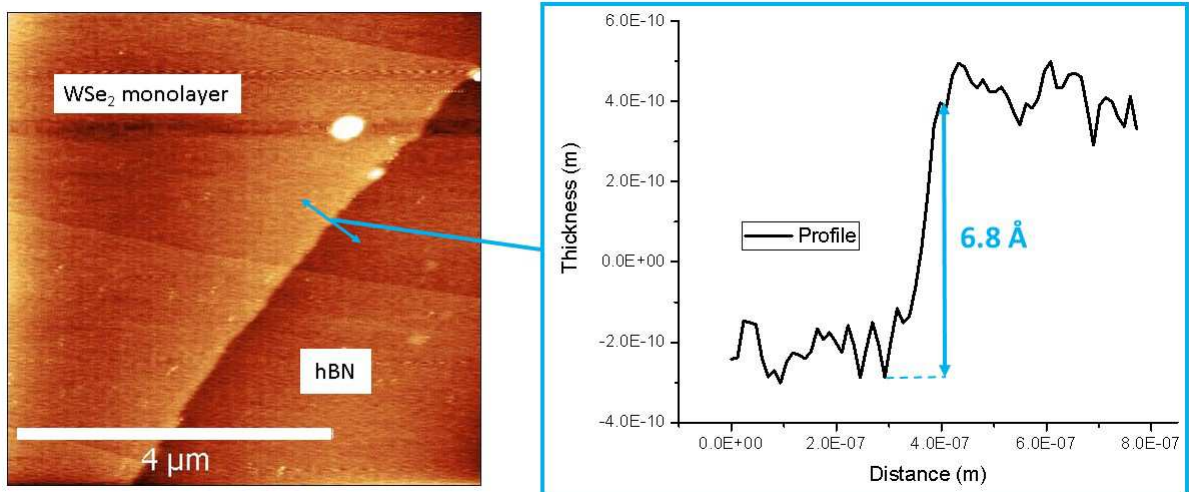


Figure 5.15: Image AFM d'une monocouche de WSe_2 déposée sur un substrat de hBN avec un PDMS laissant moins de résidus. Le profil donne la bonne épaisseur attendue pour une monocouche de TMD (entre 6 et 7 Å).

bulles plus volumineuses (voir figure 5.16). Cela permet d'obtenir des zones dépourvues de bulles où seront par la suite réalisées les expériences de spectroscopie optique.

Spectroscopie Optique de monocouches atomiques de TMD encapsulées dans du hBN

Depuis 2010, les monocouches atomiques de TMD ont été largement étudiées, cependant, pendant plusieurs années la plupart des expériences se sont focalisées sur des monocouches de TMD directement déposées sur du SiO_2 . Bien que ces échantillons donnèrent de bons résultats pour l'étude des principales propriétés, l'analyse précise des expériences de spectroscopie optique était empêchée par des largeurs à mi-hauteur trop grandes caractérisées par un fort élargissement inhomogène [138, 49, 50, 139, 48, 51, 140, 141, 56, 28].

L'effet le plus important est visible pour le MoS_2 où les largeurs à mi-hauteur peuvent atteindre ≈ 50 meV, même à des températures cryogéniques. La figure 5.17 montre des spectres de PL de monocouches de MoS_2 sur SiO_2 à température cryogénique de différents groupes. Les largeurs de raie de plusieurs dizaines de meV apparaissent clairement.

Outre l'élargissement inhomogène, les monocouches de TMD déposées sur SiO_2 sont sujettes à des propriétés optiques changeantes en fonction de l'histoire de l'échantillon et des conditions expérimentales. En effet, pour un échantillon donné, la position en énergie de l'exciton A en PL peut varier après plusieurs cycles de refroidissement dans un cryostat [139]. Ce phénomène fut attribué à des changements dans l'environnement diélectrique à différentes températures, par exemple dû à des molécules d'eau ou d'autres espèces adsorbées à la surface du matériau [138]. De plus, des expériences dépendantes en puissances ont également souligné le problème de la photodégradation et du photodoping [114, 146, 147]. Cet effet fut d'ailleurs bien mis en évidence par Cadiz et al. dans notre groupe.

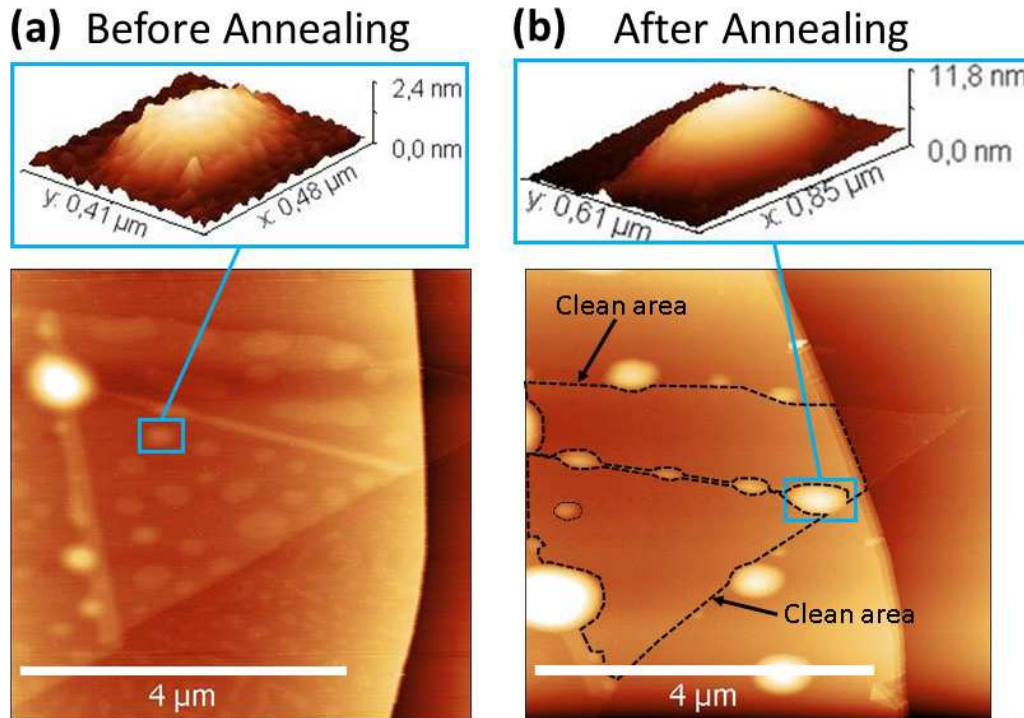


Figure 5.16: Deux images AFM d'une hétérostructure de van der Waals de type hBN/*monocouche* WSe_2 /hBN. Pour l'échantillon en question les bulles sont apparues après le dépôt de la couche supérieure de hBN. (a) Une multitude de bulles sont visible entre le hBN supérieur et le WSe_2 ainsi qu'entre le hBN supérieur et celui du dessous. (b) Après le recuit, les bulles s'agrègent pour former des bulles plus volumineuses et laisser des zones propres, sans bulles, entourées par les pointillés noirs.

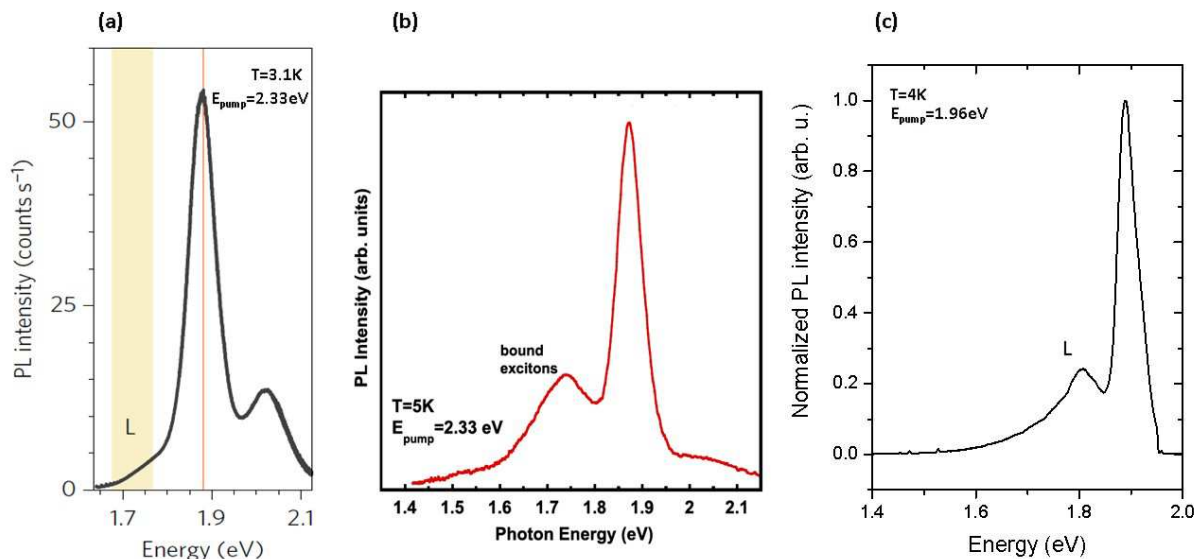


Figure 5.17: Spectres de photoluminescence de monocouches de MoS_2 de différents groupes à température cryogénique. (a) Signal de PL d'une monocouche de MoS_2 obtenue par croissance CVD sur SiO_2 . Figure extraite de [50] (b) Signal de PL d'une monocouche de MoS_2 sur SiO_2 préparée par exfoliation mécanique. Figure extraite de [139]. (c) Nos propres données expérimentales d'une monocouche de MoS_2 monolayer déposée sur SiO_2 par exfoliation mécanique.

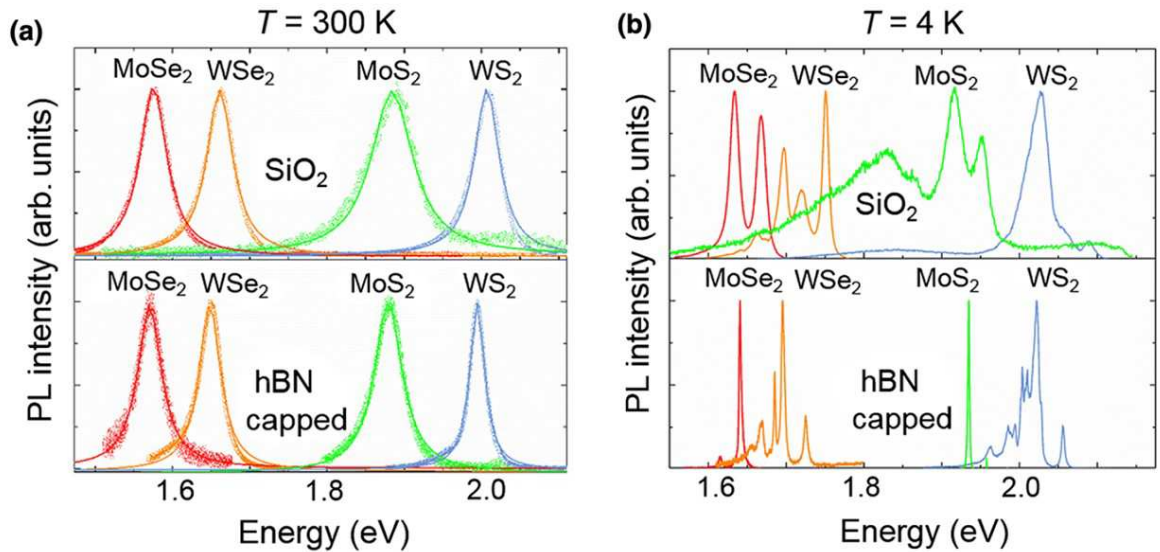


Figure 5.18: (a) Comparaison de spectres de PL pour des monocouches de TMD déposées sur SiO_2 et encapsulées dans du hBN à $T=300\text{ K}$. (b) Tout comme (a), hormis la température qui est de $T=4\text{ K}$. Figures extraites de [111].

Du fait de ces problèmes d’inhomogénéités et d’instabilités, nous encapsulons désormais nos échantillons dans du nitrure de bore hexagonal (hBN). Le hBN présente plusieurs avantages. Tout d’abord il est cristallin et atomiquement plat et ne présente donc pas de défauts de rugosité comme le SiO_2 qui peut induire des contraintes dans les monocouches de TMD. De plus, le hBN du NIMS que nous utilisons est très pur et présente des densités de défauts faibles [115]. Enfin c’est un semiconducteur à grand gap avec $E_g \approx 6\text{ eV}$.

Nous utilisons donc le hBN en tant que substrat mais de plus une fine couche de hBN est également déposée à la surface du TMD pour former une hétérostructure hBN/monocouche de TMD/hBN. Cette couche supérieure de hBN permet de protéger le TMD de l’environnement ambiant et de l’absorption de molécules à la surface.

Etude optique de monocouches de TMD encapsulées dans du hBN

Les principaux représentants de la famille des TMD (MoS_2 , MoSe_2 , WS_2 et WSe_2) ont été étudiés pour comparer la qualité des spectres optiques obtenus lorsque les monocouches de TMD sont déposées sur SiO_2 ou encapsulées dans du hBN. Les principaux résultats sont présentés dans la figure 5.18.

La première observation frappante est l’amélioration considérable de la qualité optique des spectres obtenus avec les structures encapsulées. Pour tous les matériaux, les largeurs de raies sont fortement réduites, s’approchant de la limite homogène. Du fait de cette résolution spectrale accrue, des transitions optiques qui n’apparaissent pas clairement auparavant apparaissent désormais de manière très distincte. Par exemple, si l’on considère à $T=4\text{ K}$ le cas du WS_2 , on constate que lorsque la monocouche est sur du SiO_2 , un seul pic large est visible; en revanche, pour la structure encapsulée ce qui apparaissent

avant comme un seul pic apparaît désormais comme l'addition de plusieurs transitions optiques. Le cas du MoS_2 est également un des plus impressionnants. Lorsque la monocouche de MoS_2 est sur du SiO_2 , le spectre optique est composé de plusieurs raies très larges, tandis que la structure encapsulée laisse apparaître un pic fin principal associé à la transition 1s de l'exciton A.

Ces résultats très encourageants, avec des largeurs de raies aussi fines que 1 meV, montrent que l'encapsulation dans du hBN permettent d'approcher la largeur homogène en réduisant fortement les contributions inhomogènes. Ce fut confirmé par le travail d'autres équipes [163, 146, 164, 165]. En particulier des expériences de mélange à quatre ondes ont confirmé que les contributions inhomogènes sont réduites grâce à l'encapsulation dans du hBN [165, 164].

Cette meilleure résolution spectrale ouvre en effet de nombreuses perspectives expérimentales. Par exemple, les largeurs de raies plus fines permettent de réaliser des mesures de splitting Zeeman et facteur g à des champs magnétiques relativement faibles tel qu'illustré par la figure 5.19 qui montre des résultats avec une monocouche de MoS_2 encapsulée soumise à des champs magnétiques perpendiculaires au plan de la couche.

Etats excités excitoniques: monocouches de MoS_2 encapsulées

Pour étudier les états excitoniques dans notre échantillon de MoS_2 encapsulé, nous avons réalisé des expériences de réflectivité et de PLE (Photoluminescence Excitation) à basse température. Les principaux résultats des expériences sont résumés dans la figure 5.20. Dans le spectre de réflectivité, la principale transition à 1.926 eV correspond à l'exciton A:1s. Environ 150 meV au dessus, la transition B, plus large, est visible. De plus, deux transitions, associées aux transitions A:2s et A:3s, apparaissent à environ ≈ 2.097 eV et ≈ 2.126 eV. Les mesures de PLE montrent clairement des résonances lorsque l'énergie du laser d'excitation est au niveau de ces énergies, une signature du couplage entre ces états et l'état A:1s.

En observant précisément le spectre de réflectivité, on peut être surpris par les forces d'oscillateur relatives f_2/f_1 et f_3/f_1 . En effet, selon le simple modèle hydrogénoïde en 2D, on s'attend à $f_2/f_1 \approx 0.037$ et $f_3/f_1 \approx 0.008$. Dans notre mesure de la figure 5.20 (a), nous mesurons plutôt $f_2/f_1 \approx 0.40$ et $f_3/f_1 \approx 0.09$. Nous apportons deux éléments de réponses pour essayer d'expliquer ces différences.

Tout d'abord, notre structure est constituée de plusieurs couches, et dans cette structure multicouche des effets d'interférences apparaissent. Notre objectif est de modéliser la réponse optique de la structure entière pour vérifier si l'amplitude des transitions optiques peut varier notablement du fait des interférences. Cette approche est représentée schématiquement 5.21.

Grâce à la méthode des matrices de transfert, il est donc possible de calculer r_{tot}

Valley polarization

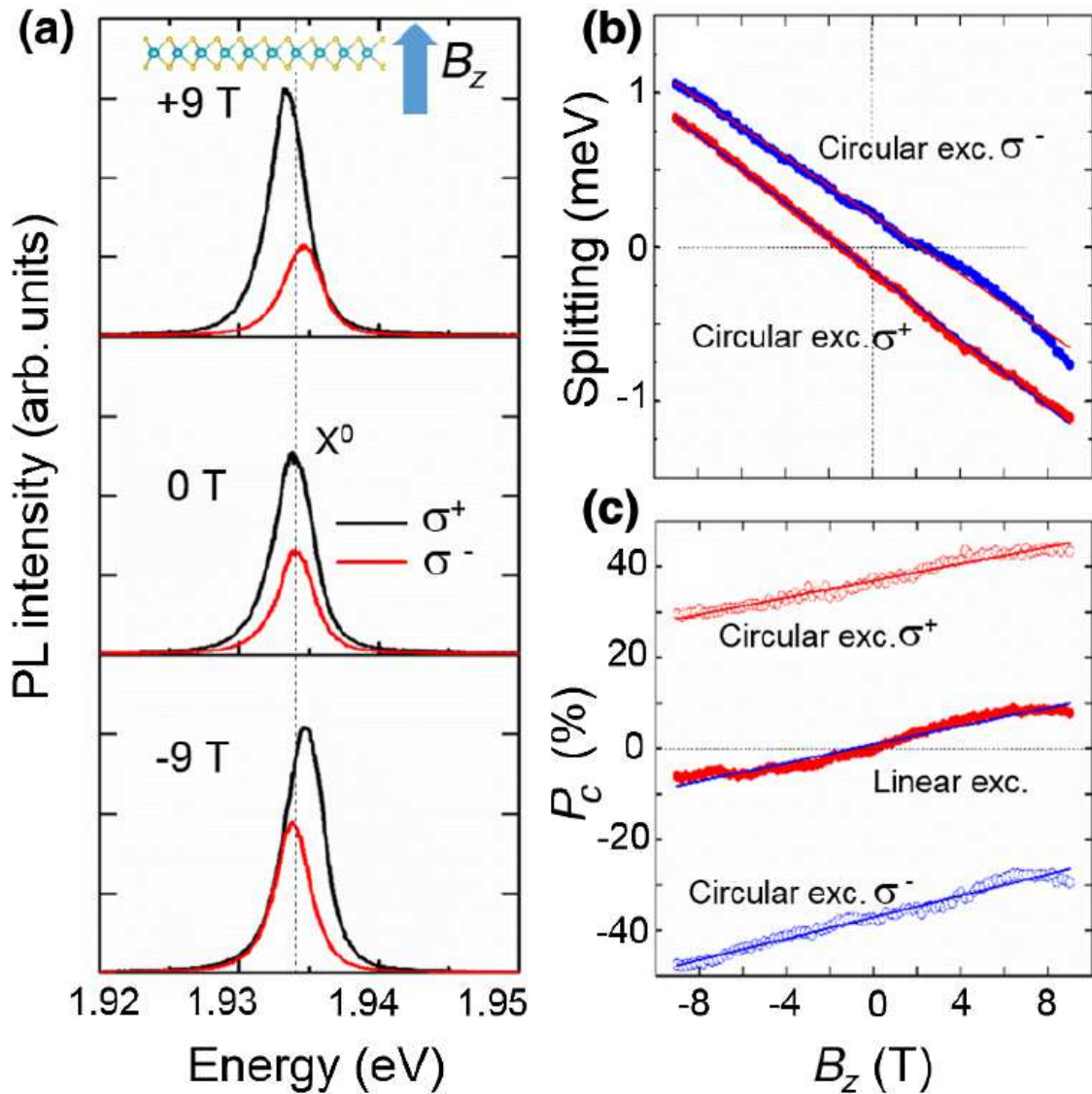


Figure 5.19: (a) Spectres de PL à -9, 0 et +9 T pour des polarisations de détection σ^+ (courbes noires) et σ^- (courbes rouges) et une polarisation d'excitation σ^+ . (b) Splitting Zeeman en fonction du champ magnétique B pour des excitations polarisées σ^+ et σ^- . (c) Mesures de degrés de polarisation circulaire P_c pour des excitations polarisées σ^+ , σ^- et linéaire. Figures extraites de [111].

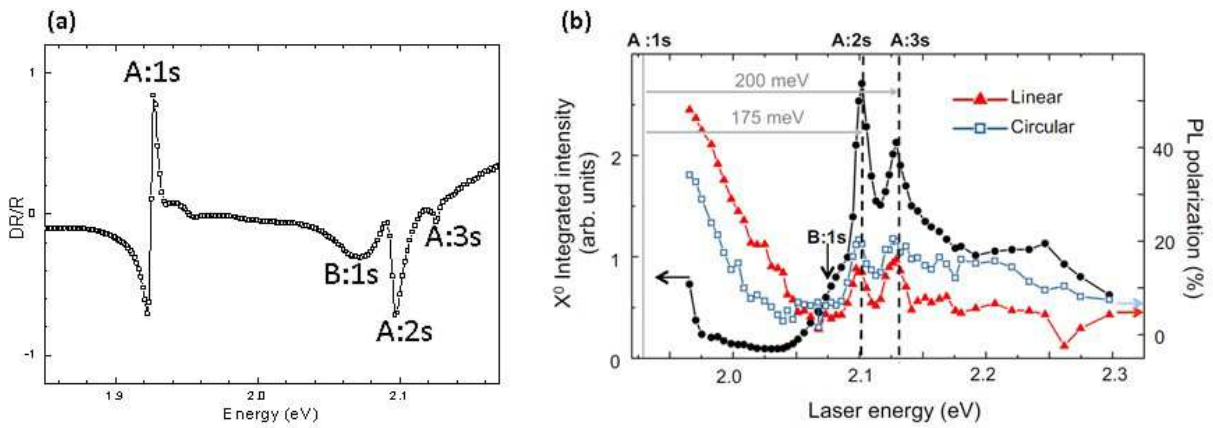


Figure 5.20: (a) Réflectivité différentielle DR/R à température cryogénique réalisée avec une lampe halogène blanche stabilisée en puissance. (b) Expérience de PLE. La PL de l'exciton A:1s est détectée alors que l'énergie du laser d'excitation est scannée sur un intervalle où se trouvent les transition B, A:2s et A:3s. L'intensité en noir, la polarisation linéaire en rouge (sous excitation linéaire) et circulaire en bleue (sous excitation circulaire) sont mesurés. Figure extraite de [181].



Figure 5.21: Structure multicouche considérée pour nos modélisation à l'aide de la technique des matrices de transfert. Dans notre cas, nous pouvons considérer que la lumière se propage perpendiculairement au plan de la monocouche. Le but est de calculer le coefficient de réflexion r_{tot} .

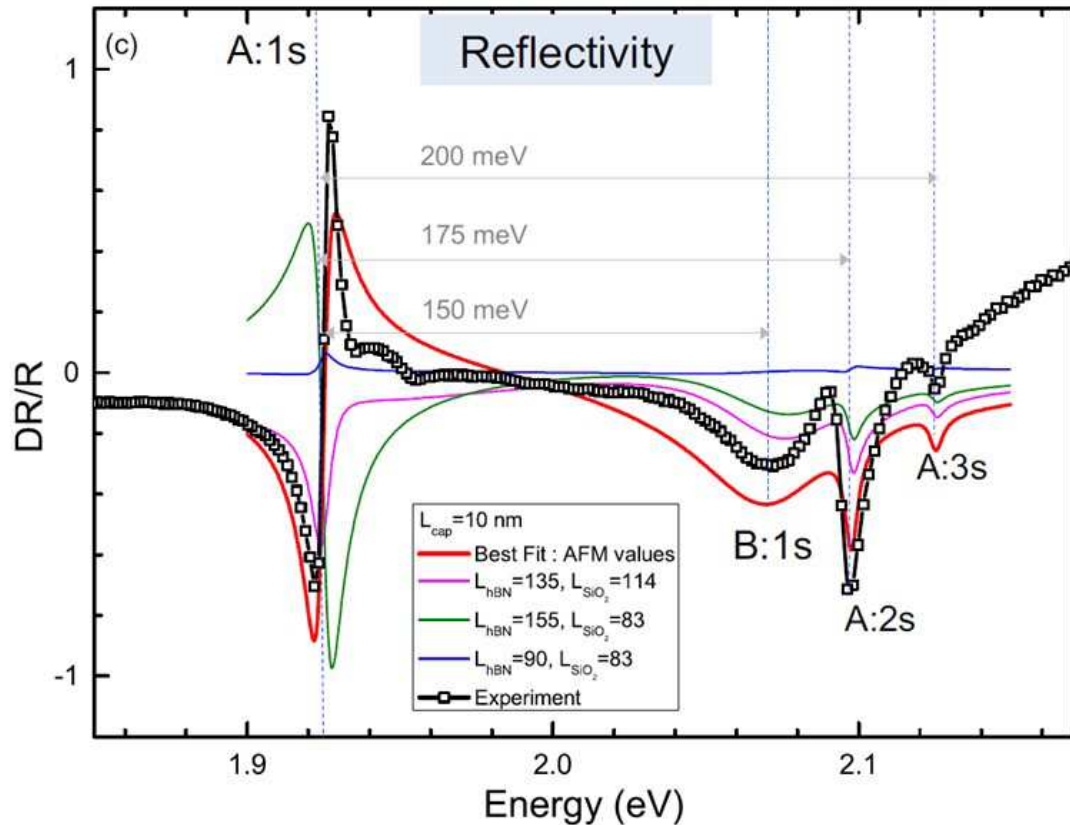


Figure 5.22: En noir, les mêmes données DR/R que dans la figure 5.20 (a). Les spectres colorés sont obtenus grâce à la technique des matrices de transfert pour différentes épaisseurs de la couche inférieure de hBN tandis que le hBN du dessus est gardé à 7 nm (valeur AFM). L'épaisseur de SiO_2 est toujours 83 nm hormis pour la courbe magenta, pour laquelle cette épaisseur est de 114 nm. La courbe rouge correspond au meilleur fit, obtenu avec une couche inférieure de hBN de 130 nm, tel que mesuré à l'AFM. Figure extraite de [181].

et de comparer la réflectance simulée avec nos données de la figure 5.20 (a). Dans nos calculs, l'épaisseur de la couche inférieure de hBN varie tandis que celle du SiO_2 est gardée constante. La comparaison entre les simulations et les données expérimentales est présentée dans la figure 5.22. La courbe la plus proche des données est la rouge et correspond aux valeurs réelles d'épaisseur: $t_{SiO_2}=83$ nm, $t_{bottomhBN}=130$ nm (valeur AFM), et $t_{tophBN}=7$ nm (valeur AFM). Il est très clair que changer les épaisseurs (notamment de la couche inférieure de hBN) peut induire de grosses différences quant aux amplitudes des transitions observées.

Il est donc important de prendre en compte toutes les couches composant l'hétérostructure quand on considère la réponse optique d'un tel système. Les amplitudes des états excitoniques apparaissant en réflectivité sont en effet modulées par la réflectivité de toute la structure. La visibilité de la transition A:2s par rapport à la A:1s peut donc être exaltée du fait de ces effets d'interférences. Depuis l'obtention de ces résultats expérimentaux, nous choisissons désormais avec précautions des couches de hBN aux épaisseurs contrôlées

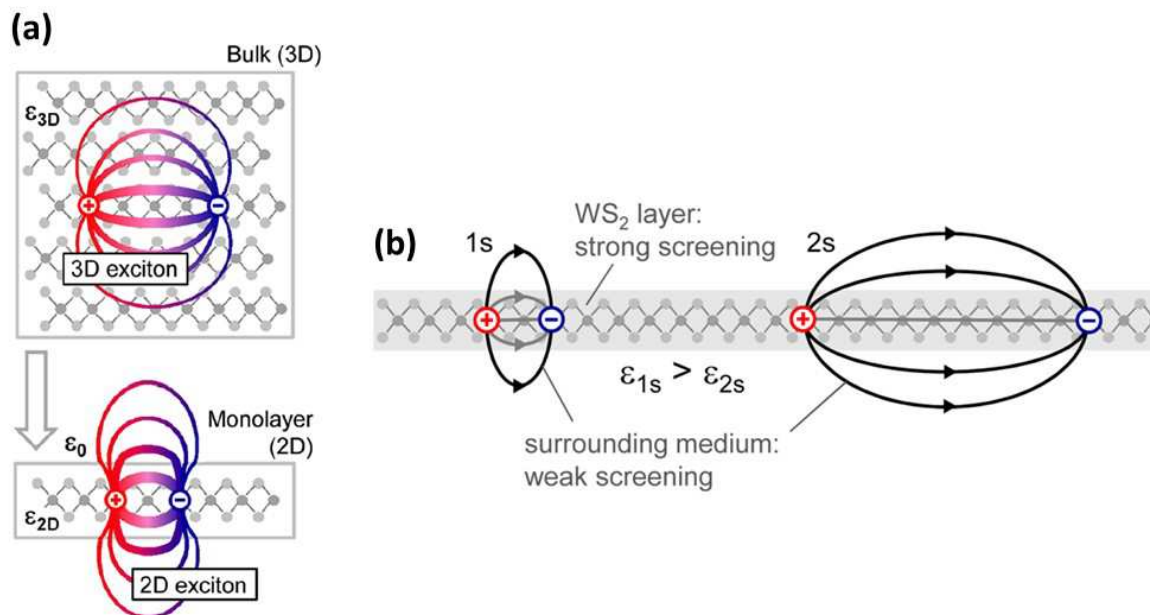


Figure 5.23: (a) Représentation d'une paire électron-trou dans l'espace réel, pour un cristal 3D et un cristal 2D. Les lignes du champ électrique sont aussi représentées. Les changements d'environnement diélectrique sont pris en compte à travers les différentes constantes diélectriques ϵ_{3D} et ϵ_{2D} ; ϵ_0 est la permittivité du vide. (b) Illustration des excitons dans les états 1s et 2s dans une monocouche de WS_2 . Leur interaction est illustrée à travers les lignes de champ électrique. Figures extraites de [27].

afin d'exalter les états excitoniques que nous voulons étudier.

Cependant, un autre effet doit être pris en compte pour expliquer les intensités des états A:2s et A:3s par rapport à A:1s. Il s'agit de prendre en compte l'effet de l'environnement diélectrique sur les énergies de liaison et les forces d'oscillateur relatives. Tel qu'illustré dans la figure 5.23 (a), dans nos monocouches de TMD, nous ne pouvons pas considérer un exciton 2D parfait. Les lignes du champ électrique de l'interaction entre le trou et l'électron dépassent de la monocouche, ressentant alors les effets de l'environnement diélectrique.

Pour modéliser l'effet de l'environnement diélectrique sur les excitons dans nos systèmes en 2D, nous considérons le potentiel de Rytova-Keldysh [32, 33, 183, 184, 185]:

$$V(r) = \frac{-e^2}{8\epsilon_0 r_0} \left(H_0 \left(\frac{\kappa r}{r_0} \right) - Y_0 \left(\frac{\kappa r}{r_0} \right) \right) \quad (5.6)$$

où e est la charge de l'électron, ϵ_0 est la permittivité du vide, r_0 est la longueur d'écrantage, κ est une constante diélectrique moyenne et H_0 et Y_0 sont les fonctions de Struve et de Neumann. La longueur d'écrantage est donnée par $r_0 = 2\pi\chi_{2D}$ avec χ_{2D} la polarisabilité 2D de la monocouche. La constante diélectrique moyenne est donnée par $\kappa = \frac{1}{2}(\epsilon_{top} + \epsilon_{bottom})$ avec ϵ_{top} et ϵ_{bottom} les constantes diélectriques des couches au dessus et en dessous de la monocouche.

L'utilisation de ce modèle pour nos hétérostructures hBN/monocouche de MoS_2 /hBN permet de réaliser des calculs et de comparer les résultats avec ceux obtenus pour un potentiel de Coulomb. La figure 5.24 montre à la fois que des différences d'énergies de

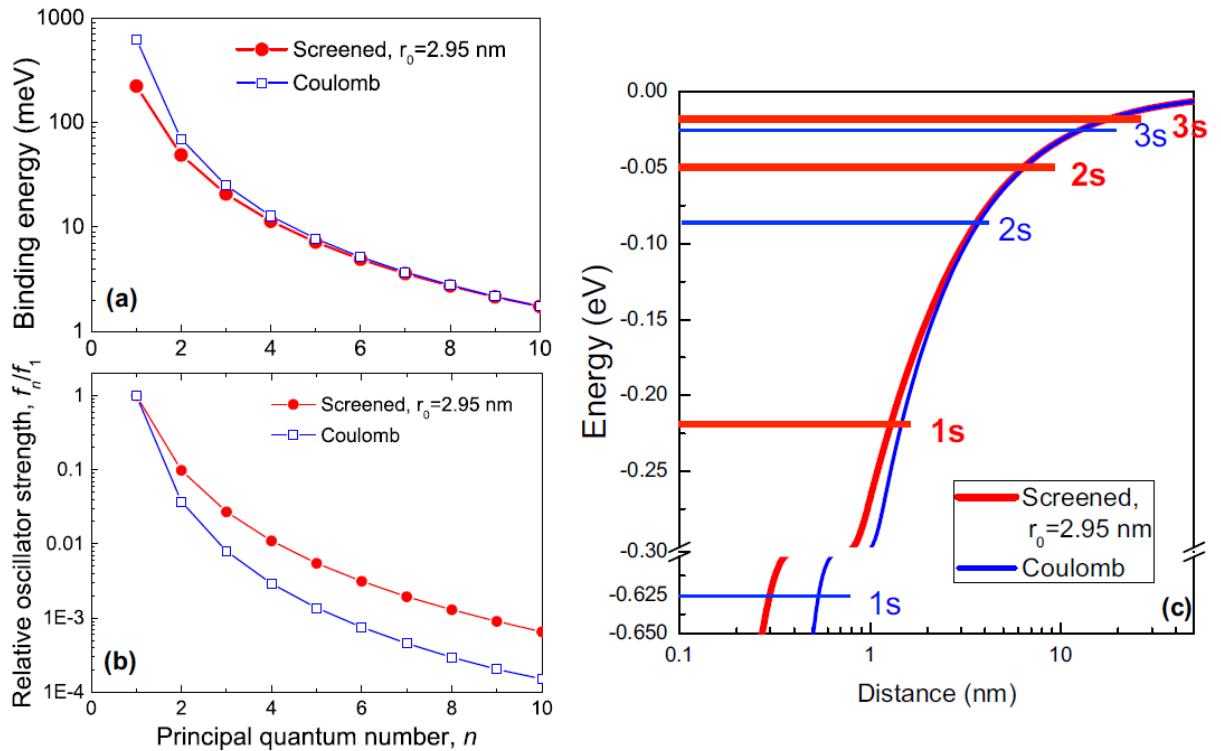


Figure 5.24: Comparaison des calculs obtenus avec deux potentiels $V(r)$: écranté (Rytova-Keldysh) et Coulomb. (a) Valeurs d'énergies de liaison calculées en fonction du nombre quantique principal n . (b) Valeurs de forces d'oscillateur relatives f_n/f_1 calculées en fonction du nombre quantique principal n . (c) Comparaison des états liés en fonction du rayon de l'exciton. Figures extraites de [181].

liaisons sont prévus et qu'il existe de grands écarts pour les forces d'oscillateur relative f_n/f_1 , où n est le nombre quantique principal. En utilisant le potentiel de Rytova-Keldysh, on se rend compte que des forces d'oscillateur relatives plus grandes sont attendues. Ce qui est bien en adéquation avec nos observations expérimentales.

Pour conclure cette partie, nous voulons souligner le fait que des résultats expérimentaux concluants ont également été obtenus avec des hétérostructures encapsulées pour lesquelles les couches inférieures de hBN avaient été obtenues par croissance MBE (Molecular Beam Epitaxy). Sur ce hBN MBE, des monocouches de TMD et des couches supérieures de hBN ont été déposées par le procédé de transfert avec le PDMS. Tout comme les hétérostructures totalement réalisées par exfoliation, ces échantillons ont présenté des qualités optiques supérieures au échantillon monocouche de TMD/ SiO_2 . Des efforts sont effectivement faits pour améliorer les procédés de fabrication pour être capable de concevoir des hétérostructures aux qualités au moins similaires à celles obtenues par exfoliation mécanique.

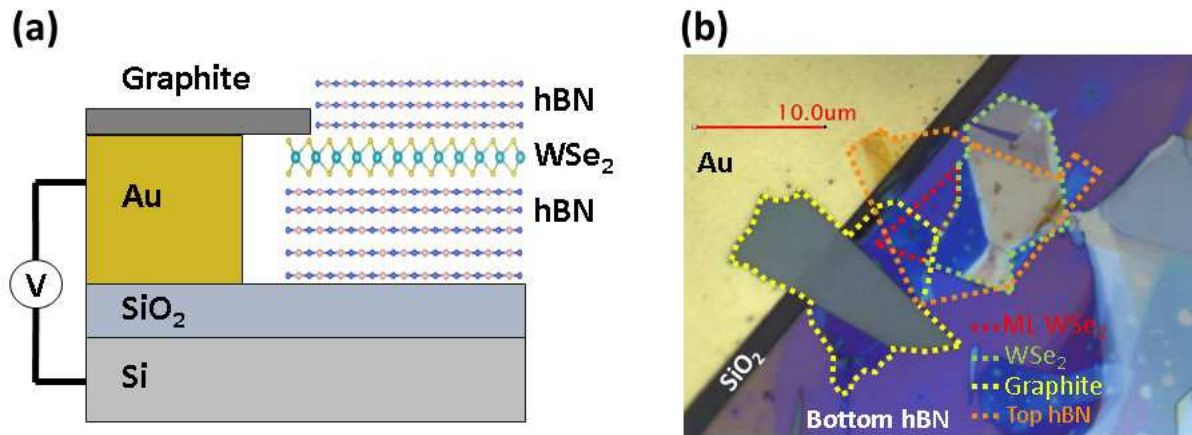


Figure 5.25: (a) Schéma d'une structure à charge ajustable hBN/WSe₂ monolayer/hBN. La monocouche de WSe₂ est connectée à l'électrode en or par une couche de graphite. Figure extraite de [189]. (b) Image microscopique correspondante. La distinction est faite entre la monocouche entourée de pointillés rouges et la partie multicouche du WSe₂ entourée par des pointillés verts.

Dispositifs à charge ajustable

Jusqu'à présent, nous nous sommes concentrés sur les excitons, composés de paires électron-trou. Ce concept de quasiparticules liées peut être étendu. C'est ainsi qu'à l'aide d'échantillons dont nous pouvons changer le dopage nous allons observer des trions composés de trois particules. En dopage n, l'injection d'électrons en excès va mener à l'observation de trions négatifs constitués de deux électrons et un trou. En dopage p, l'injection de trous en excès va mener à l'observation de trions positifs constitués de deux trous et un électron.

Un exemple de structure à charge ajustable est illustré dans la figure 5.25. Dans cette configuration, les électrodes étaient d'abord déposées puis l'hétérostructure était ensuite fabriquée à l'aide de la technique du PDMS. En revanche il est aussi possible de fabriquer d'abord l'hétérostructure puis d'ajouter les contacts en or après, à l'aide de procédés tels que la lithographie électronique.

Structure à charge ajustable de MoS₂ 2D encapsulé

Dans la figure 5.26, des données de réflectivité différentielle en fonction de la tension appliquée sont montrées pour une monocouche de MoS₂ encapsulée. Dans ce cas, les régimes neutre et dopé n sont observés. Dans le régime neutre, les transitions A:1s, A:2s et B:1s sont visibles, avec une séparation en énergie de 155 meV entre A:1s et B:1s, ce qui correspond environ au splitting spin-orbit attendu dans la bande de valence. Quand des électrons sont injectés dans la structure, les forces d'oscillateur des transitions associées à l'exciton neutre A diminuent fortement. Même si A:1s est encore visible, la transition A:2s disparaît totalement. Deux transitions à plus basse énergies comparées à A:1s et B:1s apparaissent en régime dopé n. Ces deux transitions sont associées aux trions négatifs des excitons A et B notés A⁻ et B⁻.

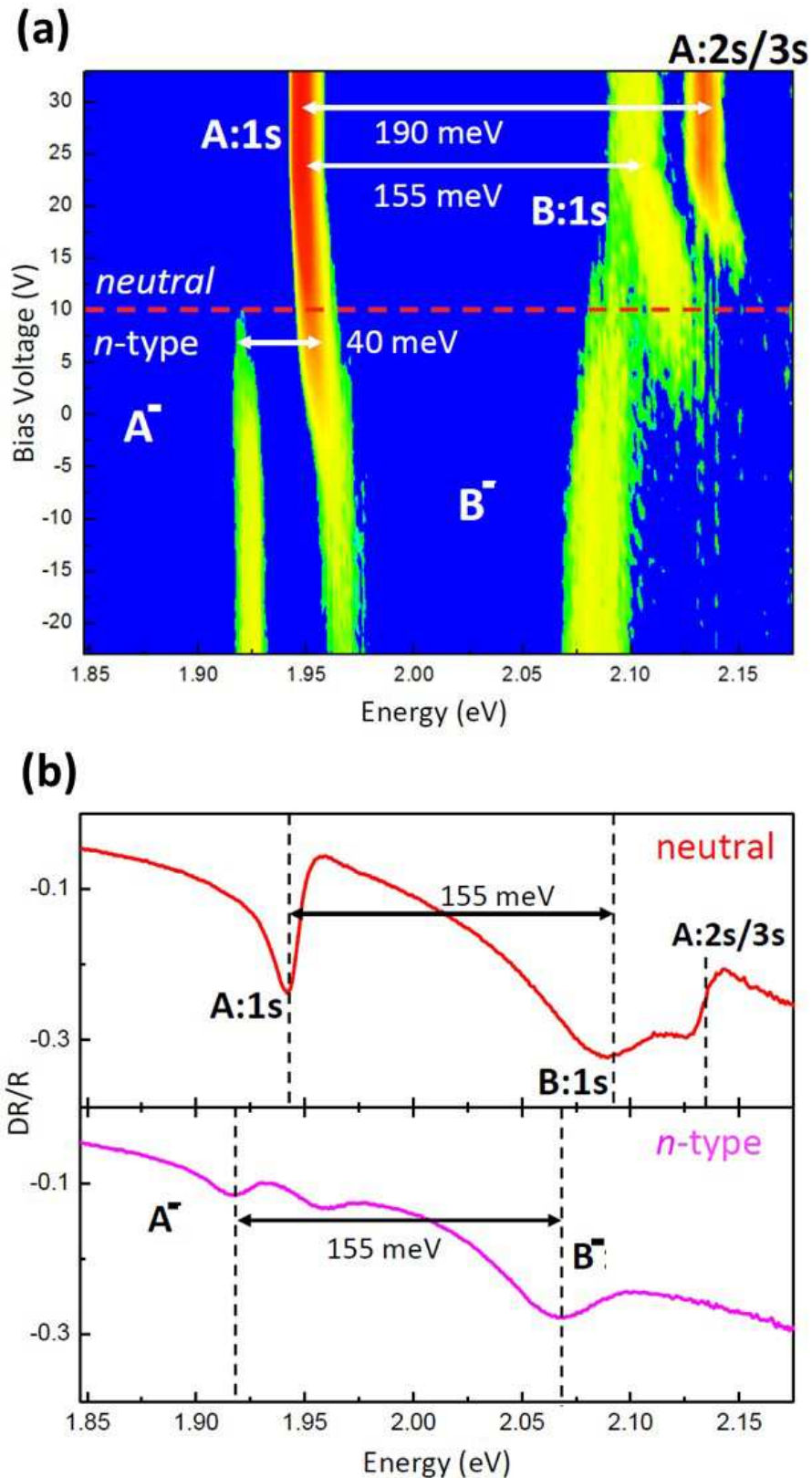


Figure 5.26: Structure à charge ajustable à base d'une monocouche de MoS_2 à température cryogénique. **(a)** Réflectivité différentielle en fonction de l'énergie et de la tension appliquée. **(b)** Spectres de DR/R à deux tensions correspondant aux régimes neutre et dopé n. Figures extraites des suppléments de [181].

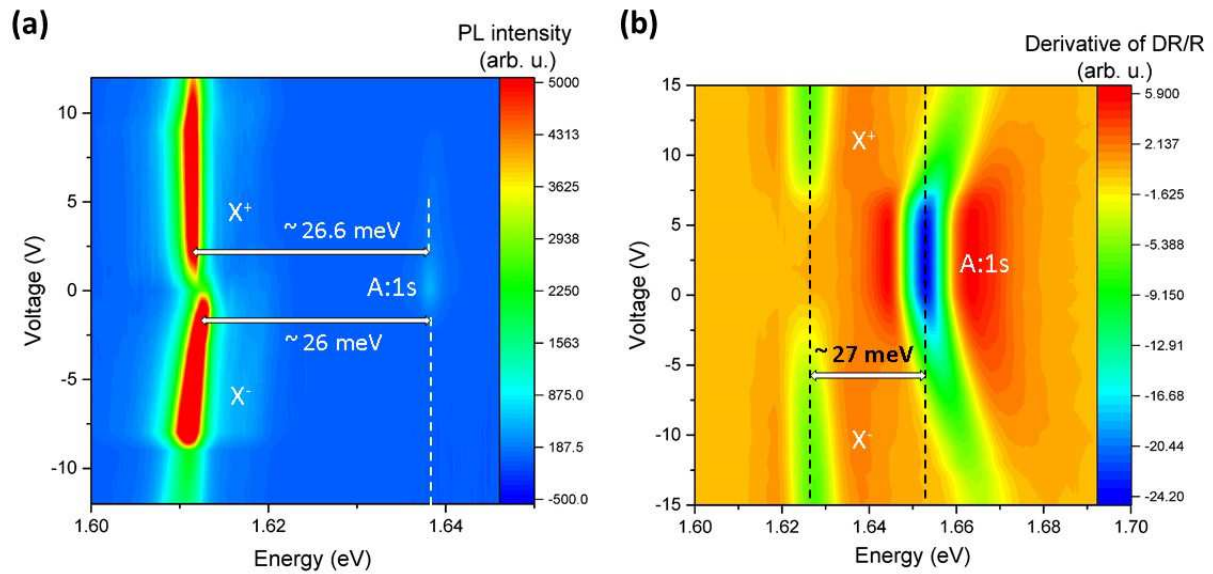


Figure 5.27: Dispositif à charge ajustable à base d'une monocouche de $MoSe_2$ à température cryogénique. Aux tensions positives des trous sont injectés dans la monocouche tandis que des électrons sont injectés aux tensions négatives. (a) Photoluminescence en fonction de l'énergie et de la tension appliquée. Les trions X^+ et X^- sont indiqués ainsi que la transition de l'exciton $A:1s$ qui est comparativement plus beaucoup plus faible en intensité. (b) Dérivée de la réflectivité différentielle DR/R en fonction de l'énergie et de la tension appliquée.

Structure à charge ajustable de $MoSe_2$ 2D encapsulé

Même dans les structures où le dopage ne peut pas être contrôlé, les monocouches de $MoSe_2$ présentent souvent deux pics en PL. Celui à plus haute énergie autour de 1.64 eV correspond à l'exciton $A:1s$ tandis que le pic qui se trouve environ 26 meV en dessous était généralement associé à un trion. Nos expériences ont en effet permis de confirmer la nature de ce pic en pouvant accéder aux différents régimes de dopage: n, neutre et p. Les résultats de PL et de réflectivité sont illustrés par la figure 5.27.

Structure à charge ajustable de WSe_2 2D encapsulé

Les spectres optiques des monocouches de WSe_2 encapsulées révèlent une structure très riche avec de nombreux pics qui doivent être identifiés. En utilisant une structure à charge ajustable, nous allons identifier les transitions associées aux trions.

Les données de la dérivée de DR/R sont présentées dans la figure 5.28. Les régimes de dopage neutre, p et n sont atteints en faisant varier la tension appliquée à l'électrode reliée à la couche. Cette fois-ci, contrairement au MoS_2 et au $MoSe_2$, des différences notables apparaissent entre les régimes de dopage p et n. Dans les deux cas, nous observons des pics qui apparaissent et qui sont associés aux trions, cependant alors qu'en régime p un seul trion positif est visible, en régime n deux trions négatifs apparaissent.

Pour expliquer cette différence entre trions négatifs et positifs, il est intéressant de

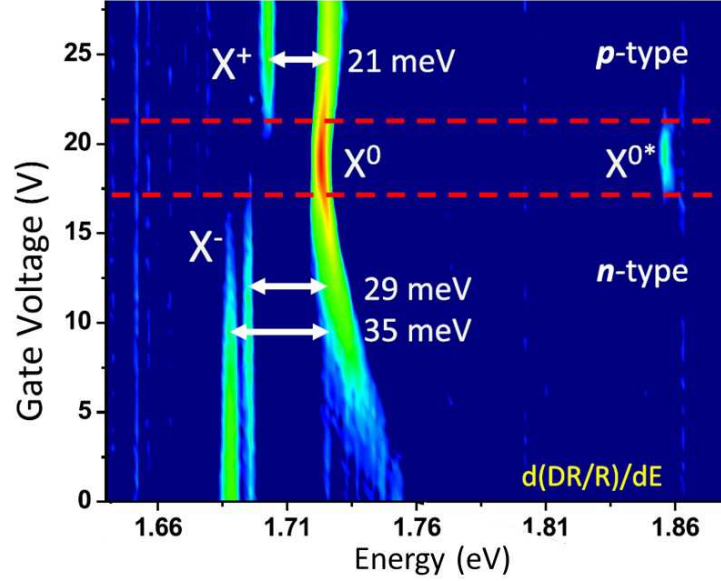


Figure 5.28: Dérivée de la réflectivité différentielle (DR/R) en fonction de l'énergie et de la tension appliquée pour un dispositif à charge ajustable de WSe_2 2D encapsulé à température cryogénique. X^0 est l'exciton neutre (A:1s), X^{0*} est un état excité de l'exciton neutre. X^+ et X^- sont les triions positifs et négatifs. Figure extraite de [189].

considérer les configurations des particules formant les triions en questions. Dans quelles bandes se trouvent-elles?

Du fait du splitting spin-orbite très grand dans la bande de valence, nous considérerons que les trous ne peuvent occuper que les bandes de valence les plus hautes en énergie.

Si nous commençons par le cas du triion positif (deux trous et un électron), les deux trous se trouvent en haut des bandes de valence dans les vallées K^+ et K^- . Il reste ensuite 4 possibilités pour l'électron ayant un spin noté s_e et un indice de vallée τ_e . Seulement deux sont brillantes et elles sont équivalentes en énergie. Le tableau ci-dessous résume ces 4 configurations:

#	s_e	τ_e	Brillant/Sombre
1	+1/2	+1	Brillant (σ^+)
2	-1/2	-1	Brillant (σ^-)
3	-1/2	+1	Sombre
4	+1/2	-1	Sombre

Table 5.3: Triions symétriques X^+ . L'état électronique est caractérisé par son spin (s_e) et son indice de vallée (τ_e).

Deux de ces configurations sont illustrées dans la figure 5.29.

Pour le triion négatif, le nombre de configurations possibles est plus grand. Il y a deux possibilités pour le trou qui peut se trouver soit en K^+ soit en K^- (indiqué par l'indice de vallée τ_h). Il y a ensuite 6 possibilités pour les deux électrons ayant des spins s_1 et s_2 et des indices de vallée τ_1 et τ_2 . Ce qui fait en tout 12 possibilités qui sont résumées dans le tableau ci-dessous:

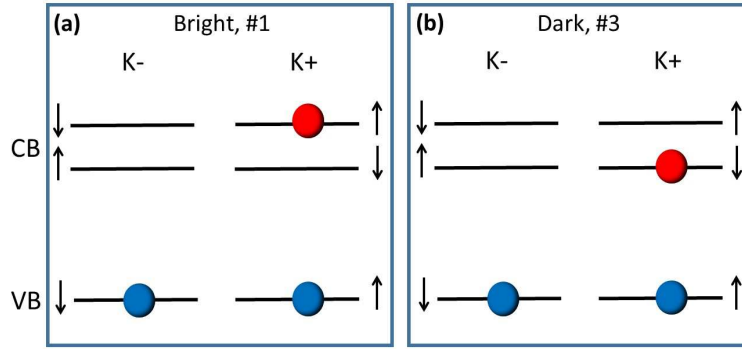


Figure 5.29: Trions positifs X^+ dans la monocouche de WSe_2 . (a) Trion brillant avec son électron dans la vallée K^+ . (b) Trion sombre avec son électron dans la vallée K^+ . Seulement les transitions conservant le spin sont actives optiquement.

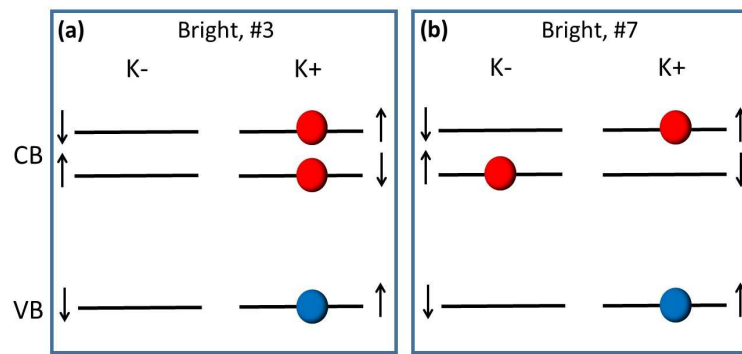


Figure 5.30: Trions négatifs X^- dans une monocouche de WSe_2 . (a) Schéma représentant un trion intravalley. (b) Schéma représentant un trion intervalley.

#	s_1	τ_1	s_2	τ_2	τ_h	Brillant/Sombre
1	+1/2	+1	-1/2	-1	+1	Brillant (σ^+)
2	+1/2	+1	-1/2	-1	-1	Brillant (σ^-)
3	+1/2	+1	-1/2	+1	+1	Brillant (σ^+)
4	+1/2	-1	-1/2	-1	-1	Brillant (σ^-)
5	+1/2	+1	-1/2	+1	-1	Sombre
6	+1/2	-1	-1/2	-1	+1	Sombre
7	+1/2	-1	+1/2	+1	+1	Brillant (σ^+)
8	-1/2	-1	-1/2	+1	-1	Brillant (σ^-)
9	+1/2	-1	+1/2	+1	-1	Sombre
10	-1/2	-1	-1/2	+1	+1	Sombre
11	-1/2	+1	+1/2	-1	+1	Sombre
12	-1/2	+1	+1/2	-1	-1	Sombre

Table 5.4: Trions symétriques X^- . Les deux électrons e_1 et e_2 sont caractérisés par leur spin (s_1 and s_2) et leur indice de vallée (τ_1 et τ_2). L'état du trou est donné par son indice de vallée τ_h (son spin est déduit immédiatement).

La figure illustre les deux catégories de trions négatifs que nous pouvons différencier: intravalley et intervalley.

Pour expliquer la différence d'énergie de liaison entre le trion inter et le trion intravalley, l'interaction d'échange à courte portée électron-électron et électron-trou doivent être prises en compte. Cela explique le splitting entre ces deux types de trions, d'environ 7 meV que l'on peut désormais mesurer expérimentalement grâce à nos structures encapsulées dans du hBN. Outre les trions, notons que les spectres de PL en fonctions de la tension appliquée montrent également de nombreuses autres transitions telles que les biexcitons ou même les biexcitons chargés.

Conclusions

Les hétérostructures de van der Waals de monocouches de TMD encapsulées nous ont permis d'améliorer grandement la qualité optique de nos échantillons. Cette amélioration notable nous a permis de réaliser des études des transitions apparaissant au cours de nos expériences de spectroscopie. En distinguant les excitons brillants ou noirs, les trions et biexcitons et leurs différentes configurations, notre compréhension des monocouches atomiques de TMD a progressé. Les hétérostructures de van der Waals ouvrent de nombreuses perspectives, telles que l'étude d'effets de proximité, par exemple avec des matériaux de van der Waals magnétique tels que le CrI_3 ou le $CrBr_3$. Nous pourrions ainsi imaginer induire un splitting Zeeman par effet de proximité dans une monocouche de TMD déposée sur le matériau magnétique. Un autre axe de recherche consiste à coupler la résonance excitonique d'une monocouche de TMD avec le mode d'une cavité photonique. Il est alors possible d'atteindre le couplage fort entre les modes excitonique et photonique. Par ailleurs l'étude des effets excitoniques dans des multicouches de TMD ou des hétérostructures combinant différents TMD est un sujet de recherche actuel, ainsi que l'observation de motifs de Moiré qui peuvent induire des variations de structure de bande. Enfin, l'amélioration des techniques de fabrication et de croissance des échantillons représentent encore à l'heure actuelle un véritable challenge si l'on veut que les monocouches de TMD deviennent viables industriellement dans le futur.

Bibliography

- [1] Kin Fai Mak et al. “Atomically thin MoS₂: a new direct-gap semiconductor”. In: *Physical review letters* 105.13 (2010), p. 136805.
- [2] Andrea Splendiani et al. “Emerging photoluminescence in monolayer MoS₂”. In: *Nano letters* 10.4 (2010), pp. 1271–1275.
- [3] •. *The Nobel Prize in Physics 2010*. 2010. URL: <https://www.nobelprize.org/prizes/physics/2010/prize-announcement/>.
- [4] Jian-Hao Chen et al. “Intrinsic and extrinsic performance limits of graphene devices on SiO₂”. In: *Nature nanotechnology* 3.4 (2008), p. 206.
- [5] Alexander A Balandin et al. “Superior thermal conductivity of single-layer graphene”. In: *Nano letters* 8.3 (2008), pp. 902–907.
- [6] Changgu Lee et al. “Measurement of the elastic properties and intrinsic strength of monolayer graphene”. In: *science* 321.5887 (2008), pp. 385–388.
- [7] Kostya S Novoselov et al. “Two-dimensional atomic crystals”. In: *Proceedings of the National Academy of Sciences* 102.30 (2005), pp. 10451–10453.
- [8] Pulickel Ajayan, Philip Kim, and Kaustav Banerjee. “van der Waals materials”. In: *Physics Today* 69 (2016), pp. 9–38.
- [9] Andre K Geim and Irina V Grigorieva. “Van der Waals heterostructures”. In: *Nature* 499.7459 (2013), p. 419.
- [10] Andres Castellanos-Gomez. “Why all the fuss about 2D semiconductors?” In: *Nature Photonics* 10.4 (2016), p. 202.
- [11] Branimir Radisavljevic et al. “Single-layer MoS₂ transistors”. In: *Nature nanotechnology* 6.3 (2011), p. 147.
- [12] Qing Hua Wang et al. “Electronics and optoelectronics of two-dimensional transition metal dichalcogenides”. In: *Nature nanotechnology* 7.11 (2012), p. 699.
- [13] Andor Kormányos et al. “k·p theory for two-dimensional transition metal dichalcogenide semiconductors”. In: *2D Materials* 2.2 (2015), p. 022001.
- [14] ZY Zhu, YC Cheng, and Udo Schwingenschlögl. “Giant spin-orbit-induced spin splitting in two-dimensional transition-metal dichalcogenide semiconductors”. In: *Physical Review B* 84.15 (2011), p. 153402.
- [15] J Frenkel. “On the transformation of light into heat in solids. I”. In: *Physical Review* 37.1 (1931), p. 17.

- [16] JA Frenkel. “On the transformation of light into heat in solids. II”. In: *Physical Review* 37.10 (1931), p. 1276.
- [17] Gregory H Wannier. “The structure of electronic excitation levels in insulating crystals”. In: *Physical Review* 52.3 (1937), p. 191.
- [18] Go Dresselhaus. “Effective mass approximation for excitons”. In: *Journal of Physics and Chemistry of Solids* 1.1-2 (1956), pp. 14–22.
- [19] Claus F Klingshirn. *Semiconductor optics*. Springer Science & Business Media, 2012.
- [20] Taewoo Jeon et al. “Hybrid perovskites: effective crystal growth for optoelectronic applications”. In: *Advanced Energy Materials* 7.19 (2017), p. 1602596.
- [21] Diana Y Qiu, H Felipe, and Steven G Louie. “Optical spectrum of MoS 2: many-body effects and diversity of exciton states”. In: *Physical review letters* 111.21 (2013), p. 216805.
- [22] MS Dresselhaus. “Solid state physics part ii optical properties of solids”. In: (2001).
- [23] Jozef T Devreese and F Peeters. “Polarons and excitons in polar semiconductors and ionic crystals”. In: vol. 127. Springer Science & Business Media, 2013. Chap. Introduction to the theory of excitons by R.J. Elliott, pp. 271–292.
- [24] Gang Wang et al. “Colloquium: Excitons in atomically thin transition metal dichalcogenides”. In: *Reviews of Modern Physics* 90.2 (2018), p. 021001.
- [25] Miguel M Ugeda et al. “Giant bandgap renormalization and excitonic effects in a monolayer transition metal dichalcogenide semiconductor”. In: *Nature materials* 13.12 (2014), p. 1091.
- [26] Keliang He et al. “Tightly bound excitons in monolayer WSe 2”. In: *Physical review letters* 113.2 (2014), p. 026803.
- [27] Alexey Chernikov et al. “Exciton binding energy and nonhydrogenic Rydberg series in monolayer WS 2”. In: *Physical review letters* 113.7 (2014), p. 076802.
- [28] Gang Wang et al. “Giant enhancement of the optical second-harmonic emission of WSe 2 monolayers by laser excitation at exciton resonances”. In: *Physical review letters* 114.9 (2015), p. 097403.
- [29] AT Hanbicki et al. “Measurement of high exciton binding energy in the monolayer transition-metal dichalcogenides WS2 and WSe2”. In: *Solid State Communications* 203 (2015), pp. 16–20.
- [30] Ziliang Ye et al. “Probing excitonic dark states in single-layer tungsten disulphide”. In: *Nature* 513.7517 (2014), p. 214.
- [31] Heather M Hill et al. “Observation of excitonic Rydberg states in monolayer MoS2 and WS2 by photoluminescence excitation spectroscopy”. In: *Nano letters* 15.5 (2015), pp. 2992–2997.
- [32] Natalia S Rytova. “Screened potential of a point charge in a thin film”. In: *arXiv preprint arXiv:1806.00976* (2018).

- [33] LV Keldysh. “Coulomb interaction in thin semiconductor and semimetal films”. In: *Soviet Journal of Experimental and Theoretical Physics Letters* 29 (1979), p. 658.
- [34] G Wang et al. “In-plane propagation of light in transition metal dichalcogenide monolayers: optical selection rules”. In: *Physical review letters* 119.4 (2017), p. 047401.
- [35] You Zhou et al. “Probing dark excitons in atomically thin semiconductors via near-field coupling to surface plasmon polaritons”. In: *Nature nanotechnology* 12.9 (2017), p. 856.
- [36] Cédric Robert et al. “Fine structure and lifetime of dark excitons in transition metal dichalcogenide monolayers”. In: *Physical Review B* 96.15 (2017), p. 155423.
- [37] MR Molas et al. “Brightening of dark excitons in monolayers of semiconducting transition metal dichalcogenides”. In: *2D Materials* 4.2 (2017), p. 021003.
- [38] Xiao-Xiao Zhang et al. “Magnetic brightening and control of dark excitons in monolayer WSe₂”. In: *Nature nanotechnology* 12.9 (2017), p. 883.
- [39] MM Glazov et al. “Exciton fine structure and spin decoherence in monolayers of transition metal dichalcogenides”. In: *Physical Review B* 89.20 (2014), p. 201302.
- [40] Thomas Mueller and Ermin Malic. “Exciton physics and device application of two-dimensional transition metal dichalcogenide semiconductors”. In: *npj 2D Materials and Applications* 2.1 (2018), p. 29.
- [41] Donald C Reynolds. *Excitons: their properties and uses*. Elsevier, 2012.
- [42] Thorsten Deilmann and Kristian Sommer Thygesen. “Finite-momentum exciton landscape in mono-and bilayer transition metal dichalcogenides”. In: *2D Materials* (2019).
- [43] C Robert et al. “Exciton radiative lifetime in transition metal dichalcogenide monolayers”. In: *Physical Review B* 93.20 (2016), p. 205423.
- [44] Tomasz Jakubczyk et al. “Radiatively limited dephasing and exciton dynamics in MoSe₂ monolayers revealed with four-wave mixing microscopy”. In: *Nano letters* 16.9 (2016), pp. 5333–5339.
- [45] Di Xiao, Wang Yao, and Qian Niu. “Valley-contrasting physics in graphene: magnetic moment and topological transport”. In: *Physical Review Letters* 99.23 (2007), p. 236809.
- [46] Wang Yao, Di Xiao, and Qian Niu. “Valley-dependent optoelectronics from inversion symmetry breaking”. In: *Physical Review B* 77.23 (2008), p. 235406.
- [47] Di Xiao et al. “Coupled spin and valley physics in monolayers of MoS₂ and other group-VI dichalcogenides”. In: *Physical review letters* 108.19 (2012), p. 196802.
- [48] Ting Cao et al. “Valley-selective circular dichroism of monolayer molybdenum disulphide”. In: *Nature communications* 3 (2012), p. 887.
- [49] Hualing Zeng et al. “Valley polarization in MoS₂ monolayers by optical pumping”. In: *Nature nanotechnology* 7.8 (2012), p. 490.

- [50] Andre Neumann et al. “Opto-valleytronic imaging of atomically thin semiconductors”. In: *Nature nanotechnology* 12.4 (2017), p. 329.
- [51] D Lagarde et al. “Carrier and polarization dynamics in monolayer MoS₂”. In: *Physical review letters* 112.4 (2014), p. 047401.
- [52] Cong Mai et al. “Many-body effects in valleytronics: Direct measurement of valley lifetimes in single-layer MoS₂”. In: *Nano letters* 14.1 (2013), pp. 202–206.
- [53] Qinsheng Wang et al. “Valley carrier dynamics in monolayer molybdenum disulfide from helicity-resolved ultrafast pump–probe spectroscopy”. In: *ACS nano* 7.12 (2013), pp. 11087–11093.
- [54] CR Zhu et al. “Exciton valley dynamics probed by Kerr rotation in WSe₂ monolayers”. In: *Physical Review B* 90.16 (2014), p. 161302.
- [55] T Yu and MW Wu. “Valley depolarization due to intervalley and intravalley electron-hole exchange interactions in monolayer MoS₂”. In: *Physical Review B* 89.20 (2014), p. 205303.
- [56] Aaron M Jones et al. “Optical generation of excitonic valley coherence in monolayer WSe₂”. In: *Nature nanotechnology* 8.9 (2013), p. 634.
- [57] Prasenjit Dey et al. “Gate-controlled spin-valley locking of resident carriers in WSe₂ monolayers”. In: *Physical review letters* 119.13 (2017), p. 137401.
- [58] Andres Castellanos-Gomez et al. “Deterministic transfer of two-dimensional materials by all-dry viscoelastic stamping”. In: *2D Materials* 1.1 (2014), p. 011002.
- [59] Riccardo Frisenda et al. “Atomically thin p–n junctions based on two-dimensional materials”. In: *Chemical Society Reviews* 47.9 (2018), pp. 3339–3358.
- [60] Lukas Dobusch et al. “Thermal light emission from monolayer MoS₂”. In: *Advanced Materials* 29.31 (2017), p. 1701304.
- [61] RS Sundaram et al. “Electroluminescence in single layer MoS₂”. In: *Nano letters* 13.4 (2013), pp. 1416–1421.
- [62] Britton WH Baugher et al. “Optoelectronic devices based on electrically tunable p–n diodes in a monolayer dichalcogenide”. In: *Nature nanotechnology* 9.4 (2014), p. 262.
- [63] Jason S Ross et al. “Electrically tunable excitonic light-emitting diodes based on monolayer WSe₂ p–n junctions”. In: *Nature nanotechnology* 9.4 (2014), p. 268.
- [64] F Withers et al. “Light-emitting diodes by band-structure engineering in van der Waals heterostructures”. In: *Nature materials* 14.3 (2015), p. 301.
- [65] D Edelberg et al. “Hundredfold enhancement of light emission via defect control in monolayer transition-metal dichalcogenides”. In: *arXiv preprint arXiv:1805.00127* (2018).
- [66] Martin Amani et al. “Near-unity photoluminescence quantum yield in MoS₂”. In: *Science* 350.6264 (2015), pp. 1065–1068.

- [67] Oriol Lopez-Sanchez et al. “Light generation and harvesting in a van der Waals heterostructure”. In: *Acs Nano* 8.3 (2014), pp. 3042–3048.
- [68] Andreas Pospischil, Marco M Furchi, and Thomas Mueller. “Solar-energy conversion and light emission in an atomic monolayer p–n diode”. In: *Nature nanotechnology* 9.4 (2014), p. 257.
- [69] Deep Jariwala et al. “Van der Waals materials for atomically-thin photovoltaics: promise and outlook”. In: *Acs Photonics* 4.12 (2017), pp. 2962–2970.
- [70] Liam Britnell et al. “Strong light-matter interactions in heterostructures of atomically thin films”. In: *Science* 340.6138 (2013), pp. 1311–1314.
- [71] Kin Fai Mak et al. “The valley Hall effect in MoS₂ transistors”. In: *Science* 344.6191 (2014), pp. 1489–1492.
- [72] Yunqiu Kelly Luo et al. “Opto-valleytronic spin injection in monolayer MoS₂/few-layer graphene hybrid spin valves”. In: *Nano letters* 17.6 (2017), pp. 3877–3883.
- [73] Kostya S Novoselov et al. “Electric field effect in atomically thin carbon films”. In: *science* 306.5696 (2004), pp. 666–669.
- [74] KS Novoselov and AH Castro Neto. “Two-dimensional crystals-based heterostructures: materials with tailored properties”. In: *Physica Scripta* 2012.T146 (2012), p. 014006.
- [75] Matthew A Meitl et al. “Transfer printing by kinetic control of adhesion to an elastomeric stamp”. In: *Nature materials* 5.1 (2006), p. 33.
- [76] AD Roberts. “Looking at rubber adhesion”. In: *Rubber Chemistry and Technology* 52.1 (1979), pp. 23–42.
- [77] Michel Barquins. “Adherence, friction and wear of rubber-like materials”. In: *Wear and Friction of Elastomers*. ASTM International, 1992.
- [78] Cory R Dean et al. “Boron nitride substrates for high-quality graphene electronics”. In: *Nature nanotechnology* 5.10 (2010), p. 722.
- [79] T Uwanno et al. “Fully dry PMMA transfer of graphene on h-BN using a heating/cooling system”. In: *2D Materials* 2.4 (2015), p. 041002.
- [80] PJ Zomer et al. “A transfer technique for high mobility graphene devices on commercially available hexagonal boron nitride”. In: *Applied Physics Letters* 99.23 (2011), p. 232104.
- [81] Riccardo Frisenda et al. “Recent progress in the assembly of nanodevices and van der Waals heterostructures by deterministic placement of 2D materials”. In: *Chemical Society Reviews* 47.1 (2018), pp. 53–68.
- [82] Grégory F Schneider et al. “Wedging transfer of nanostructures”. In: *Nano letters* 10.5 (2010), pp. 1912–1916.
- [83] L Wang et al. “One-dimensional electrical contact to a two-dimensional material”. In: *Science* 342.6158 (2013), pp. 614–617.

- [84] PJ Zomer et al. “Fast pick up technique for high quality heterostructures of bilayer graphene and hexagonal boron nitride”. In: *Applied Physics Letters* 105.1 (2014), p. 013101.
- [85] Filippo Pizzocchero et al. “The hot pick-up technique for batch assembly of van der Waals heterostructures”. In: *Nature communications* 7 (2016), p. 11894.
- [86] DG Purdie et al. “Cleaning interfaces in layered materials heterostructures”. In: *Nature communications* 9.1 (2018), p. 5387.
- [87] Xuesong Li et al. “Large-area synthesis of high-quality and uniform graphene films on copper foils”. In: *science* 324.5932 (2009), pp. 1312–1314.
- [88] Alfonso Reina et al. “Large area, few-layer graphene films on arbitrary substrates by chemical vapor deposition”. In: *Nano letters* 9.1 (2008), pp. 30–35.
- [89] Sukang Bae et al. “Roll-to-roll production of 30-inch graphene films for transparent electrodes”. In: *Nature nanotechnology* 5.8 (2010), p. 574.
- [90] Yi-Hsien Lee et al. “Synthesis of large-area MoS₂ atomic layers with chemical vapor deposition”. In: *Advanced materials* 24.17 (2012), pp. 2320–2325.
- [91] Keng-Ku Liu et al. “Growth of large-area and highly crystalline MoS₂ thin layers on insulating substrates”. In: *Nano letters* 12.3 (2012), pp. 1538–1544.
- [92] Yifei Yu et al. “Controlled scalable synthesis of uniform, high-quality monolayer and few-layer MoS₂ films”. In: *Scientific reports* 3 (2013), p. 1866.
- [93] Yongjie Zhan et al. “Large-area vapor-phase growth and characterization of MoS₂ atomic layers on a SiO₂ substrate”. In: *Small* 8.7 (2012), pp. 966–971.
- [94] Sanfeng Wu et al. “Vapor–solid growth of high optical quality MoS₂ monolayers with near-unity valley polarization”. In: *Acs Nano* 7.3 (2013), pp. 2768–2772.
- [95] Jonathan C Shaw et al. “Chemical vapor deposition growth of monolayer MoSe₂ nanosheets”. In: *Nano Research* 7.4 (2014), pp. 511–517.
- [96] Yu Zhang et al. “Controlled growth of high-quality monolayer WS₂ layers on sapphire and imaging its grain boundary”. In: *ACS nano* 7.10 (2013), pp. 8963–8971.
- [97] Hailong Zhou et al. “Large area growth and electrical properties of p-type WSe₂ atomic layers”. In: *Nano letters* 15.1 (2014), pp. 709–713.
- [98] Shivangi Shree et al. “Accessing high optical quality of MoS₂ monolayers grown by chemical vapor deposition”. In: *arXiv preprint arXiv:1907.03342* (2019).
- [99] Yusuke Hoshi et al. “Effect of a pick-and-drop process on optical properties of a CVD-grown monolayer tungsten disulfide”. In: *Physical Review Materials* 2.6 (2018), p. 064003.
- [100] A Delhomme et al. “Magneto-spectroscopy of exciton Rydberg states in a CVD grown WSe₂ monolayer”. In: *Applied Physics Letters* 114.23 (2019), p. 232104.
- [101] Kibum Kang et al. “High-mobility three-atom-thick semiconducting films with wafer-scale homogeneity”. In: *Nature* 520.7549 (2015), p. 656.

- [102] Xiaotian Zhang et al. “Diffusion-controlled epitaxy of large area coalesced WSe₂ monolayers on sapphire”. In: *Nano letters* 18.2 (2018), pp. 1049–1056.
- [103] Xin-Quan Zhang et al. “Synthesis of lateral heterostructures of semiconducting atomic layers”. In: *Nano letters* 15.1 (2014), pp. 410–415.
- [104] Amirhossein Behranginia et al. “Direct Growth of High Mobility and Low-Noise Lateral MoS₂–Graphene Heterostructure Electronics”. In: *Small* 13.30 (2017), p. 1604301.
- [105] Yongji Gong et al. “Vertical and in-plane heterostructures from WS₂/MoS₂ monolayers”. In: *Nature materials* 13.12 (2014), p. 1135.
- [106] Xiaoshuang Chen et al. “In-plane mosaic potential growth of large-area 2D layered semiconductors MoS₂–MoSe₂ lateral heterostructures and photodetector application”. In: *ACS applied materials & interfaces* 9.2 (2017), pp. 1684–1691.
- [107] Yongji Gong et al. “Two-step growth of two-dimensional WSe₂/MoSe₂ heterostructures”. In: *Nano letters* 15.9 (2015), pp. 6135–6141.
- [108] Yeonwoong Jung et al. “Chemically synthesized heterostructures of two-dimensional molybdenum/tungsten-based dichalcogenides with vertically aligned layers”. In: *ACS nano* 8.9 (2014), pp. 9550–9557.
- [109] AT Barton et al. “Transition metal dichalcogenide and hexagonal boron nitride heterostructures grown by molecular beam epitaxy”. In: *Microelectronic Engineering* 147 (2015), pp. 306–309.
- [110] Lei Fu et al. “Direct growth of MoS₂/h-BN heterostructures via a sulfide-resistant alloy”. In: *ACS nano* 10.2 (2016), pp. 2063–2070.
- [111] F Cadiz et al. “Excitonic linewidth approaching the homogeneous limit in MoS₂-based van der waals heterostructures”. In: *Physical Review X* 7.2 (2017), p. 021026.
- [112] Xin Zhang et al. “Phonon and Raman scattering of two-dimensional transition metal dichalcogenides from monolayer, multilayer to bulk material”. In: *Chemical Society Reviews* 44.9 (2015), pp. 2757–2785.
- [113] MM Benameur et al. “Visibility of dichalcogenide nanolayers”. In: *Nanotechnology* 22.12 (2011), p. 125706.
- [114] Fabian Cadiz et al. “Ultra-low power threshold for laser induced changes in optical properties of 2D molybdenum dichalcogenides”. In: *2D Materials* 3.4 (2016), p. 045008.
- [115] T Taniguchi and K Watanabe. “Synthesis of high-purity boron nitride single crystals under high pressure by using Ba–BN solvent”. In: *Journal of crystal growth* 303.2 (2007), pp. 525–529.
- [116] Léonard Schué et al. “Characterization methods dedicated to nanometer-thick hBN layers”. In: *arXiv preprint arXiv:1610.06858* (2016).
- [117] Wikipedia. *CIE 1931 color space*. •. URL: https://en.wikipedia.org/wiki/CIE_1931_color_space.
- [118] Wikipedia. *Color vision*. URL: https://en.wikipedia.org/wiki/Color_vision.

- [119] Christian. *Color System python class*. URL: <https://scipython.com/blog/convertng-a-spectrum-to-a-colour/>.
- [120] Roman V Gorbachev et al. “Hunting for monolayer boron nitride: optical and Raman signatures”. In: *Small* 7.4 (2011), pp. 465–468.
- [121] AM Goossens et al. “Mechanical cleaning of graphene”. In: *Applied Physics Letters* 100.7 (2012), p. 073110.
- [122] Daniel J Graham, David D Price, and Buddy D Ratner. “Solution assembled and microcontact printed monolayers of dodecanethiol on gold: a multivariate exploration of chemistry and contamination”. In: *Langmuir* 18.5 (2002), pp. 1518–1527.
- [123] Karin Glasmästar et al. “Silicone transfer during microcontact printing”. In: *Langmuir* 19.13 (2003), pp. 5475–5483.
- [124] Sami Yunus et al. “Diffusion of oligomers from polydimethylsiloxane stamps in microcontact printing: Surface analysis and possible application”. In: *Surface and Interface Analysis: An International Journal devoted to the development and application of techniques for the analysis of surfaces, interfaces and thin films* 39.12-13 (2007), pp. 922–925.
- [125] Achint Jain et al. “Minimizing residues and strain in 2D materials transferred from PDMS”. In: *Nanotechnology* 29.26 (2018), p. 265203.
- [126] E Khestanova et al. “Universal shape and pressure inside bubbles appearing in van der Waals heterostructures”. In: *Nature communications* 7 (2016), p. 12587.
- [127] N Levy et al. “Strain-induced pseudo-magnetic fields greater than 300 tesla in graphene nanobubbles”. In: *Science* 329.5991 (2010), pp. 544–547.
- [128] SJ Haigh et al. “Cross-sectional imaging of individual layers and buried interfaces of graphene-based heterostructures and superlattices”. In: *Nature materials* 11.9 (2012), p. 764.
- [129] Aidan P Rooney et al. “Observing imperfection in atomic interfaces for van der Waals heterostructures”. In: *Nano letters* 17.9 (2017), pp. 5222–5228.
- [130] Matthew R Rosenberger et al. “Nano-“Squeegee” for the Creation of Clean 2D Material Interfaces”. In: *ACS applied materials & interfaces* 10.12 (2018), pp. 10379–10387.
- [131] Youngwook Kim et al. “Reliable post-processing improvement of van der Waals heterostructures”. In: *arXiv preprint arXiv:1903.10260* (2019).
- [132] Jason S Ross et al. “Interlayer exciton optoelectronics in a 2D heterostructure p-n junction”. In: *Nano letters* 17.2 (2017), pp. 638–643.
- [133] Minsky Marvin. *Microscopy apparatus*. US Patent 3,013,467. Dec. 1961.
- [134] Yilei Li et al. “Measurement of the optical dielectric function of monolayer transition-metal dichalcogenides: MoS₂, MoSe₂, WS₂, and WSe₂”. In: *Physical Review B* 90.20 (2014), p. 205422.

-
- [135] Amalia Patane and Naci Balkan. *Semiconductor Research: Experimental Techniques*. Vol. 150. Springer Science & Business Media, 2012.
- [136] Louis BOUET. “Valley dynamics and excitonic properties in monolayer transition metal dichalcogenides”. Institut National des Sciences Appliquées de Toulouse, 2015.
- [137] Daniel Rhodes et al. “Disorder in van der Waals heterostructures of 2D materials”. In: *Nature materials* 18.6 (2019), p. 541.
- [138] Tobias Korn et al. “Low-temperature photocarrier dynamics in monolayer MoS₂”. In: *Applied Physics Letters* 99.10 (2011), p. 102109.
- [139] G Kioseoglou et al. “Valley polarization and intervalley scattering in monolayer MoS₂”. In: *Applied Physics Letters* 101.22 (2012), p. 221907.
- [140] Andreas V Stier et al. “Exciton diamagnetic shifts and valley Zeeman effects in monolayer WS₂ and MoS₂ to 65 Tesla”. In: *Nature communications* 7 (2016), p. 10643.
- [141] Jason S Ross et al. “Electrical control of neutral and charged excitons in a monolayer semiconductor”. In: *Nature communications* 4 (2013), p. 1474.
- [142] Galan Moody et al. “Intrinsic homogeneous linewidth and broadening mechanisms of excitons in monolayer transition metal dichalcogenides”. In: *Nature communications* 6 (2015), p. 8315.
- [143] Prasenjit Dey et al. “Optical coherence in atomic-monolayer transition-metal dichalcogenides limited by electron-phonon interactions”. In: *Physical review letters* 116.12 (2016), p. 127402.
- [144] Sandhaya Koirala et al. “Homogeneous linewidth broadening and exciton dephasing mechanism in MoT e₂”. In: *Physical Review B* 93.7 (2016), p. 075411.
- [145] Malte Selig et al. “Excitonic linewidth and coherence lifetime in monolayer transition metal dichalcogenides”. In: *Nature communications* 7 (2016), p. 13279.
- [146] Jakob Wierzbowski et al. “Direct exciton emission from atomically thin transition metal dichalcogenide heterostructures near the lifetime limit”. In: *Scientific reports* 7.1 (2017), p. 12383.
- [147] Seongjoon Ahn et al. “Prevention of transition metal dichalcogenide photodegradation by encapsulation with h-BN layers”. In: *ACS nano* 10.9 (2016), pp. 8973–8979.
- [148] Michele Buscema et al. “The effect of the substrate on the Raman and photoluminescence emission of single-layer MoS₂”. In: *Nano research* 7.4 (2014), pp. 561–571.
- [149] Yifei Yu et al. “Engineering Substrate Interactions for High Luminescence Efficiency of Transition-Metal Dichalcogenide Monolayers”. In: *Advanced Functional Materials* 26.26 (2016), pp. 4733–4739.
- [150] D Sercombe et al. “Optical investigation of the natural electron doping in thin MoS₂ films deposited on dielectric substrates”. In: *Scientific reports* 3 (2013), p. 3489.

- [151] Benjamin J Robinson et al. “Structural, optical and electrostatic properties of single and few-layers MoS₂: effect of substrate”. In: *2D Materials* 2.1 (2015), p. 015005.
- [152] Masa Ishigami et al. “Atomic structure of graphene on SiO₂”. In: *Nano letters* 7.6 (2007), pp. 1643–1648.
- [153] Myrsini Lafkioti et al. “Graphene on a hydrophobic substrate: doping reduction and hysteresis suppression under ambient conditions”. In: *Nano letters* 10.4 (2010), pp. 1149–1153.
- [154] Tsuneya Ando. “Screening effect and impurity scattering in monolayer graphene”. In: *Journal of the Physical Society of Japan* 75.7 (2006), pp. 074716–074716.
- [155] Simone Fratini and Francisco Guinea. “Substrate-limited electron dynamics in graphene”. In: *Physical Review B* 77.19 (2008), p. 195415.
- [156] MI Katsnelson and AK Geim. “Electron scattering on microscopic corrugations in graphene”. In: *Philosophical Transactions of the Royal Society A: Mathematical, Physical and Engineering Sciences* 366.1863 (2007), pp. 195–204.
- [157] SV Morozov et al. “Giant intrinsic carrier mobilities in graphene and its bilayer”. In: *Physical review letters* 100.1 (2008), p. 016602.
- [158] S Majety et al. “Semiconducting hexagonal boron nitride for deep ultraviolet photonics”. In: *Quantum Sensing and Nanophotonic Devices IX*. Vol. 8268. International Society for Optics and Photonics. 2012, 82682R.
- [159] Liam Britnell et al. “Electron tunneling through ultrathin boron nitride crystalline barriers”. In: *Nano letters* 12.3 (2012), pp. 1707–1710.
- [160] B Han et al. “Exciton States in Monolayer MoSe₂ and MoTe₂ Probed by Upconversion Spectroscopy”. In: *Physical Review X* 8.3 (2018), p. 031073.
- [161] Andreas V Stier et al. “Probing the influence of dielectric environment on excitons in monolayer WSe₂: insight from high magnetic fields”. In: *Nano letters* 16.11 (2016), pp. 7054–7060.
- [162] HH Fang et al. “Control of the Exciton Radiative Lifetime in van der Waals Heterostructures”. In: *arXiv preprint arXiv:1902.00670* (2019).
- [163] Obafunso A Ajayi et al. “Approaching the intrinsic photoluminescence linewidth in transition metal dichalcogenide monolayers”. In: *2D Materials* 4.3 (2017), p. 031011.
- [164] Tomasz Jakubczyk et al. “Coherence and Density Dynamics of Excitons in a Single-Layer MoS₂ Reaching the Homogeneous Limit”. In: *ACS nano* (2019).
- [165] Eric W Martin et al. “Encapsulation Narrows Excitonic Homogeneous Linewidth of Exfoliated MoSe₂ Monolayer”. In: *arXiv preprint arXiv:1810.09834* (2018).
- [166] HY Fan. “Temperature dependence of the energy gap in semiconductors”. In: *Physical Review* 82.6 (1951), p. 900.
- [167] KP O’Donnell and X Chen. “Temperature dependence of semiconductor band gaps”. In: *Applied physics letters* 58.25 (1991), pp. 2924–2926.

- [168] George Kioseoglou et al. “Optical polarization and intervalley scattering in single layers of MoS 2 and MoSe 2”. In: *Scientific reports* 6 (2016), p. 25041.
- [169] AA Mitioğlu et al. “Magnetoexcitons in large area CVD-grown monolayer MoS 2 and MoSe 2 on sapphire”. In: *Physical Review B* 93.16 (2016), p. 165412.
- [170] Jason W Christopher, Bennett B Goldberg, and Anna K Swan. “Long tailed trions in monolayer MoS 2: Temperature dependent asymmetry and resulting red-shift of trion photoluminescence spectra”. In: *Scientific reports* 7.1 (2017), p. 14062.
- [171] David MacNeill et al. “Breaking of valley degeneracy by magnetic field in monolayer MoSe 2”. In: *Physical review letters* 114.3 (2015), p. 037401.
- [172] G Wang et al. “Magneto-optics in transition metal diselenide monolayers”. In: *2D Materials* 2.3 (2015), p. 034002.
- [173] DV Rybkovskiy, IC Gerber, and MV Durnev. “Atomically inspired k·p approach and valley Zeeman effect in transition metal dichalcogenide monolayers”. In: *Physical Review B* 95.15 (2017), p. 155406.
- [174] M Goryca et al. “Revealing exciton masses and dielectric properties of monolayer semiconductors with high magnetic fields”. In: *arXiv preprint arXiv:1904.03238* (2019).
- [175] Patrick Back et al. “Giant paramagnetism-induced valley polarization of electrons in charge-tunable monolayer mose 2”. In: *Physical review letters* 118.23 (2017), p. 237404.
- [176] Gang Wang et al. “Control of exciton valley coherence in transition metal dichalcogenide monolayers”. In: *Physical review letters* 117.18 (2016), p. 187401.
- [177] Ziliang Ye, Dezheng Sun, and Tony F Heinz. “Optical manipulation of valley pseudospin”. In: *Nature physics* 13.1 (2017), p. 26.
- [178] Kin Fai Mak et al. “Control of valley polarization in monolayer MoS 2 by optical helicity”. In: *Nature nanotechnology* 7.8 (2012), p. 494.
- [179] Jill A Miwa et al. “Electronic structure of epitaxial single-layer MoS 2”. In: *Physical review letters* 114.4 (2015), p. 046802.
- [180] Tawinan Cheiwchanchamnangij and Walter RL Lambrecht. “Quasiparticle band structure calculation of monolayer, bilayer, and bulk MoS 2”. In: *Physical Review B* 85.20 (2012), p. 205302.
- [181] Cédric Robert et al. “Optical spectroscopy of excited exciton states in MoS 2 monolayers in van der Waals heterostructures”. In: *Physical Review Materials* 2.1 (2018), p. 011001.
- [182] Eougenious L Ivchenko. *Optical spectroscopy of semiconductor nanostructures*. Alpha Science Int’l Ltd., 2005.
- [183] Pierluigi Cudazzo, Ilya V Tokatly, and Angel Rubio. “Dielectric screening in two-dimensional insulators: Implications for excitonic and impurity states in graphene”. In: *Physical Review B* 84.8 (2011), p. 085406.

- [184] Timothy C Berkelbach, Mark S Hybertsen, and David R Reichman. “Theory of neutral and charged excitons in monolayer transition metal dichalcogenides”. In: *Physical Review B* 88.4 (2013), p. 045318.
- [185] Fengcheng Wu, Fanyao Qu, and Allan H MacDonald. “Exciton band structure of monolayer MoS₂”. In: *Physical Review B* 91.7 (2015), p. 075310.
- [186] S Nakhaie et al. “Synthesis of atomically thin hexagonal boron nitride films on nickel foils by molecular beam epitaxy”. In: *Applied Physics Letters* 106.21 (2015), p. 213108.
- [187] Joseph M Wofford et al. “A hybrid MBE-based growth method for large-area synthesis of stacked hexagonal boron nitride/graphene heterostructures”. In: *Scientific reports* 7 (2017), p. 43644.
- [188] E Courtade et al. “Spectrally narrow exciton luminescence from monolayer MoS₂ and MoSe₂ exfoliated onto epitaxially grown hexagonal BN”. In: *Applied Physics Letters* 113.3 (2018), p. 032106.
- [189] E Courtade et al. “Charged excitons in monolayer WSe₂: experiment and theory”. In: *Physical Review B* 96.8 (2017), p. 085302.
- [190] Shanshan Wang, Xiaochen Wang, and Jamie H Warner. “All chemical vapor deposition growth of MoS₂: h-BN vertical van der Waals heterostructures”. In: *ACS nano* 9.5 (2015), pp. 5246–5254.
- [191] RA Suris et al. “Excitons and Trions Modified by Interaction with a Two-Dimensional Electron Gas”. In: *physica status solidi (b)* 227.2 (2001), pp. 343–352.
- [192] Meinrad Sidler et al. “Fermi polaron-polaritons in charge-tunable atomically thin semiconductors”. In: *Nature Physics* 13.3 (2017), p. 255.
- [193] Kin Fai Mak et al. “Tightly bound trions in monolayer MoS₂”. In: *Nature materials* 12.3 (2013), p. 207.
- [194] Shinichiro Mouri, Yuhei Miyauchi, and Kazunari Matsuda. “Tunable photoluminescence of monolayer MoS₂ via chemical doping”. In: *Nano letters* 13.12 (2013), pp. 5944–5948.
- [195] Jonas Gaël Roch et al. “Spin-polarized electrons in monolayer MoS₂”. In: *Nature nanotechnology* 14.5 (2019), p. 432.
- [196] Jessica Lindlau et al. “Identifying optical signatures of momentum-dark excitons in transition metal dichalcogenide monolayers”. In: *arXiv preprint arXiv:1710.00988* (2017).
- [197] Hanan Dery and Yang Song. “Polarization analysis of excitons in monolayer and bilayer transition-metal dichalcogenides”. In: *Physical Review B* 92.12 (2015), p. 125431.
- [198] Zefang Wang et al. “Probing the spin-polarized electronic band structure in monolayer transition metal dichalcogenides by optical spectroscopy”. In: *Nano letters* 17.2 (2017), pp. 740–746.
- [199] A Thilagam. “Two-dimensional charged-exciton complexes”. In: *Physical Review B* 55.12 (1997), p. 7804.

- [200] M Van der Donck, M Zarenia, and FM Peeters. “Excitons and trions in monolayer transition metal dichalcogenides: A comparative study between the multiband model and the quadratic single-band model”. In: *Physical Review B* 96.3 (2017), p. 035131.
- [201] Murray A Lampert. “Mobile and immobile effective-mass-particle complexes in nonmetallic solids”. In: *Physical Review Letters* 1.12 (1958), p. 450.
- [202] RA Sergeev and RA Suris. “Ground-state energy of X- and X+ trions in a two-dimensional quantum well at an arbitrary mass ratio”. In: *Physics of the Solid State* 43.4 (2001), pp. 746–751.
- [203] MA Semina, RA Sergeev, and RA Suris. “Binding energies of 2D laterally confined trions”. In: *Physica E: Low-dimensional Systems and Nanostructures* 40.5 (2008), pp. 1357–1359.
- [204] Marcin Szyniszewski et al. “Binding energies of trions and biexcitons in two-dimensional semiconductors from diffusion quantum Monte Carlo calculations”. In: *Physical Review B* 95.8 (2017), p. 081301.
- [205] Bogdan Ganchev et al. “Three-particle complexes in two-dimensional semiconductors”. In: *Physical review letters* 114.10 (2015), p. 107401.
- [206] Hongyi Yu et al. “Dirac cones and Dirac saddle points of bright excitons in monolayer transition metal dichalcogenides”. In: *Nature communications* 5 (2014), p. 3876.
- [207] Aaron M Jones et al. “Excitonic luminescence upconversion in a two-dimensional semiconductor”. In: *Nature Physics* 12.4 (2016), p. 323.
- [208] Akshay Singh et al. “Long-lived valley polarization of intravalley trions in monolayer WSe 2”. In: *Physical review letters* 117.25 (2016), p. 257402.
- [209] Gerd Plechinger et al. “Trion fine structure and coupled spin–valley dynamics in monolayer tungsten disulfide”. In: *Nature communications* 7 (2016), p. 12715.
- [210] Ziliang Ye et al. “Efficient generation of neutral and charged biexcitons in encapsulated WSe 2 monolayers”. In: *Nature communications* 9.1 (2018), p. 3718.
- [211] Matteo Barbone et al. “Charge-tuneable biexciton complexes in monolayer WSe 2”. In: *Nature communications* 9.1 (2018), p. 3721.
- [212] JC Kim, DR Wake, and JP Wolfe. “Thermodynamics of biexcitons in a GaAs quantum well”. In: *Physical Review B* 50.20 (1994), p. 15099.
- [213] Andreas V Stier et al. “Magneto-optics of exciton Rydberg states in a monolayer semiconductor”. In: *Physical review letters* 120.5 (2018), p. 057405.
- [214] Riccardo Pisoni et al. “Interactions and magnetotransport through spin-valley coupled Landau levels in monolayer MoS 2”. In: *Physical review letters* 121.24 (2018), p. 247701.
- [215] Stefano Larentis et al. “Large effective mass and interaction-enhanced Zeeman splitting of K-valley electrons in MoSe 2”. In: *Physical Review B* 97.20 (2018), p. 201407.

- [216] Samuel Brem et al. “Phonon-assisted Photoluminescence from Dark Excitons in Monolayers of Transition Metal Dichalcogenides”. In: *arXiv preprint arXiv:1904.04711* (2019).
- [217] Ding Zhong et al. “Van der Waals engineering of ferromagnetic semiconductor heterostructures for spin and valleytronics”. In: *Science Advances* 3.5 (2017), e1603113.
- [218] Christian Schneider et al. “Two-dimensional semiconductors in the regime of strong light-matter coupling”. In: *Nature communications* 9.1 (2018), p. 2695.
- [219] Evgeny M Alexeev et al. “Resonantly hybridized excitons in moiré superlattices in van der Waals heterostructures”. In: *Nature* 567.7746 (2019), p. 81.
- [220] Bernhard Urbaszek and Ajit Srivastava. *Materials in flatland twist and shine*. 2019.
- [221] Iann C Gerber et al. “Interlayer excitons in bilayer MoS₂ with strong oscillator strength up to room temperature”. In: *Physical Review B* 99.3 (2019), p. 035443.
- [222] Chendong Zhang et al. “Interlayer couplings, Moiré patterns, and 2D electronic superlattices in MoS₂/WSe₂ hetero-bilayers”. In: *Science advances* 3.1 (2017), e1601459.
- [223] Kha Tran et al. “Evidence for moiré excitons in van der Waals heterostructures”. In: *Nature* 567.7746 (2019), p. 71.
- [224] Hongyi Yu et al. “Moiré excitons: From programmable quantum emitter arrays to spin-orbit-coupled artificial lattices”. In: *Science advances* 3.11 (2017), e1701696.
- [225] Kyle L Seyler et al. “Signatures of moiré-trapped valley excitons in MoSe₂/WSe₂ heterobilayers”. In: *Nature* 567.7746 (2019), p. 66.